UNIVERSITY OF SOUTHAMPTON

FACULTY OF ENGINEERING, SCIENCE & MATHEMATICS

School of Engineering and Computer Science

Fabrication and Optical Characterisation of a Photonic Crystal Integrated into a Luminescent Si-rich Silicon-Dioxide Waveguide

by

Rebecca Tarn Neal

Thesis for the degree of Doctor of Philosophy

March 2004

UNIVERSITY OF SOUTHAMPTON

ABSTRACT

FACULTY OF ENGINEERING, SCIENCE & MATHEMATICS

SCHOOL OF ELECTRONICS AND COMPUTER SCIENCE

Doctor of Philosophy

FABRICATION AND OPTICAL CHARACTERISATION OF A PHOTONIC CRYSTAL INTEGRATED INTO A LUMINESCENT SI-RICH SILICON-DIOXIDE WAVEGUIDE

by Rebecca Tarn Neal

This thesis concerns the melding of two research areas: that of light emitting silicon devices based upon silicon nanocrystals, and that of photonic crystals (PCs). The focus has primarily been working towards using photonic crystals as a method of controlling the photoluminescence emission spectrum from the silicon nanocrystals.

A method was developed for the fabrication of waveguides with a core layer of silicon-rich silicon dioxide (SRSO) which exhibited photoluminescence in the wavelength range from 600-1100nm when annealed. Ultrabroadband transmission measurements showed that while unannealed and optically quiescent SRSO waveguides had good optical transmission in the visible region, annealed waveguides were strongly absorbent below a wavelength of 700nm. Other studies also showed that the SRSO photoluminescence intensity was increased by increasing the duration of the thermal anneal stage, and that the wavelength of peak intensity could be shifted by modifying the incorporation of silicon into the SRSO layer. To explain the results obtained, several theories were advanced on the material properties of SRSO.

Once the SRSO waveguides were well characterised, they were patterned with 2D triangular lattice PCs. A laser was used to excite photoluminescence from the core region, and was measured having passed through the photonic crystal. When viewed through the photonic crystal, a strong modification of the transmitted photoluminescence spectrum was recorded. Plane wave and Finite Difference Time Domain simulations were used to identify individual higher order photonic bands in the observed spectra.

This work paves the way for the use of 2D photonic crystals as an integrated way of tailoring the propagation and group velocity dispersion of SRSO core photoluminescence through a waveguide structure, with potential applications in future integrated PC-based optical circuitry.

Table of Contents

List of Figures

Symbols

n_1	High refractive index, waveguide/optical fibre core
n_2	Lower refractive index, waveguide/optical fibre cladding
θ_i	Incident angle from the normal
θ_c	Critical angle
θ_t	Transmitted angle from the normal
$r_{//}$	Parallel reflection coefficient
$r_{\perp}$	Perpendicular reflection coefficient
$t_{//}$	Parallel transmission coefficient
$t_{\perp}$	Perpendicular transmission coefficient
k	Crystal momentum
λ_c	Central wavelength in a PAWG
ΔL	Change in length for waveguides in a PAWG
E_g	Electronic bandgap
h	Planck's constant = 6.626×10^{34} Js
c	Speed of light in vacuum = 3×10^{8} ms^{-1}
q	Unit of electronic charge = 1.6×10^{-19}J
eV	Electron Volts
a	Lattice pitch for a photonic crystal
w	Angular frequency
k	Wave vector
ε	Dielectric constant
$\mathbf{R}$	Lattice vectors
$\mathbf{a_1},\mathbf{a_2},\mathbf{a_3}$	Primitive lattice vectors
$\mathbf{G}$	Reciprocal lattice vectors
$\mathbf{b_1},\mathbf{b_2},\mathbf{b_3}$	Primitive reciprocal lattice vectors
δ_{ij}	The delta function
V	The dimensionless waveguide parameter
n_1	Core refractive index
n_2	Cladding refractive index
d	Waveguide core thickness
λ_0	Wavelength of operation of AWG
β	Propagation constant
ω	The angular frequency of the mode
b	dimensionless propagation constant
n_{eff}	effective refractive index of the guided mode
R_N	Radius of curvature of the innermost waveguide of an AWG
L_{slab}	Separation between the slab waveguides of an AWG
f	Radius of curvature of the slab waveguide section of an AWG
N	Total number of waveguides in the array of an AWG
R_0	Outermost waveguide of an AWG
S_N	Straight length of the innermost waveguide of an AWG
ΔL	Path length difference between each waveguide of the array of an AWG
λ_0	Central wavelength of operation for an AWG

α_{loss}	Bend loss coefficient
α	Offset angle of the slab waveguides in an AWG
θ_j	Angle of waveguide *j* of the AWG from the *Q*-*Q'* line
γ	Ratio of N_2O:SiH_4

Acronyms

SMF	Single Mode Fibre
TIR	Total Internal Reflection
NA	Numerical aperture
EDFA	Erbium-doped Fibre Amplifier
IOC	Integrated optical circuit
TE	Transverse Electric
TM	Transverse Magnetic
VLSI	Very Large Scale Integration
IC	Integrated circuit (electrical)
SOI	Silicon on insulator
MOS	Metal Oxide Semiconductor
PECVD	Plasma Enhanced Chemical Vapour Deposition
LTO	Low Temperature Oxidation
LPCVD	Low Pressure Chemical Vapour Deposition
TEOS	Tetraethylorthosilicate
PAWG	Phased Array Waveguide Grating
WDM	Wavelength Division Multiplexed
FBG	Fibre Bragg Grating
LED	Light Emitting Diode
PL	Photoluminescence
EL	Electroluminescence
HF	Hydrofluoric acid (silicon etchant)
PS	Porous silicon
Si-nc	Silicon Nanocrystals
ASE	Amplified Spontaneous Emission
fcc	Face-centred cubic
PC	Photonic Crystal
PBG	Photonic Band Gap
BZ	Brillouin zone
FNA	Fuming Nitric Acid
Si-nc	Silicon nanocrystals
SRSO	Silicon-Rich Silicon Dioxide
SUMC	Southampton University Microelectronics Centre
CMOS	Complementary Metal Oxide Silicon
e-beam	electron beam
RIE	Reactive Ion Etch
IBM	Ion Beam Milling
SEM	Scanning Electron Microscope
FDTD	Finite Difference Time Domain

Symbolic Representation of Elements and Material Composites

CdSe/ZnO	Cadmium Selenide/Zinc Oxide
TiO_2	Titania
Si	Silicon
SiO_2	Silicon Dioxide
SiGe	Silicon Germanium
Si_3N_4	Silicon Nitride
SiON	Silicon Oxynitride
O-H	Oxygen-Hydrogen bond
GaAs	Gallium Arsenide
InGaAsP	Indium Gallium Arsenide Phosphorus
Er	Erbium
ITO	Indium-Tin-Oxide
SiH_4	Silane
N_2O	Nitrous Oxide
$Si:SiO_2$	Silicon-Rich Silicon Dioxide
SiH_4	Silane
N_2	Nitrogen
N_2O	Nitrous Oxide
NH_3	Ammonia
Cr	Chrome

Acknowledgements

First, I would like to thank my supervisor, Prof. Greg Parker for giving me the opportunity to carry out this research, and who never disappointed when I needed his help. Many other people have assisted me over the years, with Dr. Martin Charlton and Dr. Chris Finlayson in particular sharing their experience and time beyond anything I could have expected. Other notable help has come from Dr. Caterina Netti, Prof. Jeremy Baumberg, Peter Ayliffe, and Dr. Majd Zoorob. Tribute must also be paid to the staff in the Southampton University Microelectronics Cleanroom, Mike Josey in particular, for the guidance and support provided throughout the processing stages of the research. Finally, thanks to my parents, who introduced me to the idea of a PhD in the first place, and who provided just the right kind of support exactly when it was most needed.

And to all the people in the Microelectronics group who've passed through during my time here, thanks for the good times!

1 Introduction and Literature Review

1.1 Integrated Optical Devices (passive)

It was in 1960 that Dr. Kao proposed using optical fibres for telecommunications purposes. By 1970 a practical, low-loss, optical fibre was developed at Corning Inc. [1] and the field of optical communications was born. Optical fibres are cylinders of glass, usually with a core 8μm in diameter for single mode fibres (SMF). An SMF is an optical fibre which guides only one optical mode at the specified wavelength. The glass cylinder, known as the *core*, is surrounded by a glass *cladding* which is of a lower refractive index.

Light is guided along an SMF by total internal reflection. A ray of light travelling in a theoretically lossless material of refractive index n_1, when incident upon another lossless material with refractive index n_2, will behave in one of two ways. The ray of light may be partially transmitted and partially reflected, or it may be reflected wholly back into the material of higher refractive index. Which of these actions occurs depends upon the angle at which the light ray approaches the boundary between the two materials, known as the angle of incidence (θ_i). If angle of incidence is less than the *critical* angle θ_c, measured from the normal, then the light will be partially transmitted. If the angle of incidence is greater than θ_c, the light ray will be reflected back into the material of higher refractive index. This is known as total internal reflection (TIR). θ_c is a function of the two refractive indices of the system, and is determined by the formula:

$$\theta_c = \sin^{-1}\left(\frac{n_2}{n_1}\right) \qquad , n_1 > n_2 \tag{1.1}$$

which is derived from Snell's law:

$$\frac{n_2}{n_1} = \frac{\sin\theta_i}{\sin\theta_t} \tag{1.2}$$

where n_1, n_2, θ_i, θ_t, θ_c all correspond with their representations in Figure 1.1 (a), which is located on the next page.

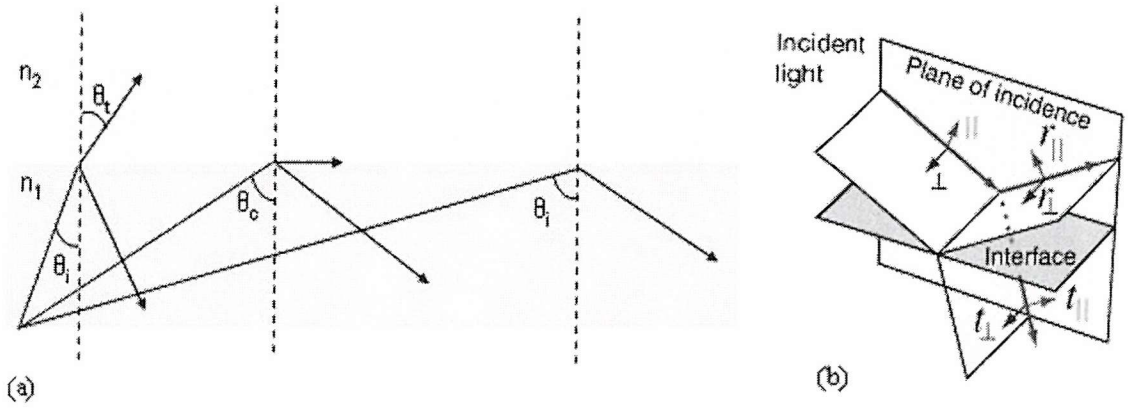

Figure 1.1 - Graphical illustrations of total internal reflection for (a) a 2D and (b) 3D representation.

The percentages of light transmitted and reflected is governed by Fresnel's Equations, which state that for light from a medium of index n_1 incident upon a medium of index n_2 at an angle of θ_i and transmitted at an angle of θ_t, the parallel ($_{//}$) and perpendicular ($_{\perp}$) reflection (r) and transmission (t) coefficients are as follows. The coefficients correspond with those in Figure 1.1 (b).

$$r_{//} = \frac{\tan(\theta_i - \theta_t)}{\tan(\theta_i + \theta_t)} \qquad |r_{\perp}| = \frac{\sin(\theta_i - \theta_t)}{\sin(\theta_i + \theta_t)} \tag{1.3}$$

$$t_{//} = \frac{2\sin\theta_t \cos\theta_i}{\sin(\theta_i + \theta_t)\cos(\theta_i - \theta_t)} \qquad t_{\perp} = \frac{2\sin\theta_t \cos\theta_i}{\sin(\theta_i + \theta_t)}$$

These coefficients are fractional amplitudes, and must be squared to get the fractional intensities for reflection and transmission. The transmission coefficient gives the

transmitted energy flux per unit area and, as the energy density changes for a different refractive index, this coefficient must be adjusted using the relationship below, which applies equally to either the parallel or perpendicular cases.

$$r^2 + t^2 \frac{n_2 \cos\theta_t}{n_1 \cos\theta_i} = 1 \tag{1.4}$$

The numerical aperture (NA), which is the mathematical sine of the fibre acceptance angle, is given by the following relation:

$$NA = \sqrt{n_1^{\,2} - n_2^{\,2}} \quad , n_1 > n_2 \tag{1.5}$$

Light launched into an optical fibre must therefore be traveling nearly exactly along the central axis of the optical fibre, and the greater the difference between the refractive indices n_1 and n_2, the larger the acceptance angle becomes. As an SMF is so narrow, and the refractive index contrast between n_1 and n_2 is typically so small (~.01%), light which is already traveling in the optical fibre will be incident upon the boundary between the core layer (n_1) and the cladding layer (n_2) at an angle approaching 90° from the normal in order to be guided along the optical fibre by TIR, as is shown in Figure 1.2 (a).

Light which has entered the fibre within the boundaries of the NA will remain confined within the core of the optical fibre for long distances. Optical absorption within the core region, combined with Rayleigh scattering from impurities and defects in the material will each contribute towards loss in the optical fibre. A loss spectrum for a typical low-loss optical fibre circa 1979 [1] is shown in Figure 1.2 (b).

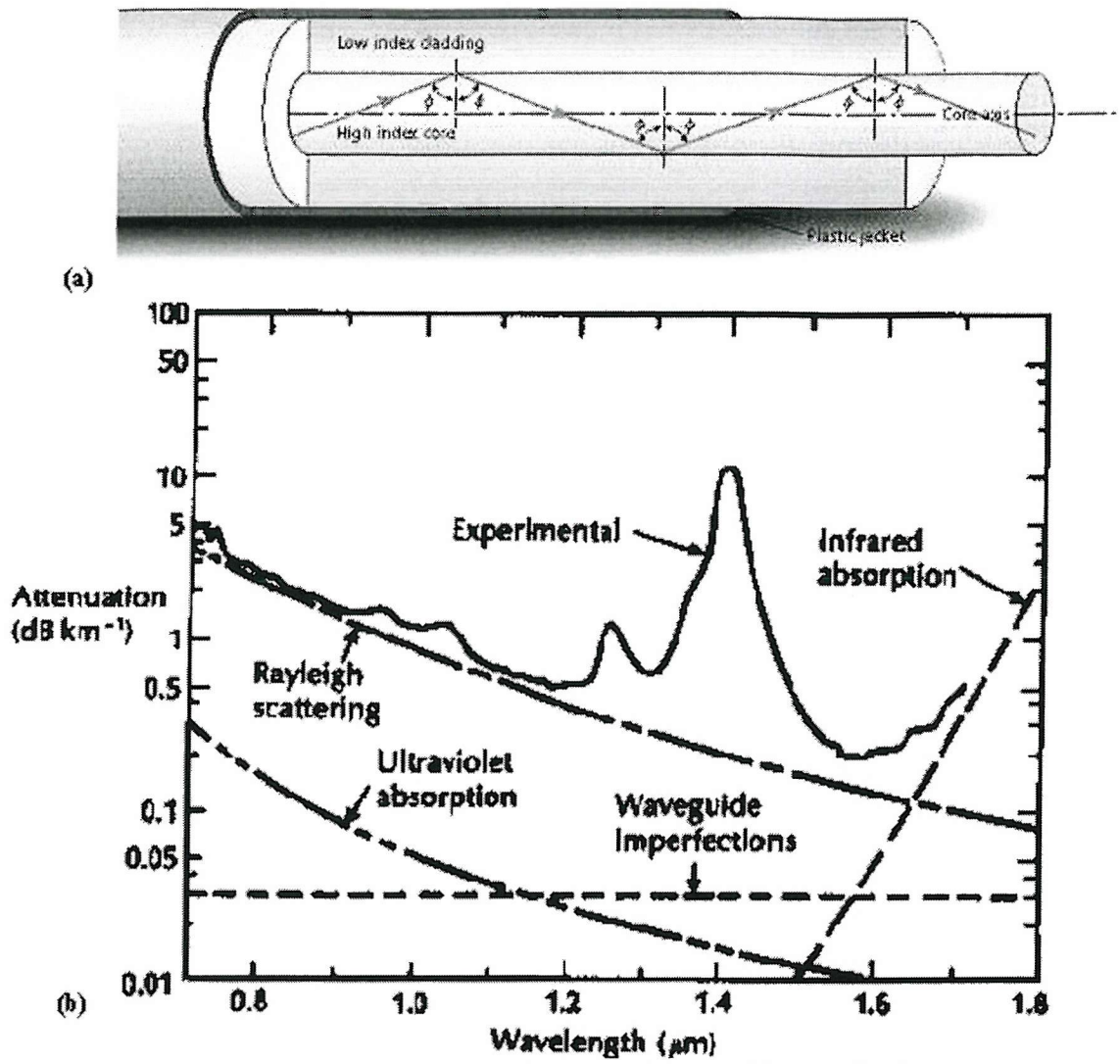

Figure 1.2 - (a) Schematic diagram of an optical fibre and (b) optical loss mechanisms

Optical transmission loss for modern telecommunications fibres is now quoted at below 0.1dB/km for the low-loss wavelength region around 1550nm, at which the Erbium-Doped Fibre Amplifier (EDFA) also operates. For telecommunications purposes, signals in a network of optical fibres pass through a series of routers, splitters, multiplexers and optical switches, all optimised for operation at a wavelength of 1550nm. Each of these optical components will have an insertion loss associated with it resulting from Fresnel reflection at the interface as described above, in addition to coupling loss, mode mismatch, and other loss mechanisms. For example the standard attenuation in a conventional low-loss optical connector is a maximum of 0.30dB, with an average of 0.097dB.

Over the past decade there has been interest in replacing discrete optical components with their integrated planar equivalents. Integrated Optical Circuits (IOCs) composed of planar optical components have the potential to be mass-produced in a similar way to the electronic microchip. IOCs would also be smaller, more robust, and simpler to manufacture than their discrete, bulk counterparts. A further incentive in the development of the IOC is that of integrating the optical circuit with the integrated electrical circuit, removing one barrier between the computer microchip and the optical fibre-based telecommunications network. The greatest advantage of the IOC however, is cost. A mass-produced IOC, developed and produced in a clean room similar to those used in microelectronics, would be significantly cheaper than a system formed from discrete optical parts which perform the same function.

The fundamental component of an IOC is the waveguide, the planar realisation of an optical fiber on a flat surface. A waveguide which confines light in only one dimension is called a slab waveguide (Figure 1.2(a)), and is formed from a layer of high refractive index with lower refractive index above and below. In these waveguides, light may travel in the entire plane of the high refractive index layer. A waveguide which is more like an optical fibre, a rib waveguide (Figure 1.2(b)) is formed of a strip of high refractive index material surrounded by lower refractive index material or materials. This confines light in two dimensions, permitting propagation along the third. As with optical fibers, the region of high refractive index is called the core region, and the region of lower refractive index is the cladding layer.

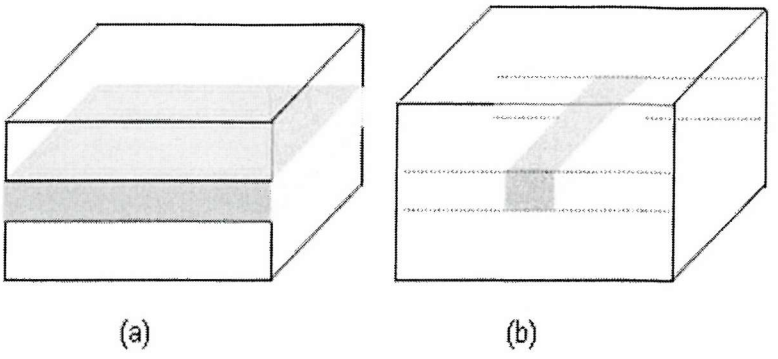

Figure 1.3 - A planar slab (a) and rib (b) waveguide

Working with waveguides, which are asymmetric components (unlike the optical fibre), it is important to be aware of the polarisation. Light, composed of orthogonal electric and magnetic fields, is defined as being in the Transverse Electric (TE) polarisation if the electric field is confined within the plane of the waveguide. Transverse Magnetic (TM) polarisation is when the magnetic field is confined within that plane.

1.1.1 Planar optical devices not in silicon

The integrated optical circuits most easily compatible with the optical fibre telecommunications industry are those fabricated upon glass substrates. Glass substrates made from low-loss glasses, have a refractive index which is similar to that of the silica glass used as the core material for an optical fibre. Glass waveguides may also be formed from fused silica.

Waveguides on a glass substrate are formed by a variety of methods, including the diffusion of a dopant into the proposed waveguide region, raising the local refractive index (Figure 1.1.1(a)) [2]. Another related method is known as ion-exchange. In this method a strip of material to be diffused into the waveguide is placed upon the surface of the wafer where a waveguide is desired, and the whole arrangement is heated, which prompts migration of that material into the substrate, replacing ions

which diffuse into the strip of meterial, which is later removed. Waveguides formed by the diffusion method commonly have a refractive index profile which is highest at the surface, and decreases with increasing depth. Modifying the diffusion temperature, duration, and dopant size it is possible to tailor the refractive index profile of the diffused waveguide.

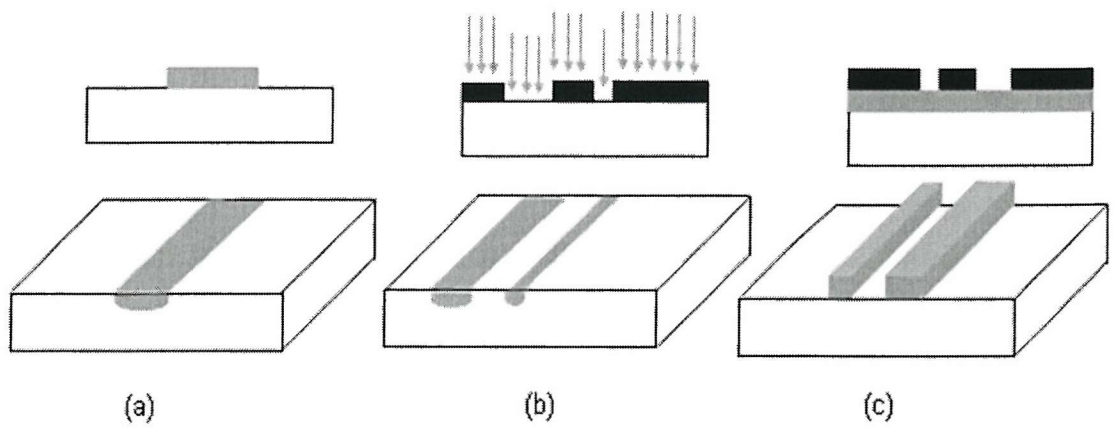

Figure 1.1.1 - Waveguide fabrication methods including (a) in-diffusion of a dopant, (b) ion implantation and (c) deposition and etching of another layer.

Ion implantation (Figure 1.1.1(b)) through gaps in a mask is another method used for producing waveguides. In this technique, ions of the dopant material are accelerated by high electric fields onto the substrate. Waveguides formed by this method have the region of highest refractive index buried slightly below the surface, at a depth depending on the energy of the implanted ions. Beyond this depth the refractive index profile tapers off in a manner similar to that of a diffused waveguide. Due to the high energy impact of the ions, waveguides which have been ion-implanted have damaged substrates. This may be cured by a thermal anneal [3].

Both diffusion and implantation cause only small changes to the refractive index of the glass substrate. The smoothly tapering refractive index profile provides weak confinement for optical modes, and the waveguides must therefore be large, frequently several times the wavelength of the light which they are guiding. This is similar to optical fibers, where a typical single mode optical fibre carrying a signal at a wavelength 1.55μm would be between 8-10μm.

The third method for waveguide fabrication shown in Figure 1.1.1(c) is that of deposition and subsequent etching of a higher refractive index layer. This method permits great flexibility in choosing the refractive index of the core layer, and also permits the use of waveguide core materials with properties not available through standard glasses, such as optical activity and piezo-electric susceptibility.

A waveguide with a large refractive index contrast between the core and the cladding region has both advantages and disadvantages. A high refractive index contrast waveguide provides strong confinement for guided light, permitting small waveguide size and decreasing the minimum radius of any waveguide bends without loss of optical power [4]. The insertion loss from an optical fiber ($n \approx 1.46$) into the waveguide due to Fresnel backreflection will however be high, reducing its compatibility with optical fiber systems. Materials which have been deposited onto the surface of glass substrates as waveguide cores include Cadmium Selenide/Zinc Oxide (CdSe/ZnO) composite coatings [5], Titania (TiO_2) [6], and organic materials [7].

1.1.2 Planar optical devices in silicon

Silicon (Si) is the element at the foundation of the microelectronics industry. It has been studied and worked with more extensively than any other material in modern times. With high end silicon fabrication facilities now working on silicon wafers with a diameter of 300mm (12 inches), silicon is without competition as the basic material upon which Very Large Scale Integration (VLSI) integrated circuits (ICs) must be based. Silicon, with a refractive index of 3.5040 at 1.319μm [169] is transparent for wavelengths longer than 1.1μm. Silicon was chosen over Germanium, the other type IV semiconductor of interest to early semiconductor research in the early 1950s, as a material on which to base the microelectronics industry. Germanium devices exhibited high leakage currents at only slightly raised temperatures, and its natural oxide, Germanium oxide, is water soluble. Silicon's natural oxide, SiO_2, is an

extremely efficient electronic insulator, is robust enough to survive most handling damage and remains invariant over a large temperature range. SiO_2 also forms a good masking layer, and can block most impurities from diffusing through it.

A recent development in the microelectronics industry is the implementation of Silicon On Insulator technology (SOI) to achieve faster computer chips operating on less power [8]. In silicon on insulator technology, a thin layer of silicon is formed on top of a thick layer of silicon dioxide. The thick layer of silicon dioxide (SiO_2) acts as an insulating barrier between the electronic components and the silicon substrate, reducing capacitance and therefore improving the switching speed of Metal Oxide Semiconductor (MOS) devices. Various methods have been used to form SOI wafers, including grind back (BESOI) and separation by implantation of oxygen (SIMOX). Another widely used commercial technique is SmartCut, a patented method owned by Soitec. In this method, illustrated in Figure 1.1.2, implanted hydrogen ions are used to weaken a layer below the surface of a silicon wafer.

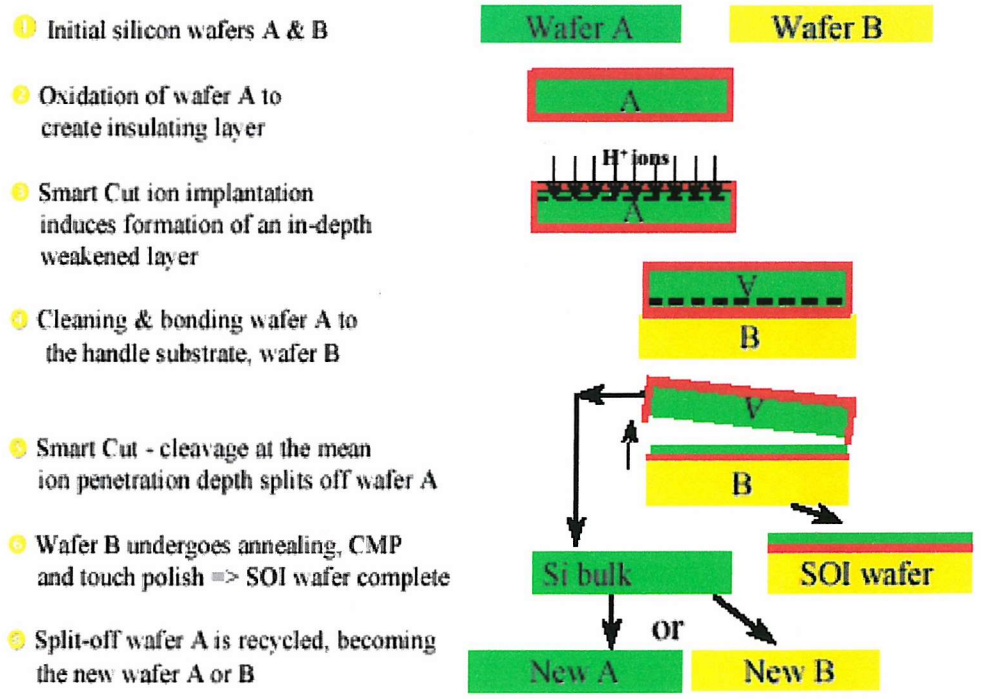

Figure 1.1.2 - The use of Smartcut for the fabrication of an SOI wafer (courtesy of Soitec)

An alternative method, used by IBM for the production of their commercial SOI-based product line, is the implantation of a large amount of oxygen. With ion implantation, the most highly doped region is buried several microns below the surface of the wafer. A long thermal anneal changes the oxygen-implanted silicon into SiO_2, with an improved layer of reasonably crystalline silicon on top with a thickness greater than 0.15μm. Integrated circuits are then formed upon the surface of the SOI wafer, as shown in Figure 1.1.3.

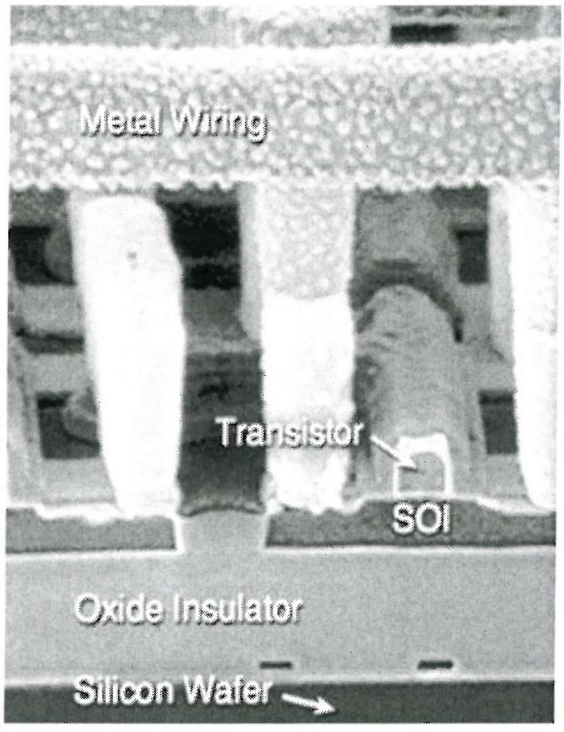

Figure 1.1.3 - An electronic circuit formed on a SOI wafer (Courtesy of IBM)

While providing enhancements for ICs, SOI technology also gives the option for optical waveguides to be formed in silicon itself. SOI wafers are often formed by bonding two thermally oxidised wafers together and thinning the silicon on one side by chemical etch, known as the bond and etch back technique. This method has been demonstrated with wafers of up to 300mm [9]. Evans et al. took propagation loss measurements for SOI waveguides formed by this method and found that even without post-processing, transmission loss was as low as 2dB/cm for a wavelength of 1.319μm [10].

More complex waveguide circuits have also been demonstrated on SOI wafers with silicon as the waveguide core material [11-12]. As stated above, silicon is only transparent for wavelengths longer than 1.1μm. For wavelengths below that, silicon is optically absorbing, and it is necessary to find another material for the waveguide core layer.

1.1.3 Waveguides formed on silicon substrates

If a waveguide is to be designed, compatible with the silicon microelectronics industry, and not made itself *of* silicon, it must be made *on* silicon. Similar rules to those which govern which materials may be used as a waveguide core for the glass substrate waveguides illustrated in Figure 1.1.1(c) also apply to waveguides built upon a substrate of silicon. The waveguide core material must be reasonably low-loss in the spectral region of interest, with a higher refractive index than that of the surrounding layers.

As stated above, silicon has a very high refractive index (3.5040 at 1.319μm), so there are few optical materials available to a microelectronic cleanroom which may be deposited onto silicon to form a waveguide core layer. A silicon-germanium (SiGe) composite material layer may be used directly upon silicon [13-14], or on SOI wafers [15] . It is necessary however for most applications to provide a buffer layer between a waveguide core layer and the silicon itself. The obvious material to use for this is SiO_2, with a refractive index of 1.46 at 633nm. A SiO_2 layer may be measured with a refractive index lower than this due to the layer being porous.

The highest quality SiO_2 is formed through thermal oxidation of silicon wafers [10], but the thickness is limited by the patience of the technician in charge of the process. At first the oxidation proceeds rapidly as the silicon and oxygen are in close proximity to each other. As the thickness of the oxide increases, it forms an ever-

thicker barrier through which the oxygen must migrate, and the oxidation slows exponentially.

Other methods for laying down thick SiO_2 include electrochemical anodisation, flame hydrolysis, plasma-enhanced chemical vapour deposition (PECVD), Low Pressure Chemical Vapour Deposition (LPCVD), and by decomposing tetraethylorthosilicate (commonly abbreviated to TEOS) in an LPCVD reactor. Each of these methods deposits SiO_2 much faster than the thermal oxidation process, but the optical quality of the SiO_2 is lower. There are more regions of strain and defects, many more impurities incorporated into the layer, and the uniformity of thickness is lower.

Once a buffer layer of SiO_2 has been deposited upon the silicon substrate, the material of the waveguide core layer must be chosen. Silicon Nitride (Si_3N_4) is an insulating layer used in the microelectronics industry with a refractive index of 2.02 at 633nm. This material may be formed by Low Pressure Chemical Vapour Deposition (LPCVD)[16], or by PECVD[17-19 (RTA and thermal anneal effects), 20].

A refractive index lower than that of Si_3N_4 may be formed by combining Si_3N_4 and SiO_2, permitting a refractive index range from 1.46 (that of SiO_2 at 633nm) to 2.02 (that of Si_3N_4 at the same wavelength). This material is known as Silicon Oxynitride, or SiON [21-25]. Unlike silicon, SiON has good optical transmission at wavelengths shorter than 1.1μm, but it does have loss due to an Oxygen-Hydrogen (O-H) peak through both the 1.3μm and 1.5μm wavelength regions of importance to optical fiber communications. The loss spectrum is shown in Figure 1.1.4.

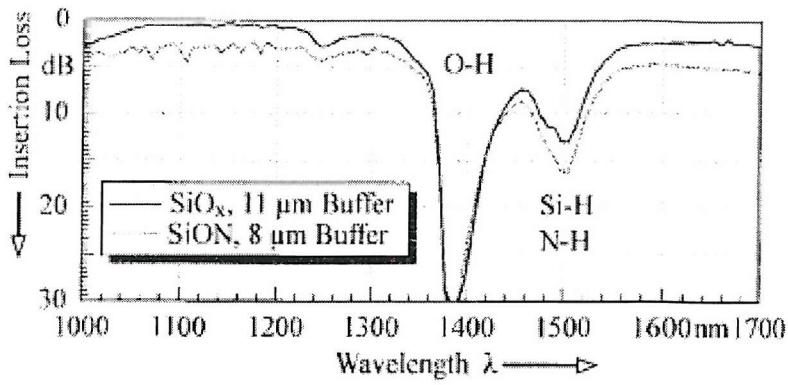

Figure 1.1.4 - The loss spectrum of Silicon Oxynitride [24] for communications wavelengths

The O-H loss peak may be significantly reduced by annealing the SiON waveguides for an hour at temperatures above 1100°, as was demonstrated by Worhoff et al. [21]. Their results are shown below in Figure 1.1.5.

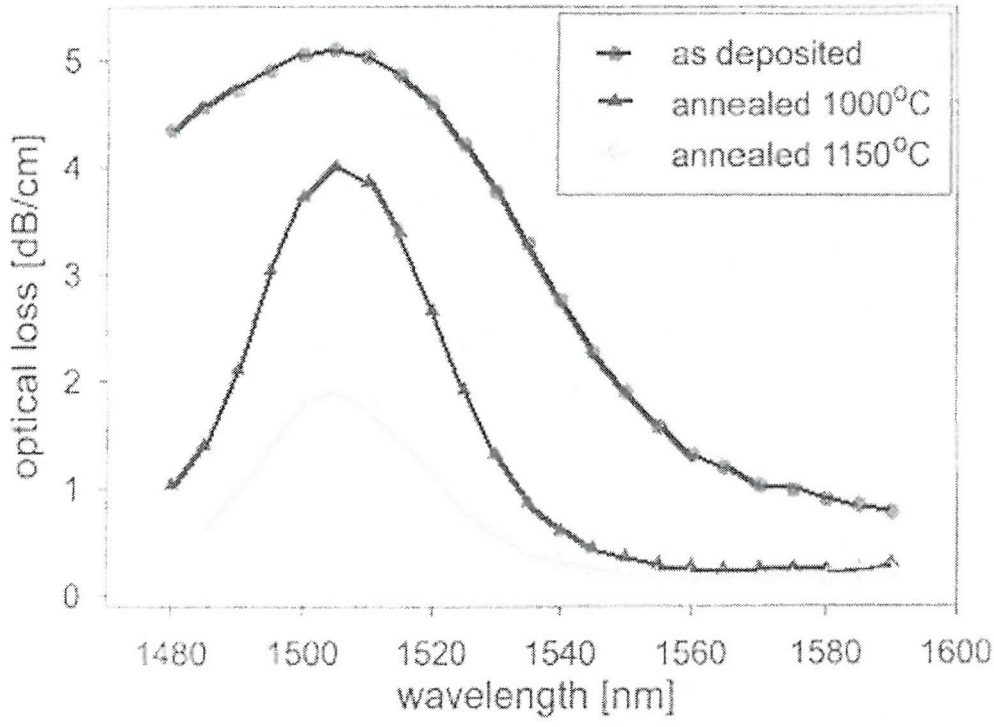

Figure 1.1.5 - Improvement of optical loss in silicon oxynitride by thermal anneal[21]

1.1.4 The Phased Array Waveguide Grating

A prime example of an integrated optical component, which is successfully replacing the bulk optical components previously used, is the Phased Array Waveguide Grating (PAWG), shown below in Figure 1.1.5. First developed in 1988 by M. Smit [26], the PAWG, also known as a phasar, is a planar integrated optical component used for the multiplexing and de-multiplexing of wavelength division multiplexed (WDM) signals.

The bulk optical component, which is currently in use, corresponding to the PAWG is the optical fibre-Bragg grating (FBG) system. This system is an optical fibre-based multiplexer for WDM purposes based upon the fibre Bragg grating [27, 28]. In 2001, Southampton Photonics developed BragNet 25, at that time the most precise FBG currently available, which theoretically allowed up to 160 wavelengths to be transmitted down a single fibre in the band from 1529 to 1562nm.

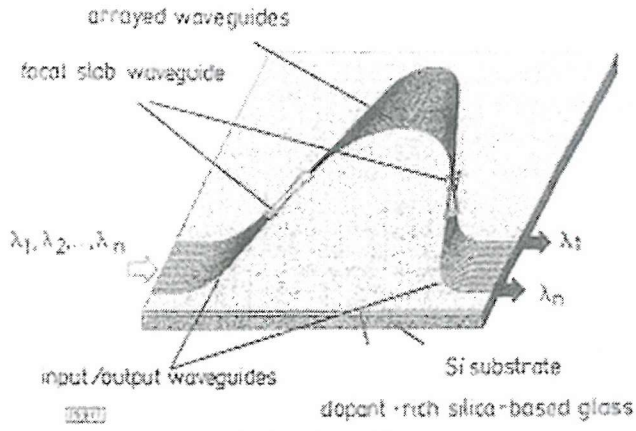

Figure 1.1.6 - The Phased Array Waveguide Grating [29]

The PAWG is designed for a small band of wavelengths around a central wavelength λ_c. Light of the central wavelength entering the PAWG is dispersed in the first slab waveguide and enters the array of waveguides on the other side. The waveguide array consists of hundreds of waveguides differing in length by an integer multiple of $\Delta L=2\pi\lambda_c$. Light of wavelength λ_c, with a small band of wavelengths determined by

the design parameters, will recombine constructively only at the entrance of the central waveguide in the output array of the exit slab waveguide.

By altering the wavelength of the light entering the waveguide, it is possibly to steer this focus point to reach other output waveguides. The PAWG therefore separates signals by their wavelength into different output waveguides, permitting demultiplexing of wavelength division multiplexed (WDM) signals. This principle also operates in reverse to multiplex signals carried at different wavelengths. For a fuller analysis of the PAWG see Smit [30].

The disadvantage of the FBG based system for DWDM is that each Bragg grating, and one is required for each of wavelength channel, is precision engineered. Each optical fibre must be spliced into the next, a costly and delicate procedure, with optical losses at each splice. The PAWG, as an integrated optical component, would be much cheaper to mass produce, and compared with the optical fibre solution, would be much smaller.

A problem with the PAWG is that it is difficult to manufacture. The length increment between each waveguide in the array, ΔL, is a parameter which cannot be reduced for a particular wavelength of operation. For a grating with hundreds of channels, there is a minimum dimension, ΔL x the number of channels. Once the minimum bend radius imposed by the refractive index contrast [4] has been taken into consideration, as must be the loss of precision due to imperfections in the fabrication process, it is very difficult to create a small, high quality grating. Gratings have been made with 128 channels, with $\Delta L = 63\mu m$ [31-32]. The resulting device size is of the order of centimetres.

1.2 Integrated Optical Devices (active)

In addition to the waveguide another fundamental component for an IOC is a light emitter, either a light emitting diode (LED) or a laser. The optical fibre boom in the telecommunications market was enhanced by the introduction of the EDFA into the system[33]. The EDFA permits the amplification of light signals, which have been attenuated by passage through kilometers of optical fibre, without the need for costly transfer to and from an electrical signal for conventional signal regeneration[1].

A photon of light is emitted from a semiconductor material when an electron in the conduction band recombines with a hole from the valence band, as shown in Figure 2.1 for Si and GaAs. The wavelength of light emitted corresponds to the energy separation of the electron and hole at the time of recombination, thus conserving the energy in the system. The difference in energy between the lowest-energy electron in the conduction band and the highest-energy hole in the valence band is known as the bandgap, E_g.

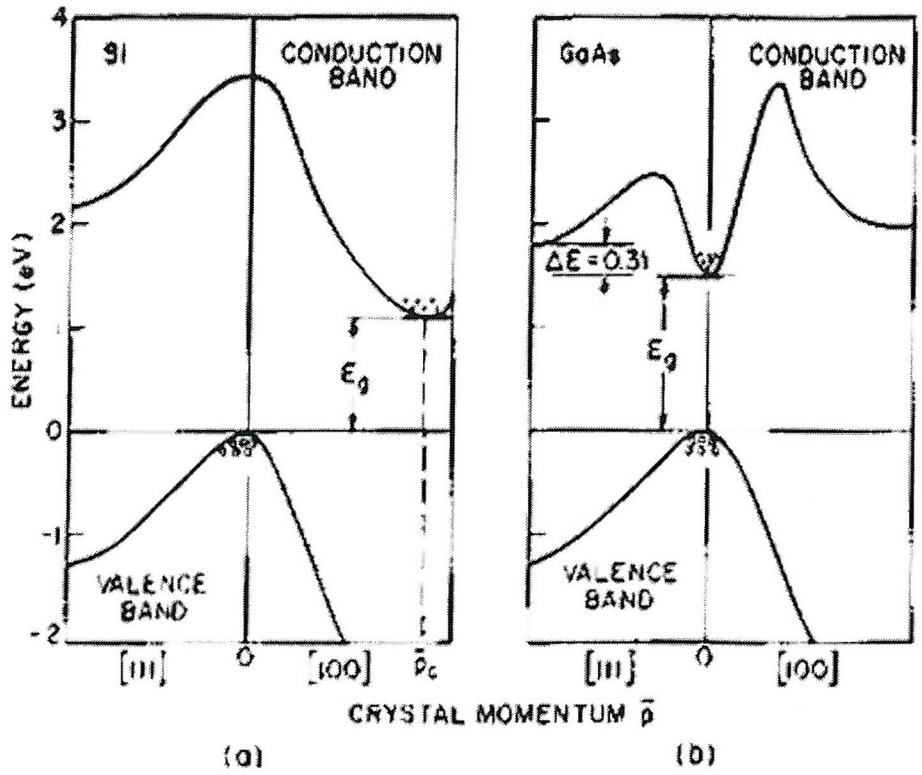

Figure 1.2.1 - Energy band structures of (a) Si and (b) GaAs [3]

In Gallium Arsenide (GaAs), the radiative recombination of an electron from the lowest energy point in the conduction band, and a hole from the highest energy point in the valence band, with a $E_g = 1.42$ eV at room temperature, yields a photon of wavelength $\lambda = 875$nm according to Equation 1.6 [3]. In addition to energy, an electron-hole recombination must conserve the crystal momentum (**k**). In GaAs, the lowest-energy electron has the same momentum as the highest-energy hole, and GaAs is therefore known as a direct bandgap semiconductor. In silicon however, an electron must lose momentum through lattice vibrations, or *phonons*, before it may recombine, making it an indirect bandgap semiconductor. In silicon, the bandgap is 1.12eV at room temperature, corresponding to a photon of 1009nm.

$$\lambda = \frac{c}{\nu} = \frac{hc}{h\nu} = \frac{1.24}{h\nu(eV)}\,\mu\text{m} \tag{1.6}$$

In the above equation, h is Planck's constant, c is the speed of light in vacuum, λ is the wavelength of the light in metres, and v is the frequency of the wave, $hv = E_g$ is the bandgap energy in electron volts [3].

Silicon, as an indirect bandgap material, is a poor natural light emitter through electron-hole recombination. This is in contrast with GaAs which, with a direct bandgap, is an efficient light emitter. GaAs, as part of the InGaAsP system, has been used extensively for solid state semiconductor lasers due to the wide range of lasing wavelengths available [3]. For an IOC based upon silicon, it is desirable to have a strong light emitter from a silicon-compatible material and process, which ideally would form a laser which may be pumped electrically, for eventual integration with electronic silicon ICs. This silicon light emitter would have to overcome the difficulties of the material's poor natural light emission [34].

Light emission from an material where the electron has been excited from the valence to the conduction band through optical means is known as photoluminescence (PL). If the electron has been excited through an applied electric field the emitted light is known as electroluminescence (EL). Every such energy transition has a certain lifetime before recombination is expected to occur; it is however possible to cause an electron and hole to recombine before this time if they are stimulated by a photon of the same wavelength as would be released through recombination. When an electron decays for this reason the photon emitted is in phase with the stimulating photon; this form of emission is called stimulated emission. If the electron-hole recombination is independent of other photons, it is known as spontaneous emission.

1.2.1 Light Emission from Bulk Silicon

Photoluminescence from the band edge of bulk Si was first measured by J.R. Haynes and H.B. Briggs in 1952 at a meeting of the American Physical Society [35]. The weakly emitted light was shown by J.R. Haynes and W.C. Westphal in 1956 to be emission at the bandgap due to indirect transitions of electrons from the conduction

band minimum to the valence band with phonon cooperation, as shown in Figure 1.2.2.

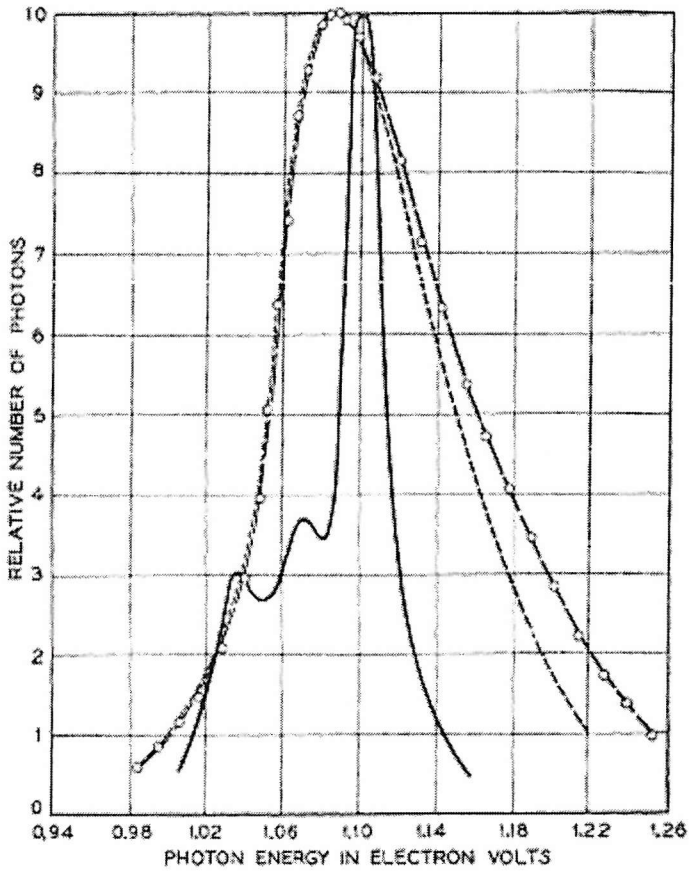

Figure 1.2.2 - Light emission from the silicon bandgap. The data points and dotted curve was obtained for a sample at room temperature, with the solid curve measured at 77K [36].

Clever materials engineering is required to achieve good light emission from bulk silicon. In March 2001 Ng et al. reported an LED fabricated from boron-doped silicon [37]. The novel use of dislocation loops between the p+ silicon and the n-type silicon regions was the basis for the new device (see Figure 1.2.3). The defects cause the silicon itself to confine the electrons in three dimensions. External quantum efficiency is quoted at up to 10^{-3} for emission from both the face and the edges included. External quantum efficiency is the measure of photons emitted from the device per electron injected.

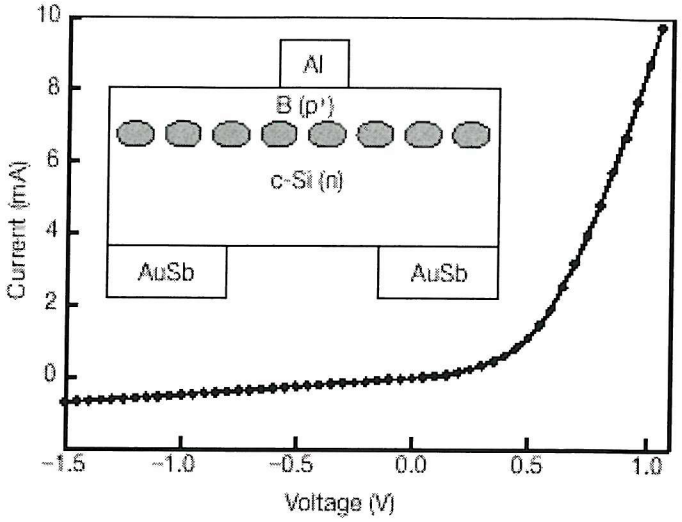

Figure 1.2.3 - A silicon-based light emitting diode [37]

Another method for improving the light emission of bulk silicon grew from work carried out on solar cells [3] in silicon by T. Trupke et al. [38]. An inverted pyramid structure, shown in Figure 1.2.4, is used to achieve EL external efficiencies as high as 6.1% at room temperature.

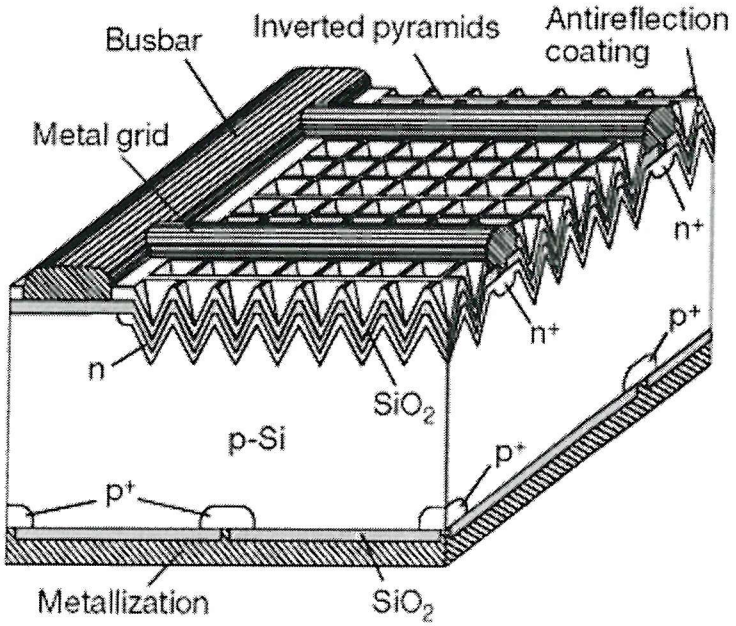

Figure 1.2.4 - An efficient Si photon emitter based upon a solar cell inverted pyramid arrangement. [39]

PL may be extracted from silicon by creating a layer of silicon so thin that the band structure is altered such as is demonstrated in Figure 1.2.5. This is known as a quantum well. In work carried out by Steigmeier et al. [40], a silicon layer of 3nm is deposited between layers of Si_3N_4 by PECVD, which is then annealed. The photoluminescence of the layers was weak, well below 1% spectral PL efficiency. In this case the efficiency is given as the number of photons in a given spectral range emitted into the hemisphere above the sample, per absorbed excitation photon.

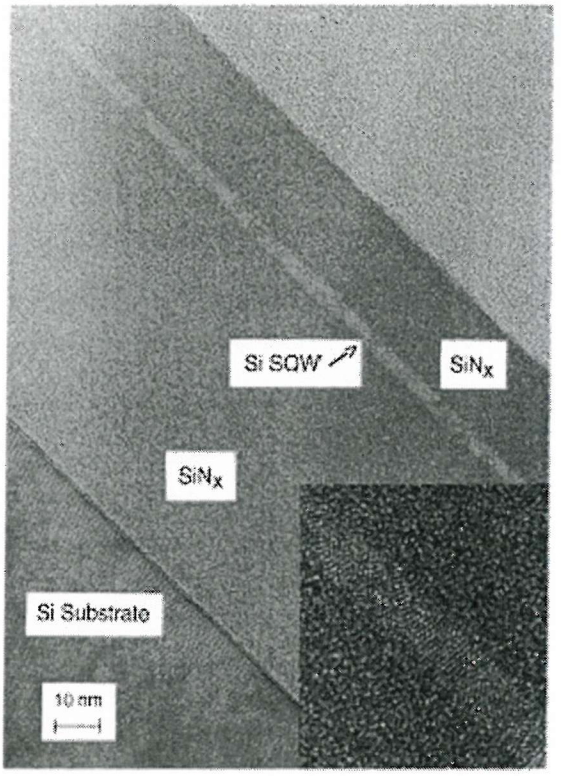

Figure 1.2.5 - A silicon quantum well arrangement. The inset clearly shows the crystalline nature of the silicon.

A further extension of this is the development of the Si/SiO_2 superlattice, consisting of many quantum wells in close proximity. The superlattice exploits radiative interface states between the silicon and the SiO_2. These lattices are generally prepared using CVD processes [41], or by magnetron sputtering [166, 167].

1.2.2 Light Emission from Doped Silicon and Silicon Dioxide

An alternate method used to extract light from silicon is to not use the silicon radiative process itself, but instead to use radiative centers of other elements introduced into the silicon as dopants. These materials have included large amounts of carbon [42], erbium, and copper [43]. Of these materials, it is erbium which has received the most attention.

Erbium (Er) is an element from the Lanthanide series in the periodic table of elements, which has an incompletely filled inner electron shell. When Er is incorporated into a host material, energy transitions forbidden to free Er ions are sometimes weakly permitted. A schematic level diagram of the Er energy levels is included in Figure 1.2.6.

For the majority of permitted radiative transitions in Er the lifetime for which an electron may remain in an any particular band is extremely short. An electron which has been excited to one of the higher energy levels from the ground state will relax quickly and non-radiatively to the lower energy levels. The final transition from the second lowest energy state to the ground state has a much longer lifetime, of up to ~20ms dependent upon the host material. From this transition light with a wavelength of 1.54μm, corresponding to an energy of 0.8eV, is efficiently emitted.

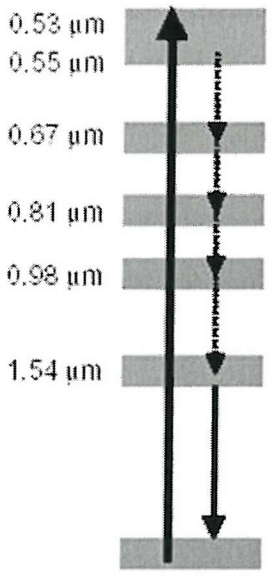

Figure 1.2.6 -Erbium energy band transfers [44]

It was found that erbium, when implanted into crystalline Si wafers, emits light at 1.55µm, [45]. The mechanisms involved in this process have since been extensively studied. [46] The photoluminescence of Erbium doped Silicon, or Er:Si however has never been strong enough to form a potential laser material, hampered by a low maximum concentration of luminescence centers, and especially by the large decrease of the luminescence intensity when the measurement temperature is raised from 77K to room temperature [47]. Because of this, research has focused in the most part on other areas described below. Erbium may be implanted into other structures on the silicon surface. In 1997, Huda et al. [48] incorporated high concentrations of erbium into strained Si/SiGe/Si multiple quantum well structures.

Another approach using dopants in Si-based materials is the implantation of SiO_2 with Ge (Ge:SiO_2). Blue-violet electroluminescence was measured from a Ge:SiO2 device with power efficiencies (defined as the ratio between the optical output and the electrical input power) up to 0.5% [47]. This has been explored by several groups, including by H. Yang only last year [49], and originally by Y. Maeda et al in 1991 [50]

1.2.3 Photoluminescence from Porous Silicon

In 1990, L.T. Canham discovered that when silicon was exposed to a chemical etch in hydrofluoric acid (HF), leaving a series of isolated nanometer silicon wires, that strong red photoluminescence may be emitted at room temperature [51]. Samples which had etched in this manner were known as porous silicon (PS). Photoluminescence from porous silicon had previously been demonstrated at 4.2K by R. Greef at Southampton in 1984, though the importance of this result was not appreciated fully at the time of publication and no room-temperature PL measurements were made [52].

Porus silicon may be modeled as silicon nanocrystals connected by thin wires [53, 54]. PS devices are flexible: the refractive index may be modified by changing only the anodisation current density [55], and waveguide structures may be formed on a silicon wafer without the use of thermal SiO_2 as a buffer layer. An example is the edge-emitting device developed by M. Araki et al., shown in Figure 1.2.7. This device emits strongly Transverse Electric (TE) polarised light. Some Transverse Magnetic (TM) polarised light was also emitted over the same wavelength range, but at a tenth the intensity.

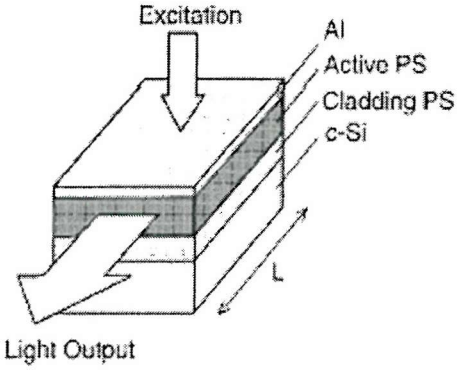

Figure 1.2.7 - a Porous silicon edge-emitting device with a PS waveguide structure [55]

High Resolution Transmission Electron Microscopy has shown that silicon nanocrystallites in PS exhibit a semi-ordered structure unlike both crystalline and

amorphous silicon [56]. This same structure was also exhibited by nanocrystals of silicon formed in silicon dioxide by PECVD and as discussed in the next subsection of this thesis.

Porous silicon emits light over the entire visible range and beyond [57,58]. However, PS is however an unstable material, susceptible to damage and contamination by handling [59]. Silicon, when exposed to air, forms a natural oxide, and PS is no exception. All research has agreed that photoluminescence from PS changes over time.

L.T. Canham studied this in his original paper [51, 60], and concluded that the PL intensity of the PS increases, narrows, and blueshifts as the silicon nanocrystallites became smaller through oxidation. This is in agreement with A. Loni et al, who studied the relationship between the storage media of PS samples and their luminescence [61]. This is, however, in contradiction with B. Zou et al.[62] who reported that the emission wavelength redshifts as the sample ages. The two sets of results are shown below.

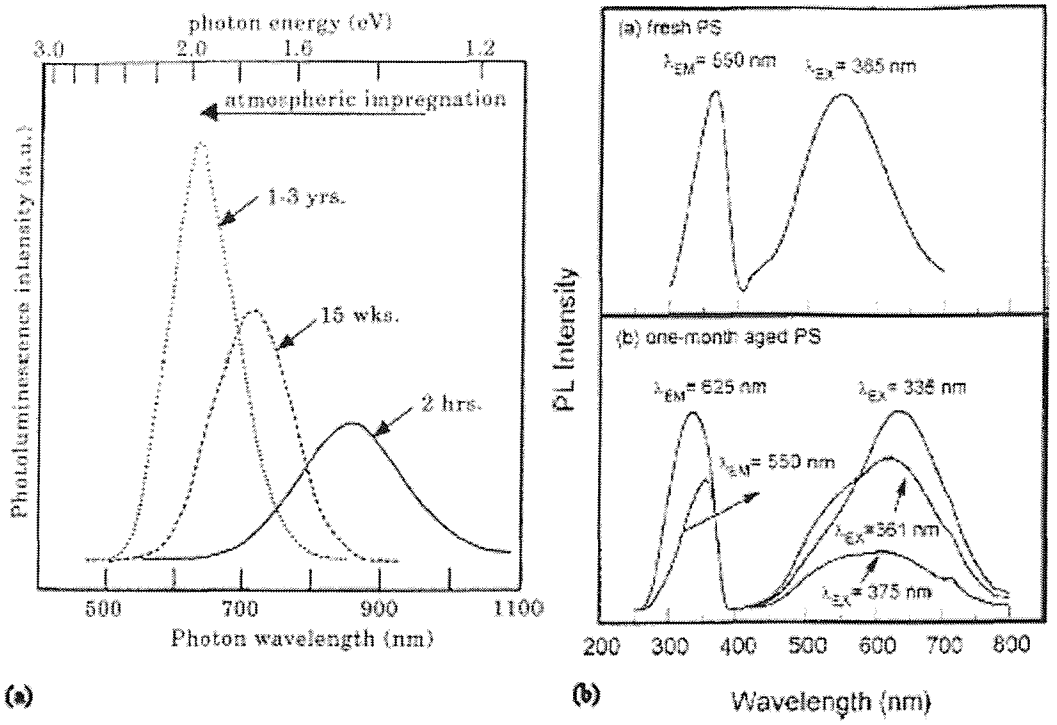

Figure 1.2.8 - Aging effects upon porous silicon showing (a) blueshift [51] and (b) redshift [62].

Photoluminescence from PS is usually stimulated by a laser with an operating wavelength below 400nm. It has also been demonstrated that PS may also emit electroluminescence. To achieve this, a 1μm layer of PS was formed on a silicon wafer, which was oxidised and then a layer of indium-tin-oxide (ITO) was deposited onto the PS as a top electrode [63]. ITO is a transparent material frequently used for the top contact of surface-emitting luminescent devices. The device, developed by B. Gelloz and N. Koshida, had an external quantum efficiency of greater than 1% with less than 5V.

1.2.4 Photoluminescence from Silicon Nanocrystals

Another type of light emitting silicon which has received much interest over the past few years is nanocrystalline silicon. Small regions of silicon, not more than several nanometers across, are surrounded by a supporting matrix of silicon dioxide. These

silicon nanocrystals (Si-nc) emit light in a characteristic broad photoluminescence from 600-1100nm.

Many methods have evolved for the formation of Si-nc. The most widely used are implantation and PECVD. In the implantation method, Si ions are accelerated into a glass substrate, or into a thick layer of SiO_2 upon a silicon substrate. This was the first method employed to form Si-nc, and was carried out by T. Shimizu-Iwayama et al. as early as 1993 [64]. In their work they found that an anneal at 1100°C radically changed the shape of the weak photoluminescence, transferring the peak to around 1.7eV, corresponding to 730nm. Implantation and subsequent annealing has become a standard fabrication technique for Si-nc fabrication.

The other main method consists of the deposition of a layer of silicon-rich silicon dioxide (SRSO) by PECVD. The incorporation of silicon into the layer is controlled by manipulation of the ratios of gasses in the chamber, universally silane (SiH_4) and nitrous oxide (N_2O). Early research into this area yielded weak PL [65, 66, 67], and even EL [59]. It was found, however, that a thermal anneal at over 1000° [69], and particularly over 1100° [68, 70] were effective in increasing the intensity of the PL. Luminescence measurements were carried out on samples of Si-nc deposited in this manner, with efficiencies of around 0.04% reported [71].

Improvements to this method include deposition of the PECVD Si-rich SiO2 at a lower temperature than the standard 300°C. In work by Wang et al. a marked increase in the PL intensity was reported with decreasing deposition temperature [72]. Their results are summarized below in Figure 1.2.9.

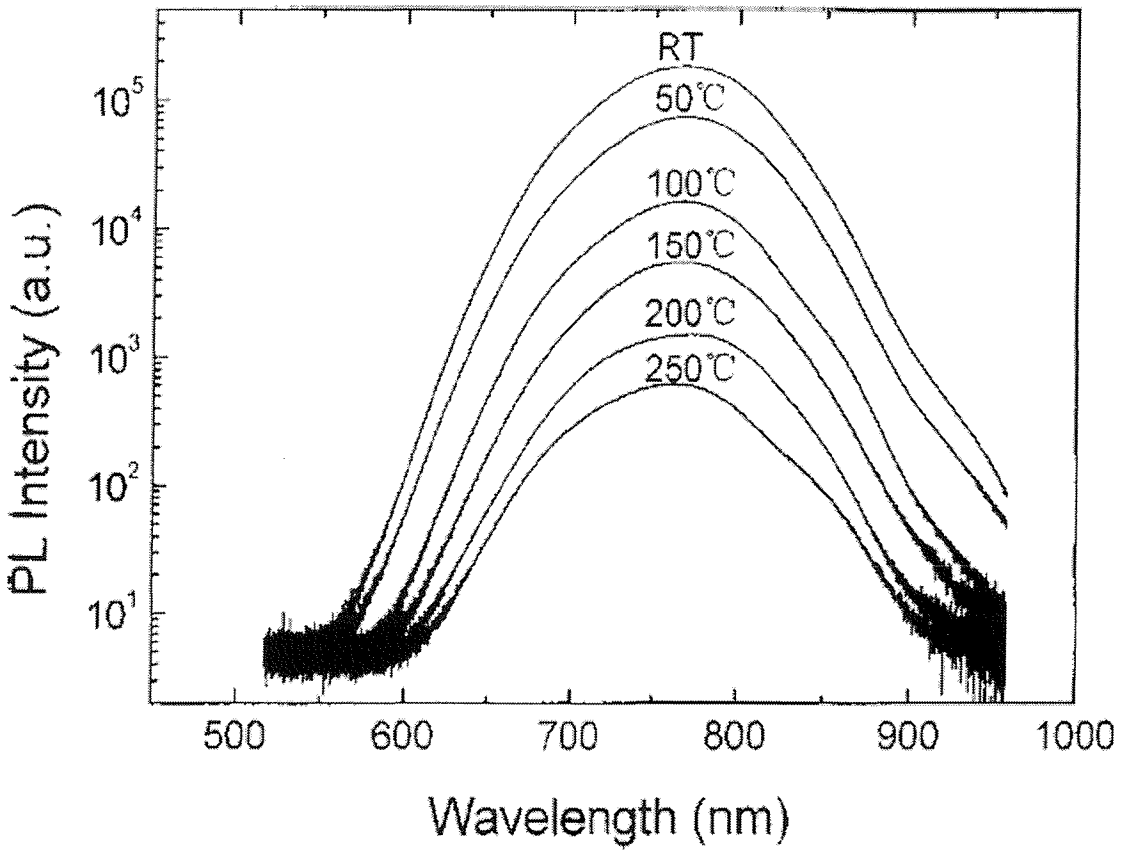

Figure 1.2.9 - Increased PL efficiency with decreasing PECVD deposition temperature [72]

Many other methods have been developed for increasing the luminescence intensity, including irradiation of the as-deposited PECVD Si-rich SiO_2 before an anneal [73] to break up any as-deposited Si clusters. Studies of the effect of the thermal anneal upon the intensity of the luminescence concluded that the annealing temperature providing the maximum PL intensity was 1100°C, and that the characteristic PL spectrum only occurs in samples which have been annealed above 900°C. [74]. Some studies showed the wavelength of peak intensity shifting with the temperature of the anneal [75] with results shown below in Figure 1.2.10 (a). It is also shown that the wavelength of peak intensity shifts with the incorporation of silicon into the silicon-rich silicon dioxide [76] (Figure 1.2.10 (b)).

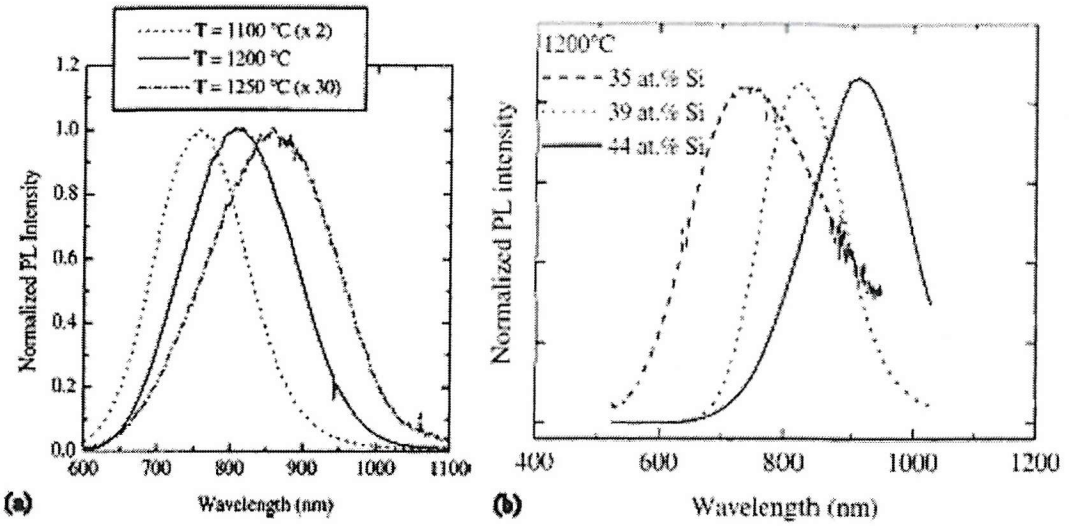

Figure 1.2.10 - Shift of the wavelength of peak intensity with (a) anneal temperature [75] and (b) silicon incorporation [76].

Other methods for nanocrystal formation include gas-phase formation by laser breakdown of silane [77-78], thermal vapourisation of Si in an Ar buffer gas [80], through electronic irradiation of amorphous SiO_2 [81], and sputtered Si and SiO_2 [82-83]. A more complex method for creating nanocrystalline silicon is the deposition and annealing of Si/SiO2 superlattices [84-87, 75]. This highly controlled method permitted very careful studies into Si-nc, with the conclusion that decreasing nanocrystal size resulted in a blue shift of the peak intensity, shown below in Figure 1.2.11

Size measurement of nanocrystals with sub-micron diameters is not a trivial problem. The photographs of nanoparticles which are most commonly presented in journal articles have been taken using a Transmission Electron Microscope (TEM). Raman scattering is another method used for the measurement of nanoparticle size distributions [74].

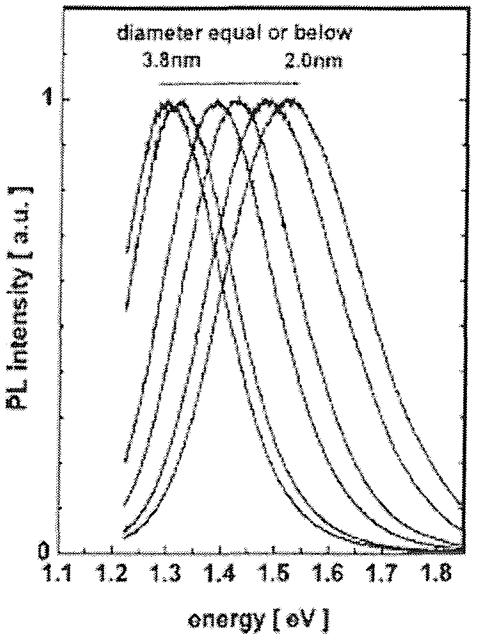

Figure 1.2.11 - Normalized photoluminescence spectra showing a blue shift correlated with nanocrystal size [84]

Although SiO_2 is an extremely effective electrical insulator, it is possible to pass current through Si-nc through a quantum tunneling current known as Fowler Nordheim transport. Measurements of current flow through silicon-rich silicon dioxide have been carried out by [59] and by K. Kim [79]. LEDs have been formed in this material [88], with results shown below in Figure 1.2.12. Electroluminescence has also been measured in PECVD-deposited Si-nc [89], in a MOS structure. LPCVD Si-nc have also exhibited EL [90]. Si-nc formed by sputtering have exhibited green EL [91, 83].

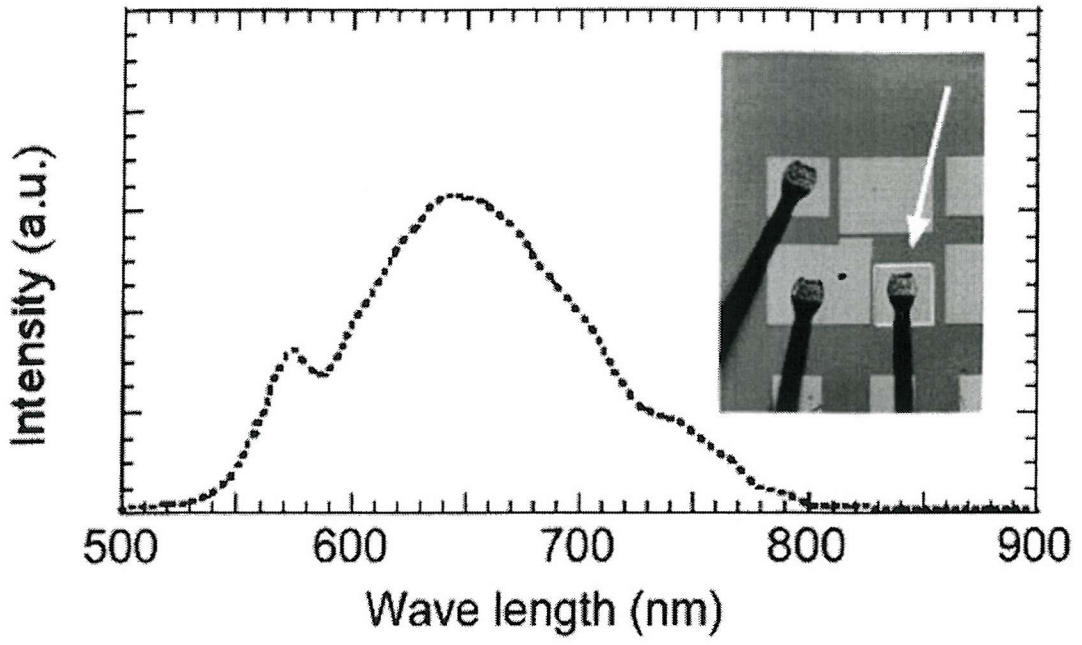

Figure 1.2.12 - A Si-nc LED

The mechanism for the luminescence from Si-nc is not fully understood. It is firmly believed that band-gap widening due to the quantum confinement effect plays a large role in the photoabsorption of the nanocrystals [92]. There has been much discussion on whether the luminescence from the Si-nc is as a result of quantum confinement [65, 78, 79, 93-94], or whether it is due to defects at the interface between the Si and SiO2 regions [68, 76, 80, 86, 92, 95-98], a defect state [77, 99], or other processes which have not received such widespread attention [64].

Several components of luminescence from Si-nc have been observed: a fast decay emitting a blue-green light component with a decay time of approximately 0.4ns, other short-wavelength components with decay times of approximately 2 and 10ns, and a slow component with a peak wavelength of emission beyond 700nm, with a decay time of the order of milliseconds [69]

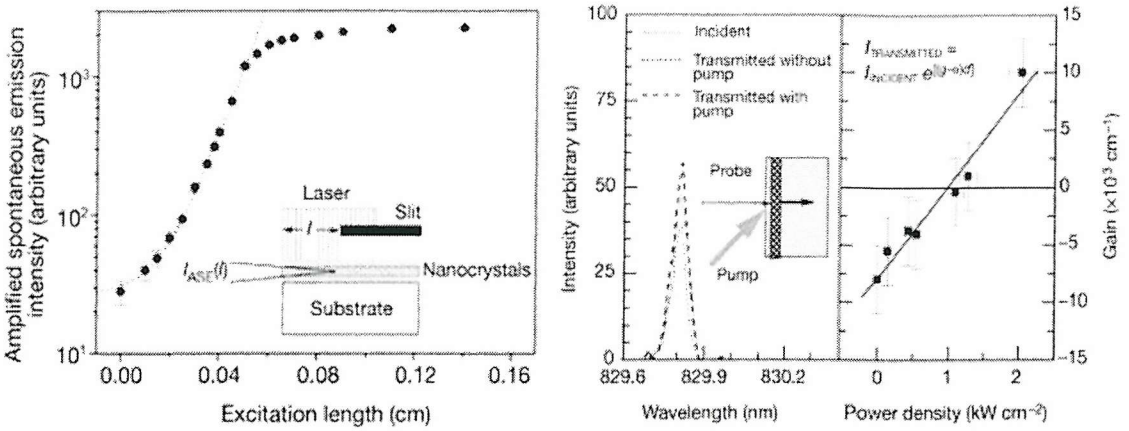

Figure 1.2.13 - (a) Applied spontaneous emission intensity plotted against excitation length, and (b) Luminescence intensity plotted against wavelength with gain plotted against power density.

In November 2000, L. Pavesi et. al. reported gain in waveguides of Si-nc formed by implantation into wafers of quartz glass and of silicon [76]. The gain reported was of the same order as that achieved in the most widely used III-V compounds, results shown in Figure 1.2.13. This provoked widespread interest in the area and provided the basis of the work in this thesis. The method used by L. Pavesi was challenged by J. Valenta in 2002, who questioned the validity of the results, suggesting that their results may have been an artifact of the measurement geometry [100]. A recent paper by L. Dal Negro, from the same group as L. Pavesi, insists that gain has been measured [101].

1.2.5 Erbium-doped Silicon Nanocrystals

It was found in a study of Erbium doping in silicon films ranging from amorphous Si to almost pure SiO_2, that Si-rich SiO_2 films containing Si-nc were very good hosts for erbium [102]. Layers of Er:SRSO were deposited by electron cyclotron resonance PECVD with post-anneal temperatures ranging from 500-900°C. Another group achieved stimulated emission at room temperature in Er:Si-nc formed by excimer laser ablation [103].

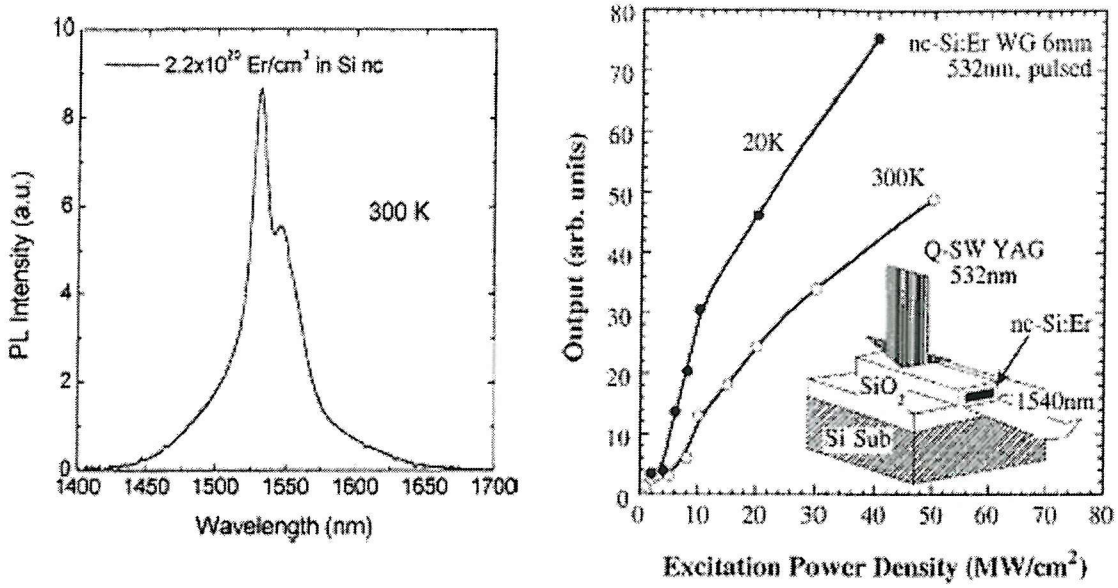

Figure 1.2.14 - (a)Luminescence from [105] and (b)Pumping power dependence of the 1550nm emission of a Er:nc-Si waveguide [102].

An analysis of carrier-induced quenching mechanisms of the Erbium luminescence found that, in SRSO, nearly all such mechanisms are suppressed. This facilitates the Er luminescence and the population inversion which is necessary for stimulated emission [104]. Another study found that the luminescence intensity was closely related to anneal temperature, and that the optimum temperature of anneal was 950°C, as shown in Figure 1.2.15.

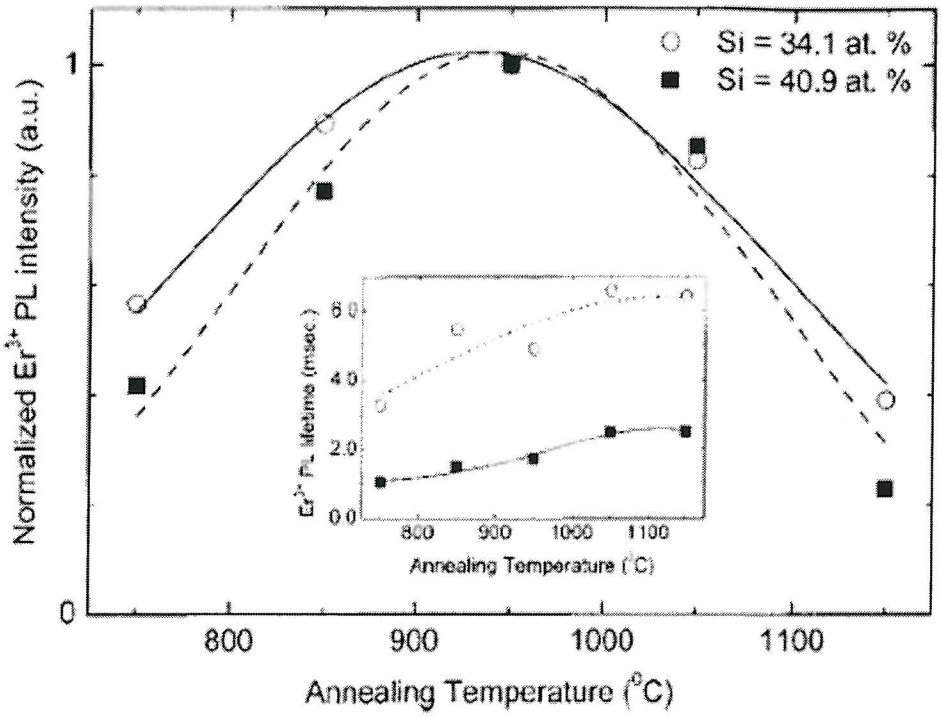

Figure 1.2.15 - The optimum anneal temperature for 1.5μm luminescence. The inset shows PL lifetime plotted against anneal temperature. [104]

In a thorough treatment by Priolo et al. [17], it was stated that Si-nc play a strong role in the excitation of the Er ions. Kenyon et al. suggested a model in which the excitation of the erbium was carried out via coupling from confined excitons generated in the usual way within the silicon nanoclusters [106].

Er:Si-nc is considered an extremely promising avenue for future research, and companies such as ST Technologies are actively pursuing a product range based upon it. [107]

1.3 Photonic Crystals

Although the first suggestion of photonics crystals was by Bykov in his 1972 paper [108], photonic crystals were independently developed and widely publicised by E. Yablonovitch [109] in 1987. The objective professed by Yablonovitch was to decrease amplified spontaneous emission (ASE). ASE is a limiting and unwanted factor in lasers, where it is desired that all emitted light be in phase. Photons resulting from spontaneous emission, but not the laser line, are amplified in addition to the laser line. Not only does this cause unwanted lines in the laser, but every unwanted recombination is one fewer photon available for the laser line.

E. Yablonovitch proposed an extension of the fibre-Bragg grating (FBG) reflectors already operating in one dimension as highly reflective mirrors for Fabry-Perot cavities. FBGs consist of layered structures in which the refractive index alternates from high to low at a period of half a wavelength. This periodic modulation creates a forbidden gap in the spectrum of light which is allowed to propagate through the mirror. E. Yablonovitch proposed creating three dimensional Bragg reflectors with an forbidden energy gap which straddled the band gap, thus inhibiting the spontaneous emission of any photons at the bandgap energy.

A gap created in the electromagnetic spectrum, to differentiate it from an electronic bandgap, became known as a photonic bandgap (PBG), and the materials in which the photonic bandgap was created became known as photonic crystals (PCs). One is able to distinguish between a Bragg Grating and a PC by the size of the refractive index contrast between the high and low index materials. In a Bragg grating, the contrast is usually of the order of .01, whereas in a PC it is at least an order of magnitude larger. As with the 1D FBG reflectors, the primary bandgap of a PC is located at a wavelength of twice the length of the photonic crystal lattice pitch: for a photonic crystal lattice pitch of 310nm, the photonic bandgap would be located around 620nm.

1.3.1 - 1D Photonic Crystals and their applications

1D photonic crystals have been in use for years as the reflective elements in distributed feedback lasers [168] as a Distributed Bragg Reflector. The primary use of 1D PCs is as highly reflective mirrors for a specific range of frequencies. 1D photonic crystals typically consist of a layered system of alternating high and low refractive index, known as a multilayer stack or film, such as is shown below in Figure 1.3.1. The structure shown below is periodic with lattice pitch a.

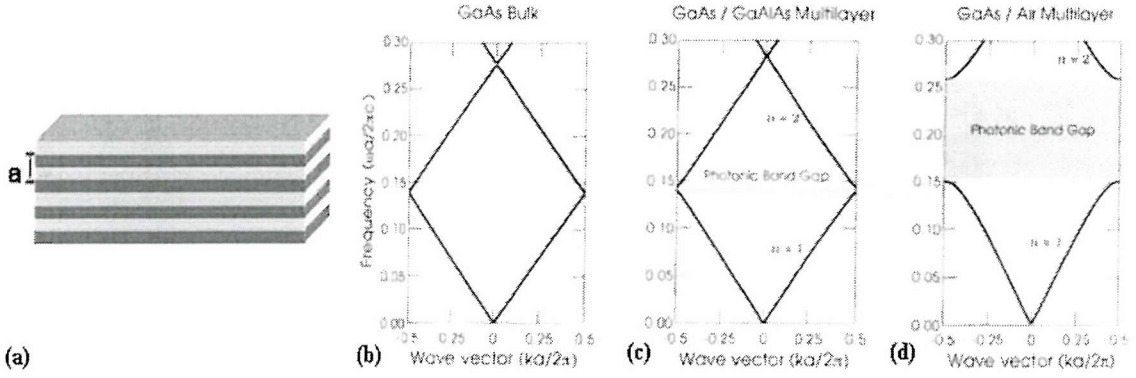

Figure 1.3.1 - A multilayer film, (a) 1D Photonic crystal, and the photonic band diagrams for refractive index ratios of (b) 1:1, (c) 13:12, and (d) 13:1 [110]

The frequency spectrum for 1D PC structures is simply the light line given by

$$w(k) = \frac{ck}{\sqrt{\varepsilon}} \tag{1.7}$$

What may be seen from Figure 3.1.0 (b) is that as the contrast between the high and low refractive indices increases ($n = \sqrt{\varepsilon}$), the width of the bandgap also increases [110]. It is also apparent that the energy position of the photonic bandgap scales with the period of the structure. A 1D PC with a lattice pitch of $2a$ will have a photonic bandgap at the same wavelengths as a PC with a lattice pitch of a which is formed of the same materials. It was found however that it was possible to dynamically shift the

location of the bandgap in the electromagnetic spectrum through the introduction of nonlinear materials into the bandgap structure [111].

Femtosecond measurements carried out on 1D PCs indicated the phenomenon of transmission of photons through the photonic bandgap in a manner very similar to that of electron tunnelling through a potential barrier [112, 113, 114]. A striking aspect of these results is that they appear to suggest superluminal tunnelling speeds for a wave packet through the system. This was shown to be not as a result of faster-than-light travel, but as a function of the material itself. The effect of the chromatic dispersion of a photonic crystal is to deform an electromagnetic wave packet such that a group which has been shaped symmetrically will appear with the amplitude distribution skewed towards the leading edge (See Figure 1.3.2). Each individual wavelength component of the wave packet has been transmitted at standard velocities, but the *group velocity* of the entire packet has travelled faster than light [112, 115]. This was predicted in photonic crystal theory [116].

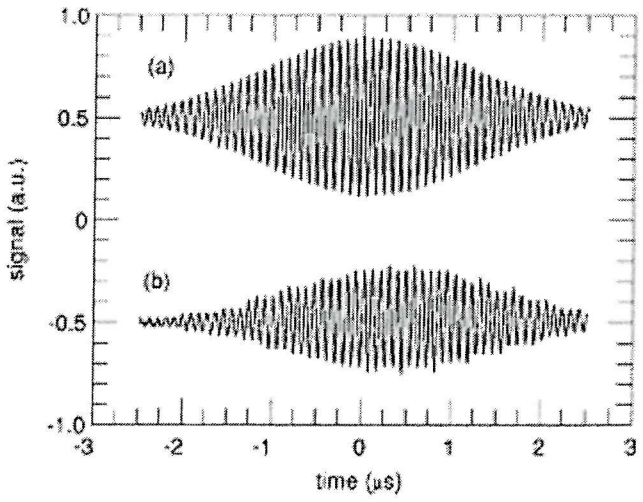

Figure 1.3.2 - Transmission of a wave packet through a 1D coaxial photonic crystal. This is not plotted to scale vertically [115].

Another group investigated the effect of the PC upon the spontaneous emission intensity of a GaAs multilayer stack [117]. It was found that close proximity of the

PBG to the electronic bandgap energy produced a 4x enhancement of the emission intensity of the system. Other studies into light emitting PCs found that, for cavities of Er doped porous silicon between Bragg mirrors, the wavelength of peak intensity may be tuned by modifying the Erbium activation temperature [118]: increasing the activation anneal temperature from 600 to 1000°C causes the microcavity emission wavelength to blueshift by up to 200nm. Results are shown in Figure 1.3.3 (b). Figure 1.3.3 (a) shows the 1D PCs forming the reflective regions above and below the microcavity.

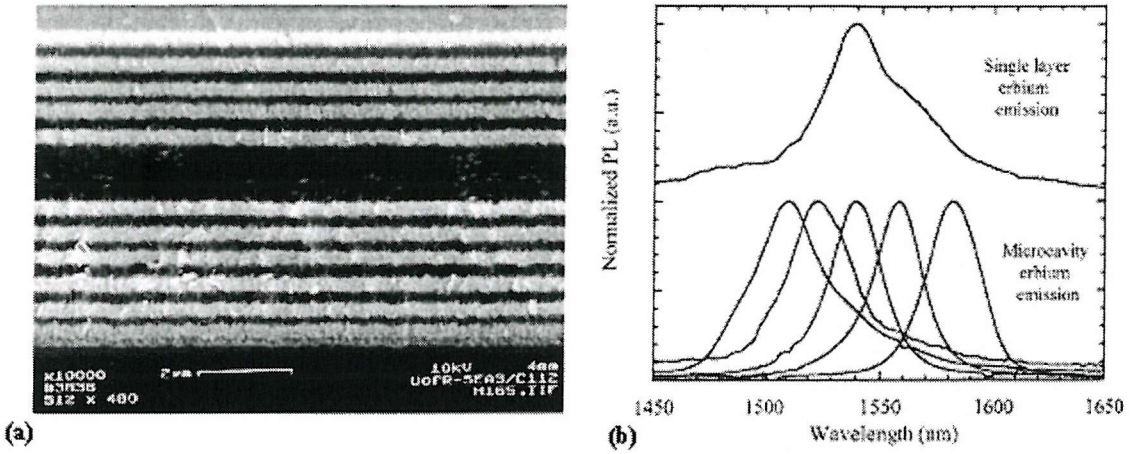

Figure 1.3.3 - (a) Scanning Electron Microscope (SEM) cross section of a PS microcavity formed with 1D PCs as reflective regions above and below. (b) Graph showing emission wavelengths for a single layer (above) and microcavities annealed at different activation temperatures (below). [118]

A similar structure to that shown in Figure 1.3.3 was fabricated by P. Ferrand [119], where a porous silicon microstructure was formed on a silicon substrate, and a 1D PC was exploited to provide single mode guidance of light, excited by a laser spot on the surface of the sample, without the use of a buffer layer of SiO_2. This is shown in Figure 1.3.4.

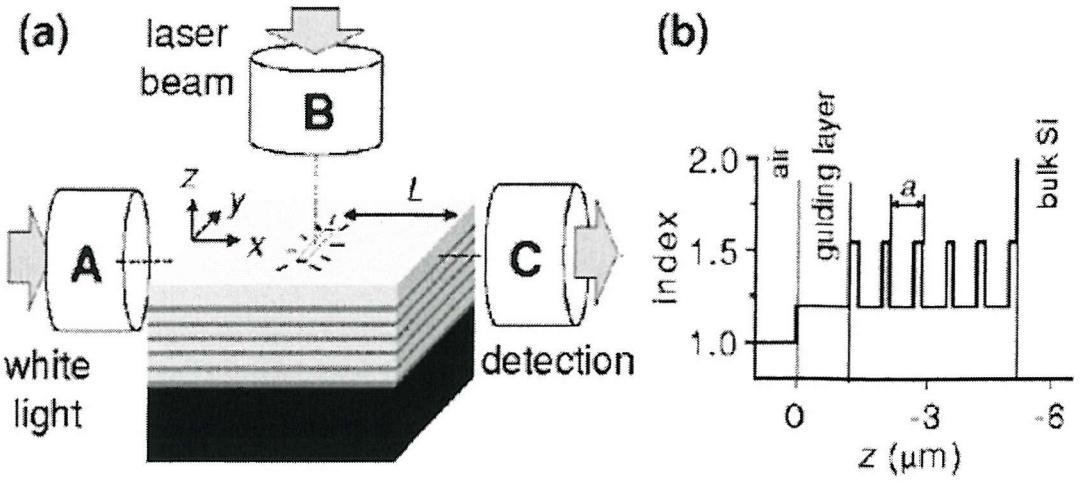

Figure 1.3.4 - (a) Scheme of a multilayered porous silicon microstructure and experimental setup used for measurement of white light transmission (A-C) and PL (B-D) and (b) refractive index profile of the sample [119].

The bandgap structure of a photonic crystal is different for the TE and TM polarisations. This was exploited by Zhao et al. to form a waveguide polariser. The experimentally measured TE/TM extinction ratio was found to be 20dB for a 3mm long sample [120].

1.3.2 2D Photonic Crystals and their applications

The extension from 1D PCs to 2D usually involves the fabrication of a field of rods either etched out of a dielectric layer, or extruded from it, the remains from an etch which has removed the surrounding layer. Examples of these two geometries are shown below.

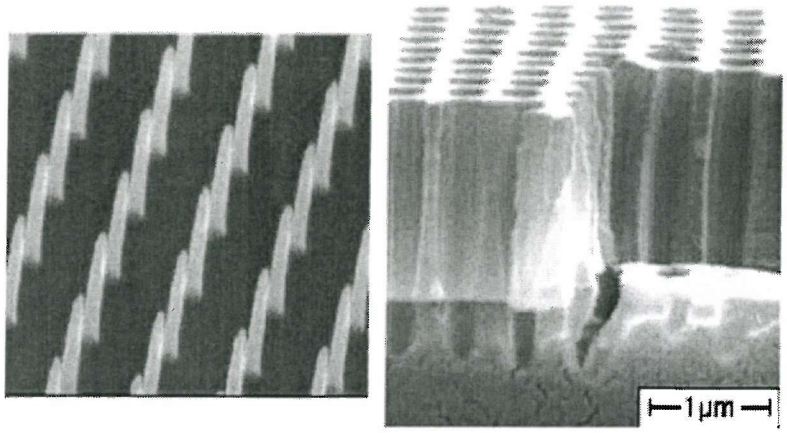

Figure 1.3.5 -SEMs showing (a) a glass cylinder in air square photonic lattice and (b) a square lattice etched into a dielectric layer.

The effect of a periodic structure such as those shown in Figure 1.3.5 is to form an arrangement of alternating high and low refractive indices which is periodic in two dimensions. When studying photonic crystals it makes understanding easier to operate in terms of the reciprocal lattice, and in terms of the Brillouin zone of the material. When operating on a lattice, one normally uses lattice vectors (**R**), which are the set of vectors which translate from one point on the lattice to another. For every lattice, there are primitive lattice vectors ($\mathbf{a}_1$, $\mathbf{a}_2$, $\mathbf{a}_3$) which are the smallest vectors pointing from one lattice point to the next, from which all vectors **R** are composed.

A periodic function f(**r**) periodic on the lattice, will satisfy the criterion f(**r**) = f(**r** + **R**). Taking the Fourier transform of these functions yields:

$$f(\mathbf{r}+\mathbf{R}) = \int dq\, g(\mathbf{q}) e^{i\mathbf{q}\cdot\mathbf{r}} e^{i\mathbf{q}\cdot\mathbf{R}} = f(\mathbf{r}) = \int dq\, g(\mathbf{q}) e^{i\mathbf{q}\cdot\mathbf{r}} \tag{1.8}$$

$g(\mathbf{q})$ is the coefficient of the plane wave with wave vector **q**. This may only be satisfied when $g(\mathbf{q}) = 0$ or when $\exp(i\mathbf{q}\cdot\mathbf{R}) = 1$, equivalently $\mathbf{q}\cdot\mathbf{R} = n2\pi$ for an integer n. The vectors **G** which are a solution to this are known as reciprocal lattice vectors. The lattice which is formed from them is known as the *reciprocal* lattice.

The primitive reciprocal lattice vectors ($\mathbf{b}_1$, $\mathbf{b}_2$, $\mathbf{b}_3$) from the reciprocal lattice may be found from the constraint $\mathbf{a}_i \cdot \mathbf{b}_j = 2\pi\delta_{ij}$ applied to the equation directly below, where l, l', m, m', n, and n' are integers:

$$\mathbf{G}\cdot\mathbf{R} = (l\mathbf{b}_1 + m\mathbf{b}_2 + n\mathbf{b}_3) \cdot (l'\mathbf{a}_1 + m'\mathbf{a}_2 + n'\mathbf{a}_3) = N2\pi \tag{1.9}$$

The solutions are given below.

$$\frac{\mathbf{b}_1}{2\pi} = \frac{\mathbf{a}_2 \times \mathbf{a}_3}{\mathbf{a}_1 \cdot \mathbf{a}_2 \times \mathbf{a}_3}$$

$$\frac{\mathbf{b}_2}{2\pi} = \frac{\mathbf{a}_3 \times \mathbf{a}_1}{\mathbf{a}_1 \cdot \mathbf{a}_2 \times \mathbf{a}_3}$$

$$\frac{\mathbf{b}_3}{2\pi} = \frac{\mathbf{a}_1 \times \mathbf{a}_2}{\mathbf{a}_1 \cdot \mathbf{a}_2 \times \mathbf{a}_3} \tag{1.10}$$

All lattice structures have two lattice structures associated with them: the ordinary lattice, and the reciprocal lattice. Vectors in the ordinary lattice have dimensions measured in length. Vectors in the reciprocal lattice have dimensions measured in 1/length.

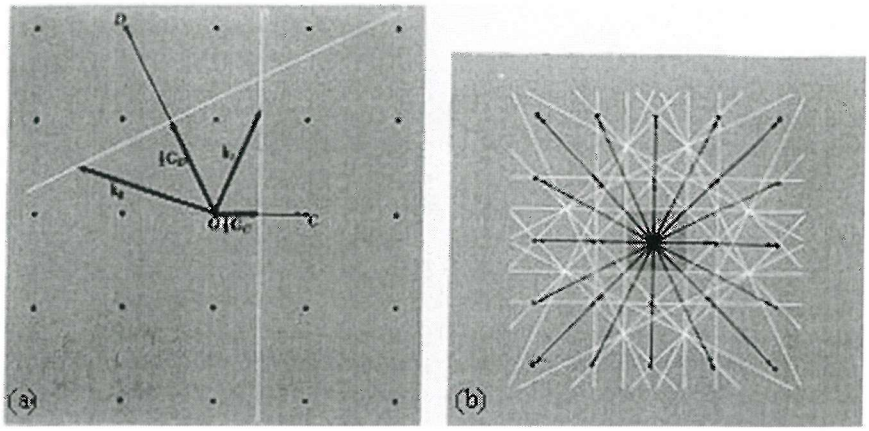

Figure 1.3.6 - (a) Construction of a Brillouin zone and (b) The Brillouin zone for a square reciprocal lattice. Reciprocal lattice vectors are shown as black arrows with their perpendicular bisectors in white[169].

The Brillouin zone is defined as a Wigner-Seitz primitive cell in the reciprocal lattice. The method for constructing a BZ is illustrated in Figure 1.3.6 (a). Choosing a reciprocal lattice point as the origin, each reciprocal lattice vector **G** is bisected by a plane at its midpoint. This set of planes forms the boundary for a region around the original reciprocal lattice point, as is shown in Figure 1.3.6 (b) for a square lattice. The central square is a primitive cell, known as the Wigner-Seitz primitive cell, of the reciprocal lattice, and is the first Brillouin Zone. From a point within the BZ it is not possible to translate within the boundary of the Brillouin zone by adding **G**.

For photonic crystals the Brillouin zone may be further reduced in size and complexity by considering the symmetries in the photonic lattice. If a region in the Brillouin zone may not be rotated, reflected, or inverted into itself, then that region is known as the *irreducible* Brillouin zone [110], which for brevity shall be termed the Brillouin Zone (BZ) for the rest of this thesis. No other Brillouin Zone shall be mentioned.

For a square lattice such as that shown in Figure 1.3.6, the BZ is a right angled isosceles triangle with the length of two sides equal to a. The inset in the band

diagram in Figure 1.3.7 (b) shows the BZ for a square lattice, with the symmetry directions between points ΓM, ΓX, and XM demonstrated.

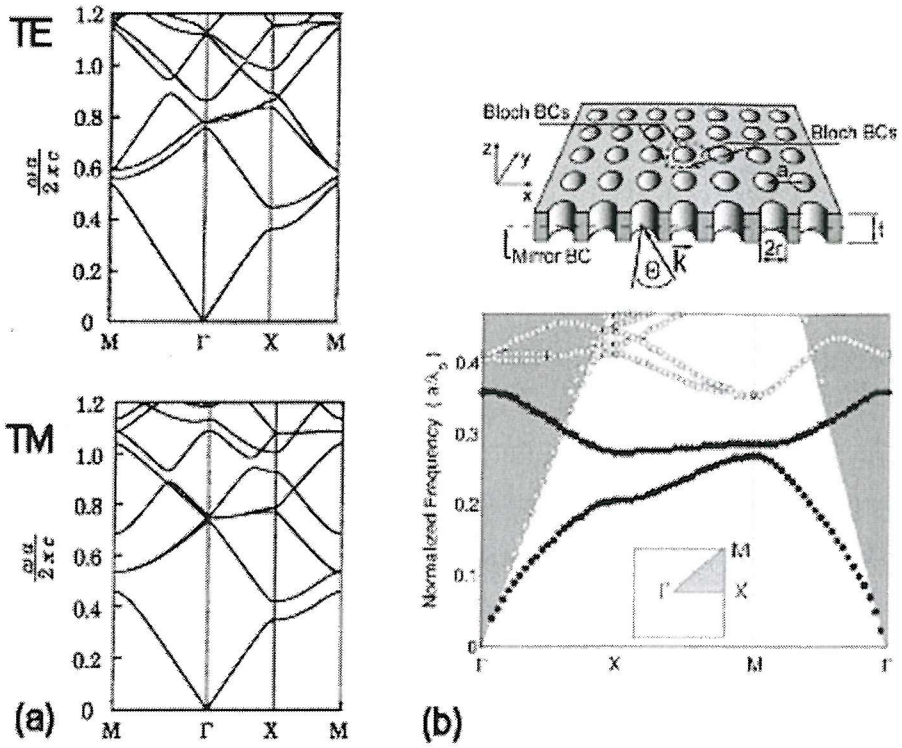

Figure 1.3.7 - Band diagrams for a square lattice for (a) pillar structures in both polarisations[122], and (b) etched hole structures in the TM polarisation [121].

The band diagram shows the photonic band structure as the wave vector goes around the edge of the BZ, from Γ to X, to M, and back to Γ. It may be seen from Figure 1.3.7(a) that there is no wavelength at which there is a photonic band for the pillar structures in air, and therefore there are no bandgaps in the system. This is also the case with the etched hole system, with no TM photonic bandgap for the square lattice (Figure 1.3.7 (b)). There is, however a photonic bandgap for the TE polarisation (not shown here). As with the 1D PC, there is a difference in the band structure between the TE and TM polarisations, as is shown in the differences between the upper and lower band diagrams in Figure 1.3.7 (a).

Using a different lattice structure for the 2D photonic crystal it is possible to achieve wider bandgaps. Figure 1.3.8 (a) shows the reciprocal lattice and the BZ for a

triangular lattice structure. Figure 1.3.8 (b) is the band diagram for a triangular lattice of glass pillars in air, while Figures 1.3.8 (c) and (d) are the TE and TM band diagrams for etched hole structures also in a triangular lattice.

Figures 1.3.8 (e) and (f) show measured transmission properties of structures corresponding with (c) and (d). A bandgap is shown in the TE polarisation which is complete for all directions, and there appears to be one in the TM polarisation too, though one can see from the band diagram that it is in fact pinched shut in one direction.

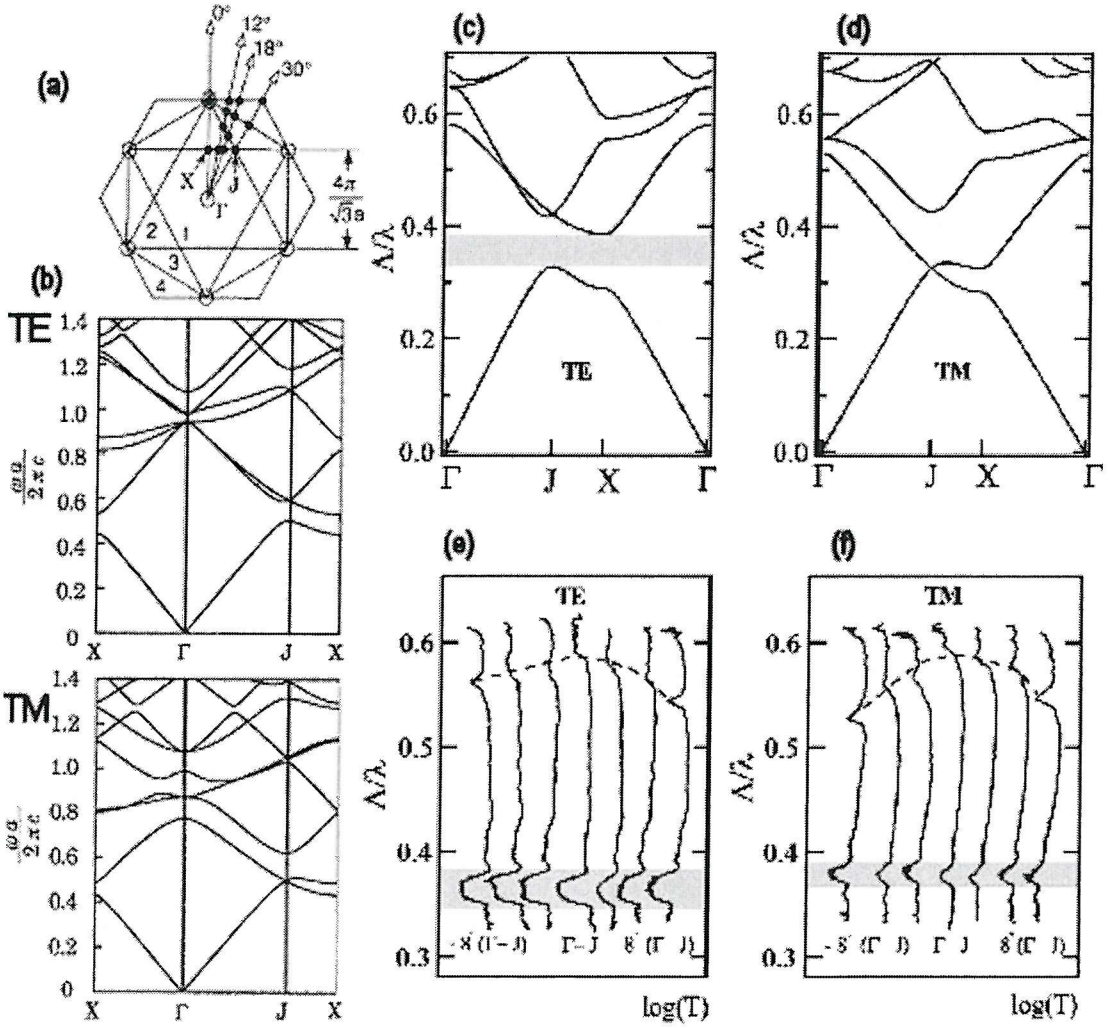

Figure 1.3.8 - (a) The reciprocal lattice [170] and BZ for a triangular lattice PC with the bandgaps for pillar [170] (b) and etched (c) and (d) structures shown in both TE and TM polarisations. Experimental transmission results are also shown (e) and (f) for the etched structures with the grey region highlighting the bandgap in almost every transmission direction at both polarisations [171].

In a PC with more than one PBG feature, the one which occurs at the longest wavelength, corresponding to the lowest-energy bandgap on the band diagrams, is known as the *primary* bandgap. The location and size of the primary PBG appearing in PCs is a function of the lattice pitch, the refractive index of the materials of which the PC is made, and also a function of the filling fraction of the PC. The filling fraction for a PC formed by etching circular holes into a dielectric layer is defined as fraction of the PC unit cell area which is taken up by the air holes. A PC with holes of a small diameter will have a bandgap located at a longer wavelengths than the same material etched with larger holes. Similarly, a PC with small holes etched at a large distance from each other will have a PBG located at longer wavelengths than the same material with the same holes etched at a smaller lattice pitch.

The greater the difference between the refractive indices of the materials forming the PC is, the deeper and wider the photonic bandgap will be. This is clearly shown in work carried out by Lin et al., the results of which are shown below in Figure 1.3.9. In this work glass pillars with a refractive index of 1.45 were immersed in liquids with refractive indices ranging down to 1.4. The strongest band features seen in the transmission spectrum was for the material which provided the strongest refractive index contrast [123].

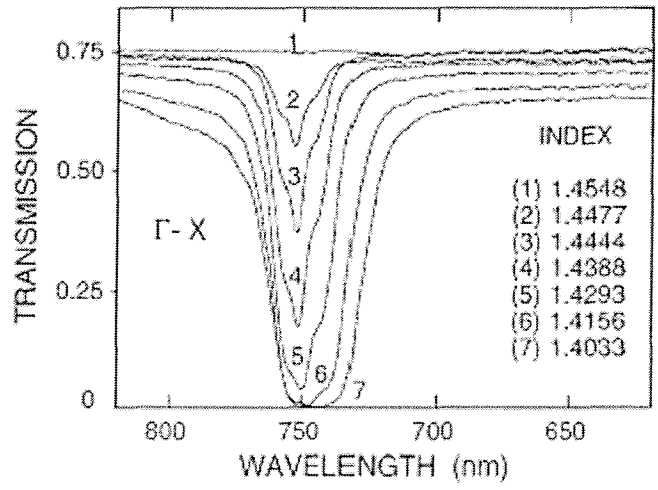

Figure 1.3.9 - Transmission of TM polarised light along the ΓX direction of a triangular 2D photonic crystal for immersion of the sample into liquids with varying refractive indices [123].

It is possible with a triangular lattice to form a complete photonic bandgap which forbids a range of frequencies in all directions of propagation and for all polarisations. This does, however, require large air holes and a high contrast in the materials used to construct the PC, for example GaAs with air-filled holes [124-127]. The PBG breadth is, however, extremely uneven, with some crystal directions having a much broader bandgap than others. It is possible to improve this by designing a PC 2D lattice with a higher order of symmetry than the standard square and triangular lattices which have no more than 6-fold symmetry.

M. Zoorob in 2000 designed a PC based upon a quasicrystalline structure composed of squares and triangles with 12-fold symmetry [127]. For this PC, although the width of the primary bandgap was reduced, it remained centered upon the same wavelength, with a PBG structure which was much more even than the triangular lattices [128].

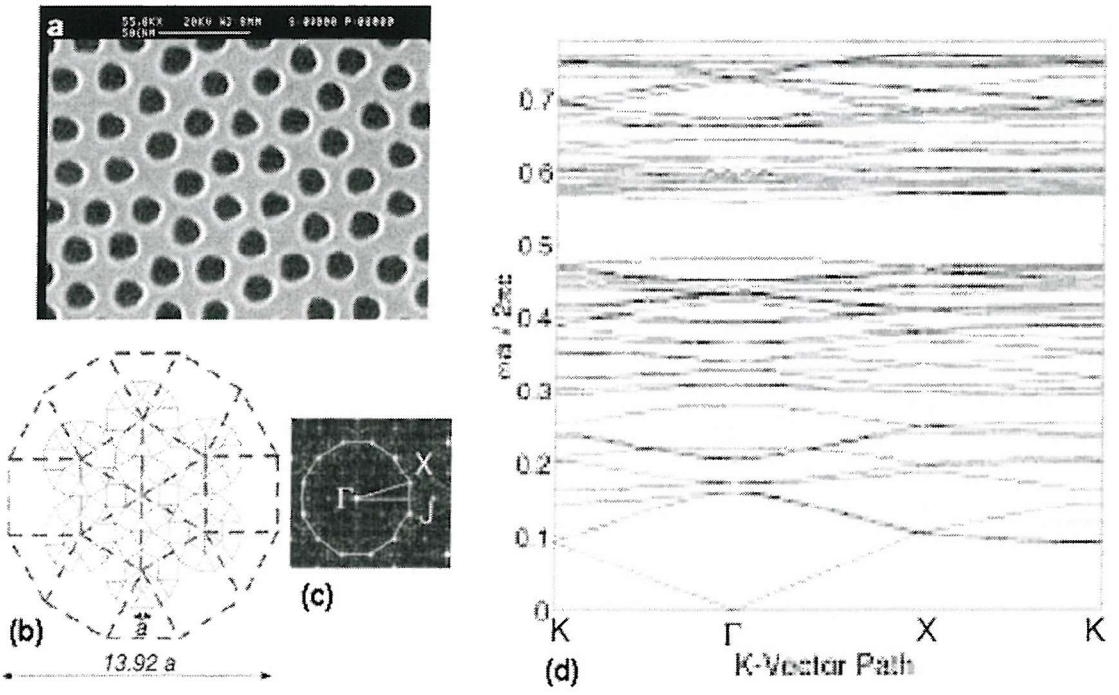

Figure 1.3.10 - (a) SEM image of the quasicrystal lattice with (b) a schematic of the implementation and the supercell (dashed line). The reciprocal lattice and brillouin zone (white dodecahedron) corresponding to the supercell shown in (b) are shown in (c) [127], while (d) shows a simulated representation of the band structure [128]

Photonic crystals, especially those which have been integrated into planar waveguide structures, have many potential applications for IOCs. The simplest has been the development of waveguides, for which a defect is formed in a 2D PC, forming a channel surrounded by what may be considered perfectly reflecting dielectric mirrors. Channel waveguides formed in this manner suffer from very high transmission loss, but this is compensated for by high isolation, low cross-talk between closely adjacent waveguides, and by the ability to make sharp bends with very small dimensions [11, 129]. An example of this is shown in Figure 1.3.11 (a) below.

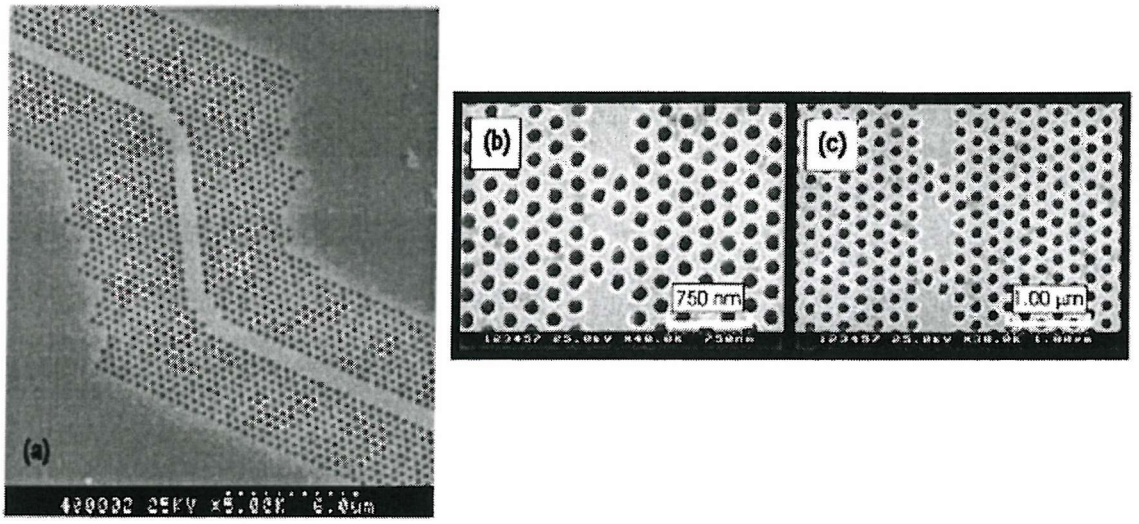

Figure 1.3.11 - (a) Ultrashort, double 60° bends for 1.55µm waveguides [129]. (b) and (c) show coupled cavity waveguides [130].

An extension of the channel waveguide is the use of coupled cavity waveguides formed by the removal of sets of holes in the PC structure (See Figure 1.3.11 (b) and (c))to tune which exact wavelength of light is permitted to transmit through the waveguide. Peaks occur in the transmission spectrum at wavelengths dictated by resonator size [130].

PCs have potential for replacing bulk optical fibre communications components, or even the larger planar waveguide IOCs. In 1999, Kosaka et al. demonstrated how a 2D PC with a triangular lattice structure had dispersive effects 500 times the strength of Newton's prism [131]. Light which varied by 1% in wavelength was dispersed

over 50° by the PC. PCs used for this application became known as superprisms, and have potential for use in ultra-dense WDM and lightbeam steering applications [132-5]. In 2000, Kosaka et al. demonstrated a spot size converter which may be used to integrate optical fibers and waveguide components [136]. In 2003, D.R. Solli et al. showed how the birefringence of 2D photonic crystals might be exploited to form waveplates, a bulk optical component widely used in the communications industry [137].

As mentioned in the 1D PC section, PCs have been used to enhance the extraction efficiency of light at the electronic bandgap [117]. M. Boroditsky et al. demonstrated six-fold enhancement in photoluminescence light extraction from an InGaAs/InP LED when surrounded by a 2D PC, as shown in Figure 1.3.12. Several different lattice constants were tried, from 600-900nm, with the 900nm lattice constant yielding the greatest enhancement.

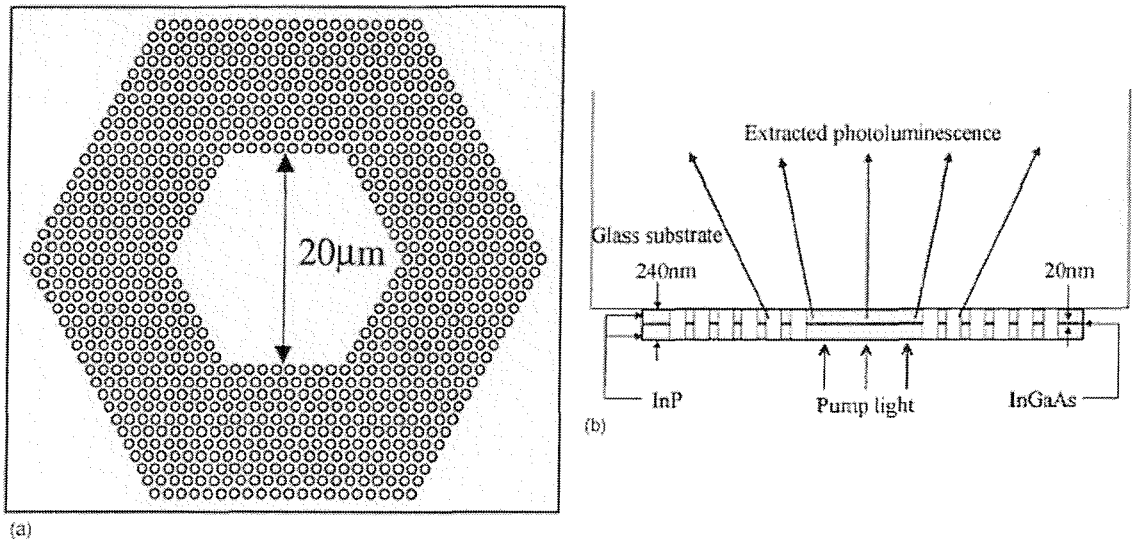

Figure 1.3.12 - (a) Top view and (b) side view of the LED geometry with PC-enhanced light extraction [139].

Other groups have worked with PC cavities in luminescent materials [140], and universally have concluded that photonic crystals have great application for the enhancement of light emission from such cavities. This work has been done universally in the III-V GaAsInP system [138, 139, 141]. Another area which has

received intense interest is that of Vertical Cavity Surface Emitting Lasers (VCSELs), the cavities of which are formed using PCs [142, 143].

1.3.3 3D Photonic Crystal fabrication methods and applications

From the beginning of PCs as a research field, there has been focus upon 3D structures [108], and Ho. et al. predicted that a 3D PC could have a complete PBG [144]. The first actually fabricated 3D structure with a full photonic bandgap was named 'Yablonovite' after its constructor, E. Yablonovitch, was manually drilled, and operated in the microwave portion of the spectrum [9, 145].

3D photonic crystals may be found occurring in the natural world [146]. Opals are an example of this [147], as are the irridescent wings of certain tropical butterflies [148]. 3D PCs are however, much more difficult to fabricate on a scale which permits a bandgap in the visible part of the spectrum. A method which has been widely used for fabrication is a lattice consisting of spheres stacked upon each other [149, 150, 151, 152, 153]. This structure results in a fcc lattice, very similar to that of an opal. In fact, these photonic crystals are sometimes called synthetic opals [154, 155, 156, 157]. SEM images of the resulting structures are shown in Figure 1.3.13.

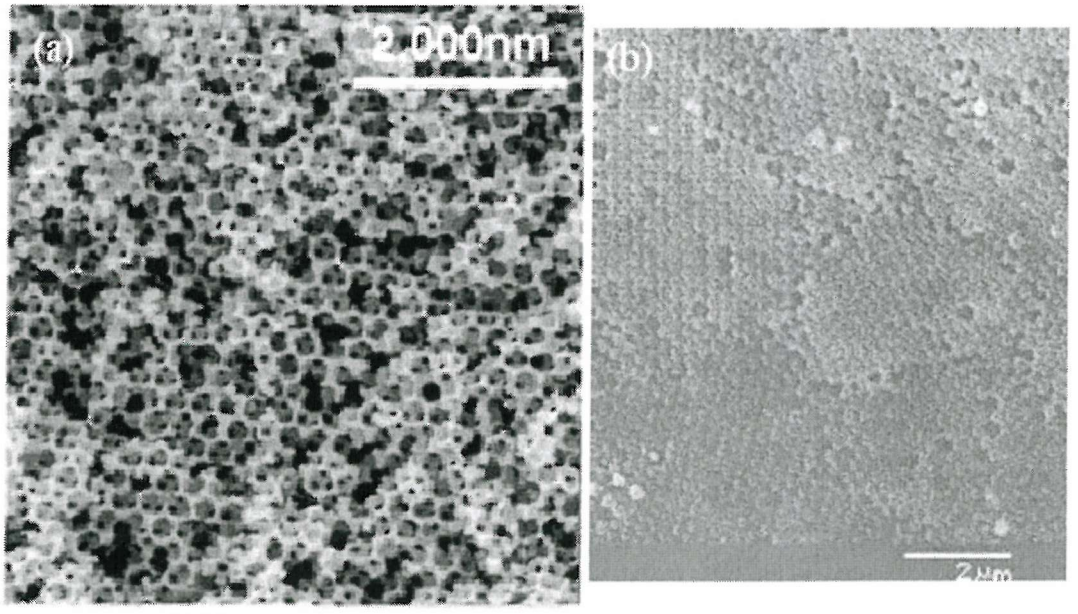

Figure 1.3.13 - SEM images of samples created by the stacked sphere method (a) using spheres as a template [155] and (b) using spheres in air[153].

Another method for the fabrication of 3D PCs is optical holography. In this method, a cubic lattice is obtained by interfering six optical beams, co-linear or perpendicular to each other, or by interfering four optical waves, each aligned along an axis of a regular tetrahedron [158] in a film of resist typically 30μm thick. This method is much more flexible than the stacking method, permitting the optical structures to be optimised by controlling the form of the interference pattern. This method also has high spatial resolution, is relatively cheap, and permits the formation of PCs from polymers with thus a wide range of material properties [159]. Samples formed by this method are shown in Figure 1.3.14. This method is limited however as polymers tend to be of low refractive index and are therefore of little use as PCs unless used as a template as is shown in Figure 1.3.14 (b).

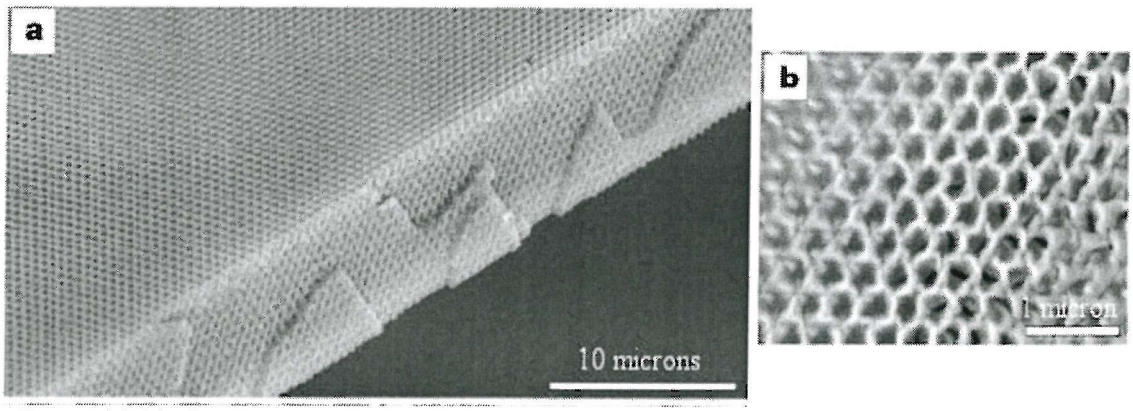

Figure 1.3.14 - SEM images of polymeric PCs created by optical holography. (a) showing the original sample and (b) showing a PC created using the polymeric sample as a template [159].

A method which uses relatively standard microelectronic fabrication technologies is the layer by layer method. Layers of one-dimensional rods with a stacking sequence which repeats every four layers is placed forming a fcc lattice [160, 161]. With this method it is possible to form PCs with photonic bandgaps at infrared wavelengths. SEM images of the structures formed are shown below.

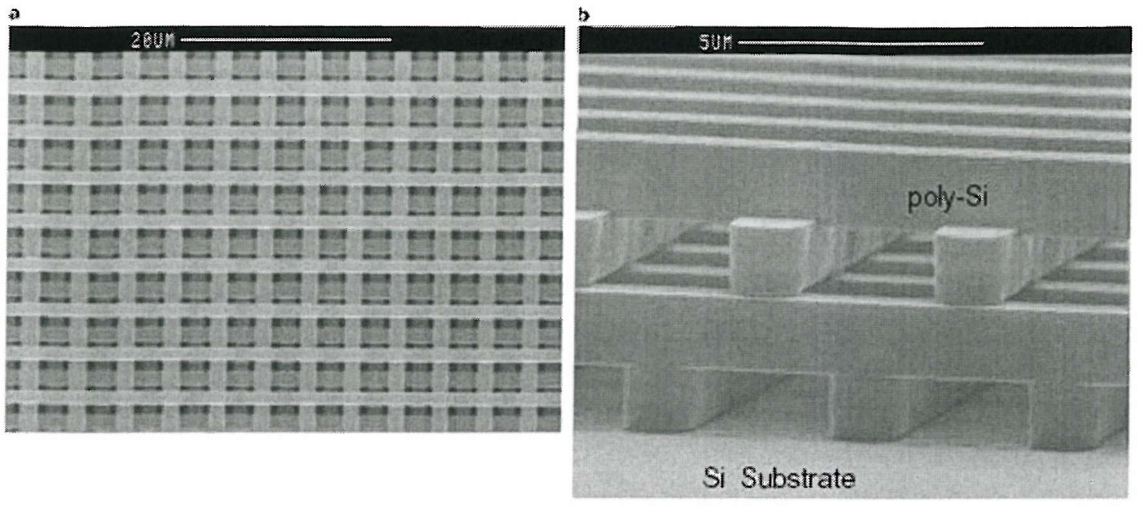

Figure 1.3.15 - SEM images from (a) above and (b) the side of a structure created by the layer by layer method [160].

Another method for 3D PC fabrication in a standard microelectronics clean room for the fabrication uses an electron-beam microscope to define a hexagonal structure, which is then etched into pits. Layers of alternating high and low refractive index are then deposited with a high degree of control, permitting the formation of waveguides normal to the surface of the wafer [162].

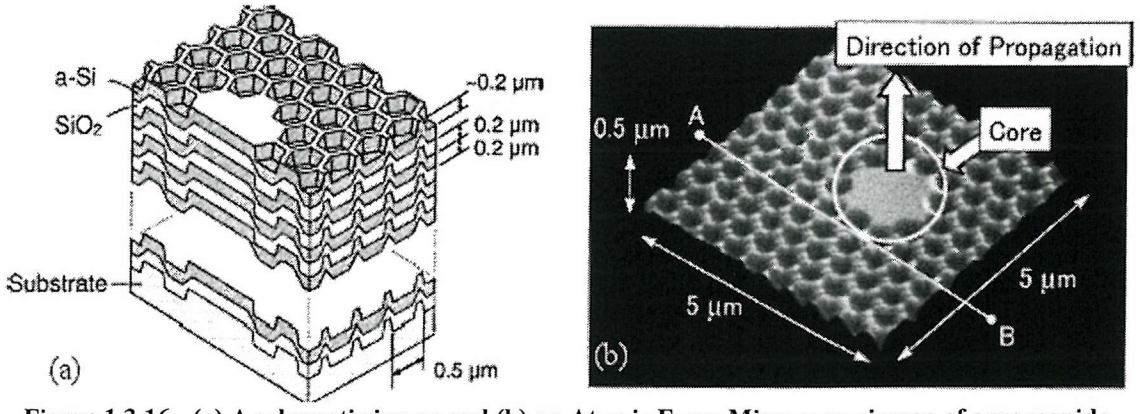

Figure 1.3.16 - (a) A schematic image and (b) an Atomic Force Microscope image of a waveguide formed perpendicular to the substrate by E-beam lithographically formed pits with deposition of alternating layers of high and low refractive index into the pits formed [162].

The superprism phenomenon was demonstrated in 3D PCs by T. Prasad et al. earlier this year [163] for an inverted fcc photonic crystal lattice. Figure 1.3.17 below shows the band structure for the lowest eight bands, computed using the plane wave method. The angular dispersion predicted for this structure is 14°/nm,

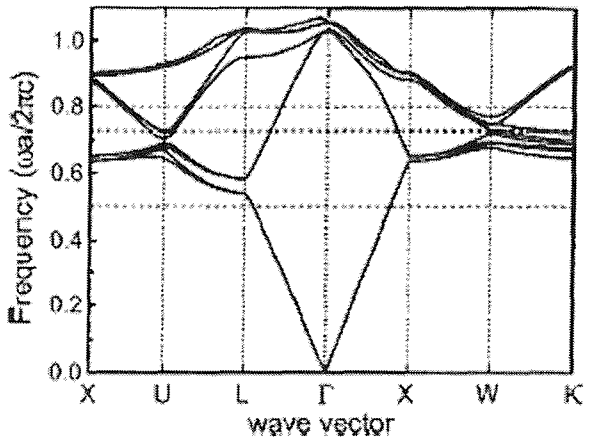

Figure 1.3.17 - The band structure for a 3D inverted fcc PC

One application for 3D photonic crystals is in the field of directional antennae [164]. Temelkuran et al. created an antennae formed by a hybrid combination of a monopole radiation source and a cavity built around a dielectric layer by layer 3D photonic crystal. The antenna had a narrow bandwidth and demonstrated a power enhancement of 180 at the resonant frequency of the cavity. This resonance was found to be tuneable within the band gap of the photonic crystal.

Further applications of polymer photonic crystals include the use of polymer PCs to flash an optical bar code incorporated into the uniform of militaries for use in the identification of friendly forces [165].

1.4 Conclusions

Integrated optical devices have sufficient advantages over traditional optical fibre and bulk optical circuits to make the large investment currently underway into their development well worth the effort. Planar optical devices, integrated on a silicon wafer particularly have the advantages of low expense, high integration, and potential integration with silicon electronic devices.

Optical fibres, while well optimised for long-haul optical telecommunications, are not appropriate for the optical circuitry used to control, reroute, and modify light, especially for signals which are not intended to travel for more than a few centimetres. Due to the increase in complexity of electrical circuitry, it is becoming clear that optical interconnects will in the future be preferred over the standard wire connects, especially for distances greater than several centimetres, such as those between separate circuit boards, as well as on-chip interconnections.

Waveguides, as the fundamental component of any integrated optical circuit, have been widely studied. In order to couple light in and out of optical waveguides with high efficiency, the refractive index of the core material should be well matched with the input system's refractive index, while for high confinement of the optical modes, and the reduction bend radii and size of the overall circuit, it is desirable that the waveguide be of a much higher refractive index than the surrounding regions.

Waveguides in silicon, while transparent for wavelengths longer than 1.1μm, are of no use in the visible region, which discounts SOI as a basis for an IOC in those wavelength ranges. Other silicon-compatible materials which may be deposited upon a buffer layer of SiO_2 include Si_3N_4 and SiON, both of which may be formed by many methods including PECVD, LPCVD, and sputtering, these are deposition methods currently in use in standard microelectronic clean rooms.

Light Emitting Devices in silicon are essential if the link between electrical and optical circuitry is ever to be realised. Silicon, as an indirect bandgap semiconductor is a poor light emitter itself. This may be overcome by many methods including those of microstructuring bulk silicon, through doping with rare-earth elements, through quantum confinement, porous silicon, and nanocrystalline silicon. Of these, nanocrystalline silicon shows the greatest stability, with erbium-doped silicon nanocrystals showing high potential for future commercial devices.

IOC components such as the AWG already provide a significant reduction in the size of the optical circuit from the bulk components, but photonic crystals permit the shrinkage of these devices by orders of magnitude beyond that. Photonic bandgaps operate in 1D, 2D and 3D structures, with 2D photonic crystals etched into waveguides are well understood and relatively simple to fabricate. The applications for waveguide bends of a very small radius in particular would permit much smaller IOCs to be fabricated using PCs.

While some researchers have explored the potential for photonic crystals in light emitting materials such as the InGaAsP system or porous silicon, there has yet to be a study on 2D PCs etched into a waveguide of a material incorporating luminescent silicon nanocrystals. It is toward this area which this thesis has been directed.

References

[1] Ghatak, A. and Thygarajan, J. *Introduction to Fibre Optics* (1998). Cambridge University Press, Cambridge, UK.

[2] A. Polman, D. C. Jacobson, D. J. Eaglesham, R. C. Kistler, J. M. Poate , Journal of Applied Physics, **70**(7) p3778-3784 (1991)

[3] Sze, S.M. *Semiconductor Devices, Physics and Technology, 2nd Edition* (2002). John Wiley & Sons, New York.

[4] C. Dragone, Electronics Letters, **29**(12) p1121-1122 (1993)

[5]O. Gomez-Daza, J. Campos, A. Sanchez, et. al., Journal of The Electrochemical Society, **148**(6) pG330-G335 (2001)

[6]A. Conde-Gallardo, M. García-Rocha, I. Hernández-Calderón, R. Palomino-Merino, Applied Physics Letters, **78**(22) p3436-3438 (2001)

[7] M.-H. Lu, J.C. Sturm, Applied Physics Letters, **78**(13) p1927-1929 (2001)

[8] IBM, *SOI Technology: IBM's Next Advance In Chip Design*

[9] M. Ito, K. Yamagata, H. Miyabayashi, T. Yonehara, Proc. 2000 IEEE International SOI conference p10-11 (2000)

[10] A. F. Evans, D. G. Hall, W. P. Maszara, Applied Physics Letters, **59**(14) p1667-1669 (1991)

[11] M. Tokushima, H. Kosaka, A. Tomita, H. Yamada, Applied Physics Letters, **76**(8) p952-954 (2000)

[12] X. F. Wang, P. Vasilopoulos , Physical Review B, **35305** (2003)

[13] B. Li, G. Li , E. Liu, et. al., Applied Physics Letters, **75**(1) p1-3 (1999)

[14] U. Fischer, B. Schuppert, K. Petermann, Photonics Technology Letters, IEEE, **5**(7) p785-787 (1993)

[15] C. Z. Zhao, A. H. Chen, E.K. Liu, G.Z. Li, Photonics Technology Letters, IEEE, **9**(8) p1113-1115 (1997)

[16] W.A.P. Claassen, W.G.J.N. Valkenburg, M.F.C. Willemsen, W.M.v.d. Wijgert, J. Electrochem. Soc, **132**(4) p893-898 (1985)

[17]L. Zambom, R. Mansano, R. Furlan *Characteristics of silicon nitride films deposited by inductively coupled plasma CVD*

[18] A. Aydinli, A. Serpengüzel, D. Vardar, Solid State Communications, **98**(4) p273-277 (1996)

[19] L. Cai, A. Rohatgi, D. Yang, M.A. El-Sayed, Journal of Applied Physics, **80**(9) p5384-5388 (1996)

[20] L. Cai, A. Rohatgi, S. Han, G. May, M. Zou, Journal of Applied Physics, **83**(11) p5885-5889 (1998)

[21] K. Worhoff, P.V. Lambeck, A. Driessen, Journal of Lightwave Technology, **17**(8) p1401-1407 (1999)

[22] B.S. Sahu, O.P. Agnihotri, S.C. Jain, R. Mertens, I. Kato, Semicond. Sci. Technol., **15**(3) pL11-L14 (2000)

[23] J. O. Roza, O. Sanchez-Garrido, J.M. Albella, Journal of Vacuum Science and Technology A, **16**(5) p2757-2761 (1998)

[24] M. Hoffmann, P. Kopla, E. Voges, IEEE Photonics Technology Letters, **9**(9) p1238-1240 (1997)

[25] K. E. Mattsson, Journal of Applied Physics, **77**(12) p6616-6623 (1995)

[26] M.K. Smit, Electronics Letters, **24**(7) p385-386 (1988)

[27] P.S. Andre, J.L. Pinto, I.Abe, H.J. Kalinowski, O.Frazao, Journal of Microwaves and Optoelectronics, **2**(3) p32-45 (2001)

[28] *Photonics Industry Overview* (2001)

[29] S. Suzuki, S. Sumida, Y. Inoue, M. Ishii, Y. Ohmori, Electronics Letters, **33**(13) p1173-1174 (1997)

[30] M.K. Smit, C. van Dam, IEEE journal of selected topics in quantum electronics, **2**(2) p236-250 (1996)

[31] K. Okamoto, K. Syuto, H. Takahashi, Y. Ohmori, Electronics Letters, **32**(16) p1474-1476 (1996)

[32] T. Miya, IEEE journal of selected topics in quantum electronics, **6**(1) p38-45 (2000)

[33] National Academy of Engineering, *Laser and Fiber Optics timeline*

[34] L. Pavesi, *Optoelectronic Integration on Silicon* (2003)

[35] J.R.Haynes, H.B. Briggs, Physical Review, **86**(4) p637-662 (1952)

[36] J.R. Haynes, W.C.Westphal, Physical Review, **101**(6) p1676-1678 (1956)

[37] W. L. Ng, et. al., Nature, **410** p192-194 (2001)

[38] T. Trupke, J. Zhao, A. Wang, R. Corkish, M.A. Green, Applied Physics Letters, **82**(18) p2996-2998 (2003)

[39] M. A. Green, J. Zhao, A. Wang, P. J. Reece, M. Gal, Nature, **412** p805-808 (2001)

[40] E.F. Steigmeier, R. Morf, D. Grutzmacher, et al., Applied Physics Letters, **69**(27) p4165-4167 (1996)

[41] L. Heikkila, T. Kuusela, H.-P. Hedman, Journal of Applied Physics, **89**(4) p2179-2184 (2000)

[42] L.T. Canham, K.G. Barraclough, D.J. Robbins , Applied Physics Letters, **51**(19) p1509-1511 (1987)

[43] H. B. Erzgräber, K. Schmalz , Journal of Applied Physics, **78**(6) p4066-4068 (1995)

[44] P. G. Kik, Thesis (2000)

[45] H. Ennen, J. Schneider, G. Pomrenke, A. Axmann, Applied Physics Letters, **43**(10) p943-945 (1983)

[46] N. Hamelin, P.G. Kik, J. F. Suyver, et. al., Journal of Applied Physics, **88**(9) p5381-5387 (2000)

[47] L. Rebohle, J. von Borany, D. Borchert, et. al., Electrochemical and Solid-State Letters, **4**(7) pG57-G60 (2001)

[48] M.Q. Huda, A.R. Peaker, J.H. Evans-Freeman, D.C. Houghton, W.P. Gillin, Electronics Letters, **33** p1182 (1997)

[49] H. Yang, X. Wang, S. Xie, F. Wang, X. Gu, Applied Physics Letters, **81**(27) p5144-5146 (2002)

[50] Y. Maeda, N. Tsukamoto, Y.Yazawa , Y. Kanemitsu, Y. Masumoto , Applied Physics Letters, **59**(24) p3168-3170 (1991)

[51] L.T. Canham, Applied Physics Letters, **57**(10) p1046-1048 (1990)

[52] C. Pickering, M.I.J. Beale, D.J. Robbins, P.J. Pearson, R. Greef, Journal of Physics C: Solid State Phys., **17** p6535-6552 (1984)

[53] T. Takagahara, K. Takeda , Physical Review B, **46**(23) p15578-15581 (1992)

[54] N. Hill , K. Whaley , Physical Review Letters, **75**(6) p1130-1133 (1995)

[55] M. Araki, H. Koyama, N. Koshida, Applied Physics Letters, **68**(21) p2999-3000 (1996)

[56] L.C. Wang, X.N. Liu, F. Yan, et. al., Applied Physics Letters, **70**(71) p2265-2267 (1997)

[57] K.Y. Suh, Y.S. Kim, S.Y. Park, H.H. Lee, Journal of The Electrochemical Society, 148(6) pC439-C442 (2001)

[58] D. Kovalev, H. Heckler, G. Polisski, F. Koch, Physica Status Solidi (b), **215**(2) p871-932 (1999)

[59] P.F.Trwoga, A.J.Kenyon, C.W.Pitt, Electronics Letters, **32**(18) p1703-1704 (1996)

[60] O. Bisi, S. Ossicini, L. Pavesi, Surface Science Reports, **38**(13) p1-126 (2000)

[61] A. Loni, A.J. Simons, P.D.J. Calcott, et. al., Applied Physics Letters, **71**(1) p107-109 (1997)

[62] B. Zou, J. Wang, C. Liu, J. Zhang, M. El-Sayed, Physical Review B, **62**(24) p16595-16599 (2000)

[63] B. Gelloz, N. Koshida, Journal of Applied Physics, **88**(7) p4319-4324 (2000)

[64] T. Shimizu-Iwayama, M. Ohshima, T. Niimi, S. Nakao, K. Saitoh, Journal of Physics: Condensed Matter, **5** pL375-L380 (1993)

[65] X. Liu, X. Wu, X. Bao, Y. He, Applied Physics Letters, **64**(2) p220-222 (1994)

[66] E. Edelberg, S. Bergh, R. Naone, M. Hall, E.S. Aydil, Applied Physics Letters, **68**(10) p1415-1417 (1996)

[67]G. Cicala, P. Capezzuto, G. Bruno, et. al., Journal of Applied Physics, **80**(11) p6564-6566 (1996)

[68]T. Inokuma, Y. Wakayama, T. Muramoto, et. al., Journal of Applied Physics, **83**(4) p2228-2234 (1998)

[69] A. Pifferi, P. Taroni, A. Torricelli, et. al., Applied Physics Letters, **70**(3) p348-350 (1997)

[70] M. L. Brongersma, A. Polman, K. S. Min, E. Boer, T. Tambo, Applied Physics Letters, **72**(20) p2577-2579 (1998)

[71] A. J. Kenyon, P. F. Trwoga, C. W. Pitt,, G. Rehm, Applied Physics Letters, **73**(4) p523-525 (1998)

[72] Y. Q. Wang, G. L. Kong, W. D. Chen, H. W. Diao, et. al., Applied Physics Letters, **81**(22) p4174-4176 (2002)

[73] T.G. Kim, C.N. Whang, Y. Sun, et. al., Journal of Applied Physics, **91**(5) p3236-3242 (2002)

[74] G. H. Li, K. Ding, Y. Chen, H. X. Han, Z. P. Wang , Journal of Applied Physics, **88**(3) p1439-1422 (2000)

[75] V. Vinciguerra, G. Franzò, F. Priolo, F. Iacona, C. Spinella, Journal of Applied Physics, **87**(11) p8165-8173 (2000)

[76] F. Iacona, G. Franzò, C. Spinella, Journal of Applied Physics, **87**(3) p1295-1303 (2000)

[77] Y. Kanemitsu , T. Ogawa, K. Shiraishi, K. Takeda , Physical Review B, **48**(7) p4883-4886 (1993)

[78] D. Zhang, R.M. Kolbas, P.D. Milewski, et. al., Applied Physics Letters, **65**(21) p2684-2686 (1994)

[79] K. Kim, Physical Review B, **57**(20) p13072-13076 (1998)

[80] L.N. Dinh, L.L. Chase, M. Balooch, W.J. Siekhaus, F. Wooten, Physical Review B, **54**(7) p5029-5037 (1996)

[81] X. Du, M. Takeguchi, M. Tanaka, K. Furuya, Applied Physics Letters, **82**(7) p1108-1110 (2003)

[82] O. Hanaizumi, K. Ono, Y. Ogawa, Applied Physics Letters, **82**(4) p538-540 (2003)

[83] X.M. Wu, L.J. Zhuge, N.Y. Tang, et. al., Surface & Coatings Technology, **154**(1) p82-87 (2002)

[84] M. Zacharias, J. Heitmann, R. Scholz, et. al., Applied Physics Letters, 80(4) p661-663 (2002)

[85] L. Khriachtchev, M. Rasanen, S. Novikov, J. Sinkkonen, Applied Physics Letters, **79**(9) p1249-1251 (2001)

[86] L. Khriachtchev , O. Kilpelä , S. Karirinne, J. Keränen, L. Lepistö , Applied Physics Letters, **78**(3) p323-325 (2001)

[87] P. Photopoulos, A.G. Nassiopoulou, D.N. Kouvatsos, A. Travlos, Applied Physics Letters, **76**(24) p3588-3590 (2000)

[88] S. Fujita, N. Sugiyama, Applied Physics Letters, **74**(2) p308-310 (1999)

[89] G. Franzò, A. Irrera, E.C.Moreira, et al., Applied Physics A - Materials Science and Processing, **74**(1) p1-6 (2002)

[90] P. Photopoulos , A. G. Nassiopoulou, Applied Physics Letters, **77**(12) p1816-1818 (2000)

[91] H. S. Bae, T. G. Kim, C. N. Whang, S. Im, Journal of Applied Physics, **91**(7) p4078-4081 (2002)

[92] T. Shimizu-Iwayama, N. Kurumado, D. Hole, P. Townsend, Journal of Applied Physics, **83**(11) p6018-6022 (1998)

[93] G. Ledoux, O. Guillois, D. Porterat, et. al., Physical Review B, **62**(23) p15942-15951 (2000)

[94] S. Guha, S. B. Qadri, R. G. Musket, M. A. Wall, T. Shimizu-Iwayama, Journal of Applied Physics, **88**(7) p3954-3961 (2000)

[95] G. G. Qin, A. P. Li, B. R. Zhang , Bing-Chen Li, Journal of Applied Physics, 78(3) p2006-2009 (1995)

[96] Y. Kanemitsu, S. Okamoto, M. Otobe, S. Oda, Physical Review B, **55**(12) pR7375-R7378 (1997)

[97] V.I. Klimov, Ch.J. Schwarz, D.W. McBranch, C.W. White, Applied Physics Letters, **73**(18) p2603-2605 (1998)

[98] J.S. Zhuravlev, A.M. Gilinsky, A.Yu Kobitsky, Applied Physics Letters, **73**(20) p2962-2964 (1998)

[99] S.M. Prokes, W.E. Carlos, S. Veprek, Ch. Ossadnik, Physical Review B, **58**(23) p15632-15635 (1998)

[100] J. Valenta, I. Pelant , J. Linnros , Applied Physics Letters, **81**(8) p1396-1398 (2002)

[101] L. Dal Negro, M. Cazzanelli, N. Daldosso, Z. Gaburro, L. Pavesi, Physica E, **16** p297-308 (2003)

[102] J.H. Shin, M.-J. Kim, S. Seo, C. Lee, Applied Physics Letters, 72(9) p1092-1094 (1998)

[103] X. Zhao, S. Komuro, H. Isshiki, Y. Aoyagi, T. Sugano, Applied Physics Letters, 74(1) p120-2 (1999)

[104] S. Seo, J. H. Shin, Applied Physics Letters, **75**(26) p4470-4072 (1999)

[105] F. Priolo, G. Franzò, D. Pacifici, V. Vinciguerra, Journal of Applied Physics, **89**(1) p264-272 (2001)

[106] A. J. Kenyon, C. E. Chryssou, C. W. Pitt , T. Shimizu-Iwayama , D. E. Hole , Journal of Applied Physics, **91**(1) p367-374 (2002)

[107] The ST website: http://us.st.com/stonline/press/magazine/challeng/3rdedi02/chal1.htm

[108] V.P. Bykov, Soviet Physics JETP, **35**(2) p269-273 (1972)

[109] E. Yablonovitch, Physical Review Letters, **58**(20) p2059-2062 (1987)

[110] Joannopoulos, J.D., Meade, R.D., Winn, J.N., *Photonic Crystals* (1995). Princeton University Press, New Jersey, U.S.A..

[111] M. Scalora, J.P. Dowling, C.M. Bowden, M.J. Bloemer, Physical Review Letters, **73**(10) p1368-1371 (1994)

[112] Ch. Spielmann, R. Szipöcs, A. Stingl, F. Krausz , Physical Review Letters, **73**(17) p2308-2311 (1994)

[113] S. Esposito, Physical Review E, **64** p026609 (2001)

[114] S. Esposito, Physics Letters A, **225**(46) p203-209 (1997)

[115] A. Haché, L. Poirier, Applied Physics Letters, 80(3) p518-520 (2002)

[116] C.G.B. Garrett, D.E. McCumber, Physical Review A, **1**(2) p305-313 (1970)

[117] M.D. Tocci, M. Scalora, M.J. Bloemer, J.P. Dowling, C.M. Bowden, Physical Review A, **53** p2799-2803 (1996)

[118] H.A. Lopez, P.M. Fauchet, Applied Physics Letters, **77**(23) p3704-3706 (2000)

[119] P. Ferrand, D. Loi, R. Romestain, Applied Physics Letters, 79(19) p3017-3019 (2001)

[120] D. Zhao, B. Shi, Z. Jiang, Y, Fan, X. Wang, Applied Physics Letters, **81**(3) p409-411 (2002)

[121]M. Loncar, J. Vuckovic, A. Scherer, *Three-dimensional analysis of dispersion properties of planar photonic crystals* (2002)

[122] M.M. Sigalas, R. Biswas, K.M. Ho, C.M. Soukoulis, Physical Review B, 58(11) p6791-6794 (1998)

[123] H.-B. Lin, R.J. Tonucci, A. J. Campillo , Applied Physics Letters, **68**(21) p2927-2929 (1996)

[124] M. Plihal, A. A. Maradudin, Physical Review B, **44**(16) p8565-8571 (1991)

[125] D. Cassagne, C. Jouanin, D. Bertho , Physical Review B, **53**(11) p7134-7142 (1996)

[126] A. Barra, D. Cassagne, C. Jouanin, Applied Physics Letters, **72**(6) p627-629 (1998)

[127] M.E. Zoorob, M.D.B. Charlton, G.J. Parker, J.J. Baumberg, M.C. Netti, Nature, 404 p740-743 (2000)

[128]B.P. Hiett, J.M. Generowicz, D.H. Beckett, et. al., 4th International Conference on Materials for Microelectronics and Nanoengineering (2002)

[129] A. Talneau, L. Le Gouezigou , N. Bouadma, M. Kafesaki, C. M. Soukoulis, Applied Physics Letters, **80**(4) p547-549 (2002)

[130] J. Moosburger, M. Kamp, A .Forchel, U. Oesterle, R. Houdré, Journal of Applied Physics, **91**(8) p4791-4794 (2002)

[131] H. Kosaka, T. Kawashima, A. Tomita, et. al., Journal of Lightwave Technology, **17**(11) p2032-2037 (1999)

[132] B.Li, J. Zhou, .L. Li. Applied Physics Letters **83**(23) p4704-4706 (2003)

[133] D. Z. Ting, Proceedings of SPIE -- Volume 4992 Ultrafast Phenomena in Semiconductors VII p 43-54 (2003)

[134] R. Rengarajan, T. Prasad, V. L. Colvin, D. Mittleman Proceedings of SPIE, Volume 4809 Nanoscale Optics and Applications (2002), pp. 17-24

[135] H. Kosaka, T. Kawashima, A. Tomita, M. Notomi, T. Tamamura, T. Sato, S. Kawakami Applied Physics Letters **74**(10) p1370-1372(1999)

[136]H. Kosaka, T. Kawashima, A. Tomita, T. Sato, S. Kawakami, Applied Physics Letters, **76**(3) p268-270 (2000)

[137] D. R. Solli, C. F. McCormick, R. Y. Chiao, J. M. Hickmann, Applied Physics Letters, **82**(7) p1036-1038 (2003)

[138] T. Yoshie, A.Scherera, H. Chen, D. Huffaker, D. Deppe, Applied Physics Letters, 79(1) p114-116 (2001)

[139] M. Boroditsky, T. F. Krauss, R. Coccioli, R. Vrijen, R. Bhat, Applied Physics Letters, **75**(8) p1036-1038 (1999)

[140] K.J. Price, L.R. Sharpe, L.E. McNeil, E.A. Irene, *Electroluminescence from amorphous silicon oxynitride films* (1997)

[141] T. Yoshie, J. Vuckovic, A. Scherer, H. Chen, D. Deppe, Applied Physics Letters, **79**(26) p4289-4291 (2001)

[142] J.P. Dowling, M. Scalora, M.J. Bloemer, C.M. Bowden , Journal of Applied Physics, **75**(4) p1896-1899 (1994)

[143] W.D. Zhou, J. Sabarinathan, B. Kochman, et. al., Electronics Letters, **36**(18) p1541-2 (2000))

[144] K. M. Ho, C. T. Chan, C. M. Soukoulis , Physical Review Letters, **65** p3152-3155 (1990)

[145] E. Yablonovitch, T.J. Gmitter, Physical Review Letters, **67**(17) p2295-2298 (1991)

[146] P. Vukusic, J. R. Sambles, Nature, **424** p852-855 (2003)

[147] A. van Blaaderen, Science, **282** p887-888 (1998)

[148] L. Plattner, Thesis, University of Southampton (2003)

[149] E.R. Brown, O.B. McMahon, Applied Physics Letters, **67**(15) p2138-2140 (1995)

[150] J. Martorell, R. Vilaseca, R. Corbalán, Applied Physics Letters, **70**(6) p702-704 (1997)

[151] A. Imhof, W.L. Vos, R. Sprik, A. Lagendijk, Physical Review Letters, **83**(15) p2942-2945 (1999)

[152] Y.A. Vlasov, M. Deutsch, D.J. Norris, Applied Physics Letters, **76**(12) p1627-1629 (2000)

[153] J. Zhou, Y. Zhou, L. Ng, et. al., Applied Physics Letters, **76**(23) p3337-3339 (2000)

[154] V.N. Astratov, Y.A. Vlasov, O.Z. Karimov, et. al., Physics Letters A, **222**(5) p349-353 (1996)

[155] Y.A. Vlasov, N. Yao, D.J. Norris, Advanced Materials, **11**(2) p165-169 (1999)

[156] Y.A. Vlasov, S. Petit, G. Klein, B. Honerlage, Ch. Hirliman, Physical Review E, **60**(1) p1030-1035 (1999)

[157] Y.A. Vlasov, M.A. Kaliteevski, V.V. Nikolaev, Physical Review B, **60**(3) p1555-1562 (1999)

[158]V. Berger, O. Gauthier-Lafaye, E. Costard, Journal of Applied Physics, **82**(1) p60-64 (1997)

[159] M. Campbell, D.N. Sharp, M.T. Harrison, R.G. Denning, A.J. Tuberfield, Nature, **404** p53-56 (2000)

[160] S. Y. Lin, J. G. Fleming, D. L. Hetherington, B.K. Smith, R. Biswas, Nature, **394** p251-253 (1998)

[161] M. Bayindir, E. Ozbay, Physical Review B, **62**(4) pR2247-2250 (2000)

[162] O. Hanaizumi, Y. Ohtera, T. Sato, S. Kawakami, Applied Physics Letters, **74**(6) p777-779 (1999)

[163] T. Prasad, V. Colvin, D. Mittleman, Physical Review B, **67** p165103 (2003)

[164] B. Temelkuran, M. Mayindir, E. Ozbay, R. Bizwas, et al., Journal of Applied Physics, **87**(1) p603-605 (2000)

[165] T. Riordan, New York Times (2002)

[166] C.L. Heng, Y. Chen, Z.C. Ma, W.H. Zong, G.G. Qin, Journal of Applied Physics, **89**(10) p5682-5686 (2001)

[167] F.L. Martinez, A. del Prado, I. Martil, et. al., Physical Review B, **63** p245320 (2001)

[168] K.-Y. Liou, Y. K. Jhee, G. Eisenstein, R. S. Tucker, R. T. Ku, Applied Physics Letters, **48**(16) p1039-1041 (1986)

[169] Kittel, C. *Introduction to Solid State Physics, 7th Edition* (1996). John Wiley & Sons, Inc. New York

[170] A. Rosenberg, R.J. Tonucci, E.A. Bolden, Applied Physics Letters, **69**(18) p2638-2640 (1996)

[171] M.C. Netti, M.D.B. Charlton, G.J. Parker, J.J. Baumberg, Applied Physics Letters, **76**(8) p991-993 (2000)

2 The Phased Array Waveguide Grating

As described in the previous chapter, the Phased Array Waveguide Grating (PAWG) is a prime example of integrated optics which may replace bulk optical components, and of which there is a promising photonic crystal alternative. In brief summary, the PAWG is an optical component, composed of slab and ridge waveguides, used to differentiate wavelength division multiplexed (WDM) signals. It may also be used in reverse to multiplex signals. In this chapter, the design of the PAWG itself, and the development of a potential material in which to fabricate it, is described.

2.1 A Matlab Modefinder

To design a system based upon waveguides, it was necessary to first create a waveguide simulation program. This program must be compatible with the method to be used for designing the PAWG, in this case the modelling program Matlab.

2.1.1 Modefinder Theory

The method used for waveguide simulation was adapted from *Introduction to Fibre Optics* by A. Ghatak and J. Thygarajan [1]. In this method, which is closely related to optical fibre simulation techniques, a dimensionless waveguide parameter (V) is found based upon the refractive indices of core (n_1) and cladding (n_2) layers, the waveguide core thickness (d), and the wavelength of operation (λ_0). For the purposes of the simulation, it is assumed that the thickness of the buffer layer is sufficient that the substrate material has no effect upon guided waveguide modes.

$$V = \frac{2\pi}{\lambda_0} d\sqrt{n_1^{\,2} - n_2^{\,2}} \tag{2.1}$$

A parameter ξ is defined as,

$$\xi = \sqrt{k_0{}^2 n_1{}^2 - \beta^2}\,\frac{d}{2} \qquad , \qquad k_0 = \frac{\omega}{c} = \frac{2\pi}{\lambda_0}$$

(2.2)

where β represents the propagation constant, and $\omega$is the angular frequency of the mode. The parameter c is the speed of light in vacuum. For Transverse Electric (TE) polarisation two equations describe the guided modes for the waveguide.

$$\xi \tan\xi = \sqrt{\left[\left(\frac{V}{2}\right)^2 - \xi^2\right]} \quad \text{for symmetric TE modes}$$

(2.3)

and

$$-\xi \cot\xi = \sqrt{\left[\left(\frac{V}{2}\right)^2 - \xi^2\right]} \quad \text{for anti-symmetric TE modes}$$

(2.4)

These two simultaneous equations may be solved to find the values for ξ which correspond with the particular V found above. Once ξ is known, the dimensionless propagation constant b may be found. b is defined as,

$$b \equiv \frac{\beta^2/k_0{}^2 - n_2{}^2}{n_1{}^2 - n_2{}^2} = 1 - \frac{\xi^2}{V^2/4}$$

(2.5)

n_{eff} ($=\beta/k_0$), the effective refractive index of the mode is then equal to

$$n_{eff} = \sqrt{n_2{}^2 + b(n_1{}^2 - n_2{}^2)}$$

(2.6)

This method may also be applied to find modes with transverse magnetic (TM) polarisation, using the following two formulae,

$$\xi \tan \xi = \left(\frac{n_1}{n_2}\right)^2 \sqrt{\left[\left(\frac{V}{2}\right)^2 - \xi^2\right]} \quad \text{for symmetric TM modes} \tag{2.7}$$

and

$$-\xi \cot \xi = \left(\frac{n_1}{n_2}\right)^2 \sqrt{\left[\left(\frac{V}{2}\right)^2 - \xi^2\right]} \quad \text{for anti-symmetric TM modes} \tag{2.8}$$

The parameters b and n_{eff} are found in the same manner for TM as for TE modes.

A short Matlab program was written to find the modes for a slab waveguide with the core and cladding refractive index, wavelength of operation, and core layer thickness as starting parameters. The program finds the first symmetric and asymmetric TE modes and the first symmetric TM mode. The Matlab code with all sub-programs for this program is shown in Appendix A.1.

2.1.2 Waveguide simulations using Wav32

The other method used for waveguide simulations is the Wav32 program developed by Steve Roberts, previously a PhD student in the Southampton Silicon-based Photonic group, which has been used for several years as an aid to waveguide design by members of the group. From the waveguide geometry and details of the refractive index, the Wav32 program is used to determine waveguide loss and the effective refractive index of guided modes for slab waveguides such as is shown in Figure 2.1.1 (a).

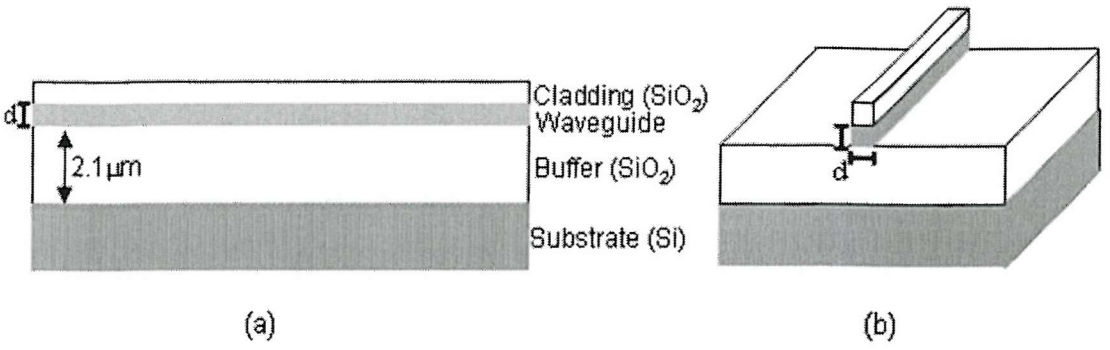

Figure 2.1.1 - A (a) slab and (b) rib waveguide

The user interface for the Wav32 program is shown in Figure 2.1.2(a), with the solutions for TM and TE as (b) and (c) respectively. In the upper section of the Wav32 interface are the waveguide parameters, showing the name of the layer, the material from which it is made, the real and complex refractive indices, and the thickness of the layer. On the right, below the waveguide geometry section, the wavelength of light guided may be selected. In the lowest section are the results of the waveguide simulation, with a calculated leakage loss for the slab waveguide. The TM0 and TE0 results correspond with Figure 2.1.2(b) and (c) respectively. These figures also show what percentage of the mode energy is carried in the cladding, the core, the buffer, and the substrate. TM0 and TE0 are the first guided modes in the TM and TE polarisation respectively.

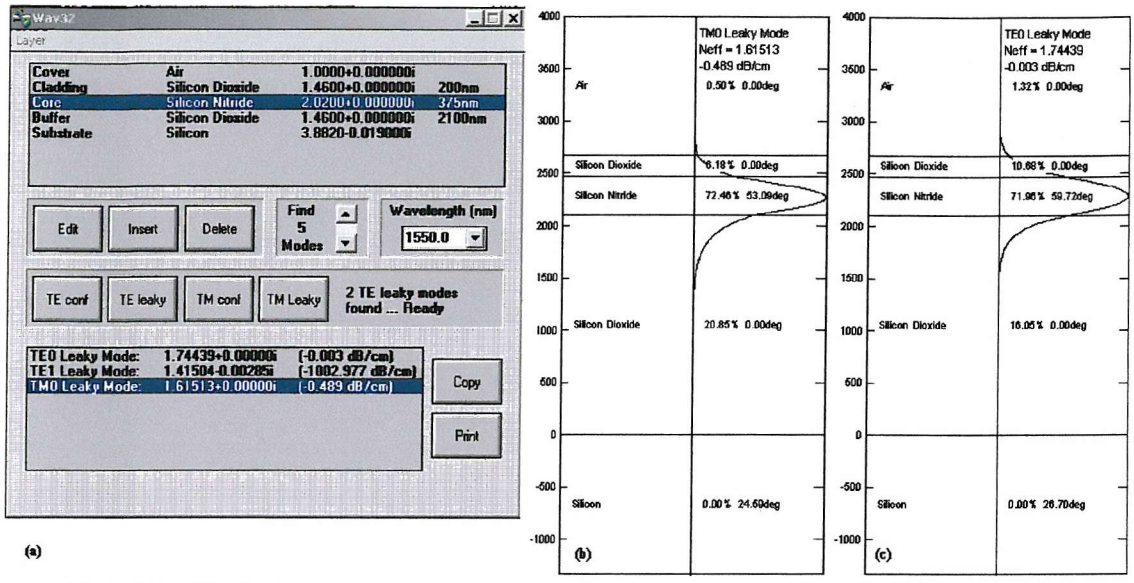

Fig2.1.2 - Wav32 solution for a Silicon Nitride slab waveguide, both TE and TM.

The Wav32 program may be adapted for the analysis of square rib waveguides of the type shown in Figure 2.1.1 (b), which are as thick as they are wide. This is managed by carrying out two iterations of the simulation process, substituting n_{eff} found in the first iteration for the core waveguide layer's refractive index in the second iteration, as is shown for the TE polarisation in Figure 2.1.3.

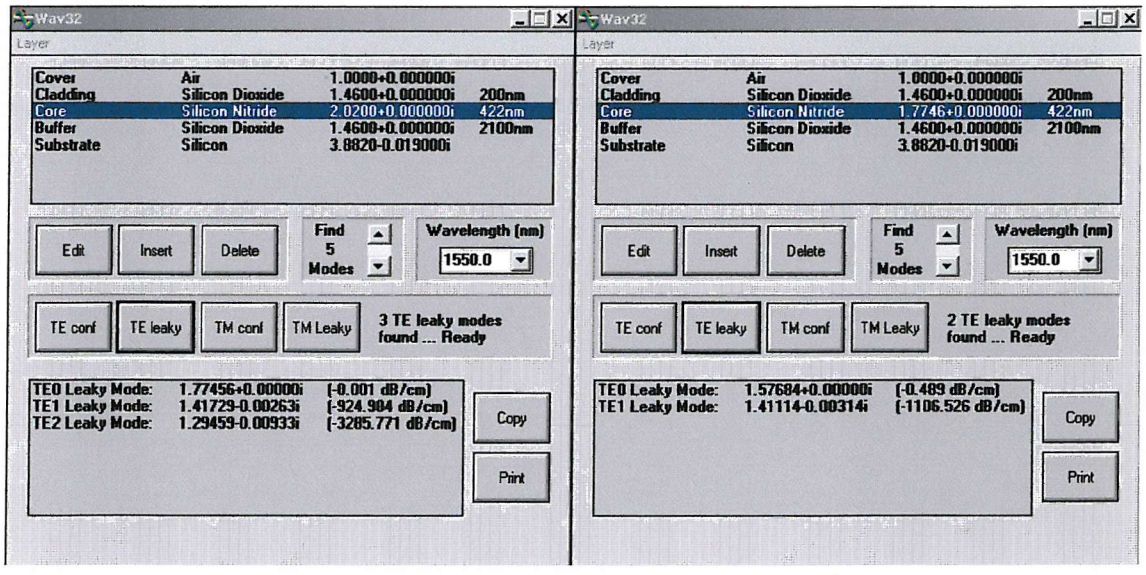

Figure 2.1.3 - The use of Wav32 to simulate a rib waveguide

Potential waveguide materials to be used for AWG fabrication are Silicon Nitride, Si_3N_4 (n = 2.02), Silicon-rich Silicon Dioxide, $Si:SiO_2$, annealed (n = 1.78) and unannealed (n = 1.62), and Silicon OxyNitride, SiON ($1.46 < n < 2.02$). The refractive indices stated are ellipsometry measurements from Chapter 3 and from the section on OxyNitride below. Table 2.1.1. summarises minimum thicknesses for waveguides formed of these three materials for TE and TM polarisations, as both slab and ridge waveguides. These minimum waveguide thicknesses are determined by requiring the loss parameter to be less than 0.5dB/cm. Each waveguide has a buffer layer of 2.1μm, a SiO_2 cladding layer of 0.2μm, and operates at 1.55μm.

Material	Si_3N_4 (n=2.02)	$Si:SiO_2$ (n=1.78)	SiON (n=1.6)
TE (slab)	205nm	412nm	718nm
TM (slab)	375nm	625nm	1710nm
TE (ridge)	422nm	730nm	1699nm
TM (ridge)	610nm	966nm	2250nm

Table 2.1.1 - Minimum thickness for waveguides of various materials at 1.55μm using Wav32

2.1.3 Comparison of Matlab modefinder and Wav32 programs

To determine the utility of results from the Matlab Modefinder described in section 2.1.1, its results were compared with those of the Wav32 program. The Wav32 program was developed by Dr Steve Roberts as part of his PhD thesis *An Investigation Into waveguiding and Light Emission for Erbium-Doped Hosts Compatible With Silicon Technology* (1996). The results from the Wav32 program have been used by the Photonics Group at Southampton University for waveguide design for many years. Its results have been consistently confirmed by both experimental results and by other commercial waveguide simulation and design packages. All waveguides have a thickness of 700nm and operate at 1.55μm.

	Wav32 Modefinder			Matlab Modefinder		
n_{eff}	TE_1	TE_2	TM_1	TE_1	TE_2	TM_1
Si_3N_4	1.88607	1.52107	1.83615	1.8861	1.5221	1.8362
Si: SiO_2	1.66335	1.43529	1.63476	1.6634	*	1.6349
SiON	1.51988	1.42096	1.51142	1.5206	*	1.5127

Table 2.1.2 - Comparisons of Wav32 and Matlab modefinders.

In each instance, the Modefinder is well within 0.01% of total agreement with the much more complex Wav32. The instances where a * is used in the place of a number is when n_{eff} for that mode was below that of the cladding region. The Matlab modefinder was not designed for that contingency, and these modes are not considered guided.

Code for the Matlab Modefinder which finds the first TE and TM guided modes' refractive index, and also the Modefinder which finds the effective refractive index for a square rib waveguide is shown in Appendix A.2.

2.2 Design and Fabrication of an Optical Material: SiON

For a silicon-based Integrated Optical Circuit (IOC), the waveguides must be fabricated in a material with low optical transmission loss, which is fabricated using silicon-compatible fabrication techniques. SiON was introduced in the previous chapter as a waveguide material which may be fabricated with a range of refractive indices ranging from that of SiO_2 (1.46) to Si_3N_4 (2.02). In this section the development of a SiON fabrication process using Plasma Enhanced Chemical Vapour Deposition (PECVD) is discussed.

2.2.1 Starting Points

SiON may be approached from two possible starting places: SiO_2 or Si_3N_4. For fabrication based upon the Deposition 90 PECVD machine in the Southampton University Microelectronics Cleanroom, the existing standard processes for SiO_2 and Si_3N_4 are listed in Table 2.2.1 below.

Process	SiH_4/ N_2 (sccm)	NH_3 (sccm)	N_2O (sccm)	Power (W)	Temperature (°C)	Pressure (mT)	n
SiO_2	157	0	710	20	300	1000	1.46
Si_3N_4	780	50	0	10	300	505	2.02

Table 2.2.1 - Standard PECVD Silicon Dioxide and Silicon Nitride Processes

2.2.2 Process Development for SiON

The deposition rate for SiO_2 is 7.7Å/s. To bring the SiO_2 process closer to the Si_3N_4 process, Ammonia (NH_3) gas was added to the Silane/Nitrogen (SiH_4/N_2) and Nitrous Oxide (N_2O) already used for PECVD silicon dioxide deposition. The presumed effect of this NH_3 would be to seed inclusion of the N_2 in which the SiH_4 was delivered into the gas plasma, to enhance the incorporation of nitrogen into the SiON.

The more N_2 in the SiON, the more closely it would resemble Si_3N_4, and the higher the refractive index would be.

The deposition parameters for SiO_2-based SiON are summarised in Table 2.2.2.

SiH_4/N_2 (sccm)	NH_3 (sccm)	N_2O (sccm)	Power (W)	Temperature (°C)	Pressure (mT)	n	Deposition rate (Å/s)
350	20	375	20	300	1000	1.53	12.08
400	20	300	20	300	1000	1.55	11.83
525	20	250	20	300	1000	1.58	10.9
615	20	215	20	300	1000	1.6	10.57

Table 2.2.2 - Deposition parameters for the SiO2-based SiON process

Figure 2.2.1 shows both measured refractive index and deposition rate plotted against the ratio of SiH_4/N_2O gas flows. Refractive index was measured using a full-spectrum ellipsometer, with each value of the refractive index taken at a wavelength of 633nm.

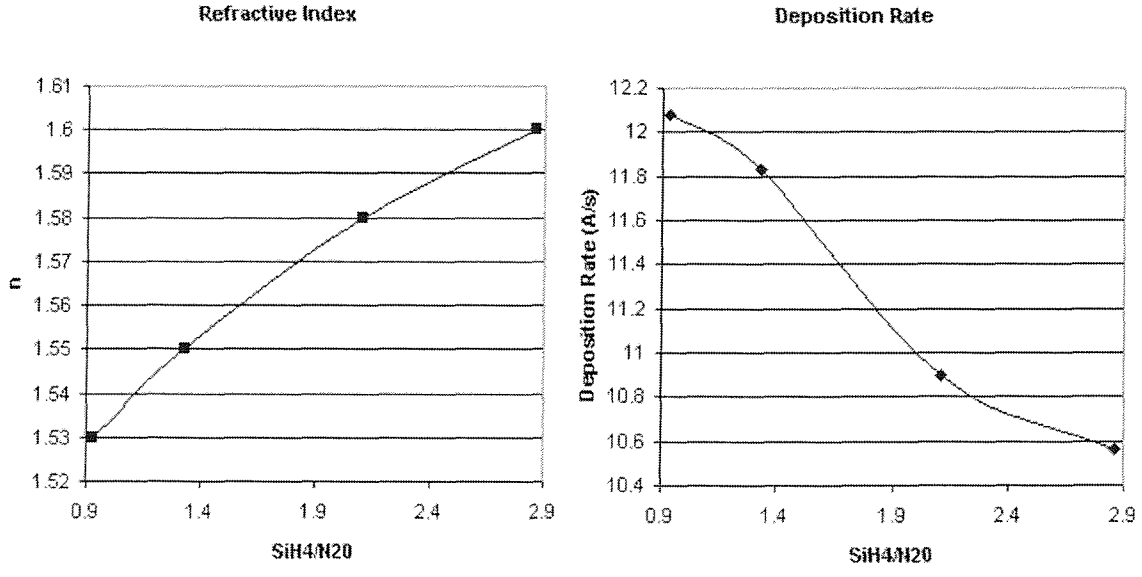

Figure 2.2.1 - (a) Refractive index and (b) deposition rate for the SiO_2-based SiON process.

The Si_3N_4 process was similarly modified Increased amounts of N_2O were added to the mixture of SiH_4 and NH_3 gasses, to lower the refractive index. The standard deposition rate for Si_3N_4 in the Dep90 machine is 1Å/s. Summaries of the deposition parameters for the Si_3N_4 are shown in Table 2.2.3.

SiH_4/N_2 (sccm)	NH_3 (sccm)	N_2O (sccm)	Power (W)	Temperature (°C)	Pressure (mT)	n	Deposition rate (Å/s)
781	50	201	10	300	505	1.68	3.14
777	50	91	10	300	505	1.745	2.38
781	50	141	10	300	505	1.75	2.58
780	50	101	10	300	505	1.776	2.43
780	50	82	10	300	505	1.777	2.242
777	50	78	10	300	505	1.782	2.235
780	50	86	10	300	505	1.787	2.3
777	50	75	10	300	505	2.03	1.2

Table 2.2.3 - Deposition parameters for the Si3N4-based SiON process

Figure 2.2.2 shows the measured refractive index and deposition rate, plotted against the ratio of SiH_4/N_2O gas flows. The refractive index was measured in the same way as it was for the SiO_2-based SiON process samples.

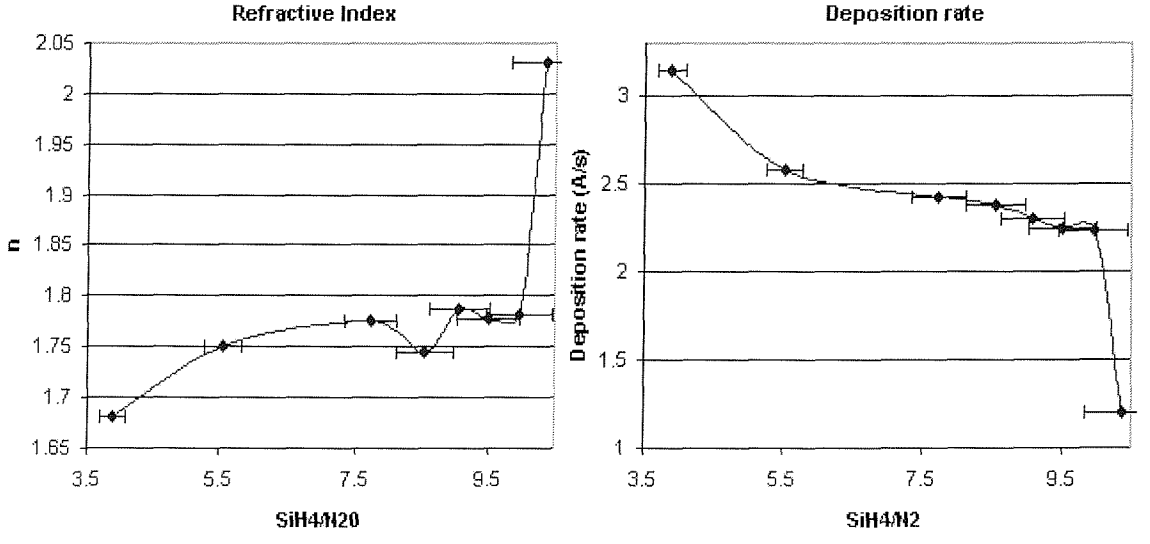

Figure 2.2.2 - (a) Refractive index and (b) deposition rate for the Si_3N_4-based SiON process.

The error bars in Figure 2.2.2 were necessary due to the very erratic flow rates for the N2O. The mass flow controller for that particular gas bottle is designed for operation around 1000sccm. While it was able to maintain the flow rates at approximately the values required by the control software, variations of ±10sccm were not uncommon. As a result of these innacuracies in measuring flow rates, it was impossible to determine at what precise gas flows was located the transition from SiON(n=1.78) to Si_3N_4 (n=2.02).

2.2.3 SiON Waveguides

To form waveguides of SiON, 2.1μm thermal SiO_2 was grown upon prime silicon p<100> wafers, which had been chemically treated with an RCA clean. Following the oxidation a fuming nitric acid (FNA) clean was carried out, and then the core layer was deposited by PECVD with the gas flows, pressures, and platten power described in the following paragraphs. The gas flows were deduced from the graphs shown in Figure 2.2.1(a) and 2.2.2 (a), with the deposition times drawn from Figure 2.2.1 (b) and 2.2.2 (b). After another FNA clean, a cladding layer of 200nm PECVD SiO_2 was deposited. Finally the wafer was cleaved for optical measurements. Between each material deposition the PECVD furnace was cooled, cleaned by CF_4 plasma, and reconditioned for deposition of the new material.

The SiO_2-based SiON waveguide was grown with 450 sccm SiH_4, 280 sccm N_2O, and 20 sccm NH_3, at 20W, 1T pressure for 390 seconds. It was intended that this waveguide should have a refractive index of 1.56, and a thickness of 450nm. When the layer had been deposited it was found to have a refractive index of 1.62 and a thickness of 444nm.

The Si_3N_4-based SiON waveguide was grown with 780 sccm SiH_4, 101 sccm N_2O and 50 sccm NH_3 at 10W, 500mT pressure for 960s. This waveguide was intended to have a thickness of 230nm, and a refractive index of 1.78.

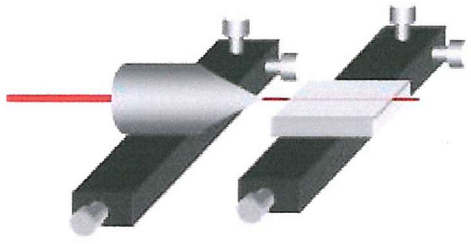

Figure 2.2.3 - Experimental setup for preliminary waveguide transmission measurements

Preliminary transmission measurements were carried out using small lasers which operated in the visible region of the spectrum. X-Y-Z tables were used to align laser light focused through a microscope objective into the core of the waveguide. It was quickly apparent that the Si_3N_4-based SiON waveguides were of very poor optical quality, as demonstrated by a laser beam injected into the waveguide not visibly penetrating by more than 0.5cm. Further investigation showed that PECVD-deposited Si_3N_4 was also a very poor optical material. This is attributed to the low process power, which with only 10W was only half the power of the SiO_2 process. It is supposed that this resulted in the inclusion of many more defects than are desirable. As PECVD Si_3N_4 has been used primarily as an electrical insulating material this was not a problem that had previously been apparent.

The SiO_2-based SiON was a superior waveguide material, with the transmission spectrum shown in Figure 2.2.4.

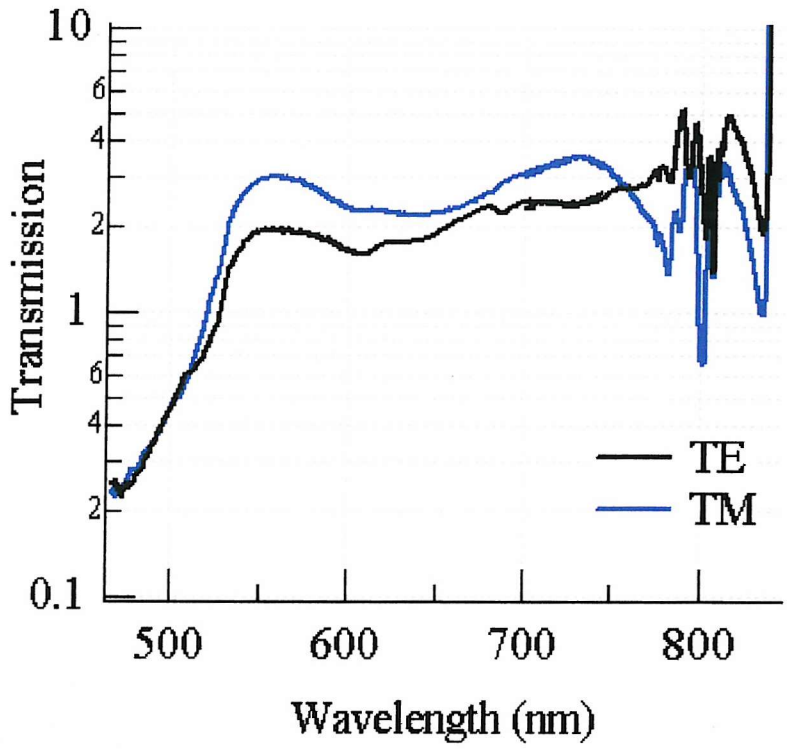

Figure 2.2.4 - Transmission measurements for a SiON waveguide with n=1.6 and d=444nm

It was concluded that SiO_2-based SiON is an acceptable material in which an AWG might be built for the visible region. The Si_3N_4-based process, while extending the range of potential refractive indices to 2.02, is not a good waveguide material and is unacceptable for this purpose.

2.3 AWG simulation

Using the Matlab modefinder discussed in section 2.1, an AWG design program was implemented for SiON and Si_3N_4.

2.3.1 Equations used in AWG simulation

In a thorough treatment of the AWG in his book *Fundamentals of Optical Waveguides* [2], Okamoto derived three equations for an AWG of the type shown in Figure 2.3.1.

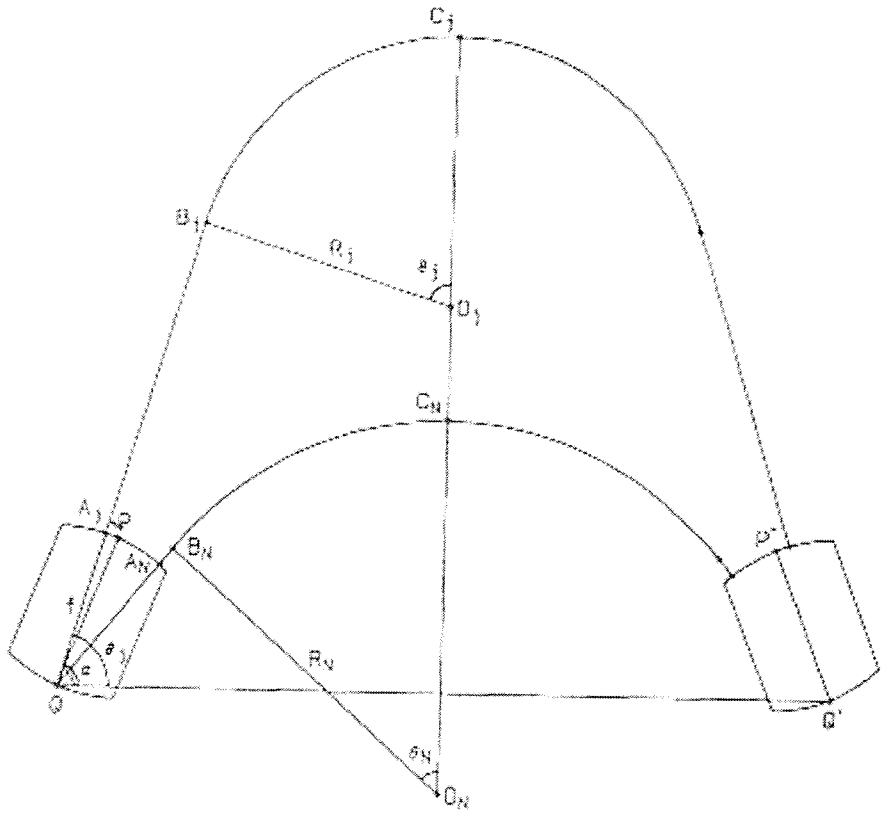

Figure 2.3.1 - Schematic waveguide layout for an AWG design

The first equation specifies the radius of the innermost waveguide bend:

$$R_N = \frac{L_{slab}/2 - (f + S_N)\cos\theta_N}{\sin\theta_N} \tag{2.9}$$

where R_N is the radius of curvature of the innermost waveguide, L_{slab} is the separation between the points Q and Q', f is the radius of curvature of the slab waveguide section, and N is the total number of waveguides in the array. The second equation specifies the radius of every other waveguide bend, from R_0 to R_{N-1}:

$$R_j = \frac{L_{slab}/2 - \left[f + S_N + R_N + (N-j)\Delta L/2\right]\cos\theta_i}{(\sin\theta_i - \theta_i\cos\theta_i)} \tag{2.10}$$

where S_N is the straight length of the innermost waveguide and ΔL is the path length difference between each waveguide in the array. The third equation specifies the length of the straight waveguide section connecting point A_j at the slab waveguide exit to point B_j at the start of the curved section,

$$S_i = S_N + (R_N\theta_N - R_i\theta_i) + (N-j)\Delta L/2 \tag{2.11}$$

For the purpose of the waveguide program, certain assumptions are made:

- The central wavelength of operation, λ_c=1.55μm
- The core region is surrounded by cladding of SiO_2, n_2=1.46
- $S_N = 0$
- $L_{slab} \geq 0.1\mu m$;
- All rib waveguides are square waveguides, with the same width and depth
- There is no spacer between the exit waveguides of the slab waveguide regions
- The AWG is symmetrical in the axis bisecting the line between points Q and Q'
- There is no taper in the exit waveguides

Requiring the waveguide width, core refractive index, number of waveguide channels, and the channel spacing of the grating, the AWG program is designed to find the smallest circuit which will satisfy the equations given above, and also have a reasonably low bend loss (α_{loss}), determined by the equation below

$$\alpha_{loss}(dB/cm) = 4.343\left(\frac{\pi}{4aR_N}\right)^{1/2}\left[\frac{U}{VK_1(W)}\right]^2 \frac{1}{W^{3/2}}\exp\left[-\frac{2W^3}{3k_0^{\,2}a^3n_1^{\,2}}R_N\right] \tag{2.12}$$

Where

$$U = a\sqrt{k_0^{\,2}n_1^{\,2} - \beta_2^{\,2}} \qquad W = a\sqrt{\beta_2^{\,2} - k_0^{\,2}n_2^{\,2}} \qquad a = \frac{d}{2} \tag{2.13}$$

and K_1 is the modified Bessel function. The code for the Matlab AWG design program is listed in Appendix A.3.

2.3.2 The User Interface

A person operating the AWG design program would see on their screen what appears in Figure 2.3.2 below,

```
>> ThesisAWG
Please enter waveguide width (nm):   500
Please enter core index:   1.6
Please enter number of phasor channels:   32
Please enter channel spacing (nm):   .01
valid alpha_offsets   bend (um)     X (um)        Y (um)      Bend Loss     Separation (cm)   Row#
        80.00          34.07       44239.72      44286.20       1.36           0.70          1.00
        79.00          48.65       44396.96      44451.78       1.11           0.90          2.00
        79.00          99.23       44473.62      44524.10       0.72           1.00          3.00
        78.00          48.80       44548.53      44618.88       1.11           1.10          4.00
        79.00         149.81       44550.27      44596.41       0.54           1.10          5.00
        78.00          99.54       44624.83      44690.03       0.72           1.20          6.00
        79.00         200.38       44626.92      44668.73       0.43           1.20          7.00
which row to print? (type "0" to exit)   :   5
```

Figure 2.3.2 - The AWG program user interface

Having chosen the waveguide width, core index, number of waveguides, and channel separation, the user is then given a list of possible AWG designs which they may select. The parameters displayed are the angle α, the bend radius of the tightest bend

(R_N), the length and width of the device, the bend loss of the tightest bend, and the separation of points Q and Q' on the waveguide slabs (referring back to Figure 2.3.1).

The value of the angle α is of interest as the input and output waveguides will be entering and leaving the AWG at this angle. While this does not affect the size of the AWG itself, it does affect how the waveguide will fit as part of a larger IOC. The bend loss of the smallest bend radius is the parameter of major interest for choice of which AWG design to implement.

If no further elaboration of the AWG design is required, the operator should enter '0' at the next prompt. Alternatively, the user may select one of the AWG designs to display in more detail by choosing one of the row numbers, listed to the right of the screen. Once the user has chosen a design, a graphic representation is created to scale on the screen (Figure 2.3.3). In this representation, each waveguide is of the width specified by the user. For the purpose of the display, red indicates the straight, green the curved, and blue the slab sections of the AWG. The user may explore the image,

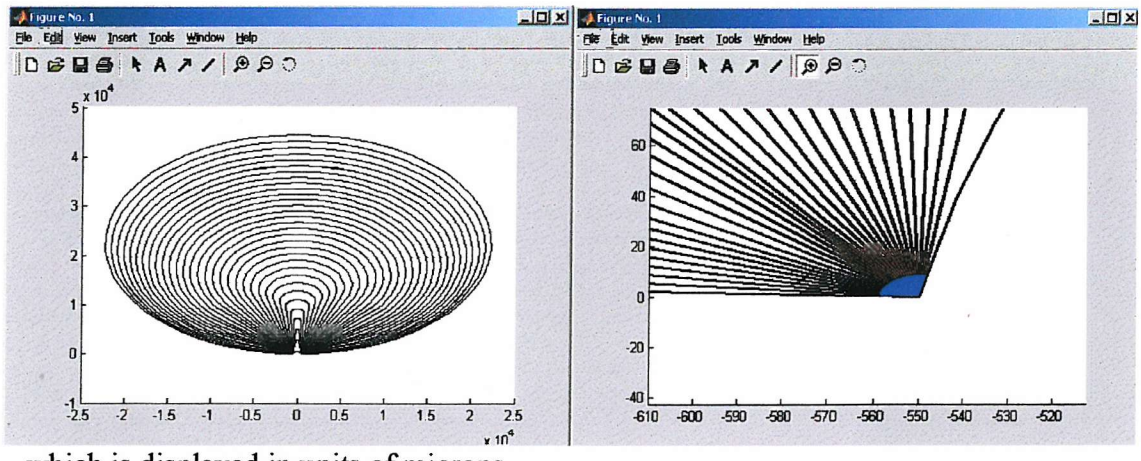

which is displayed in units of microns.

Figure 2.3.3 - The graphical output from the AWG design program

In addition to the graphic display, the full dimensions of the chosen AWG design is printed out on the screen, with all the parameters required for fabrication. For each waveguide in the array, the angle θ_j, the bend radius, and the length of the straight

sections are given in μm. The full AWG program user interface, including the numerical printout for AWG design #5 is shown in Figure 2.3.4.

Command Window

```
>> ThesisAWG
Please enter waveguide width (nm):   500
Please enter core index:   1.6
Please enter number of phasor channels:   32
Please enter channel spacing (nm):   .01
valid alpha_offsets   bend (um)     X (um)        Y (um)      Bend Loss     Separation (cm)   Row#
         80.00          34.07      44239.72      44286.20         1.36          0.70          1.00
         79.00          48.65      44396.96      44451.78         1.11          0.90          2.00
         79.00          99.23      44473.62      44524.10         0.72          1.00          3.00
         78.00          48.80      44548.53      44618.88         1.11          1.10          4.00
         79.00         149.81      44550.27      44596.41         0.54          1.10          5.00
         78.00          99.54      44624.83      44690.03         0.72          1.20          6.00
         79.00         200.38      44626.92      44668.73         0.43          1.20          7.00
which row to print? (type "0" to exit)   :   7
Current plot held
Current plot released
           n        theta(deg)    Radius (um)   Straight (um)
dimensions in microns
          1.00        178.05      22317.08        150.27
          2.00        174.86      21611.15       1334.29
          3.00        171.66      20902.16       2448.72
          4.00        168.47      20188.17       3498.81
          5.00        165.27      19467.41       4488.76
          6.00        162.07      18738.33       5421.87
          7.00        158.88      17999.52       6300.65
          8.00        155.68      17249.73       7126.85
          9.00        152.49      16487.87       7901.54
         10.00        149.29      15713.02       8625.13
         11.00        146.10      14924.41       9297.38
         12.00        142.90      14121.48       9917.38
         13.00        139.71      13303.89      10483.57
         14.00        136.51      12471.58      10993.65
         15.00        133.32      11624.79      11444.59
         16.00        130.12      10764.18      11832.48
         17.00        126.93       9890.87      12152.51
         18.00        123.73       9006.60      12398.80
         19.00        120.54       8113.87      12564.27
         20.00        117.34       7216.12      12640.46
         21.00        114.15       6317.97      12617.31
         22.00        110.95       5425.58      12482.83
         23.00        107.76       4547.01      12222.84
         24.00        104.56       3692.75      11820.48
         25.00        101.37       2876.46      11255.69
         26.00         98.17       2115.76      10504.58
         27.00         94.98       1433.53       9538.58
         28.00         91.78        859.34       8323.40
         29.00         88.59        431.62       6817.73
         30.00         85.39        200.38       4971.52
         31.00         82.20        231.03       2723.84
         32.00         79.00        609.49             0
Slab waveguide radius (um)
          8.97
```

Figure 2.3.4 - Screen printout of the chosen AWG design

2.3.3 Use of the AWG in determining design parameters

The AWG design used as an illustration in the previous section is for an AWG with 32 channels, designed in SiON, with a core refractive index of 1.6. The average size of the eventual AWG design is 44x45mm. If the same AWG is implemented in Si_3N_4 with a core refractive index of 2.02, the size of the AWG does not change appreciably, although the bend losses for the designs proposed by the design program do decrease. The printout for the Si_3N_4 designs from the design program are shown in Figure 2.3.5. The average size of an AWG implemented in Si_3N_4 is 42x42mm.

```
Command Window
>> ThesisAWG
Please enter waveguide width (nm):   500
Please enter core index:   2.02
Please enter number of phasor channels:   32
Please enter channel spacing (nm):   .01
valid alpha_offsets   bend (um)     X (um)       Y (um)      Bend Loss     Separation (um)   Row#
         86.00          6.20      42318.83      42520.74        0.11          100.00          1.00
         87.00         45.00      42325.45      42477.35        0.00          100.00          2.00
         88.00         49.68      42327.59      42439.65        0.00          100.00          3.00
         89.00         49.83      42325.40      42407.72        0.00          100.00          4.00
         90.00         50.00      42319.03      42381.66        0.00          100.00          5.00
which row to print? (type "0" to exit)   :   2
```

Figure 2.3.5 - Screen printout for a Si_3N_4 AWG design

Despite this seeming invariance in size, the refractive index is an important parameter in the design. If the Matlab modefinder is unable to find a guided mode for a particular waveguide geometry, the AWG design program is unable to find a solution. If the same AWG design parameters are attempted for a core refractive index of 1.5 is attempted, the program simply crashes. A greater waveguide depth must be employed. In this case the thickness of the waveguide must be 800nm or greater for solutions to be possible.

Both designs shown above are for an AWG with only 32 channels. An AWG with 256 channels, which is standard for dense WDM applications, with a channel spacing of 0.01nm as before, is only slightly larger than for an AWG with 32 waveguide

channels. For a Si_3N_4 AWG the average dimensions are 45x45mm. The same AWG implemented in SiON, n=1.6 has dimensions of 49x49mm. Printouts for both SiON and Si3N4 designs are shown in Figure 2.3.6.

```
>> ThesisAWG
Please enter waveguide width (nm):   500
Please enter core index:   2.02
Please enter number of phasor channels:   256
Please enter channel spacing (nm):   .01
valid alpha_offsets   bend (um)     X (um)       Y (um)      Bend Loss     Separation (cm)   Row#
        85.00          9.88      44792.28     44852.13         0.03          0.20          1.00
which row to print? (type "0" to exit)   :   0
>> ThesisAWG
Please enter waveguide width (nm):   500
Please enter core index:   1.6
Please enter number of phasor channels:   256
Please enter channel spacing (nm):   .01
valid alpha_offsets   bend (um)     X (um)       Y (um)      Bend Loss     Separation (cm)   Row#
        72.00         42.06      48118.10     48104.30         1.21          2.60          1.00
        71.00         29.44      48339.55     48311.52         1.47          2.90          2.00
        71.00         81.59      48413.19     48361.15         0.82          3.00          3.00
        71.00        133.75      48486.83     48450.78         0.59          3.10          4.00
        70.00          4.03      48555.10     48519.21         4.14          3.20          5.00
        71.00        185.90      48560.47     48520.41         0.46          3.20          6.00
which row to print? (type "0" to exit)   :   0
>>
```

Figure 2.3.6 - Designs for 256 waveguide channel AWGs in SiON and Si_3N_4

Waveguides of different width have little effect upon the final size of the AWG design, as is shown in Figure 2.3.7 for waveguides of differing width in SiON, although a higher refractive index is necessary for smaller waveguide dimensions for confinement. An observable result is that the broader the waveguide, the smaller the separation necessary between slab waveguides, though this is not indicative of the final AWG size.

Command Window

```
>> ThesisAWG
Please enter waveguide width (nm):   500
Please enter core index:   1.6
Please enter number of phasor channels:   256
Please enter channel spacing (nm):   .01
valid alpha_offsets   bend (um)     X (um)       Y (um)      Bend Loss     Separation (cm)   Row#
        72.00          42.06      48118.10     48104.30        1.21          2.60          1.00
        71.00          29.44      48339.55     48311.52        1.47          2.90          2.00
        71.00          81.59      48413.19     48381.15        0.82          3.00          3.00
        71.00         133.75      48486.83     48450.78        0.59          3.10          4.00
        70.00           4.03      48555.10     48519.21        4.14          3.20          5.00
        71.00         185.90      48560.47     48520.41        0.46          3.20          6.00
which row to print? (type "0" to exit)   :   0
>> ThesisAWG
Please enter waveguide width (nm):   600
Please enter core index:   1.6
Please enter number of phasor channels:   256
Please enter channel spacing (nm):   .01
valid alpha_offsets   bend (um)     X (um)       Y (um)      Bend Loss     Separation (cm)   Row#
        84.00           3.27      50256.11     50314.47        2.47          0.30          1.00
        85.00          49.04      50237.87     50306.62        0.52          0.30          2.00
        84.00          53.48      50334.82     50391.30        0.49          0.40          3.00
        85.00          99.19      50317.00     50384.76        0.29          0.40          4.00
which row to print? (type "0" to exit)   :   0
>> ThesisAWG
Please enter waveguide width (nm):   700
Please enter core index:   1.6
Please enter number of phasor channels:   256
Please enter channel spacing (nm):   .01
valid alpha_offsets   bend (um)     X (um)       Y (um)      Bend Loss     Separation (cm)   Row#
        87.00           7.04      52936.10     53215.40        1.01          0.10          1.00
        88.00          30.47      52948.09     53160.15        0.38          0.10          2.00
        89.00          44.76      52954.44     53112.00        0.27          0.10          3.00
        90.00          50.00      52955.34     53071.06        0.25          0.10          4.00
        91.00          52.11      52950.99     53037.46        0.24          0.10          5.00
        92.00          54.23      52941.57     53011.32        0.23          0.10          6.00
        93.00          56.37      52927.25     52992.79        0.22          0.10          7.00
        94.00          58.54      52908.23     52982.01        0.21          0.10          8.00
which row to print? (type "0" to exit)   :   0
```

Figure 2.3.7 - The effect of waveguide width upon AWG design

It is the channel spacing which has the largest effect upon the eventual overall AWG size. For an AWG capable of distinguishing differences in wavelength of .01nm (such as the ones described above), the size is reasonable. For a waveguide which operates with a channel spacing of .001nm, the size of the eventual device increases to 450x450mm. For a channel spacing of 0.1nm, the AWG dimensions are reduced to 5.5x5.5mm, a much more acceptable scale for an IOC. This is shown in Figure 2.3.7.

```
Command Window
>> ThesisAWG
Please enter waveguide width (nm):   500
Please enter core index:   2.02
Please enter number of phasor channels:   256
Please enter channel spacing (nm):   .001
valid alpha_offsets   bend (um)     X (um)        Y (um)      Bend Loss     Separation (cm)   Row#
        85.00          29.01     447372.76     447975.17        0.00          1.80          1.00
which row to print? (type "0" to exit)   :   0
>> ThesisAWG
Please enter waveguide width (nm):   500
Please enter core index:   2.02
Please enter number of phasor channels:   256
Please enter channel spacing (nm):   .01
valid alpha_offsets   bend (um)     X (um)        Y (um)      Bend Loss     Separation (cm)   Row#
        85.00           9.88      44792.28      44852.13        0.03          0.20          1.00
which row to print? (type "0" to exit)   :   0
>> ThesisAWG
Please enter waveguide width (nm):   500
Please enter core index:   2.02
Please enter number of phasor channels:   256
Please enter channel spacing (nm):   .1
valid alpha_offsets   bend (um)     X (um)        Y (um)      Bend Loss     Separation (cm)   Row#
        80.00           6.21       4578.83       4587.52        0.11          0.10          1.00
        81.00          14.32       4580.21       4585.97        0.01          0.10          2.00
        82.00          21.49       4581.17       4585.10        0.00          0.10          3.00
which row to print? (type "0" to exit)   :   0
>> ThesisAWG
Please enter waveguide width (nm):   500
Please enter core index:   2.02
Please enter number of phasor channels:   256
Please enter channel spacing (nm):   1
valid alpha_offsets   bend (um)     X (um)        Y (um)      Bend Loss     Separation (cm)   Row#
        52.00           0.40        595.19        590.28        2.49          0.20          1.00
        45.00           4.50        657.47        634.70        0.22          0.30          2.00
        46.00          14.51        659.37        634.74        0.01          0.30          3.00
which row to print? (type "0" to exit)   :
```

Figure 2.3.8 - The effect of channel spacing upon AWG size

2.4 Conclusion

In this chapter, conventional planar optical components were explored, with the AWG as a prime example of a successfully implemented integratable optical component. In the first section, the use of Matlab to find the effective index of a waveguide with known core refractive indices was demonstrated. The Matlab modefinder was accurate to within 0.1% of more complex simulation packages such as Wav32, with which the Matlab modefinder was compared. The Matlab modefinder was shown to be useful to simulate both slab and rib waveguides

A process for the development of SiON, a material which may be deposited with a range of refractive indices from 1.46-2.02, was formulated. This process was shown to produce good optical material for the process derived from PECVD SiO_2, but resulted in poor waveguides for the process derived from Si_3N_4. The SiO_2-based SiON process made optical circuits possible with a core refractive index ranging from 1.46-1.6. A waveguide was deposited with the maximum refractive index and transmission measurements were carried out.

In the third section of this chapter the Matlab modefinder developed at the start of this chapter was put to use as part of a program for the design of AWGs. The use of this program was demonstrated for waveguides of differing thickness, refractive index, for AWGs composed of different numbers of waveguides, and for AWGs designed for WDM with different channel spacings.

It is widely accepted that the AWG is extremely difficult to fabricate, and we made no attempt to do so. Fabrication difficulties include the extremely precise etch techniques which would be necessary to form separate waveguides at the exit of the slab waveguide such as those shown in Figure 2.4.1, and the extremely small tolerances required to gain the desired output from the AWG.

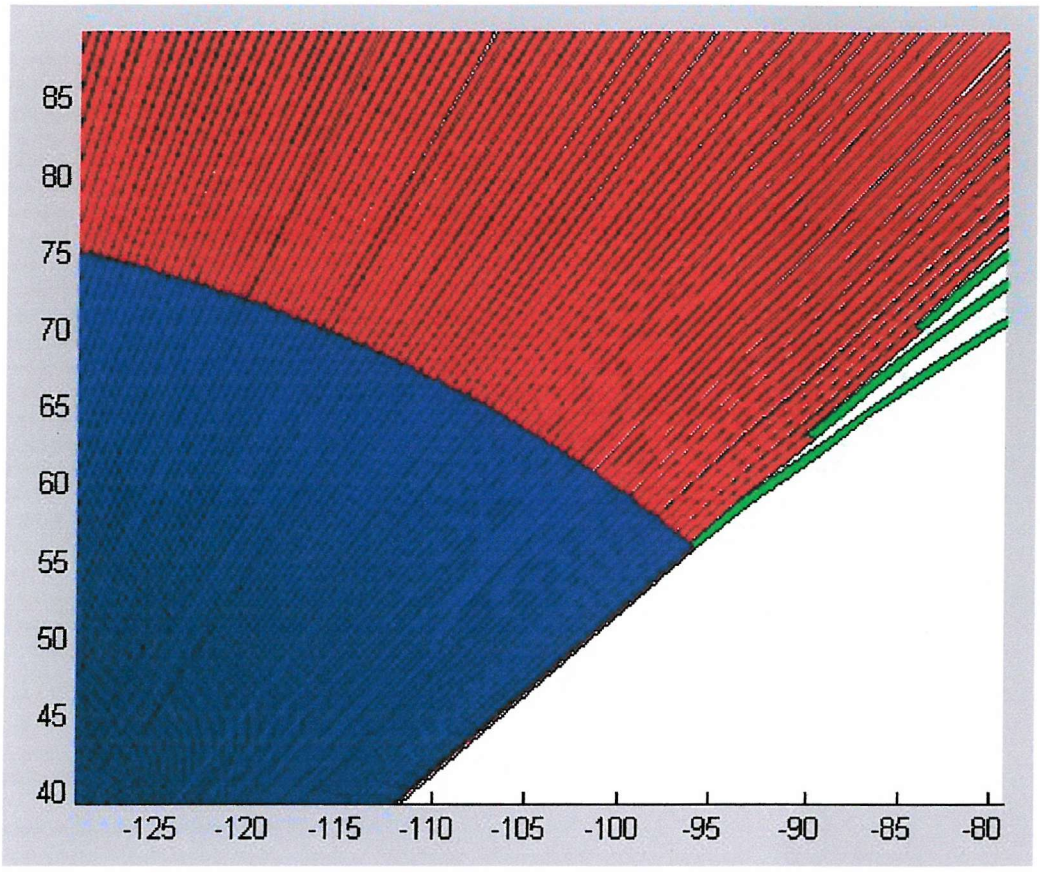

Figure 2.4.1 - Close up of the output section of an AWG slab waveguide

While planar optical components such as the AWG are much smaller than their bulk counterparts, they are still tricky to fabricate. They are also much larger than photonic crystal elements such as the superprism described in Section 1.3.2. The potential applications of photonic crystal as compact optical components in silicon-based optical circuits are sufficiently interesting to prompt further study.

References:

[1] Ghatak, A. and Thygarajan, J. *Introduction to Fibre Optics* (1998). Cambridge University Press, Cambridge, UK.

[2] K. Okamoto, *Fundamentals of Optical Waveguides* (2000). Academic Press, London, UK.

3 Silicon-Rich Silicon Dioxide

As described in Chapter 1, silicon (Si), as an indirect bandgap material, is a poor light emitter through standard electron-hole recombination. Of the many methods used to overcome this, luminescent silicon nanocrystals suspended in a matrix of silicon dioxide (SiO_2) are a promising approach. A major advantage to this approach is that the manufacture of silicon nanocrystals does not require the use of dopant materials not usually found in a standard microelectronics cleanroom.

Silicon nanocrystals (Si-nc), with diameters of several nanometers, possess a semi-ordered structure unlike either crystalline or amorphous silicon [1]. Photoluminescence (PL) from Si-nc, which has been stimulated by a laser operating at wavelengths shorter than 550nm, is over a broad band of wavelengths from 600-1100nm. The mechanism by which the PL is emitted from the Si-nc is not a matter of consensus, with some groups believing it to be attributable to quantum confinement while others prefer a model involving recombination at defect states on the interface between the Si and the SiO_2.

The work carried out in this, and the following chapter, was organised into batches for similar work, described by such names as r2140, for example. Full listings of the work carried out upon each wafer in each batch may be found in Appendix D.

3.1 Nanocrystalline Silicon Fabrication

The method used in this thesis to form Si-nc was adapted from a paper published by Iacona et al. [2]. The method used in their 2000 paper for creating luminescent silicon nanocrystals by Plasma Enhanced Chemical Vapour Deposition (PECVD) involved modifying the flow ratios of silane (SiH_4) and nitrous oxide (N_2O) used in standard PECVD SiO_2, as is summarised in Figure 3.1.

Composition (in at. %) of SiO_x films prepared by using different values of the N_2O/SiH_4 flow ratio (γ), as obtained from RBS measurements.

		Composition (at. %)		
γ	Sample	Si	O	N
15	S0	33	58	9
10	S1	35	51	14
8	S2	37	51	12
7.5	S3	39	49	12
6.5	S4	42	48	10
6	S5	44	47	9

Figure 3.1.1 - Table showing the use of modified flow ratios in altering Si incorporation [2]

Adapted from Iacona's work with the assistance of Mr. Mike Josey, an initial recipe for Silicon-Rich Silicon Dioxide (SRSO) was attempted in batch number r2062. The total gas flow in the Dep 90 PECVD furnace was 650 sccm with a ratio (γ) of N_2O:SiH_4 equal to 6. The SiH_4 used, unlike the SiH_4 used by Iacona, was diluted to 5% SiH_4 in N_2 as the highly dangerous undiluted SiH_4 is not legal in the UK. All samples in batch number r2062 were annealed for an hour at 1150°C in a Nitrogen (N_2) atmosphere.

The gas flows for SiH_4/N_2 and N_2O were determined using the simultaneous equations shown below:

$$20x + y = 650 \qquad \gamma x = y \tag{3.1}$$

x = SiH_4 gas flow y = N_2O gas flow

SiH_4:N_2 = 1:19 $SiH_4 + N_2$ gas flow = $20x$

Wafer #	SiH_4/N_2 (sccm) 1:19	N_2O (sccm)	γ	Power (W)	Temperature (°C)	Pressure (mT)	Anneal Time (h)	Anneal Temperature (°C)
1,2	500	150	6	20	300	505	1	1150
3	448	202	9	20	300	505	1	1150
4	406	244	12	20	300	505	1	1150
5	371	279	15	20	300	505	1	1150

Table 3.1.1 - Processes for PECVD deposition of SRSO, batch r2062

The effect of the anneal upon the wafers in batch r2062 is shown in Figure 3.1.2. Photographs were taken of each wafer before and after the anneal. The dark dot and line in each figure are not features, being reflected images used in each photograph to ensure a consistent angle of observence. The shift in colour from a green-yellow to the characteristic red tinge of Si-nc may easily be observed.

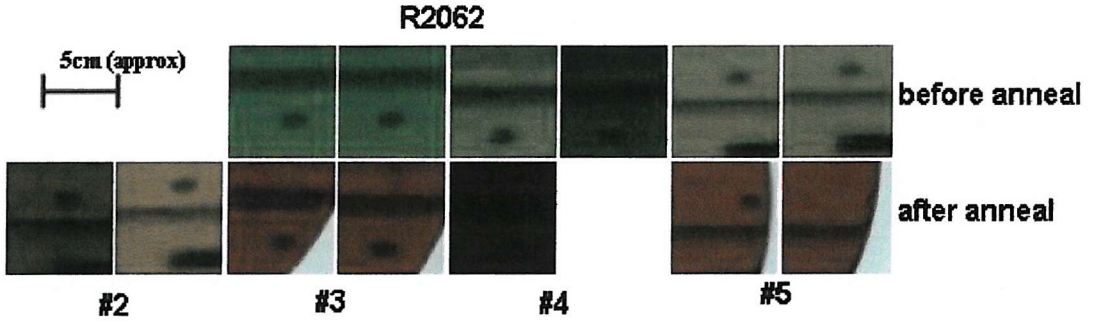

Figure 3.1.2 - Photographs demonstrating the colour change for wafers from batch R2062

Following promising results from initial PL measurements, a second batch numbered r2140 was commenced, this time with a deposition pressure of 1000mT, which is the pressure used in the standard SiO_2 deposition process. Batch r2140 was designed in part to explore deposition of silicon-rich silicon nitride (Si_3N_4), but these samples failed to display any photoluminescence.

Photoluminescence spectra were taken for the Si-rich Si_3N_4 both at room temperature and at 60K, using a 514nm wavelength Argon Ion laser. None of these resulted in photoluminescence beyond that caused by various semiconductor filters. It was thus concluded that silicon nanocrystals formed in Si-rich Si_3N_4 were optically inactive.

Other wafers making up batch r2140 were used for an exploration into the effects of various anneal conditions for Si-rich SiO_2. All Si:SiO_2 wafers were deposited to an exact repetition of the deposition conditions for r2062#3 ($\gamma = 9$), which had been the recipe which proved the most brightly luminescent in batch number r2062. Samples were then annealed for varying time periods at the temperatures listed in Table 3.1.2.

Wafer #	Deposition Time (mins)	Anneal Time (h)	Anneal Temperature (°C)	n	Layer Thickness (nm)
6	15	0.5	1150	1.79±0.04	513±14
7	15	1	1150	1.78±0.02	513±9
8	15	3	1150	1.78±0.12	506±40
9	15	1	1200	1.80±0.02	506±11
10	15	0	-	1.62±0.02	398±16

Table 3.1.2 - Processes for exploring the effect of varied anneal conditions, batch r2140

The values for layer thickness and refractive index given in Table 3.1.2 were measured using the ellipsometer in the Southampton University Microelectronics Centre (SUMC). Unlike the ellipsometer used for refractive index measurements of the SiON described in the previous chapter, the ellipsometer used for this purpose was a single-wavelength ellipsometer operating at 633nm. These measurements were repeated at intervals over the subsequent two years, and the measured average result was consistent to 3 significant figures.

Other attempts were made to determine the thickness of the SRSO layers through the matching of measured reflectance fringes to theoretically calculated ones. This was

not found to be a practical method, due to the large number of variables to be juggled; it was a lengthy task to match the thicknesses of three layers, with one of them an unknown refractive index. SEM imagery, another potential method for determining thickness, was found to be of too low resolution to distinguish SiO2 from SRSO layers.

A study into the effect of the anneal upon the refractive index and thickness of the layers is summarised in Figure 3.1.3 below, batch number k2351. The samples shown below were samples of SRSO deposited directly onto the surface of a silicon wafer at a pressure of 500mT. The change in refractive index due to the anneal occurs within the first 30 minutes of that anneal. Annealing beyond the first 30 minutes causes a slight reduction in the raised refractive index. The sample with the highest silicon incorporation, the sample with the gas mixture 500/150 of SiH_4/N_2O (γ = 6), exhibited the largest change of refractive index, of 12-13%. The gas mixture with the lowest silicon incorporation (γ = 15) exhibited the smallest change in refractive index, of 2-3%.

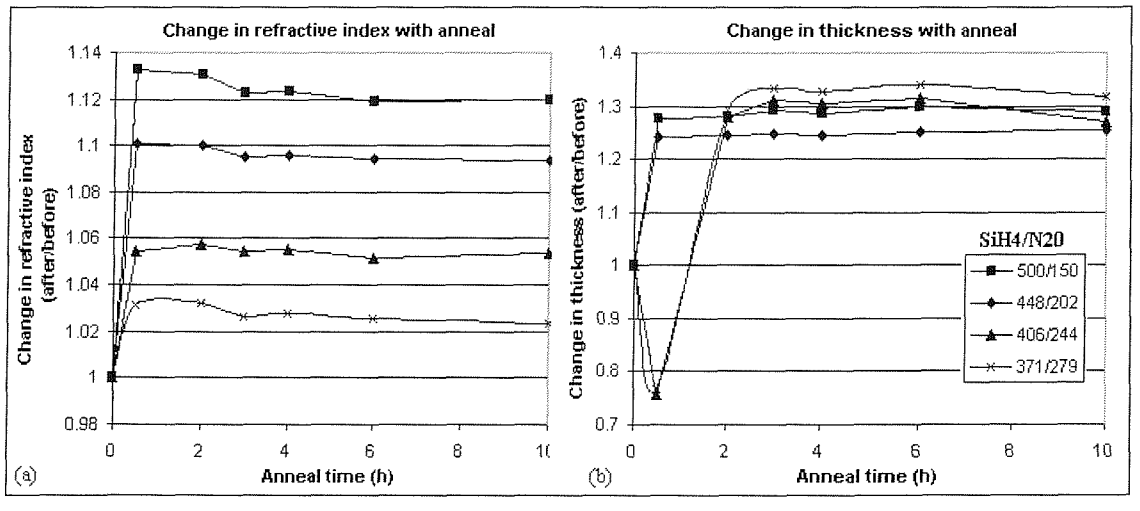

Figure 3.1.3 - Effect of an anneal upon (a) the refractive index and (b) the layer thickness

While the change in refractive index is strongly linked to the silicon incorporation, this is not the case for the change in the layer thickness. The change in thickness of SRSO layers during an anneal is not a function of the silicon incorporation. The thickness of the layer of SRSO also remains constant for prolonged anneals once the

initial increase in thickness has occurred. This implies a very rapid change in the material properties of SRSO as a result of reaching the required temperature for activation.

Later batches, numbered r2198 and k2351 (see Appendix D for full listings), involved fabrication of waveguides of SRSO. Waveguides of approximately 450nm SRSO were deposited onto Si wafers which had been thermally oxidised to a thickness of 2.1μm. A cladding layer of 210nm PECVD SiO_2 was deposited onto the top surface of the whole structure. The typical geometry of the waveguides fabricated is shown in Figure 3.1.4. Following the deposition stages, the whole waveguides were annealed at 1150°C for durations varying from 0-10 hours.

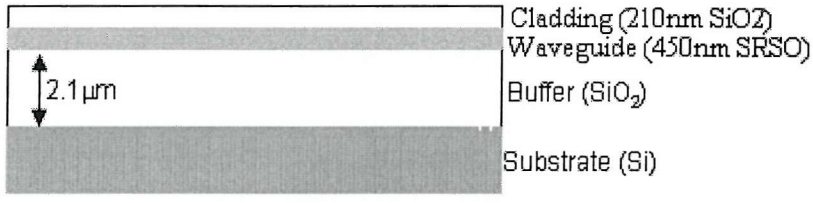

Figure 3.1.4 - Geometry of SRSO waveguides for batch r2198

After waveguide fabrication, some wafers were processed further, as is described in Chapter 4, though some regions on the processed wafers remained unaltered . Three types of SRSO were used in the waveguide structures, which are described in Table 3.1.3 below,

Type	γ (N_2O/SiH_4)	n (before)	Thickness (Å, before)	Annealed for (h)	n (after)	Thickness (Å, after)
A	9	1.605	4345	0.5,1,3,6	1.685	5720
B	12	1.575	4524	0.5,1,3,6	1.576	3850
C	15	1.547	4621	0.5,1,3,6	1.528	4047

Table 3.1.3 - Refractive index and thickness for SRSO waveguides from batch k2351

In summary, wafers of type 'A' had waveguide cores of SRSO of the type first deposited on wafer r2062#3. Type 'B' had a waveguide core which repeated the layer on wafer r2062#4, and Type 'C' had a waveguide core which was a repeat of r2062#5. Core refractive indices and thicknesses were inferred from ellipsometry

measurements taken for small "check" pieces of silicon which were placed in the PECVD machine with each deposition stage, and were subsequently annealed with the waveguides.

Page 111 is missing from volume

been annealed for 1 hour, and over 8x the intensity of the sample which was annealed for only half an hour. The unannealed sample did not under any circumstances emit any photoluminescence.

Wafers from batch k2351 were annealed for times ranging from half an hour to 10 hours. It was found that a sample which had been annealed for 2 hours was almost twice as strongly luminescent as one which had been annealed for half an hour. A sample which had been annealed for 4 hours was over 4x as strongly luminescent as one which had only been annealed for half an hour. However, a Si-nc sample which had been annealed for 10 hours was only slightly more luminescent than the 4-hour sample. These results are shown in Figure 3.2.2 (b). The Si-nc samples used for these measurements were the ones containing the highest silicon incorporation, with $\gamma = 6$.

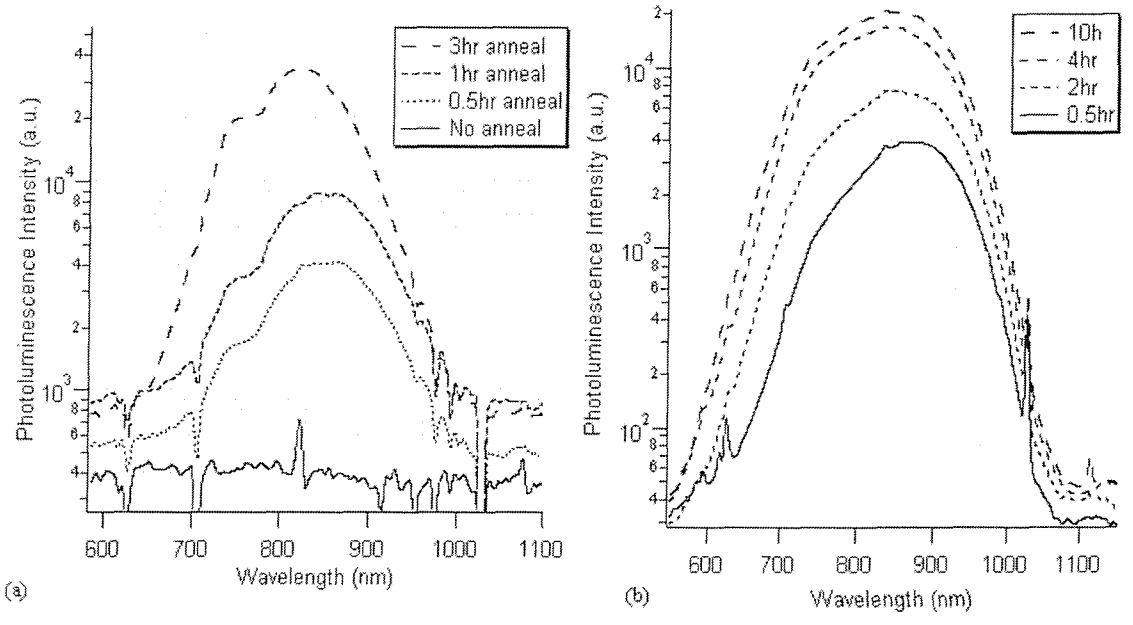

Figure 3.2.2 - The effect of increased anneal time upon photoluminescence intensity for (a) a 0-3 hr range in anneal times (r2140) and (b) a 0.5-10 hr (k2351), all annealed at 1150°C

The graphs in Figure 3.2.2 show that a longer anneal time results in an increase of PL intensity from the same pump conditions. While unannealed waveguides exhibit no measurable PL, after only 30 minutes anneal at 1150°C PL is observed in a broad band from 600-1050nm. Photoluminescence from a Si wafer with a layer of Si-nc

deposited upon it may continue on past the cutoff of a silicon detector, to 1150nm, as is shown in Figure 3.2.3 below, which shows how the PL from a layer of Si-nc varies with the pump power.

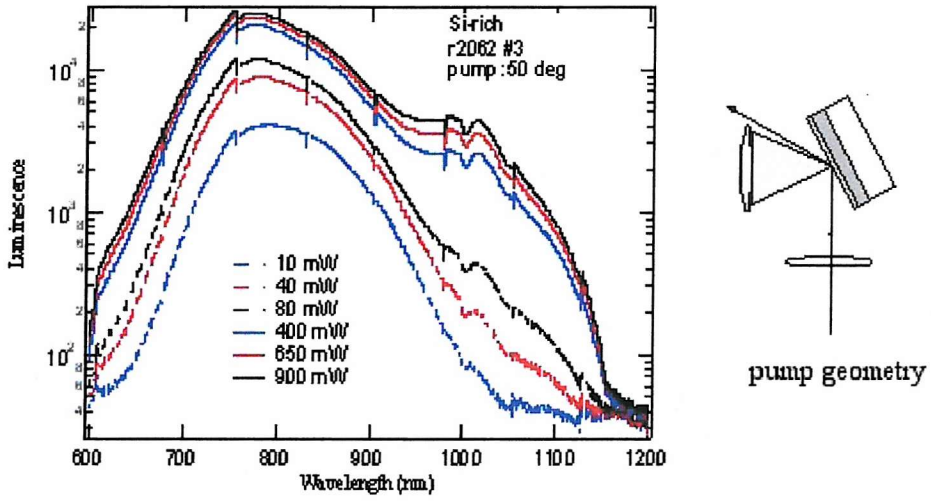

Figure 3.2.3 - Pump power-dependent photoluminescence measurements from Si-nc

For the measurements presented in Figure 3.2.3 above, a 532nm laser beam was focused onto the surface of wafer r2062#3, as is shown on the right of the graph, and the photoluminescence from the surface was guided into a spectrometer. It was found that an increase of pump power resulted in an increase in PL intensity, as expected, but also that at high pump powers a second feature around 1050nm appears. Above approximately 400mW pump power it appears that a saturation in the PL emission intensity occurs, with increases in pump power to 650mW and 900mW resulting in no significant increase in photoluminescence emission intensity, although the second peak around 1050nm shows continued increase in its emission intensity. The feature at 1050nm is not visible in waveguides of SRSO containing Si-nc, as is shown in Figure 3.2.4 in the next section.

3.2.1 Photoluminescence from Si-nc in a waveguide structure

In order to determine the photoluminescent properties of SRSO waveguide samples, a 30mW beam from an Argon Ion laser (λ=514nm) was focused into a spot of

approximately 20μm diameter on the surface of the waveguide and used to photo-excite the SRSO. This power density was used because the active layer is so thin at normal incidence, and the absorbing Si nanoparticles fill <1% of the volume (see Fig3.3.3), leading to inefficient optical pumping in this geometry. The resulting photoluminescence was collected at the edge of the waveguide and collimated using a 90x microscope objective. This light was then coupled into a spectrometer, as is shown in Figure 3.2.4.

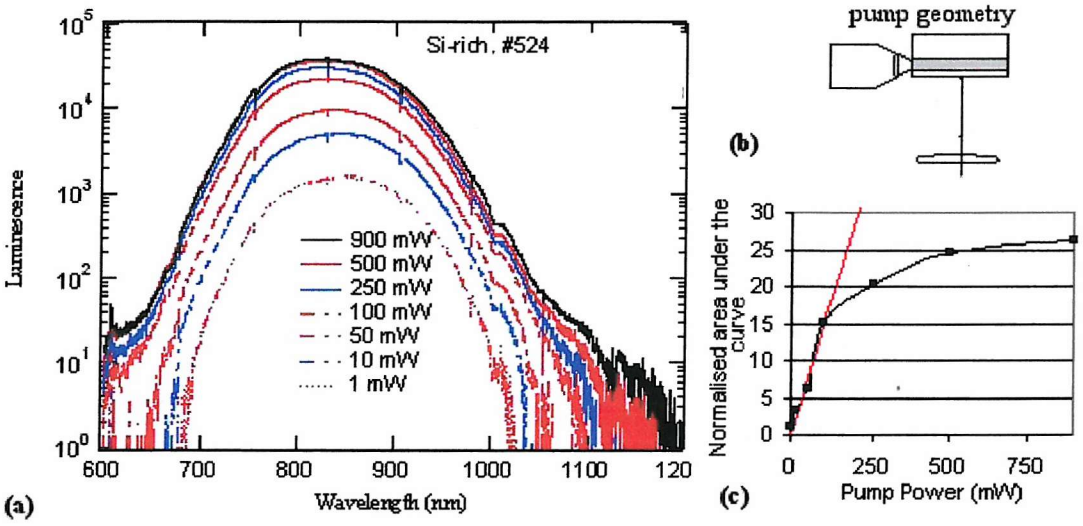

Figure 3.2.4 - (a) Pump power-dependent photoluminescence measurements from waveguide of SRSO with the pump geometry (b) and a graph plotting (black curve) the normalised area under the curves (c). The red line in this figure is a best fit line.

The results shown in Figure 3.2.4 (a) are for waveguides of type 'A' as described in Table 3.1.3, with waveguide cores of SRSO, $y = 9$. It may be seen that unlike the PL spectrum of a layer of SRSO containing Si-nc which has been deposited directly onto a Si wafer, there is no second peak at 1050nm appearing at higher pump powers. Again, higher pump powers result in stronger PL intensity, but as before a 2x increase in pump power does not result in a greater than 2x increase in PL emission. It also appears that saturation of PL emission intensity occurs around 500mW, as a further increase of pump power to 900mW yields no improvement in PL emission intensity. The area under the curves, plotted in Figure 3.2.4 (c) increases linearly up to 100mW, after which it levels off towards saturation.

Figure 3.2.5 shows how the wavelength of peak intensity of PL from Si-nc varies with the silicon incorporation into the SRSO layer. In this graph, A, B, and C refer to the types of SRSO waveguide core layer described in Table 3.1.3.

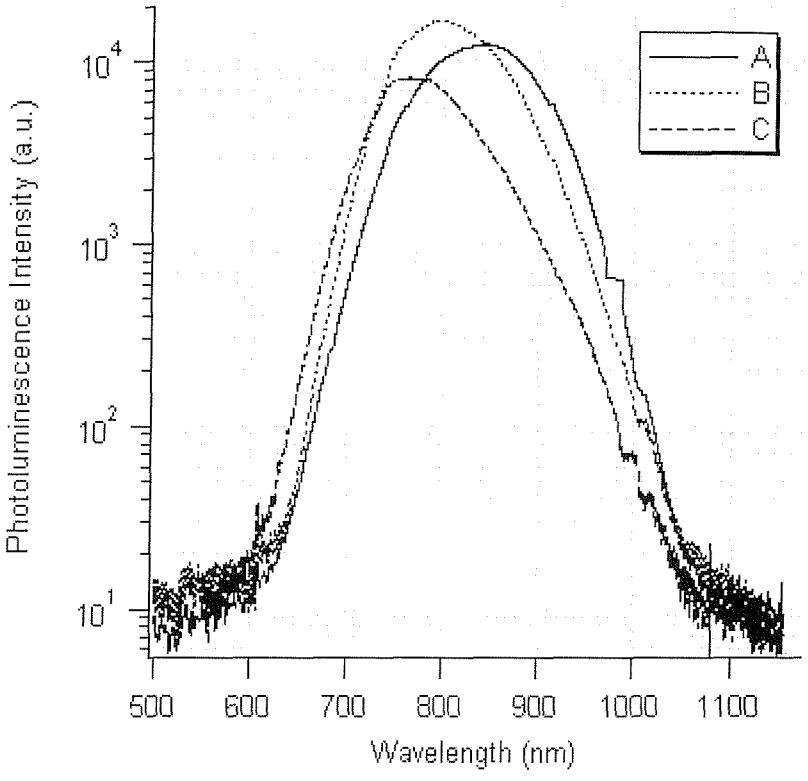

Figure 3.2.5 - Photoluminescence spectra for SRSO waveguides showing the redshift in peak intensity wavelength with increasing silicon incorporation into the core layer

Of the samples shown in Figure 3.2.5, Sample 'A' has the highest silicon incorporation in the core layer, and Sample 'C' the least silicon. This is reflected in the refractive index of the core layers both before and after the anneal. Figure 3.2.5 shows how, with greater silicon incorporation into the core layer of the waveguide, the wavelength of photoluminescence peak intensity shifts towards longer wavelengths and therefore towards lower energy.

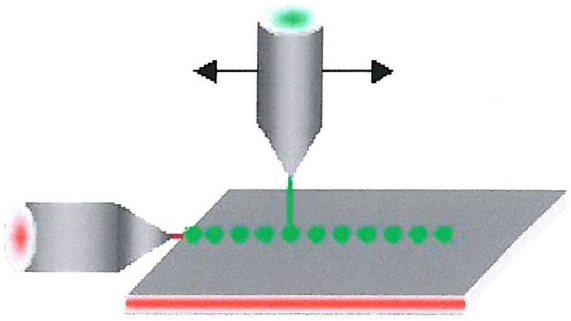

Figure 3.2.6 - Experimental setup for measuring how propagation distance affects the measured PL spectrum

A final set of photoluminescence spectra were taken to study how the distance of the excitation spot from the waveguide facet affected the measured PL spectrum, as is shown in Figure 3.2.6. These PL measurements were polarisation-dependent. The sample used for this was a waveguide of type 'A' SRSO which had been annealed for an hour, as part of the photonic crystal batch r2198 (to be described in Chapter 4). There was no particular reason why one hour should be chosen over a longer or a shorter anneal duration. One hour was the anneal time used for all the early SRSO batches, before the results from R2140 had been assimilated, and before it was known that PL emission intensity was increased by increasing anneal duration.

This particular sample, R2198#5_100, had been unaffected by the photonic crystal patterning process (to be described in Chapter 4). Figure 3.2.7 (a) shows the TE-polarisation measurements for a waveguide as the excitation spot is moved away from the facet in increments of 0.18mm. Figure 3.2.7 (b) shows the first three measurements for TE (solid) and for TM (dashed) as the excitation spot was moved away from the facet; the greatest intensity was recorded with the emission spot placed at the facet.

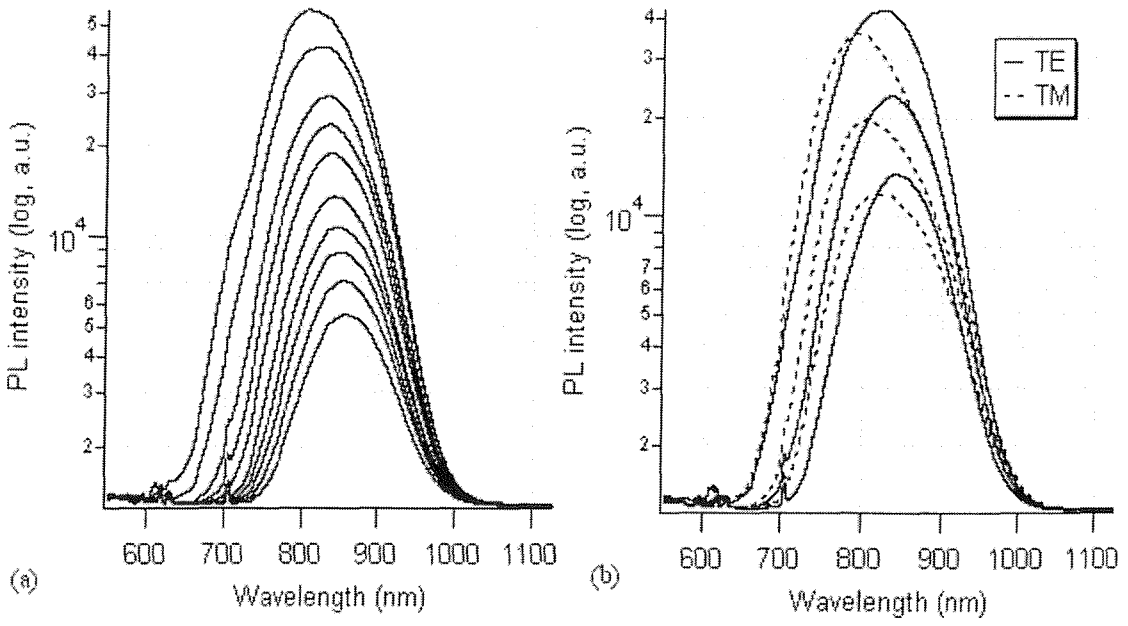

Figure 3.2.7 - Photoluminescence spectra showing diminishing PL intensity for increasing distances of the excitation spot from the facet for (a) TE only and (b) for both TE and TM polarisations.

It may be seen from Figure 3.2.7 (a) that as the excitation spot for the PL is moved further and further into the waveguide, the intensity of the measured photoluminescence is not only decreased, but the wavelength of peak intensity is also shifted towards longer wavelengths. Some of the loss in PL intensity is attributable to geometric effects, but it is clear that the waveguide itself is absorbing the higher energy light at wavelengths below 700nm. In addition, the PL emitted from the Si-nc is different for TE and for TM polarisations. The TM-polarised light was found to have a slightly shorter wavelength of peak intensity than the TE-polarised light, also with lower light intensity.

3.3 SRSO-Core Waveguide Transmission Measurements

It was clear from the photoluminescence spectra in Figure 3.2.7, that waveguides of Silicon-Rich Silicon Dioxide (SRSO) absorb the shorter wavelength section of the visible spectrum. As was described in Chapter 1 of this thesis, waveguides are fundamental to the operation of an integrated optical circuit in the same way as wires are to an integrated electrical circuit. An optical circuit to be made from luminescent silicon nanocrystals will have the waveguide as its fundamental element. There are no broadband measurements available in the current research literature setting out the critical transmission properties of waveguides of SRSO. These properties, essential to the fabrication of integrated circuits in SRSO, are reported in this section of the thesis.

Waveguides of SRSO were fabricated as was described in Section 3.1 above. Table 3.3.1 is a duplicate of Table 3.1.3, repeated here for convenience. The waveguide geometry is shown in Figure 3.1.3, and consists of 2.1μm of thermally grown SiO_2 upon a Si substrate. Approximately 450nm SRSO was deposited by PECVD onto the cleaned surface of the thermal SiO_2, followed by a deposition of 210nm of PECVD SiO_2. After the deposition stages, the wafers were cleaned and annealed at 1150°C for the times detailed in Table 3.1.3 and its duplicate, Table 3.3.1.

Type	γ (N_2O/SiH_4)	n (before)	Thickness (Å, before)	Annealed for (h)	n (after)	Thickness (Å, after)
A	9	1.605	4345	0.5,1,3,6	1.685	5720
B	12	1.575	4524	0.5,1,3,6	1.576	3850
C	15	1.547	4621	0.5,1,3,6	1.528	4047

Table 3.3.1 - Measured refractive index and thickness for SRSO waveguides, batch k2351

3.3.1 Modelling SRSO waveguides

Using the Wav32 program introduced in Chapter 2, the transmission properties of the annealed and unannealed waveguides described in Table 3.3.1 were modelled. The program interface and mode intensity profile for an annealed waveguide of type 'C' is shown in Figure 3.3.1. Waveguide transmission loss is described in Table 3.3.2 below for several wavelengths of interest. 600nm is the wavelength below which Si-nc do not emit photoluminescence. 800nm is approximately the wavelength of peak PL intensity for Si-nc. 1100nm is the bandgap wavelength of silicon, and 1550nm is the wavelength at which optical fibre communications most commonly operate. All results shown in Table 3.3.2 are for the TE polarisation.

Type	Annealed (y/n)	n	t (Å)	Waveguide Loss (dB/cm)			
				600nm	800nm	1100nm	1550nm
A	n	1.605	4345	0.00	0.002	0.74	38.397
A	y	1.685	5720	0.00	0.00	0.002	0.946
B	n	1.573	4524	0.00	0.017	3.041	71.734
B	y	1.576	3850	0.00	0.045	6.513	106.821
C	n	1.547	4621	0.00	0.145	10.681	117.999
C	y	1.528	4047	0.016	2.037	43.851	206.458

Table 3.3.2. - Calculated waveguide transmission loss for SRSO waveguides

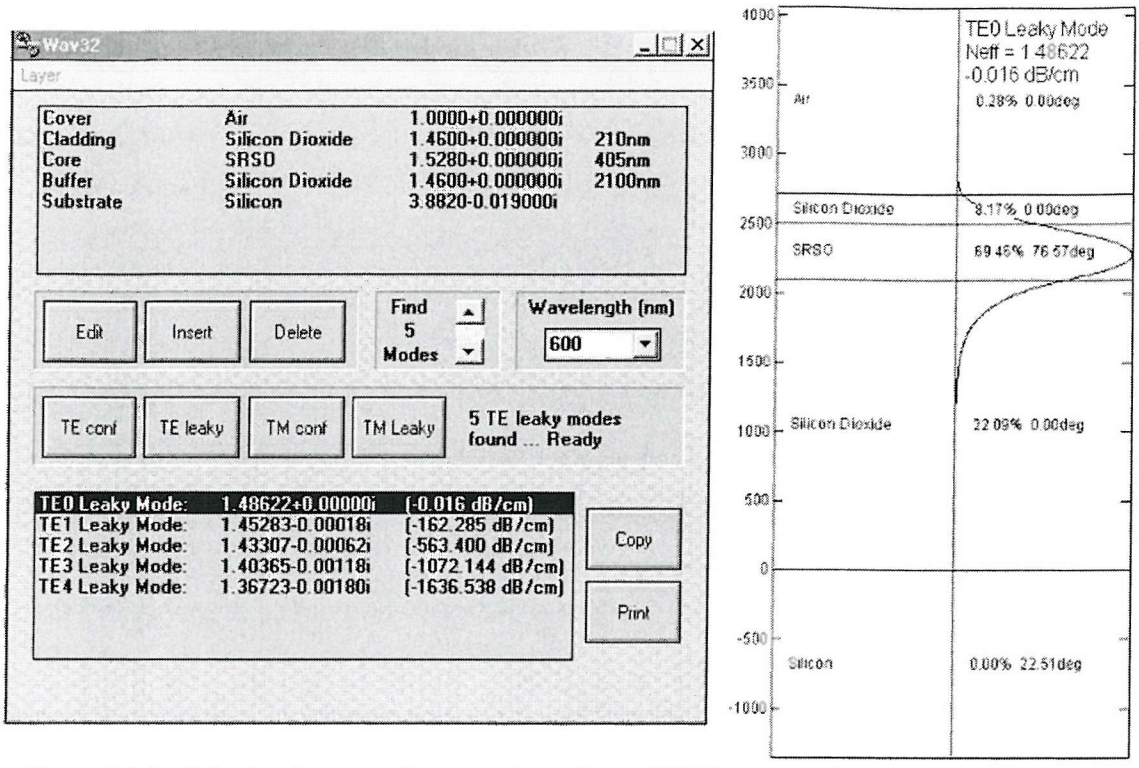

Figure 3.3.1 - Calculated waveguide transmission loss of SRSO waveguides using Wav32

The effective refractive index for guided modes in annealed waveguides of type 'A', 'B', and 'C' were modelled using a plane wave expansion technique by Dr. Martin Charlton. The results (shown in Figure 3.3.2) illustrate how the effective refractive index of the guided mode decreases towards the refractive index of the cladding layers, at which wavelength the mode is no longer guided, known as *cutoff*. The waveguide mode in which we are most interested is the fundamental mode (blue lines). The red and green lines show other waveguide modes, with cutoff wavelengths much shorter than that of the fundamental mode, which are not of relevance to this work.

Figure 3.3.2 (a) shows how a waveguide of type 'A' is multimode for guided light with a wavelength below 800nm, and continues to guide light well beyond 1550nm. Figure 3.3.2 (b) shows how a waveguide of type 'B' will still guide light at 1550nm, but that it is very near cutoff. Figure 3.3.2 (c) indicates that a waveguide of type 'C' will not guide light with a wavelength longer than 1100nm.

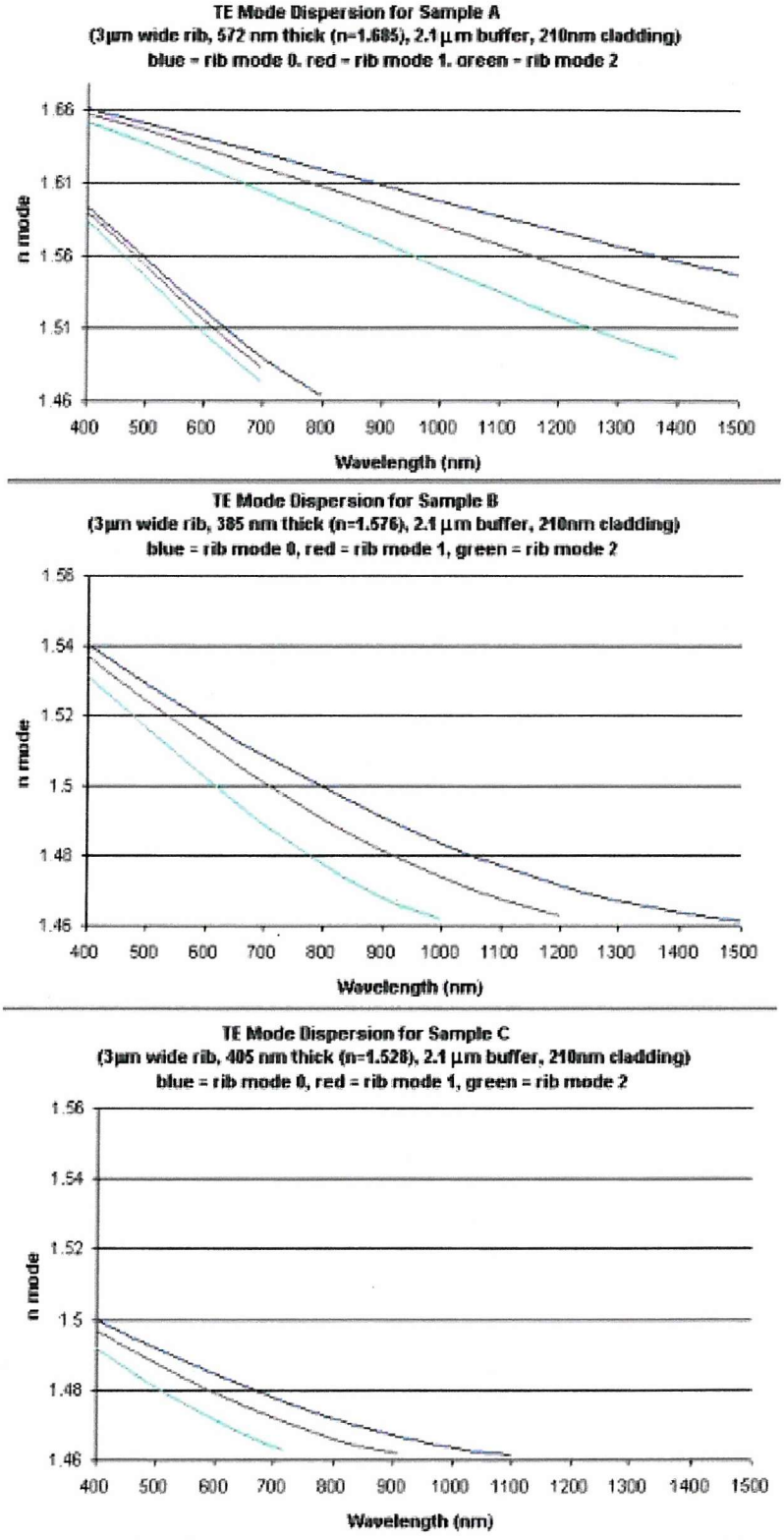

Figure 3.3.2 - Effective refractive index calculations for annealed waveguides of types (a) A, (b) B, and (c) C.

A model for the transmission properties of a waveguide layer of SRSO type 'A' was carried out by Prof. Jeremy Baumberg, which assumes a waveguide uniformly loaded with different densities of silicon. The optical data for Si was taken from an interpolated table of optical constants for silicon, by Don Groom published in SPIE in 1998. Figure 3.3.3 (black line) shows the fit for 0.06% of silicon in the waveguide. The red line is the measured waveguide transmission for a waveguide layer of type 'A', which has been included in this graph for comparison.

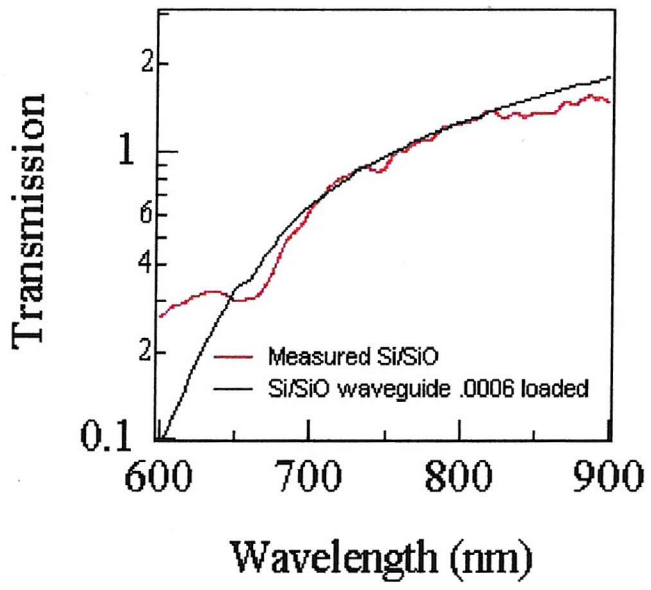

Figure 3.3.3 - Calculated transmission of type 'A' SRSO waveguides (black line) and measured transmission results (red line)

3.3.2 Transmission Measurements of SRSO Waveguides

Waveguide transmission measurements were carried out using an ultra-broadband continuum generated from a nonlinear photonic crystal "holey" fibre. The fibre was pumped using the 150fs λ=1100nm idler output from a pulsed optical parametric amplifier derived from a regeneratively amplified Ti:sapphire femtosecond-pulsed laser. The resulting super-continuum ranged from 600nm to 1600nm in wavelength and was tightly focused into the core layer of the SRSO waveguides. The transmitted light was measured using both a peltier-cooled Si CCD (500nm – 1100nm) and an

InGaAs infrared detector (900nm – 1800nm) in order to cover the full spectral range. A reference beam was routed around the waveguide to allow the relative transmittance spectra to be accurately derived. The experimental setup used in these experiments is shown in Figure 3.3.4 below, with the inset showing how XYZ tables were used to focus the supercontinuum into and out of the waveguide..

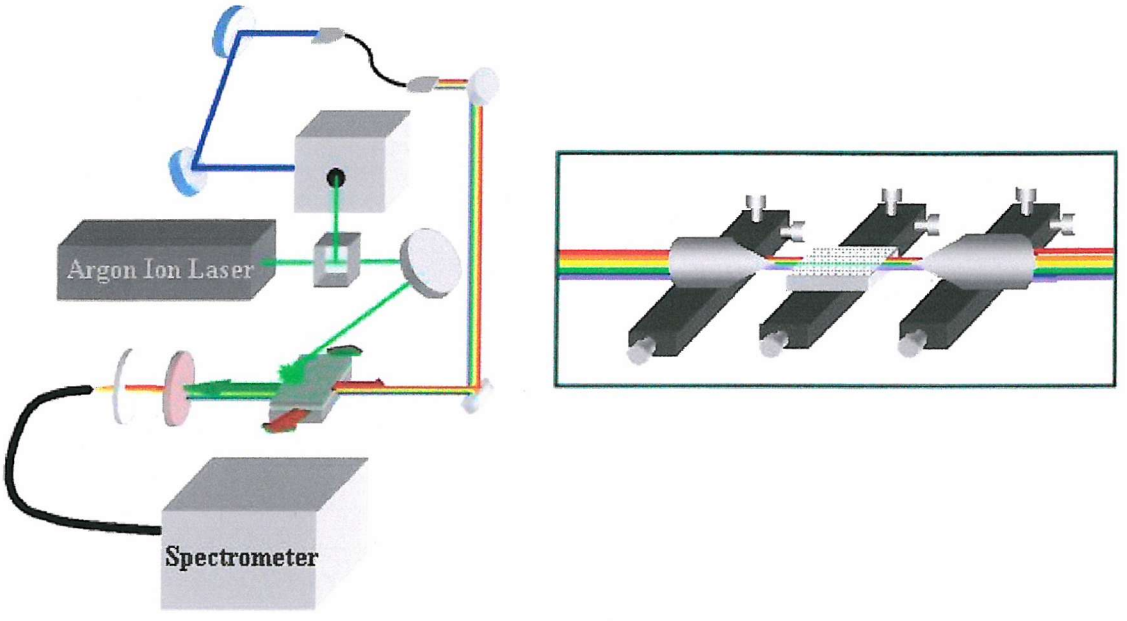

Figure 3.3.4 - Experimental setup for transmission and photoluminescence measurements

Figure 3.3.5 shows the transmission spectra for through each waveguide type which has been annealed for 1hr (solid line), transmission through an unannealed waveguide (short dashed line), and the photoluminescence (long dashed line), each for the same waveguide sample. It may be seen that the unannealed waveguide has much better transmission properties in the visible portion of the spectrum, although it exhibits no photoluminescence, while the annealed waveguides have improved waveguide transmission in the IR portion of the spectrum. The photoluminescence spectrum of each sample has been appended to each graph in Figure 3.3.5 to illustrate how closely the absorption losses at shorter wavelengths matches the onset of the photoluminescence.

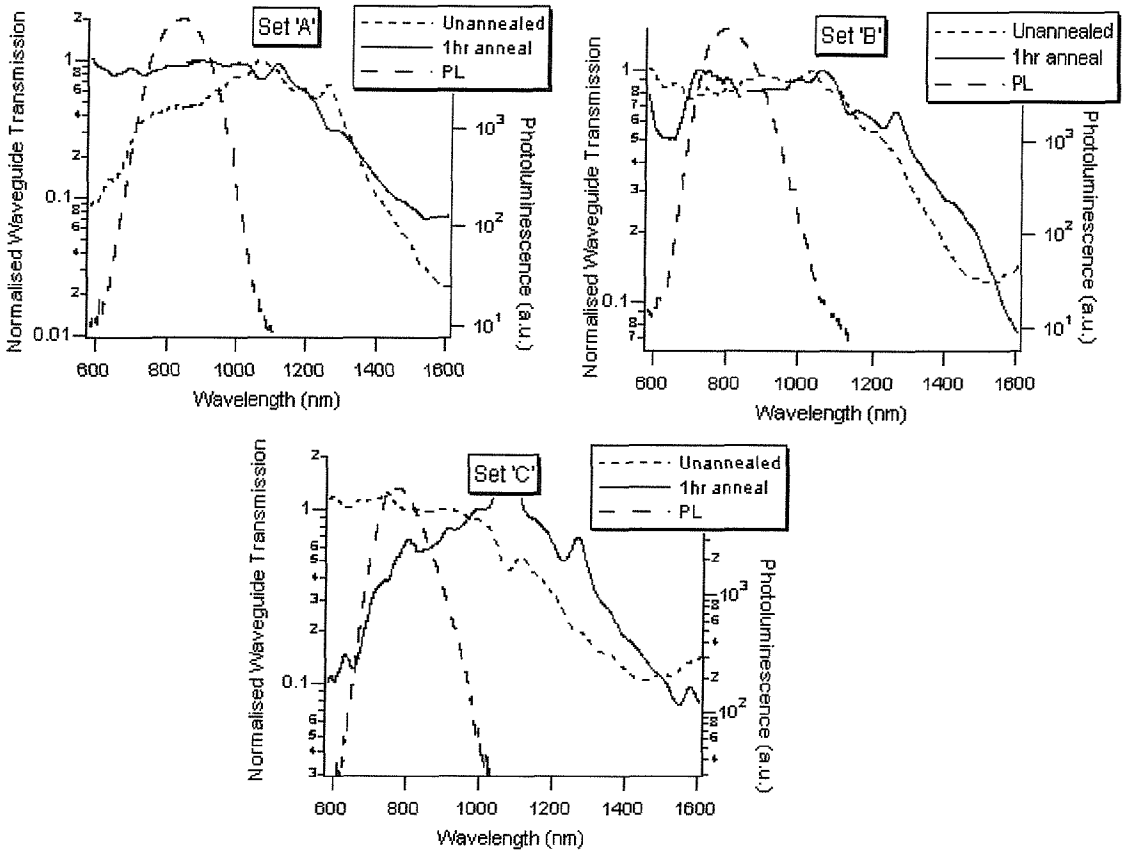

Figure 3.3.5 - Transmission spectra for annealed and unannealed SRSO waveguides of type A, B, and C. Photoluminescence data is also appended to each graph.

The visible transmission measurements for a waveguide of type 'B' SRSO which had been annealed for 1 hour appear to be very poor. In fact, the waveguide trasnmission for this waveguide portion was much better than the other annealed waveguides, so much so that the collection time had to be reduced by 3/10 to avoid saturating the silicon detector. This was not an issue with the other sets of measurements.

Focusing upon the visible portion of the spectrum, data comparing visible transmission spectra for waveguides which have been annealed for differing lengths of time is shown in Figure 3.3.6. The waveguides used for this study had waveguide cores of SRSO type 'A', and were annealed at 1150°C for durations ranging from 0-6 hours.

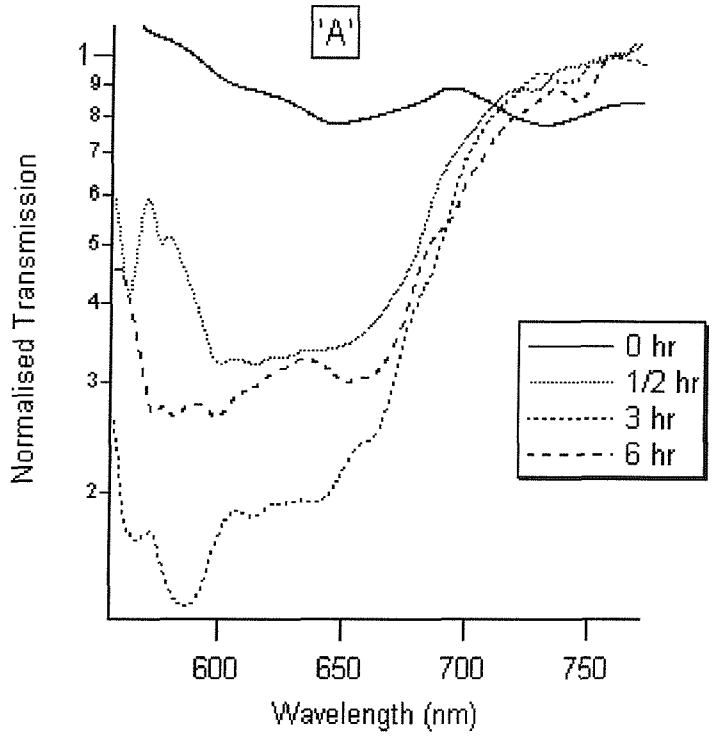

Figure 3.3.6 - Visible transmission spectra for SRSO waveguides which have been annealed for durations from 0-6 hours.

Continuing the focus upon the visible portion of the spectrum, Figure 3.3.7 contrasts visible transmission spectra for waveguides of all types of SRSO with different amounts of silicon incorporated into the core layer of the waveguide. Each of the waveguide samples used for these measurements had been annealed for 6 hours at 1150°C.

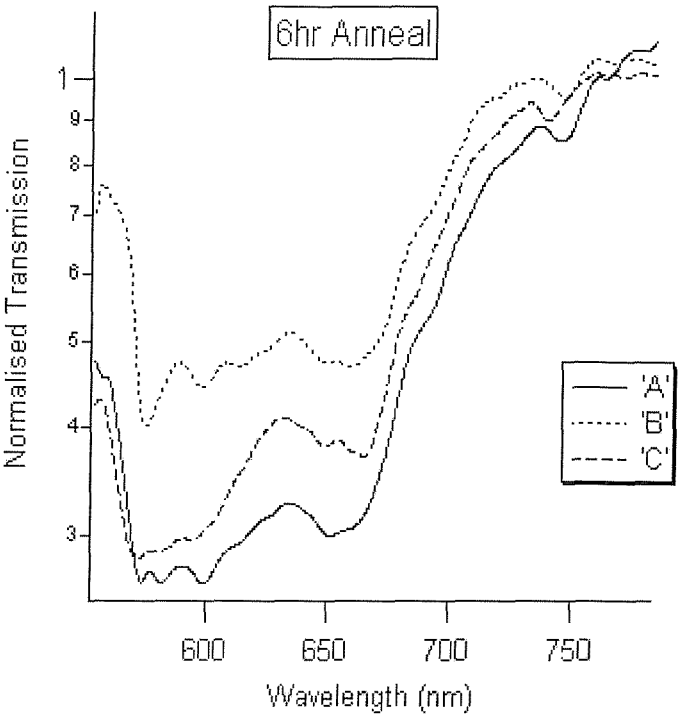

Figure 3.3.7 - Visible transmission spectra for SRSO waveguides incorporating different concentrations of silicon.

While all the measurements reported in this section were taken in the TE polarisation, measurements were also carried out for the TM polarisation. Figure 3.3.8 below illustrates how similar waveguide transmission measurements were for TE and for TM polarisations.

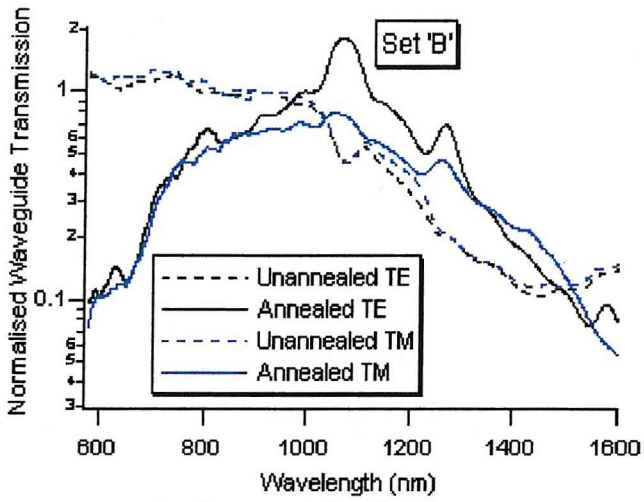

Figure 3.3.8 - Transmission spectra for annealed and unannealed SRSO waveguides for both the TE (black) and TM (blue) polarisations.

3.4 SRSO Gain Measurements

As described in the first chapter of this thesis, in November 2000 L. Pavesi et. al. reported gain in waveguides of Si-nc formed by the implantation of silicon ions into wafers of quartz glass and of silicon [3]. The gain reported was of the same order as was achieved in the most widely used III-V compounds, with the results shown in Figure 2.4.5. Pavesi's work provoked widespread interest in the area and provided the basis of the work in this thesis. The method used for gain measurements by L. Pavesi was challenged by J. Valenta in 2002, who questioned the validity of the results, suggesting that their results may have been an artifact of the measurement geometry [4]. A recent paper by L. Dal Negro, from the same group as L. Pavesi, insists that gain has been measured [5].

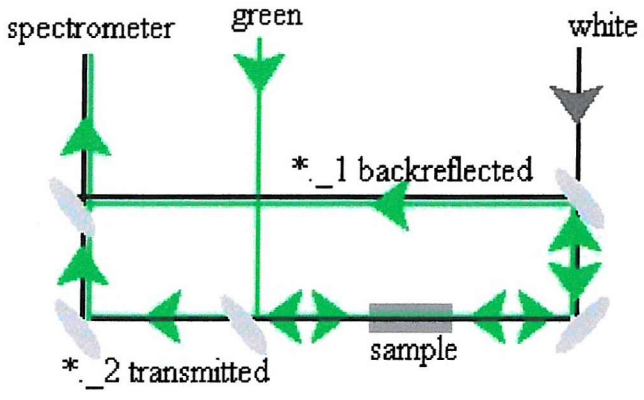

Figure 3.4.1 - Experimental setup for measuring gain of silicon nanocrystals

With the guidance of Dr. Caterina Netti, the experimental setup shown in Figure 3.4.1 was used to measure gain in waveguides of type 'B' SRSO, which had been annealed for 6 hours. The fabrication methods and refractive index profiles of the type 'B' SRSO waveguide is described in Sections 3.2 and 3.3. A white light supercontinuum, generated as was shown in Figure 3.3.4, was termed the *probe*, and was focused into the core layer of the waveguide measured. At the same time, the green 514nm line of an Argon Ion laser was focused into the opposite face of the sample. The green line

was termed the *pump*. Using mirrors and beam splittters, the pump and probe laser beams were aligned so that they were operating in the same region of the Si-nc waveguide.

Using the same mirrors and lenses used to focus the probe beam into the waveguide, the pump beam which had been transmitted through the waveguide sample was collected and guided into the spectrometer, which was a peltier-cooled Si CCD (500nm – 1100nm). The probe light which had been transmitted through the waveguide sample was collected using the same optics which had been used to focus the pump beam into the waveguide core layer, and guided by mirrors into the same spectrometer as was used for the transmitted pump beam. A filter was used to reduce the powerful 514nm green laser line before either beam entered the spectrometer.

The terminology for the two signals collected from each end of the waveguide sample derives from the white light probe signal. Light from the probe signal which had been transmitted through the waveguide sample, along with any backreflected pump signal, was termed the *transmitted* beam. Light from the probe signal which had been backreflected from either facet of the waveguide sample, plus the transmitted probe signal, was termed the *backreflected* beam.

The full area of the Si CCD was used to measure both the transmitted and backreflected beams at the same time. Results from the measurements were in 3 discrete numerical data streams, differentiated by a suffix. Those signals which terminated in _0 contained the information about the wavelength measured. The signals terminating in _1 were the measurements for the *backreflected* signal, while those terminating in _2 were the *transmitted* signal.

By collecting and recording all light which passed through or was emitted from the annealed SRSO waveguide sample, it was possible to determine whether or not the Si-nc were capable of emitting gain or not. Measurements were carried out at two power settings for the pump laser, with data taken for three laser combinations. *Pump*

only measurements were carried out with the probe switched off or blocked. *Probe only* measurements were taken with only the white light continuum switched on or passing through the waveguide. *Pump plus probe* measurements were taken with both pump and probe lasers passing through the waveguide sample.

It was anticipated that once the pump at 514nm had been removed from the measured signal through the use of filters, both transmitted and backreflected signals would be waveguided Si-nc photoluminescence spectra such as were shown in Figures 3.2.4 and 3.2.7. Experimental data for the transmitted (upper set) and backreflected (lower set) *pump-only* signals is shown in Figure 3.4.2 for both high (solid line) and low (dashed line) power.

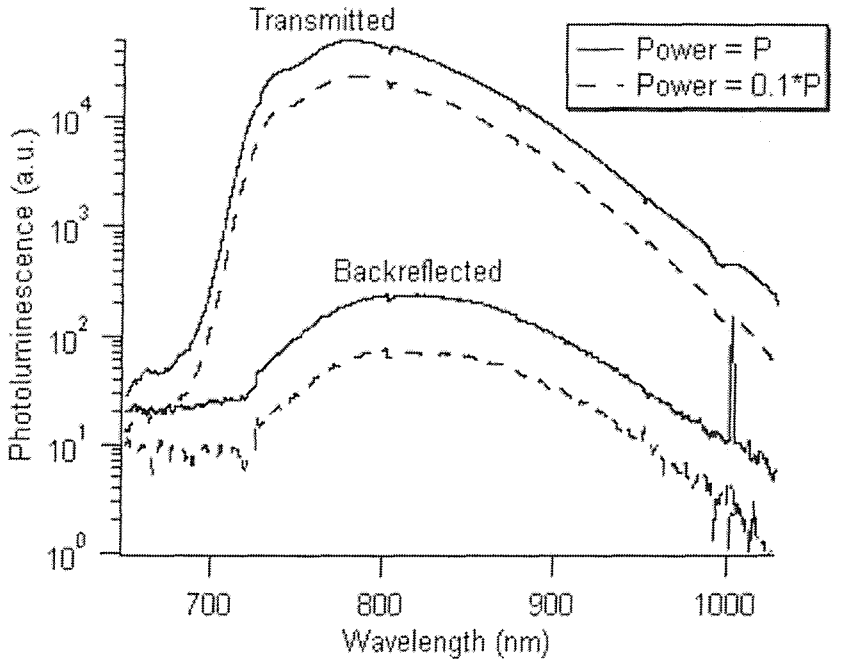

Figure 3.4.2 - High (solid line) and low (dashed line) power transmission spectra for transmitted and backreflected *pump-only* measurements

It was also anticipated that without the pump in operation at all, *probe only* measurements would result in the white light transmission spectrum through an annealed waveguide of type 'B' SRSO. The measured spectra should be unaffected by the power applied to the pump signal, though there should be a marked difference

between the backreflected signal and transmitted signal due to the SRSO waveguide absorption below 750nm. Experimental data for the probe only measurements are shown in Figure 3.4.3.

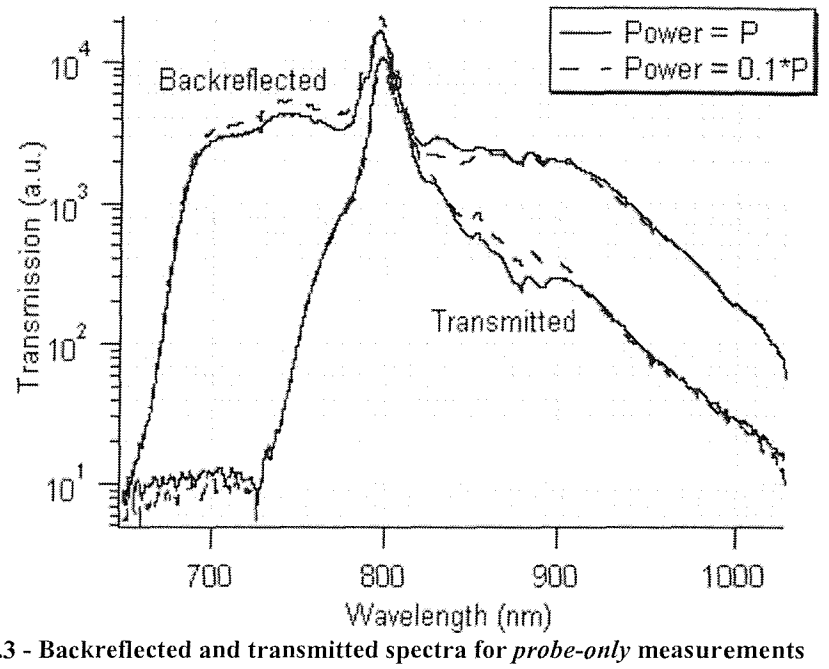

Figure 3.4.3 - Backreflected and transmitted spectra for *probe-only* measurements

If gain were present in the system, it should be apparent from the pump and probe measurements, when both pump and probe signals are passing through the waveguide sample. The experimental data for these measurements are shown in Figure 3.4.4.

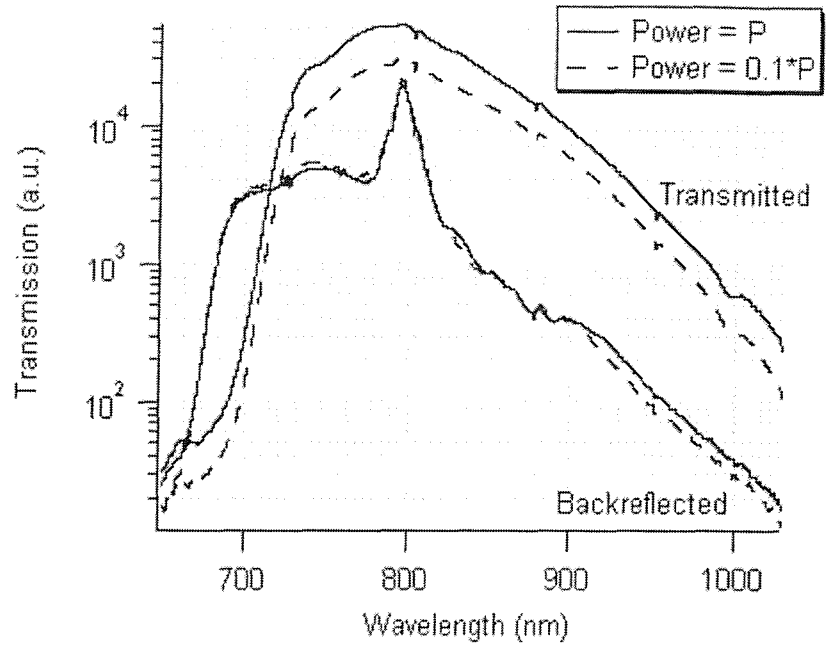

Figure 3.4.4 - Backreflected and transmitted spectra for *pump plus probe* measurements, both high and low power

The (a) high power and (b) low power backreflected spectra for all laser arrangements are shown in Figure 3.4.5 below. The (a) high and (b) low power transmission spectra are shown in Figure 3.4.6 beneath.

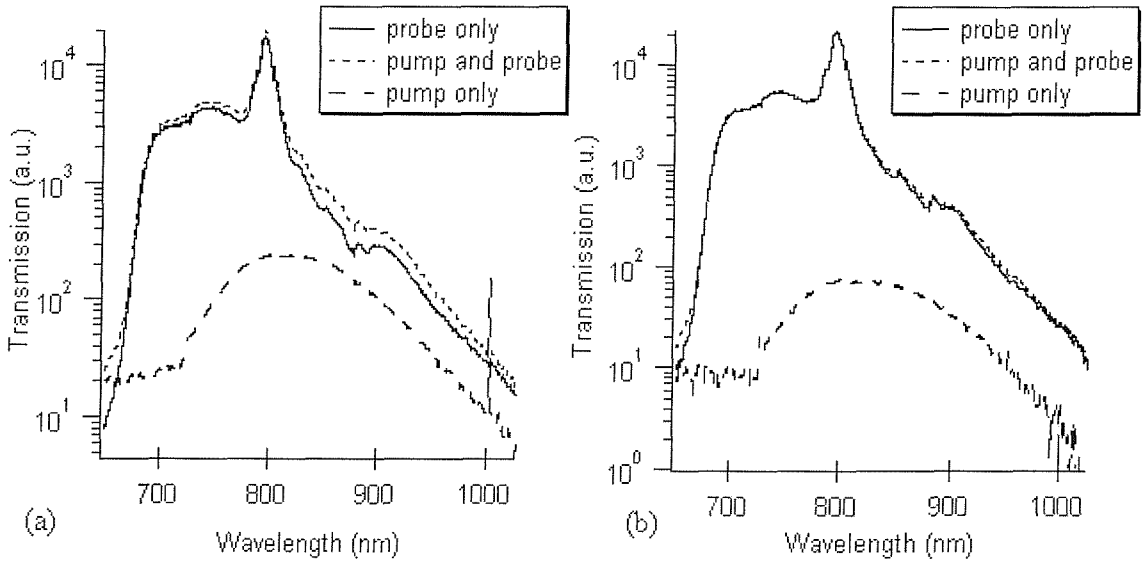

Figure 3.4.5 - (a) High power and (b) low power backreflected spectra for a SRSO type 'B' waveguide

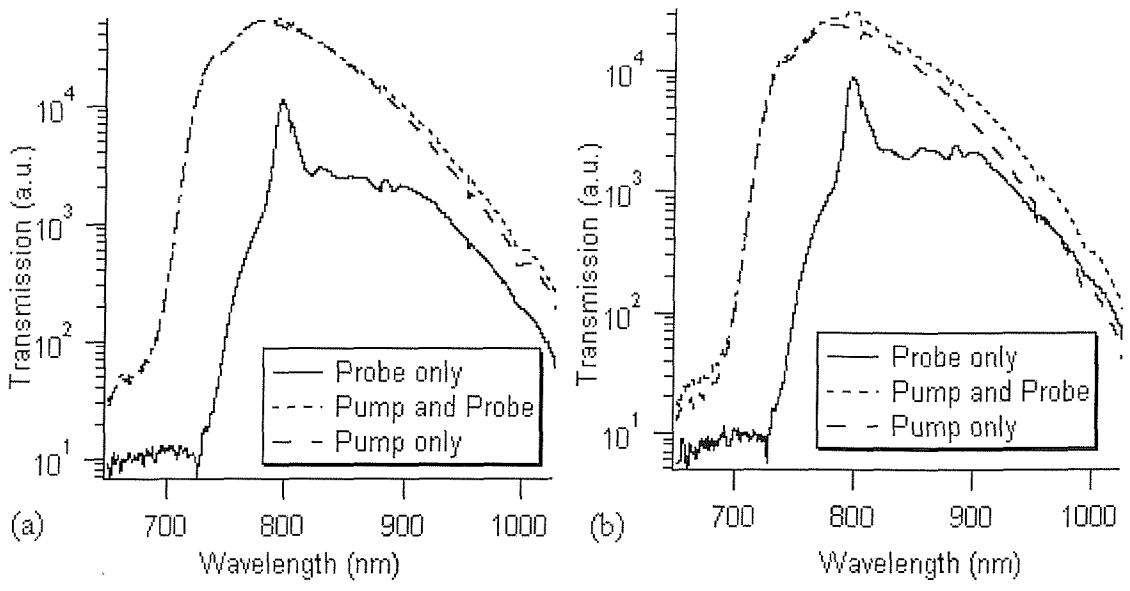

Figure 3.4.6 - (a) High power and (b) low power transmitted spectra for a SRSO type 'B' waveguide

3.5 Discussion of SRSO Properties based upon Results

3.5.1 Deposition

The SRSO processes developed in Section 3.1 allow deposition of SRSO with a refractive index range of 1.55-1.71. These depositions are at a rate of 12-13Å/s for deposition at a pressure of 1000mT, and at a rate of 4-5Å/s for deposition at 500mT. SRSO layers which are deposited at a pressure of 500mT have a refractive index marginally higher than layers which have been deposited at a pressure of 1000mT. The difference is approximately 1% for SRSO of type 'A', and 0.3% for SRSO types 'B' and 'C'.

A thermal anneal at temperatures of 1150°C or 1200°C raises the refractive index of the SRSO layer by a percentage which is dependent upon the silicon incorporation in the layer. As is shown in Figure 3.1.3 (a), the change in refractive index is greatest (~13%) for samples which have been fabricated with $\gamma = 6$. For SRSO fabricated with $\gamma = 15$, the refractive index change is much smaller (~3%). Modifying the anneal temperature to 1200°C from 1150°C had no effect upon either the refractive index of the layer or upon the eventual photoluminescence spectrum.

Figure 3.1.3 (a) also shows how the size of the change in refractive index of SRSO during an anneal is reduced by prolonging the duration of a thermal anneal beyond the first 30 minutes. The scale of the reduction is similar for all types of SRSO, approximately 1% of the change in refractive index. From Figure 3.1.3 (b) we conclude that while the refractive index is affected by the duration of the anneal, the thickness of the layer is unchanged.

Once the thermal anneal has been completed, the achievable refractive index range for SRSO is 1.53-1.92. This is a broader continuous range of refractive index than was achieved through the silicon oxynitride (SiON) fabrication process described in Chapter 2.

3.5.2 Photoluminescence

Photoluminescence measurements in Section 3.2 show a photoluminescence band from SRSO at wavelengths of approximately 600-1000nm. Measurements were carried out on layers deposited onto the surface of a silicon wafer, and also for SRSO as the core layer of a planar slab waveguide.

Figure 3.2.2 presents clear evidence that as the anneal time increases, so does the intensity of the luminescence from the SRSO waveguides of type 'A'. These results are in contrast with those reported by M. L. Brongersma et al. [6]; this may be attributed to the fact that his anneal was carried out in an oxygen atmosphere, not the nitrogen atmosphere used in our work, therefore causing oxidation of the silicon nanocrystals. The increase shown in photoluminescence peak intensity is sharp for the first few hours of the anneal, but approaches saturation for anneal times beyond 6 hours. The portion of the spectrum most affected by the increase is the shorter wavelengths, especially around 700nm. Between half an hour and ten hours there is a 5.4x increase in the photoluminescence efficiency for PL at 850nm while there is a 14.1x increase for PL at 700nm. This leads to a slight shift in the wavelength of peak intensity from 877nm to 859nm. These conclusions are drawn from the results shown in Figure 3.2.2 (b).

The photoluminescence spectrum for SRSO is shown to be not only dependent upon the anneal time, but also upon the amount of silicon incorporated into the SRSO layers. For SRSO with $\gamma = 9$, with the highest silicon incorporation, the wavelength of peak intensity for 3-hour annealed waveguides is 837nm. For SRSO with $\gamma = 15$, with the lowest silicon incorporation, the wavelength of peak intensity is 761nm. This is shown in Figure 3.2.5.

A feature which is visible in layers of SRSO deposited directly onto silicon but not in waveguides of SRSO is the power-dependent second peak in the photoluminescence around 1050nm. In Figure 3.2.3 this second peak is easily visible for pump powers of

400mW and greater, but in Figure 3.2.4 it is not there at any pump power. This second peak is not at the correct wavelength to be silicon band-edge recombination, although it might conceivably be recombination from defect states in the bulk silicon substrate at slightly lower energy than the silicon conduction band, which have been populated by electrons which are spilling over from fully populated nanocrystal states. These states could not be populated in the waveguide samples through the thick SiO_2 buffer which separates the waveguide core layer and the substrate.

Lastly, the TE and TM polarised photoluminescence spectra for SRSO waveguides of type 'A' were shown to differ in wavelength by approximately 30nm. This was for PL which was excited at the very edge of the waveguide, and so was unaffected by any waveguide absorption. Photoluminescence spectra from an excitation spot located some distance from the waveguide facet at which measurements were taken were shown in Figure 3.2.7 to suffer significant reabsorption in the shorter wavelength portions of the PL spectrum. This is attributed to waveguide absorption, which is discussed in the next section.

3.5.3 Transmission

Waveguide transmission measurements presented in Section 3.2 show that for unannealed waveguides of all types of SRSO, there is good transmission up to approximately 1200nm. Above this wavelength the quality of transmission worsens swiftly as the wavelength increases. For all waveguides there is improvement in the waveguide loss at longer wavelengths once the thermal anneal has taken place.

All annealed SRSO waveguides show large absorption below 700nm. This was predicted by the model from Prof. Baumberg which suggested that the wavelength below which this material absorption occurs is determined by the level of silicon incorporation in the SRSO layer (Figure 3.3.3). While the match between the calculated and measured transmission spectra is appealing, this explanation for the transmission spectra is inconsistent with the good waveguide transmission at short

wavelength for the unannealed waveguides. During the anneal in N_2 it is not possible that there is any increase in the actual silicon which is incorporated into the layer, especially for waveguides which are isolated from the Si substrate by a thick SiO_2 buffer layer.

The model in Figure 3.3.3 is also contradicted by results shown in Figure 3.3.7, which shows how the wavelength below which the silicon nanocrystal absorption occurs is unchanged by varying the silicon incorporation into the SRSO waveguide core layer. The duration of the anneal also causes no change in the wavelength below which absorption occurs.

The waveguide losses below 700nm may be attributed to bandgap absorption by silicon nanocrystals, which are formed during the thermal anneal. This is consistent with the occurrence of characteristic silicon nanocrystal photoluminescence only in those samples which have been annealed. We also believe that the relatively broad material absorption band below 700nm illustrates the cluster size range, and the invariant lower-energy edge at 700nm suggests a bandgap energy of 1.77eV for the largest optically active silicon nanocrystals. This is in agreement with work done by Ma et al. in 1999[7], who reported a similar consistent absorption edge between 1.65 - 1.8eV, corresponding to 690 – 776nm.

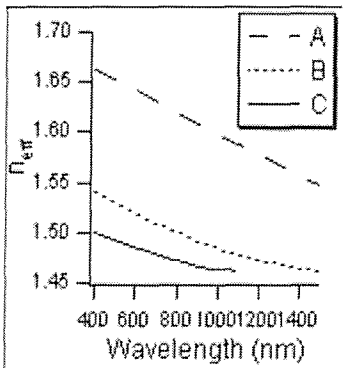

Figure 3.5.1 - Calculated effective refractive index for SRSO waveguides

We believe that the improved waveguide transmission for all samples in the IR portion of the spectrum after the thermal anneal is a result of the raised refractive index of the core layer. Figure 3.5.1 shows how the effective refractive index of the

waveguide core layer varies as a function of wavelength, from the calculations by Dr. Charlton presented in Figure 3.3.2. As all samples measured exhibited similar infra red losses, it is not probable that waveguide cutoff is the sole loss mechanism. We would expect that absorption losses in the SiO_2 cladding layers will cause attenuation of the waveguide modes in the core layer. It is noted that the losses above 1300nm are very similar to the characteristic IR absorption losses, which are amongst the major loss factors in SiO_2 optical fibres[8].

Finally, the photoluminescence of each sample was also been appended to each graph in Figure 3.3.5 to illustrate how closely the absorption losses at shorter wavelengths matches the onset of the photoluminescence. For each SRSO type, 'A', 'B', or 'C', the material absorption begins at a wavelength which is very similar to the peak wavelength of the photoluminescence. It is not at the *same* wavelength, as the wavelength of peak intensity for nanocrystal photoluminescence is dependent upon the silicon incorporation, while the lowest-energy absorption wavelength is not.

3.5.4 Gain Measurements

An experiment to measure gain in waveguides of Type 'B' SRSO which had been annealed for 6 hours was described in Section 3.4. A pump signal of the 514nm line of an Argon Ion laser was aligned with a white light supercontinuum probe signal in the core layer of a cleaved waveguide. The pump signal propagated through the waveguide sample in the direction opposite to the probe signal. Light emitted or reflected from both waveguide facets was collected and focused into a peltier-cooled Si CCD, with a wavelength range of 500nm – 1100nm. The signals were aligned such that both propagating (*transmitted*) and counterpropagating (*backreflected*) probe signals could be measured by the CCD at the same time.

By collecting all the light in the system, it was hoped to isolate definitively whether there was, or was not, gain in our Si-nc material. Three sets of data were taken. The first was *pump only*. The pump signal at 514nm excited photoluminescence from the

Si-nc in the waveguide core layer, which was measured emitting from both facets, with the results shown in Figure 3.4.2. The second set of data taken was *probe only*. The transmitted and backreflected spectra for the white light supercontinuum are shown in Figure 3.4.3. Finally the transmitted and backreflected spectra were taken for *pump and probe*. These spectra are shown in Figure 3.4.4. If gain is present in the system, it would be expected that the result of *pump and probe* should be greater than the sum of *probe only* and *pump only*.

Figure 3.4.2 shows the photoluminescence spectra measured for transmitted and for backreflected signals at both high and low pump powers. The photoluminescence is shown to be greater emitting from the facet onto which the pump light is focused (*transmitted* spectra) than the facet from which the pump light exits (*backreflected*). The photoluminescence measured is clearly emitted from Si-nc at or near the edge of the waveguide, as it has suffered from little of the waveguide loss which results from transmission through annealed SRSO wafers. The photoluminescence measured from the far facet of the waveguide sample (*backreflected*) has clearly been excited further from that facet, as it has suffered from the Si-nc waveguide reabsorption, resulting in a wavelength of peak intensity which is at a much longer wavelength.

The change in power from P to 0.1P had the effect of reducing the peak intensity of the signals by 3.3x for the backreflected data, while it only had a 2.1x reduction for the transmitted spectra. The greater sensitivity of the backreflected spectrum to modifications in the pump power is a likely result of the penetration of the 514nm pump beam into the waveguide. With the transmitted spectra, both high and low power, the majority of the measured light is unaffected by waveguide absorption, and the decrease in PL intensity for the low power spectra is similar to the power-dependent PL measurements presented in Figure 3.2.4. For the "backreflected" spectra, with increased power there will be a corresponding increase in the depth of penetration, which is borne out by the slightly redshifted shape of the higher power spectrum.

The *probe only* transmitted and reflected spectra are shown in Figure 3.4.3. These spectra are similar to the results presented in Section 3.3, especially Figure 3.3.5, but with the results in Figure 3.4.3 presented exactly as they were recorded. The seeming discrepancy between these results and those presented in Figure 3.3.5 for a waveguide of type 'B' SRSO is because the results in Figure 3.3.5 were normalised to provide 0 loss where the waveguides were guiding best. What may be easily seen from both sets of data is the waveguide absorption below 750nm.

Finally, *pump and probe* measurements were presented in Figure 3.4.4. The backreflected data is very similar to the backreflected *probe only* data, while the transmitted data is very similar to the *pump only* data, each reflecting their major components.

The backreflected and transmitted spectra for all laser configurations are shown in Figures 3.4.5 and 3.4.6, with (a) presenting the high power spectra and (b) presenting the lower power measurements. The short-dashed line in each graph represents the *pump and probe* measurements, and it may be seen that for wavelengths above approximately 800nm it begins to be differentiable from the spectrum of its major component, whether that is the white light transmission spectra of the probe, or the PL spectra of the pump.

To assist in analysis, each spectrum is allocated a letter:

a = Probe only
b = Pump and probe
c = Pump only

Two further spectra may be added. If the pump and probe spectra are the sum of the probe and pump signals, then subtracting the *probe only* spectrum from *pump and probe* should result in the *pump only* spectrum. *i.e.*

$d = b - a$

Similarly, the sum of both pump only and probe only spectra should result in the pump and probe spectrum. *i.e.*

$e = c + a$

These additional spectra are shown in Figure 3.5.2 for backreflected (a) high power and (b) low power, and for transmitted (c) high power and (d) low power.

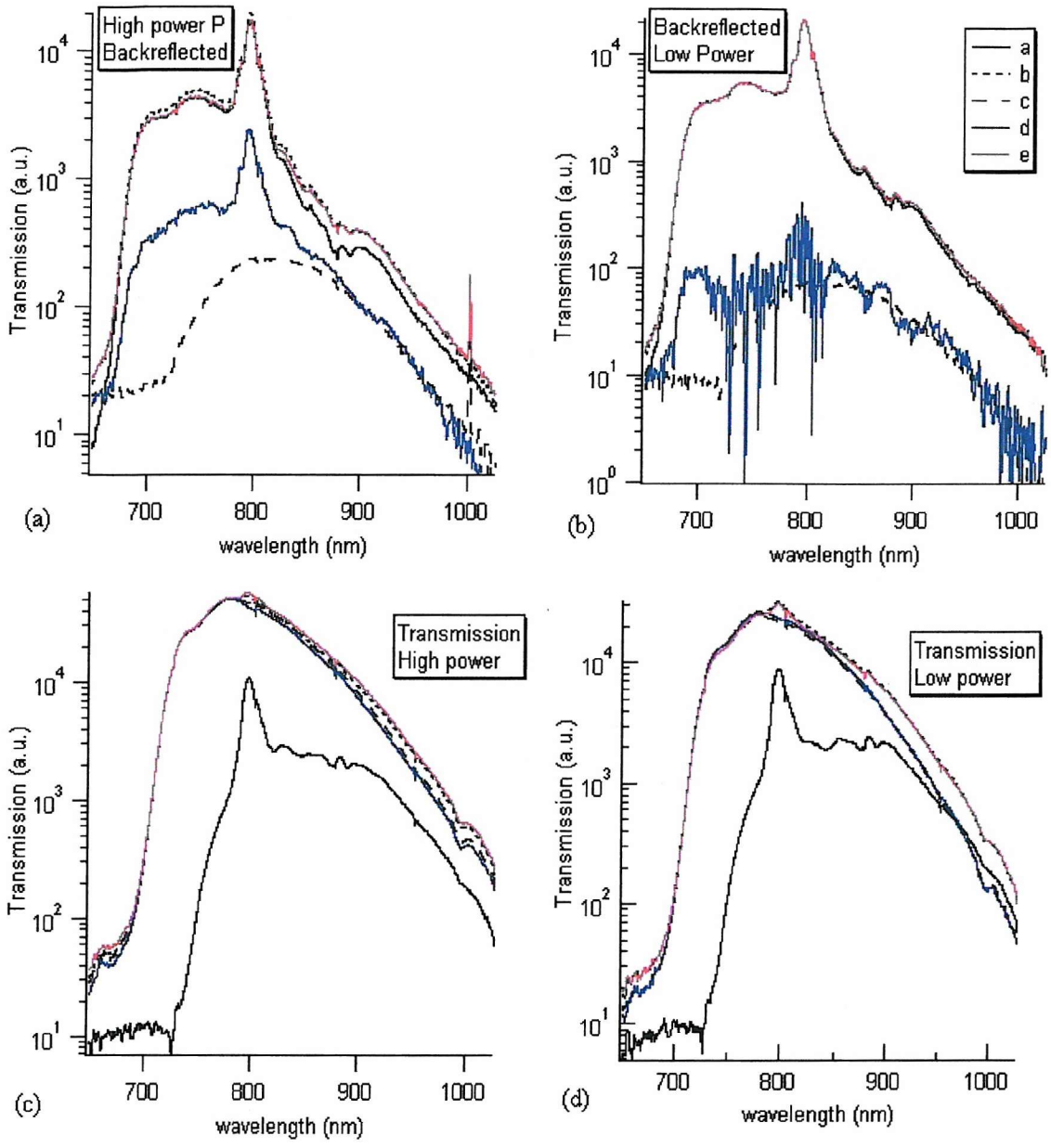

Figure 3.5.2 - Data analysis for backreflected (a) high and (b) low power, and transmitted (c) high and (d) low power transmission spectra for a SRSO waveguide.

For each set of spectra shown in Figure 3.5.2, there is a very good match between the red lines (spectra *e*), and the short-dashed black line (*pump and probe*). The only noticeable divergence is in the wavelength region from 700-800nm in Figure 3.5.2 (a). In this region, the red line representing spectrum *e* is in close agreement instead with the solid black line of probe only, spectrum *a*. For the transmission spectra in Figures 3.5.2 (c) and (d), the blue lines (spectra *d*) show very good agreement with

the long-dashed black line of spectrum *c* (pump only). All this is as would be expected if *pump and probe* were indeed the sum of *pump only* and *probe only*.

The unexpected result is shown by the blue lines of spectra *d* in Figures 3.5.2 (a) and (b). Here the expected result would be for the blue line to follow the long dashed line of pump only (spectra c), but instead, especially for the high power measurements, the blue line follows most closely the white light backreflected spectrum of *a*. This spectrum, though not so easily visible for the lower power measurements, strongly suggests that as the pump signal is injected into a waveguide which is already transmitting a white light signal, that the white light supercontinuum is backreflected from the input facet more strongly. In addition the results in Figures 3.5.2 (a) and (b) suggest that this phenomenon occurs more strongly for greater pump powers.

An alternate explanation for this may be to consider the fluctuation in the power of the white light supercontinuum. In Figure 3.5.3 (a), a green line has been added, which is the result of subtracting the high power backreflected spectrum shown in Figure 3.4.3 from the low power spectrum. These spectra were taken with the system entirely isolated from the pump signal. While the green comparison spectrum does not exactly mirror the blue *d* spectrum, the similarities are compelling, especially when the *pump only* signal is added to the difference, as is shown by the green line in Figure 3.5.3 (b).

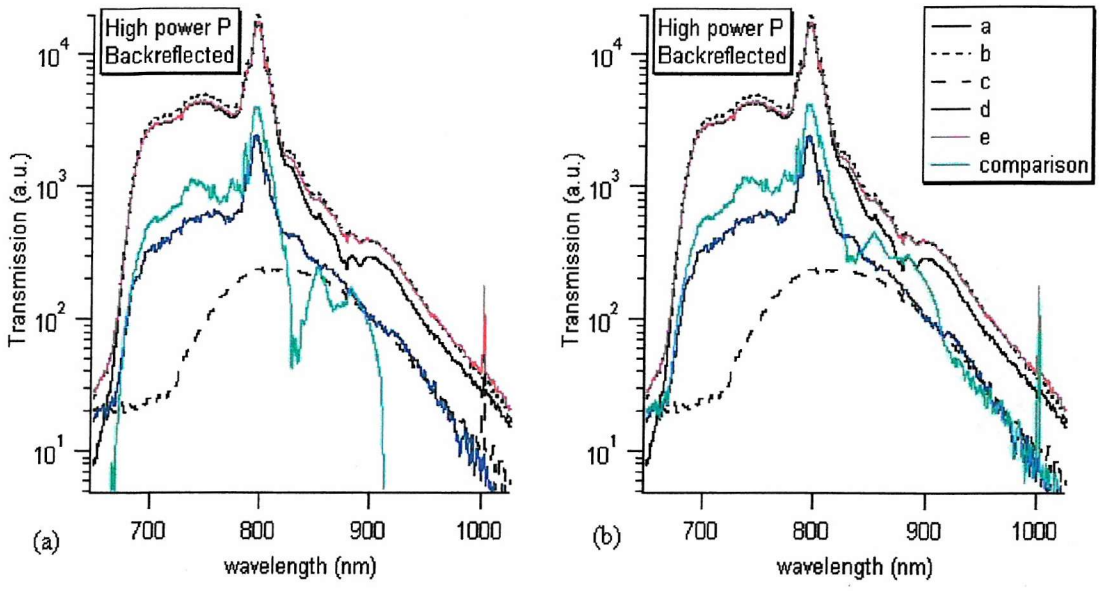

Figure 3.5.3 - Data analysis for backreflected high power transmission spectra for an SRSO waveguide, with the addition of (a) the difference between two backreflected spectra taken without the addition of the pump and (b) the same spectrum but with the pump only spectrum added

The similarity between the green comparison spectrum and the blue difference spectrum shown in Figure 3.5.3 (b) is sufficient to allow the conclusion that the *pump and probe* spectra are the summation of the *pump only* and *probe only* spectra, and that no gain is present in our SRSO system. The reason this is so much more clearly visible in the backreflected spectra than the transmitted, is that in the backreflected spectra the PL resulting from the 514nm pump beam was reduced enough to not swamp the white light data.

3.6 Conclusions

At the start of this chapter a fabrication process for Silicon-Rich Silicon Dioxide (SRSO) was adapted from work carried out by Iacona [2]. This fabrication process permits the deposition of SRSO layers with a refractive index range of 1.55-1.71, a range which increases to 1.53-1.92 after a thermal anneal at 1150°C has been carried out. The change in refractive index is dependent upon the silicon incorporation into the SRSO layer. Layers with a large amount of silicon have an initial refractive index change of approximately 13% while a layer which bore only lightly increased amounts of silicon have a refractive index change of only 3%.

To form photoluminescent silicon nanocrystals, it was necessary to perform a thermal anneal at high temperature. 1150°C was found to be sufficiently hot, and an increase in anneal temperature to 1200°C did not alter the SRSO layer's measurable properties. While a large change in refractive index was perceived after the first 30 minutes anneal, prolonging the anneal beyond this reduced the change in refractive index from the unannealed value by approximately 1%.

Photoluminescence measurements were carried out upon SRSO layers and waveguides. It was found that the intensity of emission from silicon nanocrystals is dependent upon the duration of the thermal anneal. This anneal was shown to have greatest effect on increasing the PL intensity at the short wavelength end of the nanocrystal emission spectrum. The PL spectrum for the silicon nanocrystals was also shown to be dependent upon the silicon incorporation of the layer, with a higher silicon incorporation leading to a lower energy wavelength of peak PL intensity.

Models were presented for SRSO waveguides of types 'A', 'B', and 'C', showing how waveguides of their measured refractive index and thickness would be expected to guide light. Plane wave expansion models were also carried out to illustrate where

the waveguide cutoff would be expected to occur, and a materials model for absorption below 700nm was shown.

Waveguide transmission measurements were carried out, which provided both agreement and contradiction with the calculated transmission spectra. Despite strong absorption below 700nm and above 1300nm, waveguides of luminescent SRSO are efficient waveguides for the near infra-red portion of the electromagnetic spectrum. This is especially pertinent for the 700 – 1100nm portion of the spectrum, in which SRSO generates photoluminescence. The waveguide will, however, reabsorb the higher energy portion of the photoluminescence spectrum as it passes through the material.

While the optical absorption of SRSO is attributed to bandgap absorption in delocalised states of the silicon nanocrystals, the photoluminescence clearly originates from a different mechanism. Photoluminescence is attributed to radiative recombination from interface states between the silicon nanocrystals and the surrounding SiO_2 matrix[3]. While the shift in the wavelength of peak intensity may be considered a result of different cluster size distributions as the silicon incorporation of the SRSO changes, we believe the increase in photoluminescence intensity as a function of anneal time is either due to the continued formation of radiative interface states or to the annealing out of non-radiative recombination pathways associated with defects formed during the amorphous PECVD process. Detailed luminescence lifetime measurements may in future allow this issue to be clarified.

Finally, gain measurements were carried out for a waveguide of type 'B' SRSO which had been annealed for 6 hours, using colinear pump and probe laser beams at both high and low pump powers. Once results had been analysed it was possible to state that the addition of a 514nm pump signal, or increasing the intensity of that pump signal, had no effect upon a white light beam which was travelling in the same

waveguide. This permits us to state that for this SRSO material, there is no optical gain.

In summary, waveguides of luminescent (annealed) and non-luminescent (unannealed) SRSO were fabricated using PECVD. Photoluminescence was measured at wavelengths from 600-1100nm from annealed waveguides, most intensely from those waveguides which had been annealed longest. Unannealed waveguides exhibited good transmission qualities throughout the visible spectrum, while annealed waveguides were absorbing below 700nm. The onset wavelength for this absorption was invariant with changes to the anneal time and silicon incorporation in the waveguide core layer. This demonstrates that waveguides of SRSO exhibit favourable optical properties for the portion of the electromagnetic spectrum in which the core material is photoluminescent. It was also shown that this material does not exhibit any optical gain. This work prepares the way for integrated devices incorporating luminescent SRSO waveguides as a fundamental component, although not as a laser as was originally hoped.

3.7 Publications associated with this chapter

R.T. Neal, M.D.C. Charlton, C.E. Finlayson, M.C. Netti, M.Josey, G.J. Parker. *High Intensity Photoluminescence in Waveguides of Silicon-Rich Silicon dioxide*, Poster Session, Symposium J, 2003 MRS Spring Meeting, San Francisco, CA

R.T. Neal, M.D.C.Charlton, G.J. Parker, C.E. Finlayson, M.C. Netti and J.J. Baumberg. *Ultrabroadband Transmission Measurements on Waveguides of Silicon-Rich Silicon Dioxide*. Applied Physics Letters **83**(22), p4598-4600 (2003)

R.T. Neal, C.E. Finlayson, M.D.C. Charlton, G.J. Parker, J. J. Baumberg, M.C. Netti, M.E. Zoorob, *Ultra-Broadband Spectroscopy of Waveguides of Nanocrystalline Silicon-rich Silica*. Presented in Liverpool to the RSC (2003)

References

[1] L.C. Wang, X.N. Liu, F. Yan, et. al., Applied Physics Letters, **70**(71) p2265-2267 (1997)

[2] F. Iacona, G. Franzò, C. Spinella, Journal of Applied Physics, **87**(3) p1295-1303 (2000)

[3] L. Pavesi, L. Dal Negro, C. Mazzoleni, G. Franzo, F. Priolo, Nature, **408** p440-444 (2000)

[4] J. Valenta, I. Pelant , J. Linnros , Applied Physics Letters, **81**(8) p1396-1398 (2002)

[5] L. Dal Negro, M. Cazzanelli, N. Daldosso, Z. Gaburro, L. Pavesi, Physica E, **16** p297-308 (2003)

[6] M. L. Brongersma, A. Polman, K. S. Min, E. Boer, T. Tambo, Applied Physics Letters, **72**(20) p2577-2579 (1998)

[7] Z. Ma, X. Liao, G. Kong and J. Chu, Appl. Phys. Lett., **75**, 1857 (1999)

[8] A. Ghatak and K. Thygarajan, Introduction to Fibre Optics (Cambridge University Press, Cambridge, 1998)

4 Photonic Crystals

Integrated optical components such as the arrayed waveguide grating introduced in Chapter 1 of this thesis and expanded upon in Chapter 2, provide a reduction in the size of an optical circuit from discrete bulk components such as the fibre Bragg grating. Photonic crystals, also introduced in Chapter 1, permit further reduction in the size of an optical component by several orders of magnitude beyond what is possible with planar integrated optics.

Photonic crystals (PCs) [1] are periodic dielectric structures, which have the ability to restrict propagation of light into discrete energy bands and localise the optical fields to very small volumes of space. Consequently PCs have important applications in controlling the flow of light in optoelectronic devices fabricated on a sub-micron scale [2-5]. PCs have recently been fabricated in luminescent materials such as GaAs[6], and porous silicon[7] in an effort to enhance photoluminescence (PL) extraction efficiency.

As stated in the first chapter of this thesis, while some researchers have explored photonic crystals in light emitting materials such as the InGaAsP system or porous silicon, there had yet to be a study on 2D PCs etched into a waveguide core incorporating luminescent silicon nanocrystals. In this chapter the fabrication, simulation, optical measurements, and properties of 2D photonic crystals fabricated in waveguides of Silicon-Rich Silicon Dioxide (SRSO) containing silicon nanocrystals (Si-nc) is described. We believe this to be the first demonstration of a 2D photonic crystal bandgap in a stable, CMOS process, silicon-compatible luminescent material.

4.1 Photonic Crystal Fabrication

Slab SRSO core layer waveguides were used as the basic structure onto which 2D photonic crystals were patterned. The fabrication of the SRSO waveguides by Plasma Enhanced Chemical Vapour Deposition (PECVD) is discussed in detail in Chapter 3. The structure of a typical waveguide is shown in Figure 4.1.1.

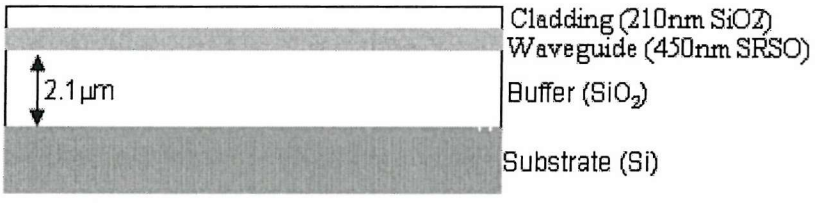

Figure 4.1.1 - Geometry of SRSO waveguides formed as in Chapter 3

Several batches of photonic crystal waveguides were fabricated. The first batch, r2198, was carried out with waveguide cores of type 'A' SRSO which had been annealed at 1150°C for 1 hour. A second batch, r2256, had a slightly thinner core layer of type 'A' SRSO, deposited at half pressure, also annealed for 1 hour. A final photonic crystal batch, k2351, resulted in two patterned waveguides. Wafer k2351#39 had a waveguide core of type 'A' SRSO and k2351#40 had a waveguide core of type 'C' SRSO. Both wafers were annealed for 6 hours at 1150°C.

4.1.1 Creation of a Chrome Mask

Once waveguides had been fabricated, a layer of chrome was evaporated onto the surface of the waveguide by Mr. Richard Bayley. The purpose of this chrome layer was to serve as a mask for the Reactive Ion Etch (RIE) which would be used to drive the photonic crystal pattern through the core layer of the SRSO waveguide. Different chrome thicknesses were tried, from 50nm in batch r2198, to 120nm in r2256. Once the chrome layer had been formed, a layer of photoresist was spun onto the chrome surface. The photoresist used, UV 3.5, is a photoresist optimised for use in electron beam (e-beam) direct write machines.

The e-beam processing stage was carried out by Dr. Martin Charlton for batches r2198 and r2256, using a pattern which he had designed. The precision required for the patterning of very small-pitch photonic crystals was beyond the reach of the e-beam machine in the Southampton University Microelectronics Centre (SUMC). It was therefore decided to send the wafers in batch k2351 for external patterning. The wafers from this batch were sent to QUDOS, a company specialising in e-beam patterning. QUDOS carried out the chrome evaporation, resist spin, and electron beam stages. The pattern used for all photonic crystal wafers consisted of several hundred discrete chips, arranged into rows and columns, with tracks of developed resist clearly separating each numbered chip.

Following the e-beam stages, the pattern which had been drawn into the photo resist was transferred onto the chrome layer. Two methods were used: Ion Beam Milling (IBM), an anisotropic dry etch method; and an isotropic wet Chrome (Cr) etch. The first method, IBM, involves the use of high energy ions to remove all chrome which is not protected by the developed photoresist. Conditions used for the IBM in the Southampton University Microelectronics Cleanroom are detailed in Table 4.1.1.

Base Pressure	V_b (V)	I_b (A)	V_a (V)	I_a (A)	RF Power (W)	I_{neut} (A)	I_{dn} (A)	V_{dn} (V)	Temp (°C)	Tilt (°)	Time (min)
$7x10^{-6}$	390	201	275	20	287	250	268	269	16	0	7

Table 4.1.1 - Ion Beam Milling conditions

Following the IBM stage wafer k2198#2, which had been patterned with a triangular 2D photonic crystal, looked as is shown in Figure 4.1.2. The image shown was taken using the SUMC Scanning Electron Microscope (SEM). In this image, the black circles are holes which have been etched through the chrome layer, and the grey between them is the remaining chrome layer. It was anticipated that use of an anisotropic etch would result in a clearly defined chrome mask with a vertical etch profile.

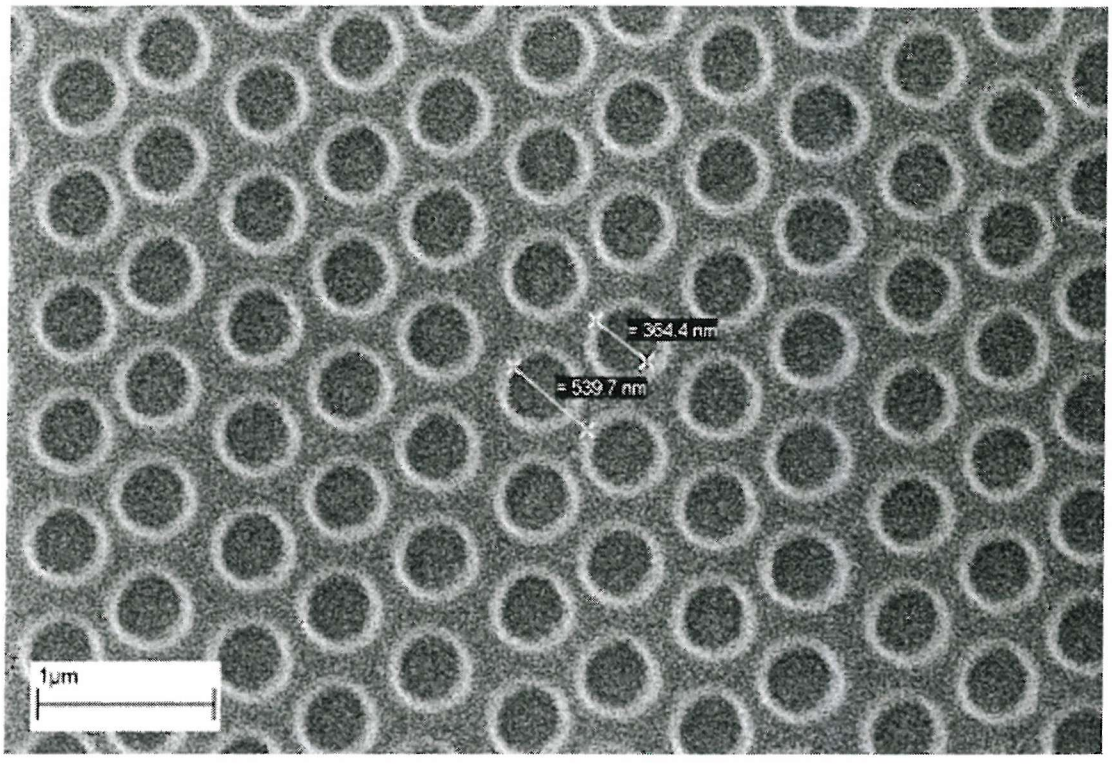

Figure 4.1.2 - SEM image of wafer r2198#2 after the Ion Beam Milling stage

If an IBM stage is carried out with highly increased current, such as wafer r2256#1 by D. Sager in the Optoelectronics Research Centre cleanroom, the result is as shown in Figure 4.1.3.

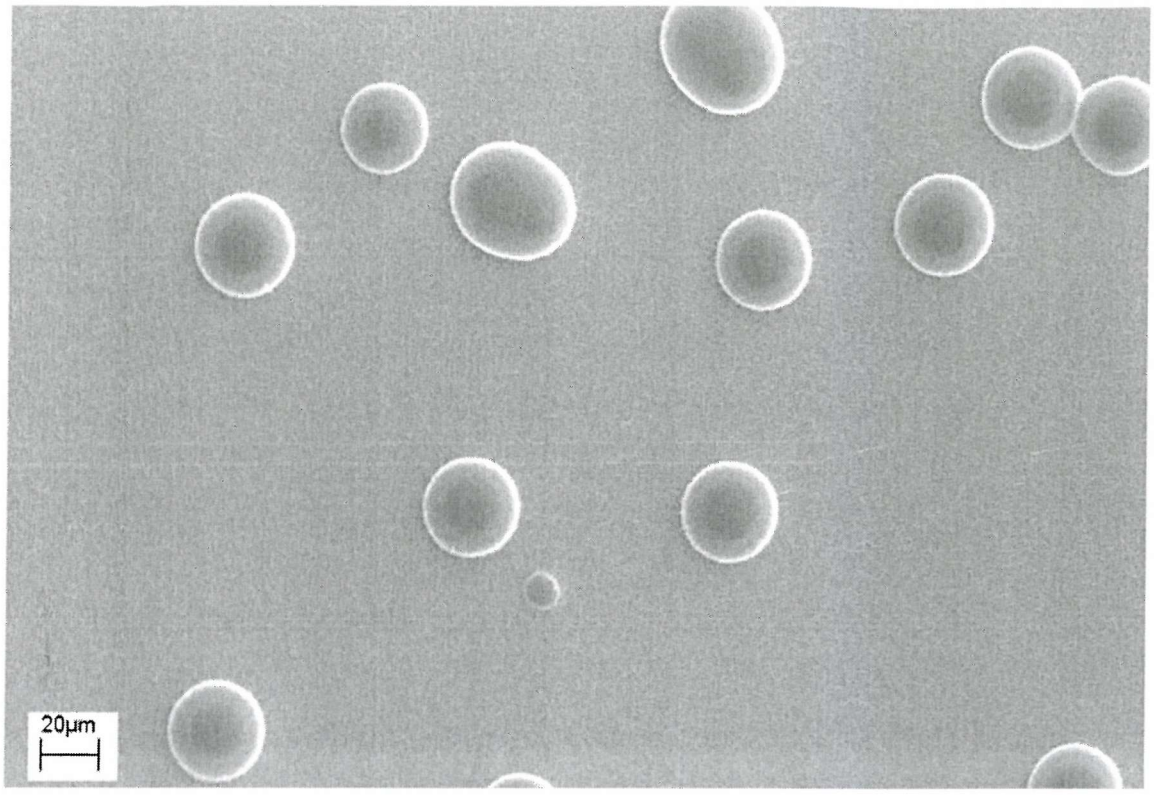

Figure 4.1.3 - The effect of too-high current on an IBM stage

Looking more closely, the extent of the damage may be seen, with the photoresist having separated into fibrous strands, shown in Figure 4.1.4. This is known as *reticulation*. When photoresist has been heated beyond its heat tolerance - normally specified by manufactuers- it then starts to coalesce into the wrinkles shown in Figure 4.1.4. This results in a layer of resist which varies in thickness from twice the intended thickness to almost nothing. For very short dry etches, for which a very thin resist layer may be used, this is not a problem, but beyond that, the photoresist layer may be considered no longer resistant to etching. Wafer r2256#1 was subsequently treated to a reactive ion etch, and the resulting wafer was devoid of all PC features.

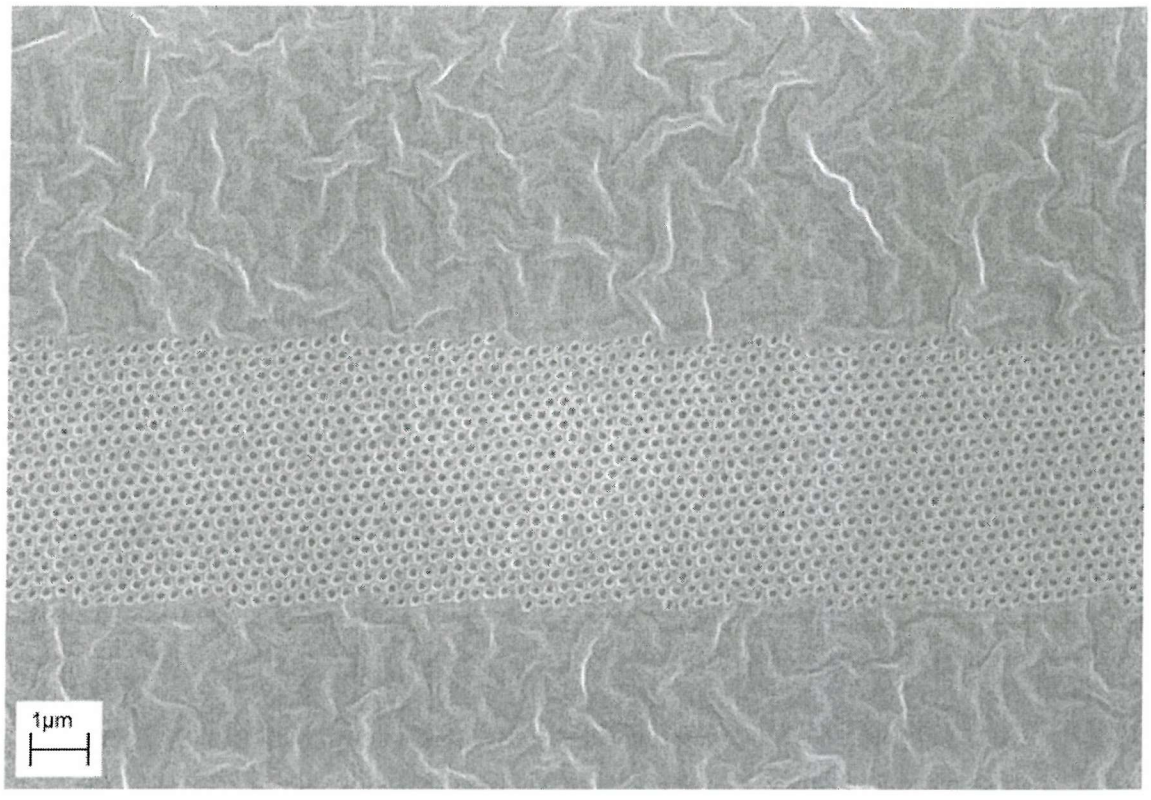

Figure 4.1.4 - Close view of wafer r2256#1, having been burned in an IBM stage

The alternative method for pattern transfer from developed photoresist to the chrome layer was the use of a wet chrome etch lasting approximately one minute. Cr etch is a standard cleanroom etchant containing acetic acid and ceric ammonium nitrate. The completed Cr etch resulted in patterned chrome as is shown in Figure 4.1.5. The black circles are holes which have been etched through the chrome. The dark grey regions around that are the chrome itself, while the lightest grey regions are where photoresist remains.

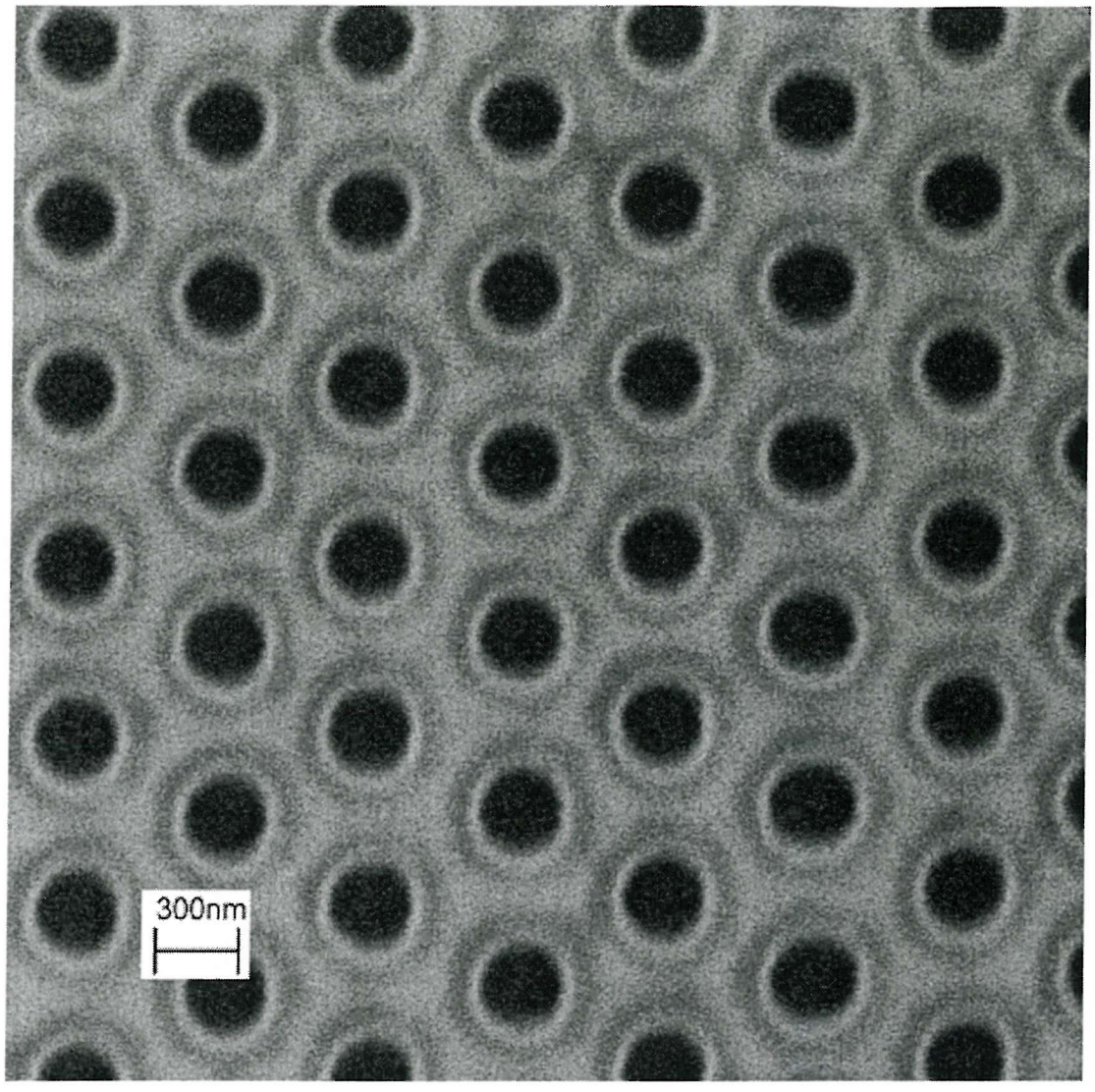

Figure 4.1.5 - SEM image of wafer k2351#39 after 100s wet chrome etch

A nanospectrometer, a piece of apparatus in the clean room usually used for carrying out thickness measurements in standard materials such as silicon dioxide and silicon nitride, was used to determine when the Cr etch was completed. The wafer would be dipped in the acid for a period of time, then cleaned and dried. The nanospectrometer measures thickness by matching reflection fringes to those of known materials. When the reflection fringes from nanospectrometer measurements, carried out upon the 200μm wide scribe lanes separating each individual chip, changed from the highly oscillatory fringes of chrome to that of silicon dioxide, the Cr etch had completely penetrated the mask layer.

It was concluded from the final result, once the dry etch had been carried out, that the wet chrome etch was a much more efficient manner for the transferral of a photonic crystal pattern from developed photoresist to the chrome mask layer than IBM. The resulting holes through the mask layer were clearly defined and no ill effects were observed due to the isotropy of the method.

4.1.2 The Reactive Ion Etch

Once the chrome mask has been created, it is used as the mask for a dry etch (RIE). The reactive gas used was trifluoromethane (CHF_3), with the etch conditions shown below in Table 4.1.2.

Run Pressure (mT)	Gas	Flow Rate (sccm)	Argon Flow rate (sccm)	RF power (W)	DC bias (V)	Etch Time (minutes)
26	CHF_3	12	12	200	420	60

Table 4.1.2 - Etch Conditions for Reactive Ion Etch

In order to measure how deep the etch had driven the holes which would comprise the photonic crystal pattern, a small section of the wafer was cleaved off from the main portion of the wafer. A wet chrome etch lasting five minutes was used to remove any residual chrome mask which had survived the RIE stage. To remove the last traces of chrome, the wafer section was then placed in a plasma asher for 90 minutes.

Once removed from the plasma asher, the sample was placed in a gold sputterer for 3 minutes. The gold film formed along the top surface of the sample was used to dispel the static charge which builds up in an unearthed silicon dioxide sample in a SEM, making it possible to get good quality images. The wafer pattern used in later batches was designed for this purpose, with several chips consisting of ten test devices, with

rows of holes with diameters ranging from several hundred nanometres to less than 100nm.

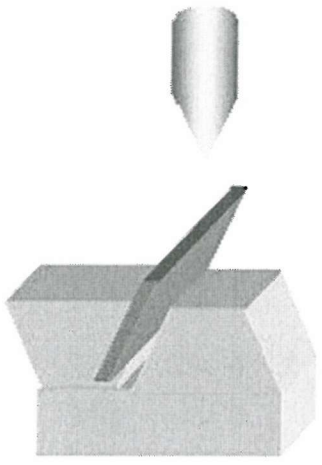

Figure 4.1.6 - Schematic diagram of the SEM angled sample holder

Figure 4.1.7 shows SEM images from k2351#39 after it had been etched by RIE for 30 minutes. The thickness measurements shown are not the true depths, as the sample was measured at an angle as is shown in Figure 4.1.6. For the sample shown in Figure 4.1.7 (a) the true etch depth was 381.6nm, while for the smaller holes in Figure 4.1.7 (b) the true etch depth was only 314.2nm. This depth was not sufficient to perforate the waveguide core layer, and sample k2351#39 was therefore treated with a further 20 minutes RIE.

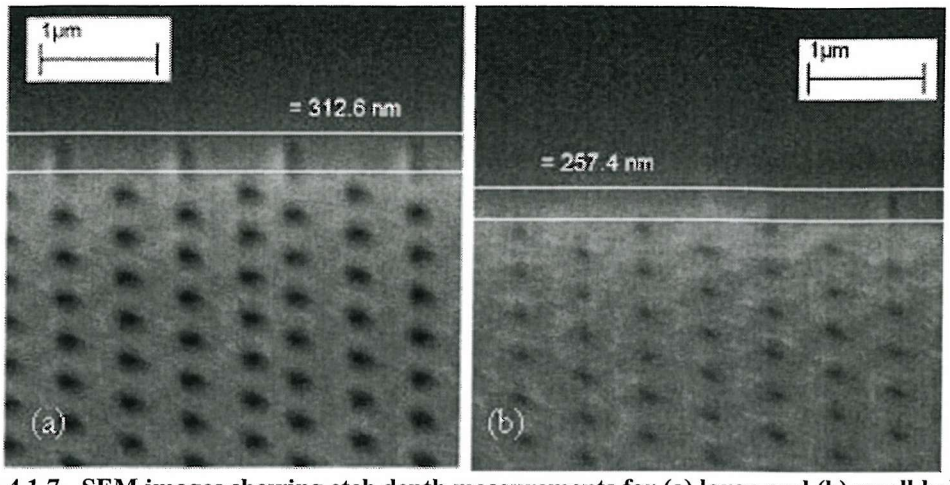

Figure 4.1.7 - SEM images showing etch depth measurements for (a) large and (b) small holes after 30 minutes RIE

After the extra 20 minutes RIE, the true etch depth for holes corresponding to the ones shown in Figure 4.1.7 (a) and (b) are 808.3nm and 722nm respectively. Figure 4.1.8 (a) and (b) show SEM images for each. Figure 4.1.8 (c) shows how for the largest holes of several hundred nm in diameter, the etch depth is over 1.1μm.

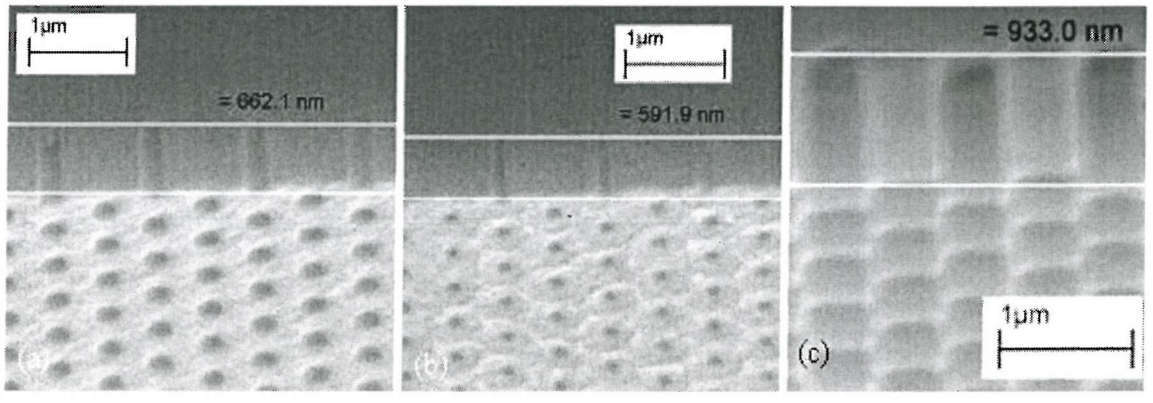

Figure 4.1.8 - SEM images showing etch depth measurements for (a) large, (b) small, and (c) largest holes after 50 minutes RIE

The images shown above were taken from a sample which had been cleaved from the opposite side of the wafer. As with the first measurements, first a chrome etch, then a plasma ash, and finally a layer of sputtered gold was used to ready this sample for SEM depth measurements. A plot of etch depth against hole diameter is shown below in Figure 4.1.9.

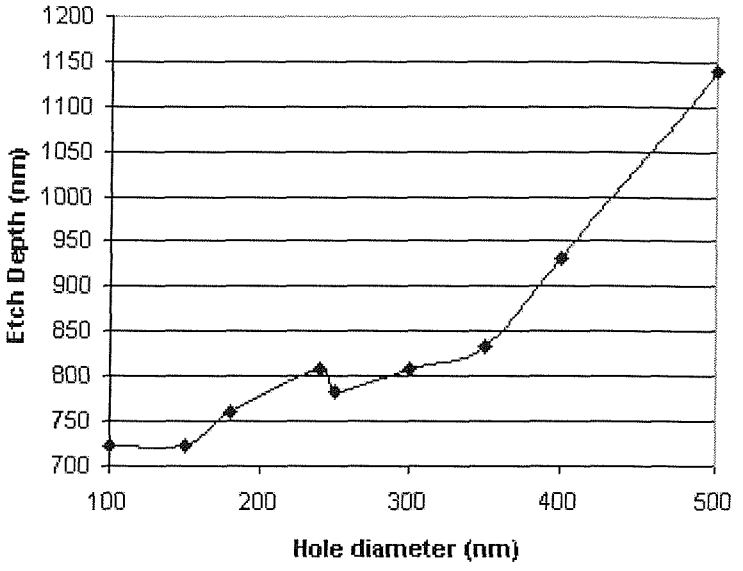

Figure 4.1.9 - RIE Etch Depth plotted against PC hole diameter for k2351#39

Once the etch depth was sufficient at 725nm, the entire wafer was placed first in wet Cr etch and finally in the plasma asher. No gold was sputtered onto the surface of the photonic crystal samples which were to be used for optical measurements. Once the plasma ash had been completed, the wafer was inspected under an optical microscope to determine which devices had been successfully made, and finally the wafer was removed from the cleanroom for cleaving and optical measurements.

4.1.3 Wafer Numbers, Layouts and Chip Designs

Two different designs were used to pattern PCs, designed by Dr. Martin Charlton. Batch r2198 resulted in two successfully fabricated wafers of photonic crystals, wafers #1 and #5, both of the ROTLINES photonic crystal pattern. Batch r2256 was fabricated with SRSO which did not guide light at the photoluminescence wavelengths, and so no useful devices came from that batch. Due to refinements in the process including the wet chrome etch and the use of sputtered gold to assess etch depth by SEM imagery, both wafers #39 and #40 from batch k2351 were successfully fabricated and yielded useful devices both of the PRISMS photonic crystal pattern.

Wafer r2198#5 was the best wafer resulting from early fabrication of photonic crystals. Figure 4.1.10 shows how many chips on the wafer were patterned at all, and

of those, which "good devices" demonstrated regular arrays of holes, with few or no stitching errors resulting from the e-beam stage.

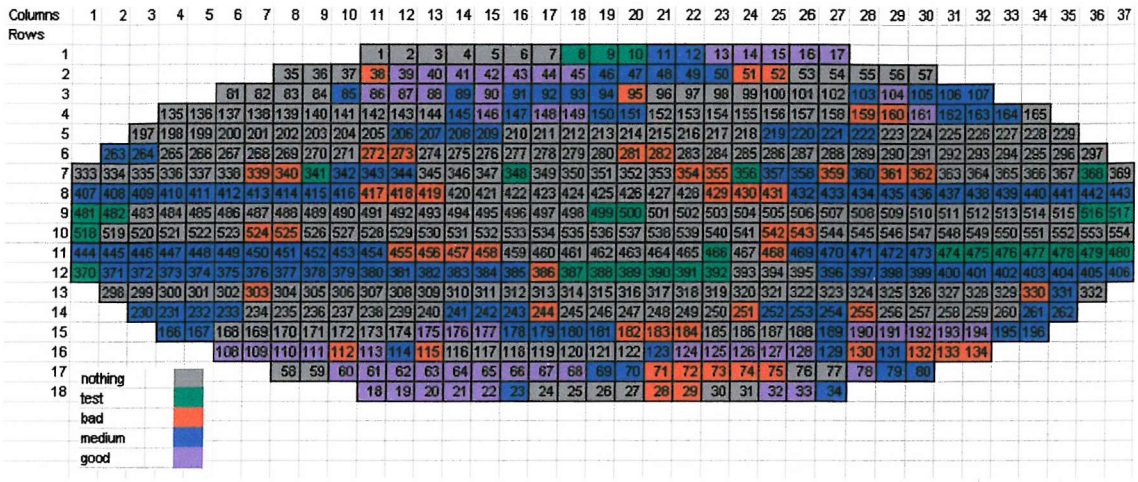

Figure 4.1.10 - Wafer map of r2198#5 showing good, bad and blank devices.

The wafer layouts for ROTLINES and PRISMS are shown in Appendix B.1 and B.2 respectively. These appendices describe the designs with which each individual chip was patterned. For the ROTLINES design each chip was of the standard pattern shown in Figure 4.1.11.

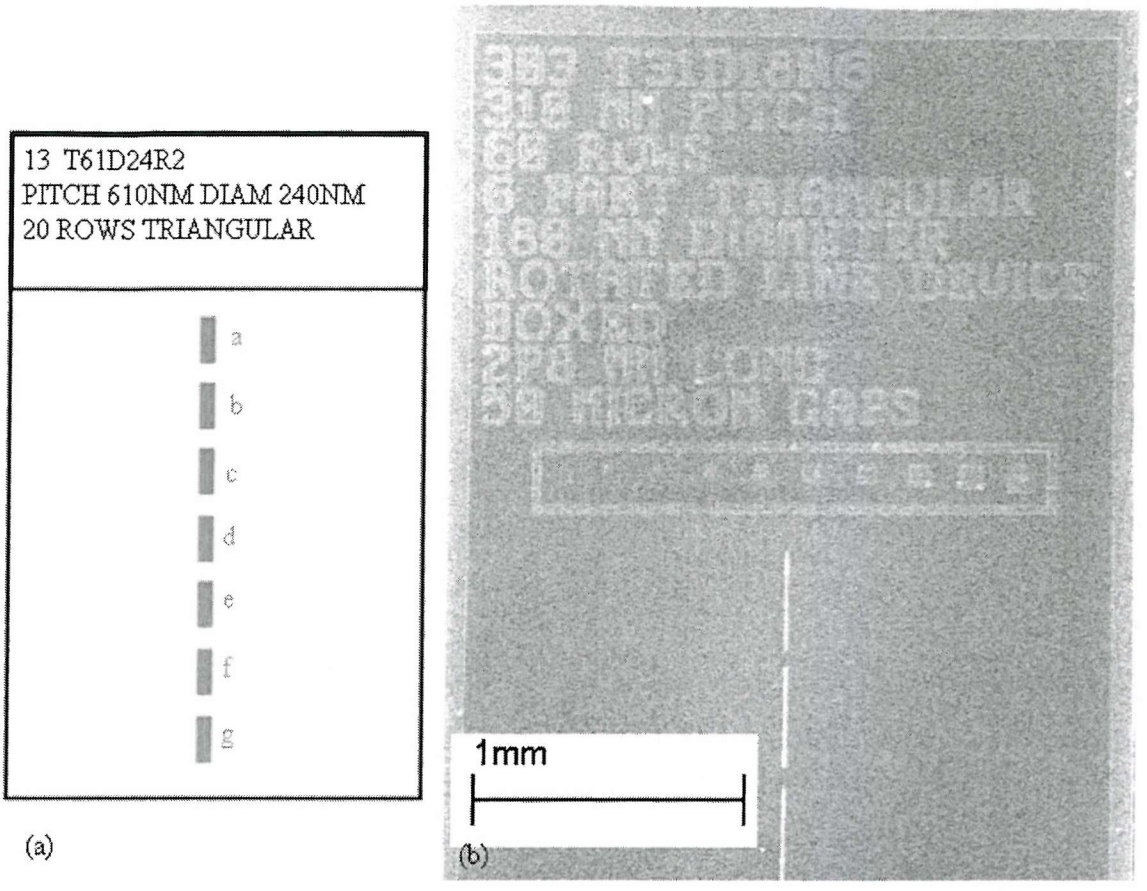

Figure 4.1.11 - Chip design schematic for photonic crystals in the ROTLINES pattern with (b) a SEM image of the same

In Figure 4.1.11 (a) the design schematic for a chip from the ROTLINES photonic crystal pattern is shown, with an SEM image shown in Figure 4.1.11 (b). Everywhere with a black line the RIE had been performed to its full depth. The grey regions labelled from a-g are each separate regions of photonic crystal. The lettering was not part of the chip design, as may be seen from the SEM image. It became convenient to allocate a name to each particular photonic crystal in the pattern, with the convention shown in the diagram. For example the uppermost PC of the row of seven, on the 13th chip of the 5th wafer from batch r2198 would be designated r2198#5_13-a. An SEM image of this specific PC is shown in Figure 4.1.12 below.

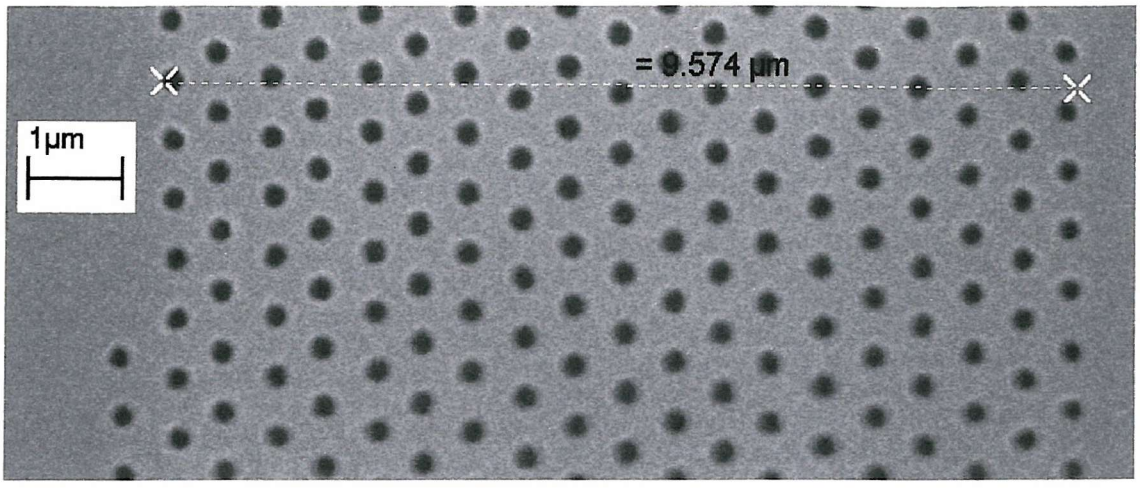

Figure 4.1.12 - SEM image of photonic crystal r2198#5_13-a

PC r2198#5_13-a is oriented so that light passing through it in the direction of the dotted white line is passing along the ΓJ crystal direction. Crystal directions were introduced in Chapter 1. PCs b-g of the same chip feature the same design, but are each rotated 5° from the photonic crystal above. Therefore chip d is rotated 15° from the ΓJ direction, and chip g is rotated a full 30° from the ΓJ direction, making it aligned along the ΓX direction.

	1	2	3	4	5	6	7	8	9	10	11	12	13	14	15	16	17	18
1						1	2	3	4	5	6	7	8					
2				17	18	19	20	21	22	23	24	25	26	27	28			
3												50						
			310	310	310	310	310	310	310	360	360	360	360	360	360	360		
4		69				73		75		77	78	79	80	81		83		
		410	410	410	410	410	410	410	410	410	260	260	260	260	260	260	260	
5		101																
		310	310	310	310	310	310	310	310	310	310	360	360	360	360	360	360	
6	133	134		136	137		139		141	142	143	144	145	146	147			150
	410	410	410	410	410	410	410	410	410	260	260	260	260	260	260	260	260	
7	169	170	171															186
	TEST	360	360	360	360	360	360	360	360	360	360	360	360	410	410	410	410	TEST
8	205	206	207	208	209	210	211	212	213	214								
	260	260	260	260	260	260	260	260	260	260	310	310	310	310	310	310	310	310
9	241	242	243					248	249	250				254		256		258
	410	410	410	410	410	410	410	410	TEST	TEST	410	410	410	410	410	410	410	410
10	259	260	261	262	263	264	265	266	267	268	269	270	271	272			275	276
	260	260	260	260	260	260	260	260	TEST	TEST	260	260	260	260	310	310	310	310
11	223	224	225	226	227	228	229										239	240
	310	310	310	310	360	360	360	360	360	360	360	360	360	360	360	360	410	410
12	187	188	189	190	191	192	193				197		199	200	201	202	203	204
	TEST	410	410	410	410	410	410	410	410	410	410	410	410	410	410	260	260	TEST
13	151	152	153	154	155	156								164	165	166	167	168
	TEST	260	260	260	260	310	310	310	310	310	310	310	310	310	310	310	310	TEST
15		85	86	87	88	89	90	91	92	93	94	95	96	97	98	99	100	
		TEST	TEST	TEST	TEST	TEST	TEST	TEST	TEST	260	260	260	260	260	310	310	TEST	
16			55	56	57										67	68		
			360	360	360	360	360	410	410	410	410	410	410	410	410	410		
17				29	30	31	32		34	35				39	40			
				260	260	260	260	260	260	260	310	310	310	310	310			
18						9	10	11	12	13	14	15	16					
	1	2	3	4	5	6	7	8	9	10	11	12	13	14	15	16	17	18

Figure 4.1.13 - Wafer map of k2351#40 showing good devices

Figure 4.1.13 shows a wafer map of k2351#40, with good devices marked in red. The wafer maps produced also show the pitch size of the photonic crystal samples produced. It may be seen that the larger pitch sizes were more easily fabricated than those with smaller pitch sizes. Almost every PC sample patterned with a lattice pitch of 410nm was successfully developed, while only very few photonic crystal samples with a pitch size of 260nm were produced.

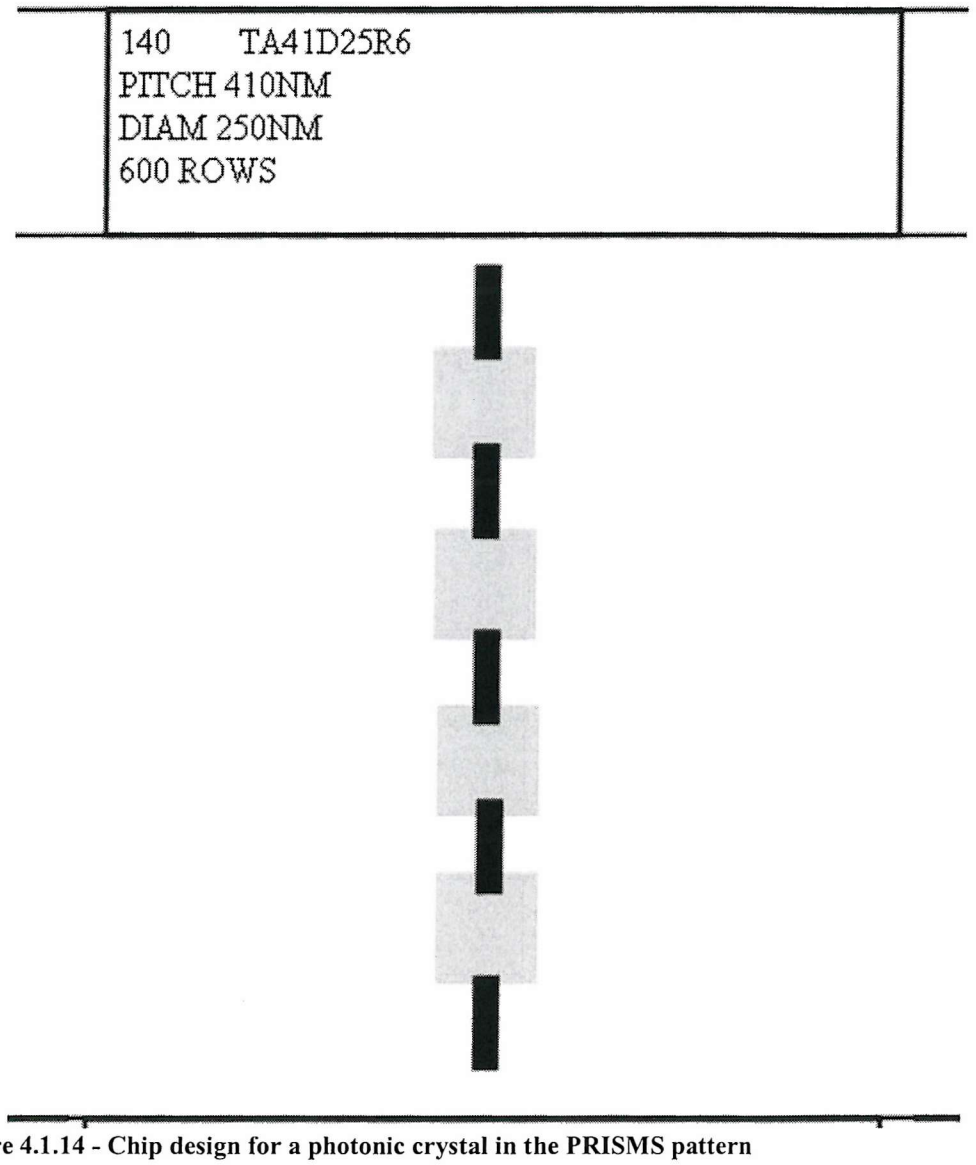

Figure 4.1.14 - Chip design for a photonic crystal in the PRISMS pattern

The schematic for an optical chip from the PRISMS photonic crystal pattern is shown in Figure 4.1.14. As with Figure 4.1.11 (a), every black line was etched through to

the underlying SiO_2 layer, while the grey regions show where photonic crystals were situated. The device shown in Figure 4.1.14 was a 600 row photonic crystal chip. Each of the four photonic crystal regions was oriented along the same crystal direction, not rotated as the ROTLINES photonic crystals were. An entire chip would be patterned with photonic crystals aligned in the ΓJ direction (direction '0') or in the ΓX direction (direction '1'). A new feature of the PRISMS photonic crystal pattern was the trenches etched through the waveguide layer between each photonic crystal region. This barrier was to prevent leakage of light through the waveguide around the photonic crystal.

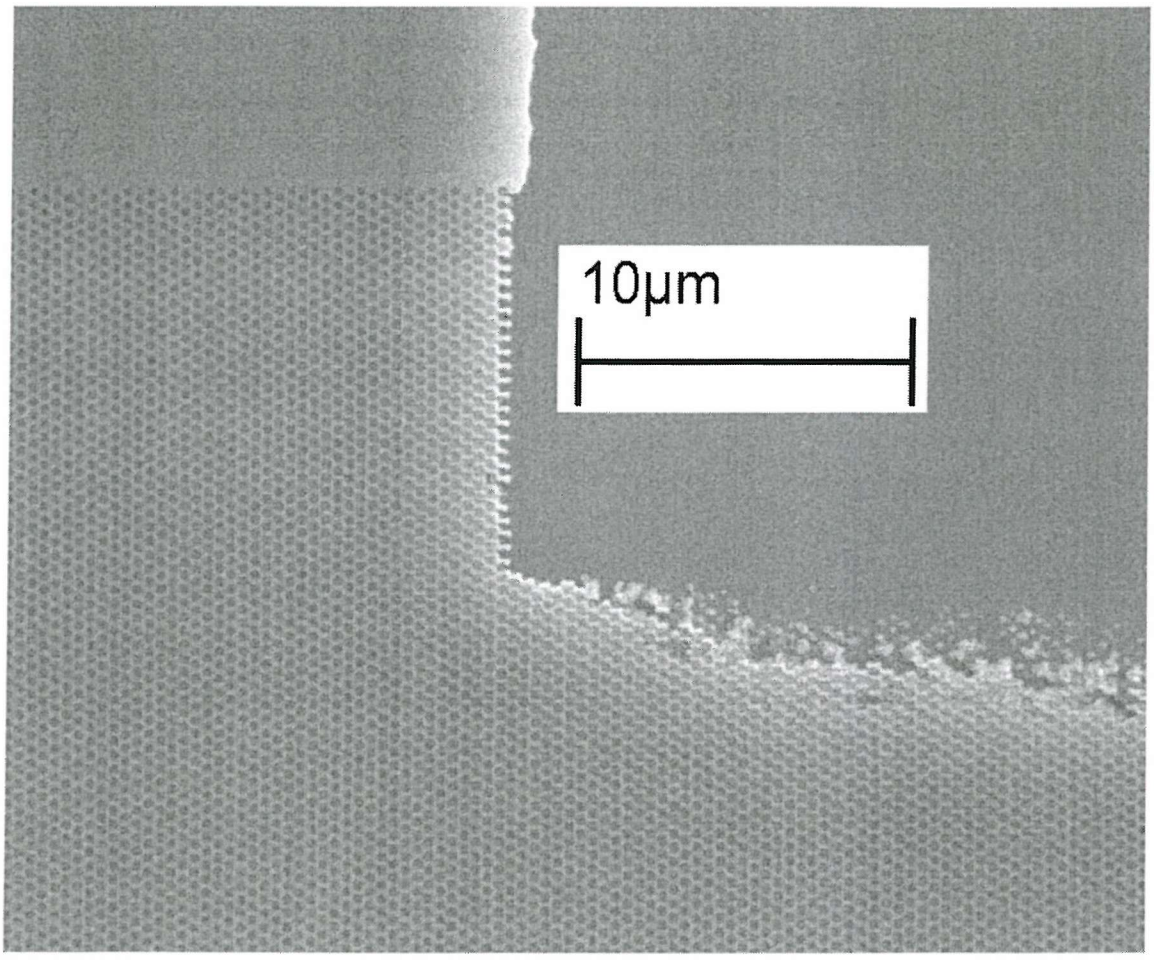

Figure 4.1.15 - SEM image of photonic crystal k2351#39_140

An example of a larger-pitch device which was successfully developed is sample k2351#39_140, an SEM of which is shown in Figure 4.1.15. The deeply etched

trench is shown in the top right corner, as is the photonic crystal itself, and the surrounding waveguide region in the top left corner. A SEM image on this scale is also a very good illustration of the quality of the patterning. There were much fewer stitching errors than there had been for photonic crystals fabricated in batch r2198. The photonic crystal sample shown here is a 600 row photonic crystal with a lattice pitch of 410nm and a hole diameter of 250nm., and is aligned so that light passing through it at right angles to the etched trenches will travel along the ΓJ direction.

4.1.4 Light Injection and Optical Facet Quality

The method used for the first fabricated photonic crystal wafers (batch r2198), to separate photonic crystals from each other was mechanical sawing. Vertical lines were sawn along the side of each chip, and horizontally across every third chip, leaving a chip consisting of three different PC designs, as is shown in Figure 4.1.16 (a). The half-sawed wafer was then separated along the saw lines. This was a good procedure as SRSO was found to be a very tough material, difficult to cleave.

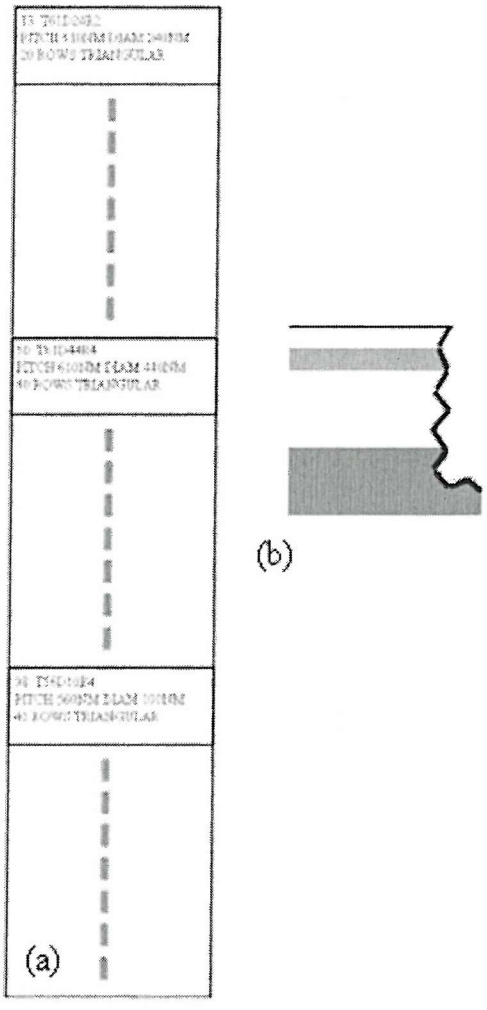

Figure 4.1.16 - (a) schematic layout of a sawn ROTLINES triple sample (b) showing the damage to the waveguide facet caused by sawing.

The disadvantage of the partial sawing method was that the saw damaged the waveguide core itself, leaving a shattered facet (shown in Figure 4.1.16(b)) into which it was difficult to efficiently inject light. To improve this, mechanical polishing was attempted, with the whole side of the waveguide being ground back beyond the region which was saw-damaged.

The sample to be polished was placed between two pieces of perspex glass, held with resin. This was to prevent snapping of the slender sample during polishing. Once the assembly had set rigidly, the whole structure was mounted in a polishing rig, and suspended with the jagged facet facing down as shown in Figure 4.1.17. The sample was then ground back beyond the jagged region, and then polished smooth. The assembly was then dismounted from the polishing rig, and heated to separate the photonic crystal sample and the protective perspex glass. The whole process was repeated for the opposite facet. Polishing in this way was found to improve the efficiency of light injection into the core layer of the waveguide.

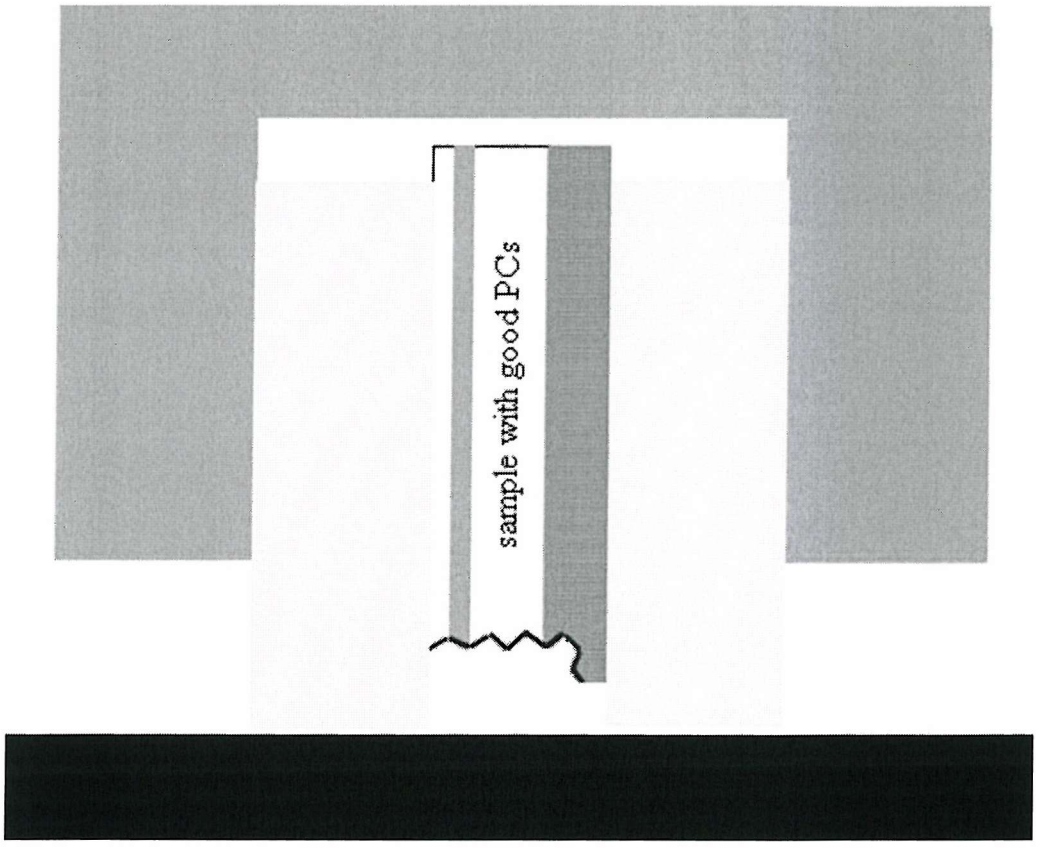

Figure 4.1.17 - A diagram illustrating the polishing process for improving the quality of the waveguide facet

It was shown that cleaving by an expert hand was preferable to mechanical polishing of every good device to be tested optically. Manual cleaving without prior sawing provided a better facet into which to launch light and was also a much simpler

operation. The polishing process might take a full day's labour for only two samples. Any attempt to speed this by polishing several samples together in a sandwich arrangement proved unsuccessful. For the last-fabricated devices, both wafer k2351#39 and k2351#40 were cleaved professionally at LUMIS, an American company specialising in this process. This unsurprisingly provided the best optical facet, though at far greater expense.

4.1.5 SEM Images of Photonic Crystals

Photonic crystals to be patterned with small pitch sizes were found to be more difficult to successfully write and etch than those with larger pitch size. Figure 4.1.18 shows a SEM image of photonic crystal r2198#5_13-a. This PC sample was patterned with a lattice pitch of 610nm and a hole diameter of 240nm. As was shown in Figure 4.1.12, r2198#5_13 was fabricated successfully, resulting in 20 evenly spaced rows of well-defined circular holes of the predicted size.

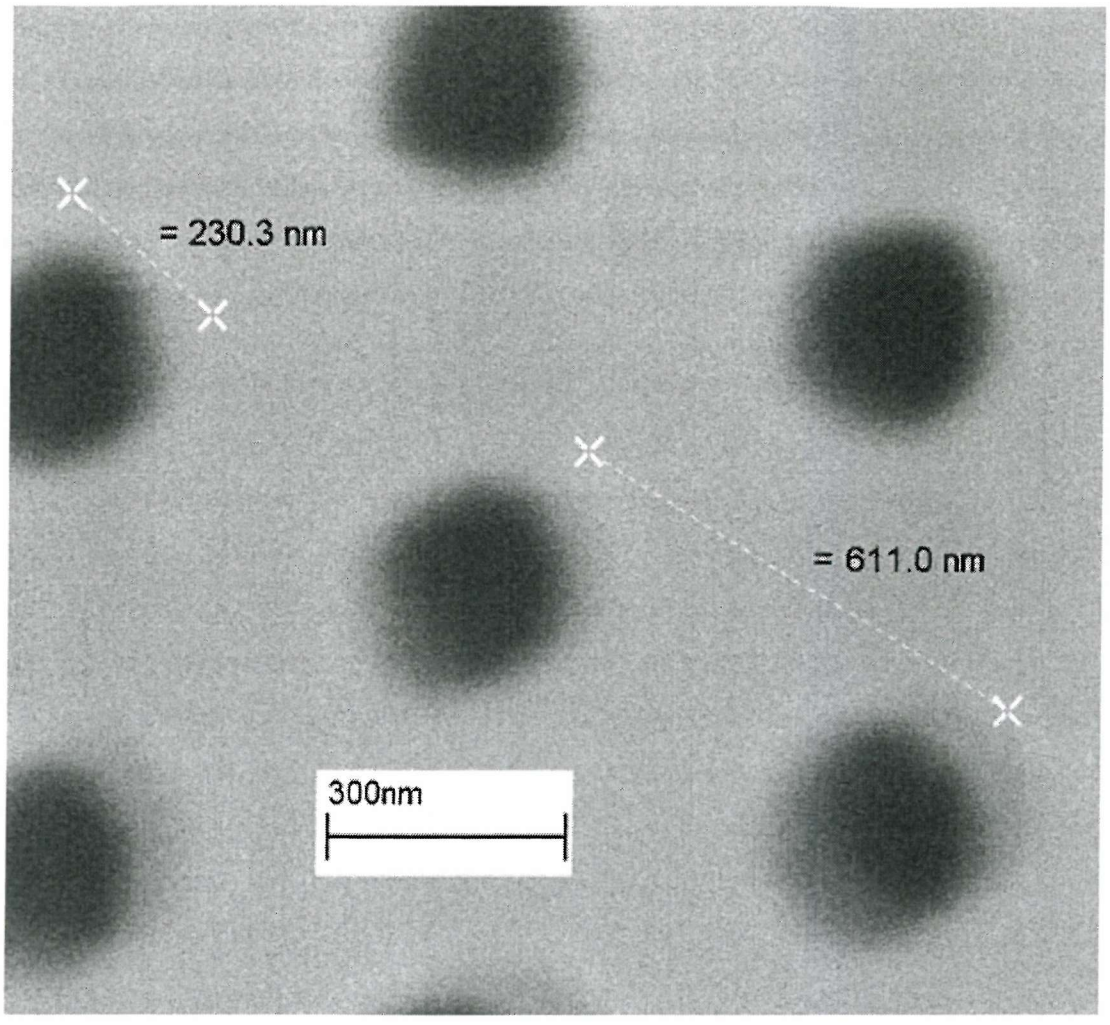

Figure 4.1.18 - Magnified view of photonic crystal r2198#5_13-a: lattice pitch 610nm, hole diameter 240nm

While large-pitch photonic crystals were easily fabricated, when the pitch size was decreased from 610nm to 360nm the same quality of the photonic crystal was more difficult to attain. Figure 4.1.19 shows device r2198#5_262-c. This photonic crystal was designed with a hole diameter of 180nm, and as is shown in the inset, this was far exceeded. The regularity of the holes and their spacing was also much less even than for the larger-pitch devices.

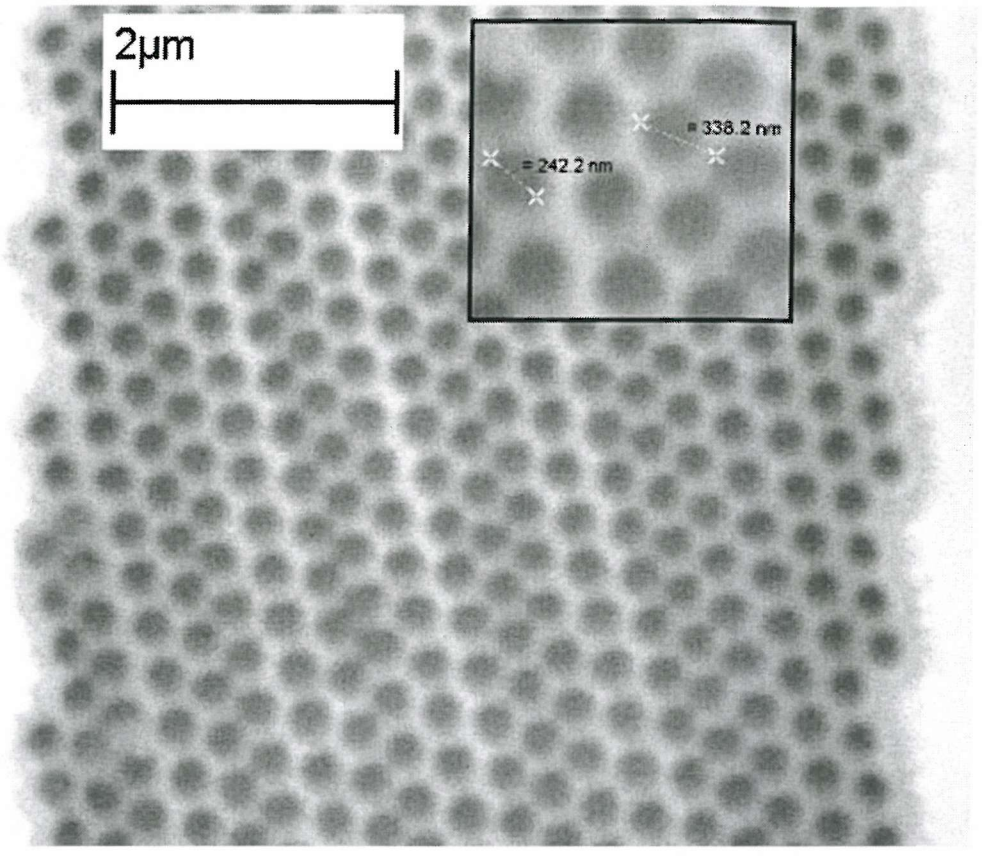

Figure 4.1.19 - Photonic crystal r2198#5_262-c: lattice pitch 360nm, desired hole diameter 180nm

The SEM image in Figure 4.1.20 illustrates how a typical small-pitch photonic crystal fabricated with the ROTLINES pattern was markedly inferior to the larger-pitch devices on the same wafer. This sample, r2198#5_303-a, was patterned with a lattice pitch of 310nm and a hole diameter of 180nm. The hole diameter over the 60 rows of the device was uneven, and there were errors in the writing of the lattice itself, with holes in separate rows merging into each other. However, despite the irregularity over the entire structure, the majority of the successfully fabricated holes were found to have a 180nm diameter and were placed in a 310nm pitch lattice.

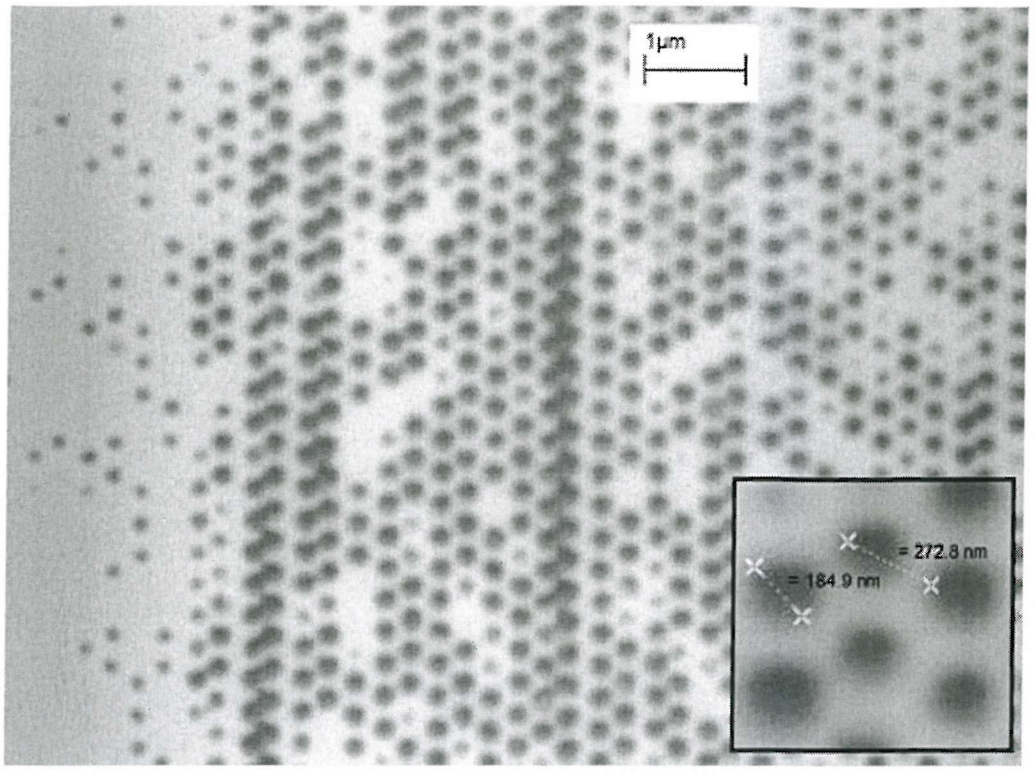

Figure 4.1.20 - A failed small-pitch photonic crystal device

Once the full process for the development of PCs had been decided upon, many photonic crystal samples with lattice pitch sizes of as little as 260nm were successfully fabricated. Sample k2351#40_33 is a good example of the uniformity and lack of stitching errors possible with a well-refined process. An SEM image of this PC sample is shown in Figure 4.1.21.

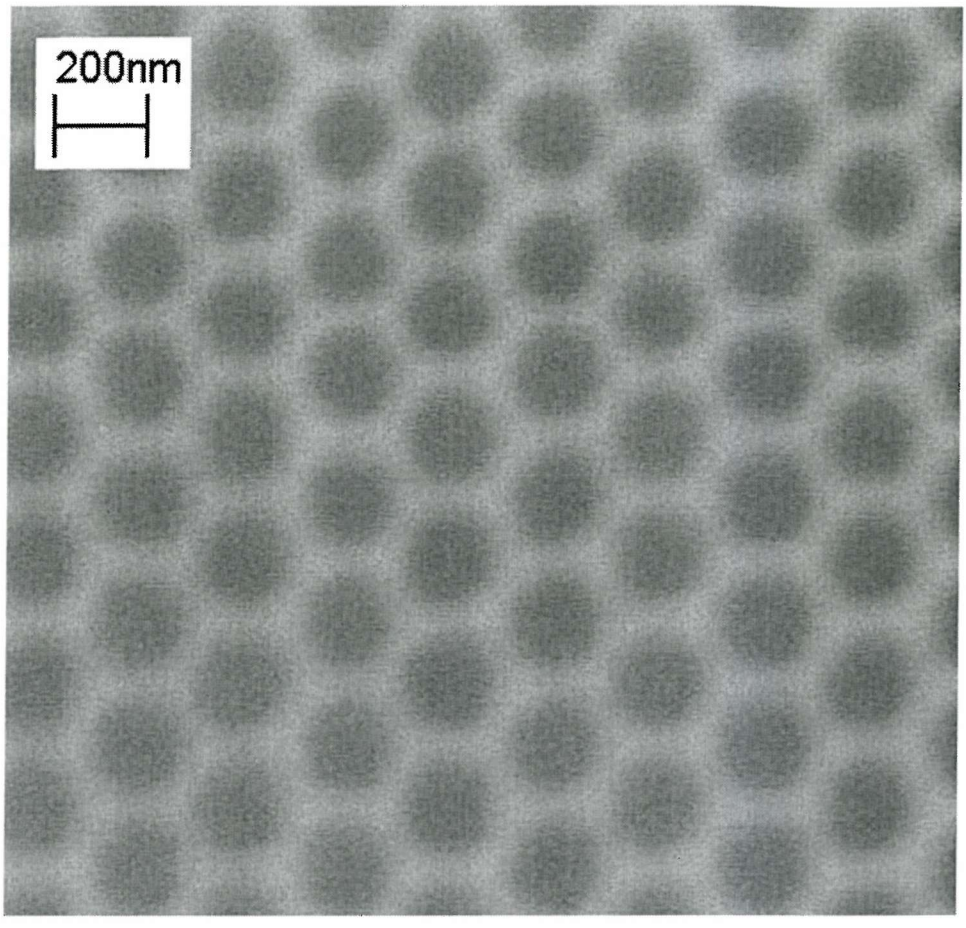

Figure 4.1.21 - k2351#40_33 a successfully produced photonic crystal with a pitch size of 260nm and a hole diameter of 160nm

With the last-fabricated devices, it was not the e-beam which limited the yield of good devices from a wafer. Wrinkles formed in the photoresist left shadows on some completed devices, such as the error shown in Figure 4.1.22 for PC device k2351#40_53, with a pitch of 360nm and a hole diameter of 210nm.

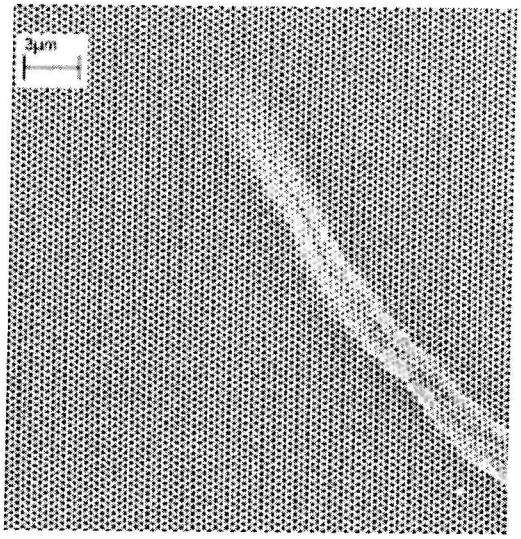

Figure 4.1.22 - k2351#40_53 a photonic crystal device made with a pitch size of 360nm and a hole diameter of 210nm showing a shadow from a wrinkle in the resist

4.2 Measurement

The previous section discusses the patterning of slab waveguides with an SRSO core layer with 2D photonic crystals. In this section, the measurement techniques used to evaluate the effect of these photonic crystals on waveguided photoluminescence are discussed and results presented.

4.2.1 Experimental Setup for photonic crystal measurements

The experimental setup used to measure the effect of incorporating a photonic crystal into a waveguide structure was similar to the setup used for measuring guided photoluminescence in SRSO waveguides (shown in Figure 3.3.4 in the preceding chapter). Unlike the setup used for waveguide full-spectrum transmission measurements, the setup for PC waveguide measurements (shown in Figure 4.2.1) only required the green 514nm line of an argon ion laser, and also required that only one facet of the SRSO waveguide be aligned with a microscope objective. The reduction in the complexity of the setup considerably reduced the difficulty of taking the results presented in the next section compared with white light transmission spectra.

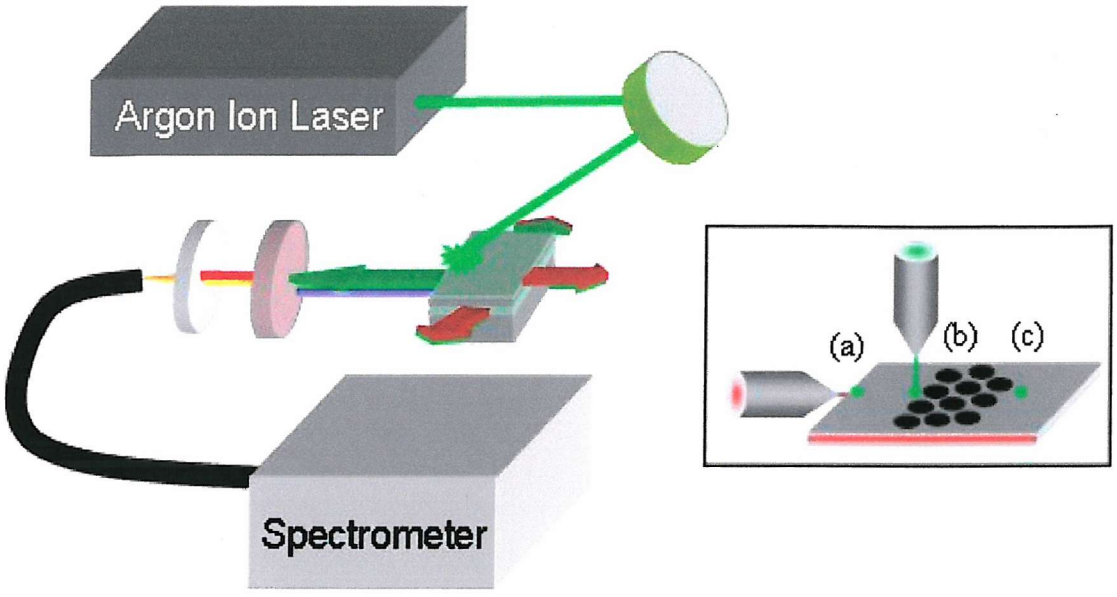

Figure 4.2.1 - Experimental setup for photonic crystal transmission measurements

As with the SRSO waveguide transmission measurements, a 30mW beam from an Argon ion laser (λ=514nm) was focused into a spot of approximately 20μm diameter and used to photo-excite the SRSO. The resulting PL was collected at the edge of the waveguide and collimated using a 90x microscope objective. This light was then linearly polarised to allow independent detection of both the TE and TM waveguide modes and then coupled into a spectrometer. A nitrogen-cooled Si CCD detector was used, which gave a spectral resolution of 0.1nm up to the cut off wavelength of 1.1μm.

To measure the effect of the photonic crystal on the waveguided photoluminescence (PL), a ratio of intensities as a function of wavelength was taken comparing the emission for different positions of the excitation spot relative to the photonic crystal. The inset in Figure 4.2.1 shows the three positions on the photonic crystal waveguide sample onto which the spot of the Argon Ion laser was focused. The first, position *a* provided a reference PL signal. Positions *b* and *c* were at either side of the photonic crystal region, and it is the spectra from excitation spots at these points from which

the ratio of intensities is derived. All emitted photoluminescence was collected from the facet at position *a*.

4.2.2 Results Demonstrating Higher-Order Photonic Bandgaps

Figure 4.2.2 (a) shows the absorption of the unpatterned SRSO waveguide in contrast with the unmodified PL emerging *normally* from the layer. It can clearly be seen from the overlap between the photoluminescence and absorption spectra that light emitted from the SRSO suffers significant re-absorption of the shorter wavelength end of the spectrum from the SRSO as it passes through the waveguide. The reduced transmission below 800nm is caused by absorption from the Si nanocrystals in the silica matrix. PL from the nanocrystals continues up to ~1200nm, but is not detected by the Si-CCD used here.

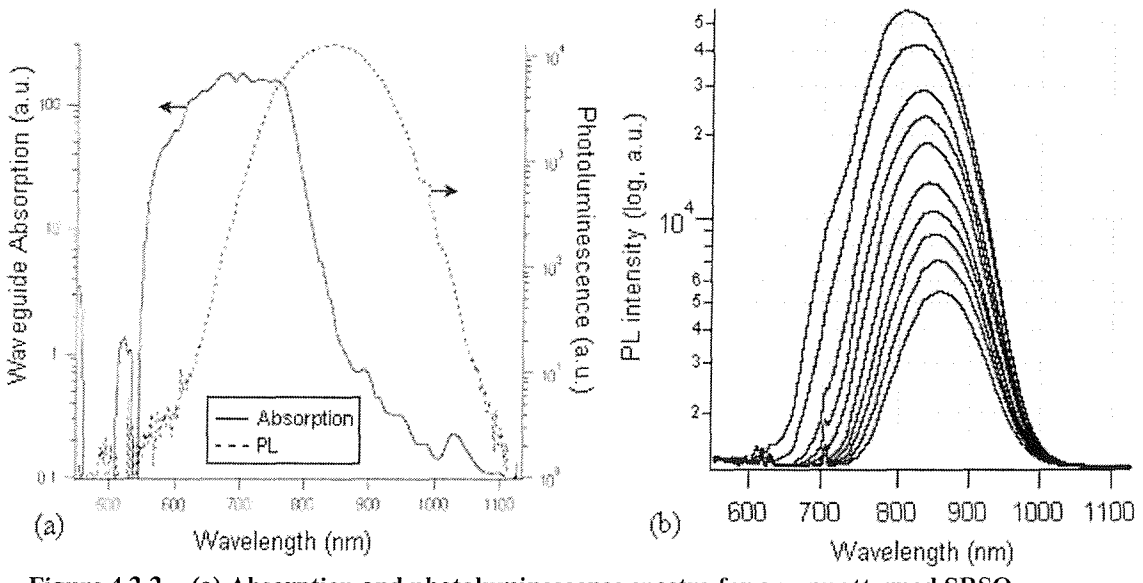

Figure 4.2.2 - (a) Absorption and photoluminescence spectra for an unpatterned SRSO waveguide and (b) spectra illustrating how waveguide absorption affects the emitted photoluminescence as the excitation spot is moved further from the facet

The photoluminescence spectra which result from progressively moving the excitation spot further from the measurement facet is shown in Figure 4.2.2 (b). The effect of a photonic crystal upon the luminescence of the SRSO is shown in Figure 4.2.4 below, and may be recognized directly by comparing PL transmitted from an

excitation spot 20μm before the near side of the PC (Figure 4.2.2 b), with the spectrum which has passed through the PC from an excitation spot 20μm beyond the far side (Figure 4.2.2c).

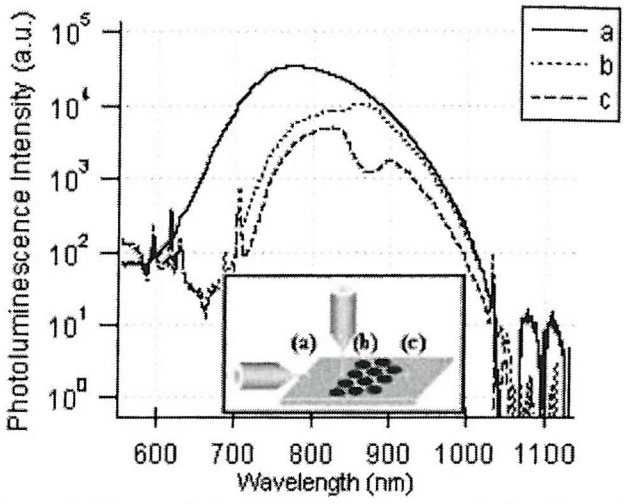

Figure 4.2.3 - Photonic crystal transmission spectra as measured. Spectrum (a) is a reference signal while spectra (b) and (c) show photoluminescence on the near and far sides of the photonic crystal region respectively.

The waveguided photoluminescence is referenced to the PL measured with an excitation spot at the edge of the waveguide (Figure 4.2.2a), and is unaffected by waveguide absorption. The peak in (b) from 850-900nm is a result of light with a wavelength lying within the photonic band gap being efficiently reflected back from the photonic crystal, thus increasing the collected PL intensity. In contrast, the corresponding dip in (c) over the same wavelength range arises from light within the photonic band gap being rejected by the photonic crystal. The reflectivity coefficient (A) and extinction coefficient (α) for the bandgap wavelengths was determined using the formulae shown below:

$$I = I_0 e^{-\alpha d}$$

$$\frac{I}{I_0} = 10^{-A} = 0.6 \qquad (4.1)$$

I is the light intensity measured from excitation at spot b, I_0 is the light intensity at the same wavelength measured from excitation at spot c, and d is the width of the photonic crystal region. Using the experimental data presented in Figure 4.2.3, it was

determined that the reflectivity coefficient was approximately 40%, giving an extinction coefficient of 41.8cm^{-1} for 20 rows, at a thickness of 12.2μm. The contributive effects of the photonic-crystal reflection to the observed bandgap make this an excellent technique for perceiving weaker bandgap features.

Measurements for 20-row photonic crystals with 610nm lattice pitch were carried out for hole diameters of 240, 250, and 280nm, with filling fractions of 0.14, 0.15, and 0.19 respectively. The samples used were r2198#5-13, 14, and 15, further details of which may be found in Appendix B. As was described in Section 4.1.3, photonic crystals were fabricated with varying orientations to the incident light, from the ΓX to the ΓJ direction, incremented in 5° steps. This range covers all angles in the reduced Brillouin zone, which was introduced in Chapter 1 of this thesis. The wavelengths of the measured photonic bandgaps can be deduced from the ratio of the photoluminescence intensity passing through the photonic crystal to that which has not, such as curves b and c in Figure 4.2.3.

Transmission results for sample r2198#5_13, twenty-row photonic crystals with a lattice pitch of 610nm and a hole diameter of 240nm, are shown in Figure 4.2.4. Both Transverse Electric (TE) and Transverse Magnetic (TM) polarisations are shown. For comparison, transmission spectra for unpatterned waveguides for both the TE and TM polarisations were shown in Figure 3.3.8.

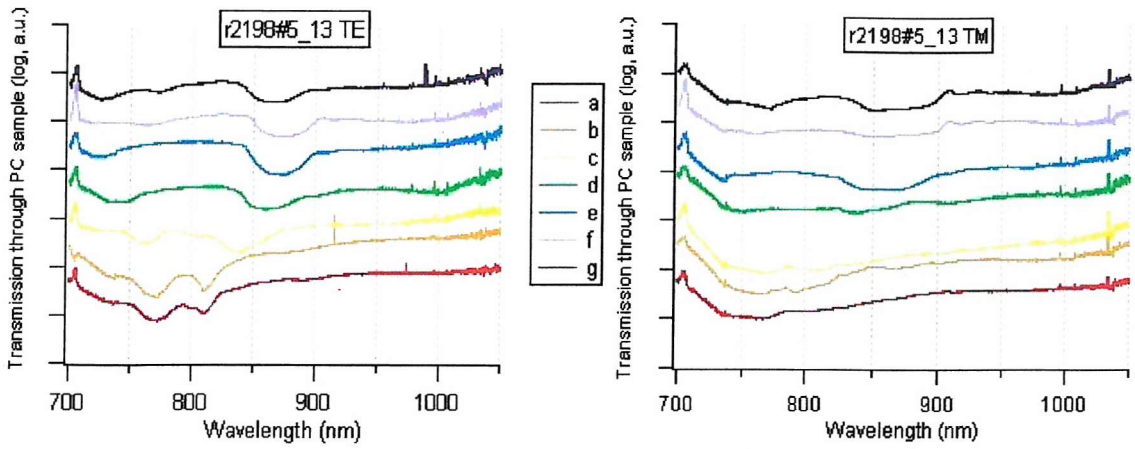

Figure 4.2.4 - TE (left) and TM (right) polarisation transmission measurements for photonic crystal sample r2198#5_13, lattice pitch 610nm, diameter 240nm. In the legend a-g refer to rotations from 0-30° in 5° increments, as described in Section 4.1.3.

Measurements from samples r2198#5_14 and r2198#5_15 showed the effect of increasing the hole diameter to 250 and 280nm respectively upon the transmission spectra. The TE and TM polarisation spectra for samples 14 and 15 are shown in Figure 4.2.5 and Figure 4.2.6 respectively.

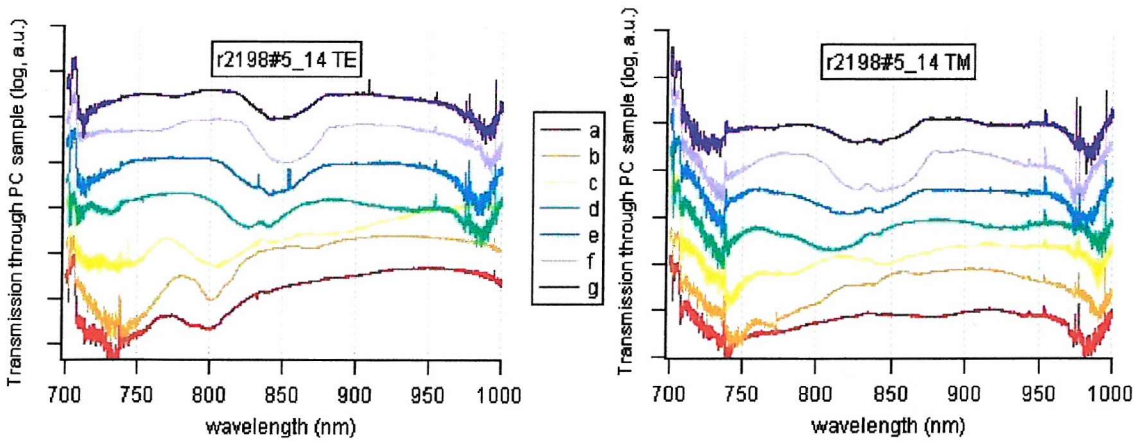

Figure 4.2.5 - TE (left) and TM (right) polarisation transmission measurements for photonic crystal sample r2198#5_14, lattice pitch 610nm, diameter 250nm.

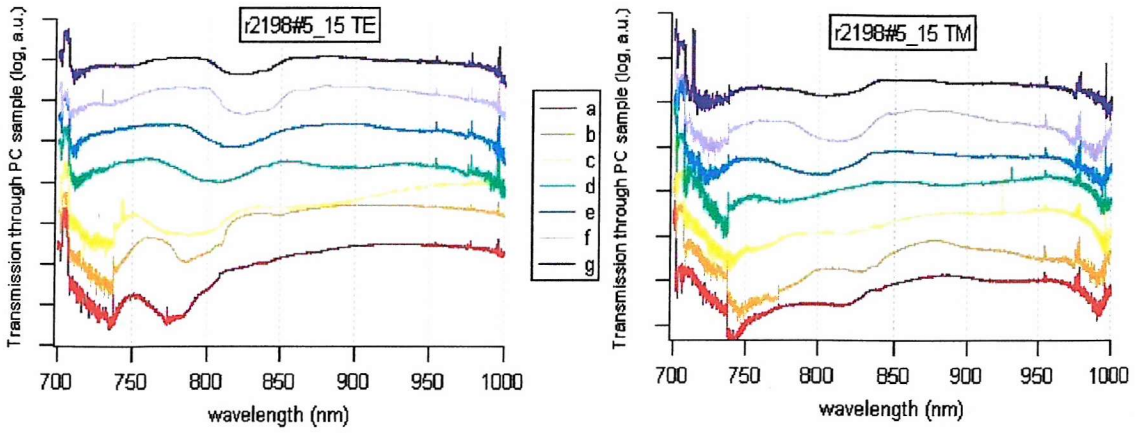

Figure 4.2.6 - TE (left) and TM (right) polarisation transmission measurements for photonic crystal sample r2198#5_15, lattice pitch 610nm, diameter 280nm.

Further measurements were carried out on photonic crystal samples with twice the number of rows: sample r2198#5_41. Sample r2198#5_41 had a pitch of 610nm and a diameter of 280nm, but had 40 rows - twice the number of rows in sample r2198#5_15. Transmission measurements for sample r2198#5_41 are presented in Figure 4.2.7 below.

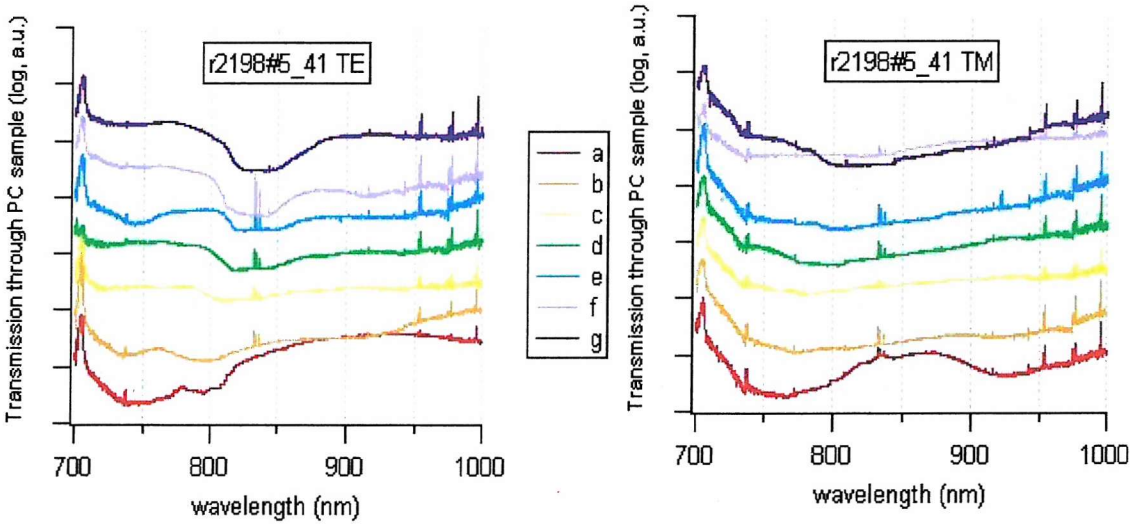

Figure 4.2.7 - TE (left) and TM (right) polarisation transmission measurements for photonic crystal sample r2198#5_41, a duplicate of r2198#5_15 but with twice the number of rows

In addition to the 610nm lattice pitch devices which are presented in Figures 4.2.4 - 4.2.7, transmission measurements were carried out on r2198#5_86, a device with a lattice pitch of 560nm and a hole diameter of 250nm, the same hole diameter as

r2198#5_14. The TE and TM transmission spectra for this device are shown in Figure 4.2.8 below.

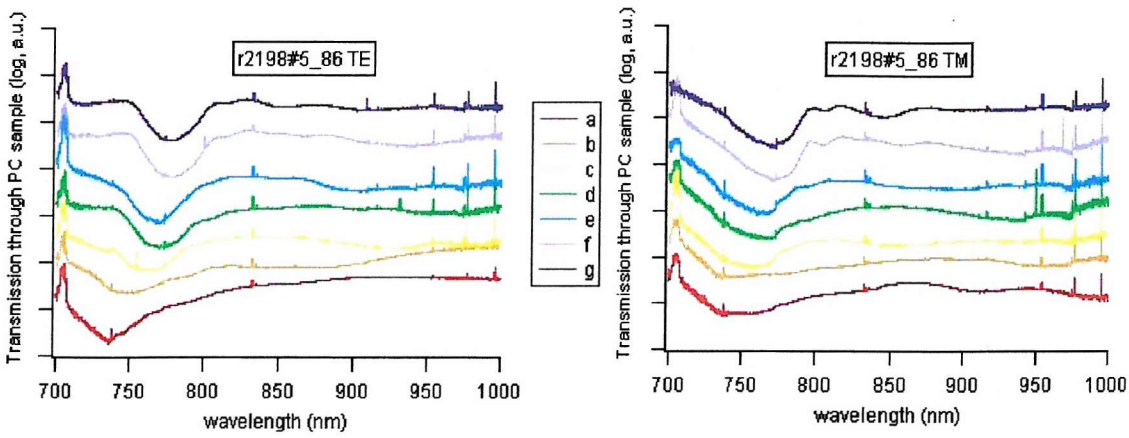

Figure 4.2.8 - TE (left) and TM (right) polarisation transmission measurements for photonic crystal sample r2198#5_86, lattice pitch 560nm, diameter 250nm.

Each of these sets of transmission spectra show how the photonic bandgaps are shifted as the direction light follows as it traverses the photonic crystal is rotated from the ΓJ direction (a, red) to the ΓX direction (g, violet).

4.2.3 Analysis of Higher-Order Photonic Bandgap Results

If the results in Section 4.2.1 are rearranged from the standard format used in Figures 4.2.4 - 4.2.8, the effect of changes in the diameter of the holes which make up the photonic crystal becomes clearer. Samples r2198#5_13, 14 and 15 were all 20-row PC devices fabricated with lattice pitches of 610nm, but had hole diameters of 240nm, 250nm, and 280nm respectively. Figure 4.2.9 and Figure 4.2.10 show the TE and TM polarised transmission spectra for all three samples with the same crystal directions placed upon the same graph.

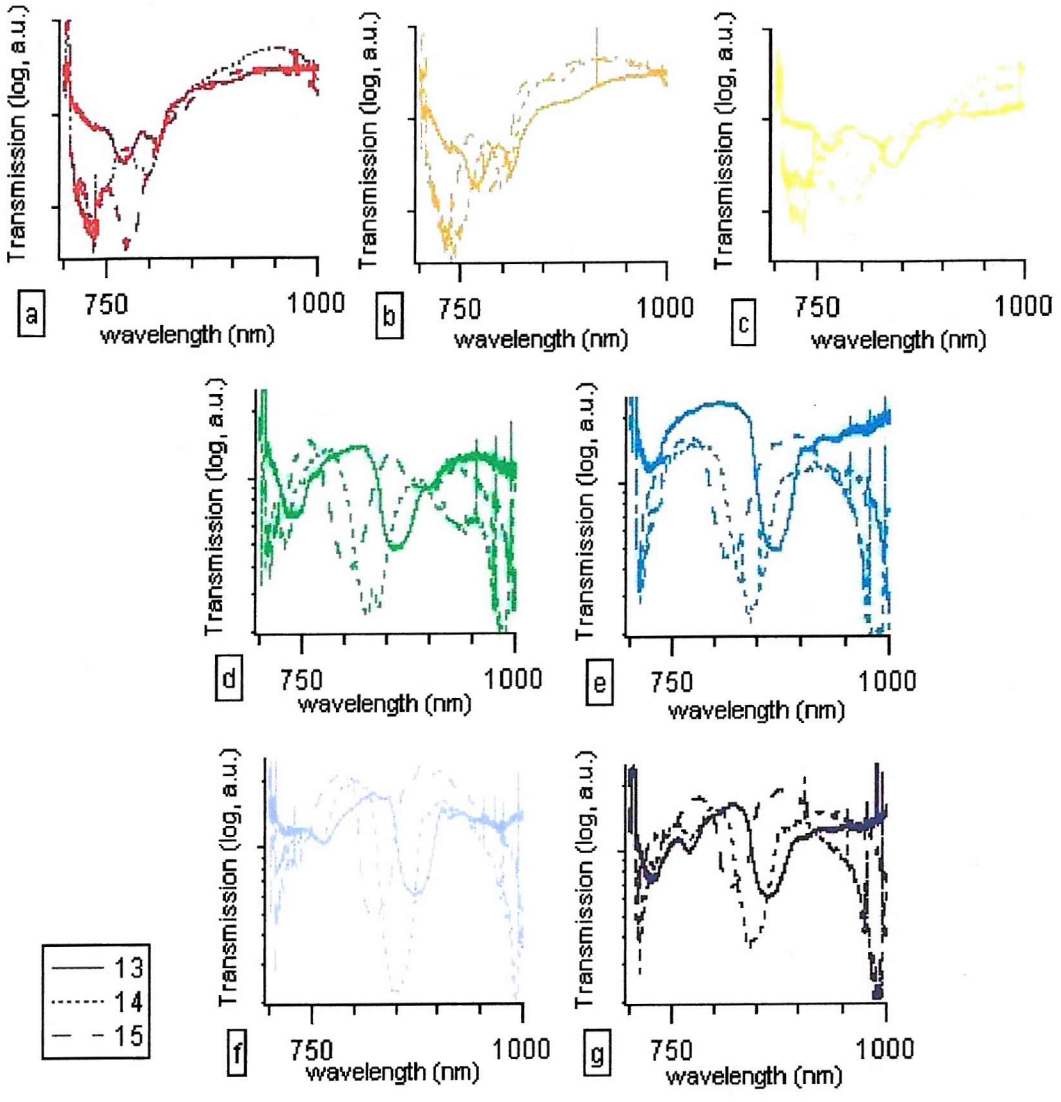

Figure 4.2.9 - TE-polarisation transmission spectra for transmission along 5° increments from the ΓJ direction (a, red) to the ΓX direction (g, violet) for samples r2198#5_13, 14 and 15.

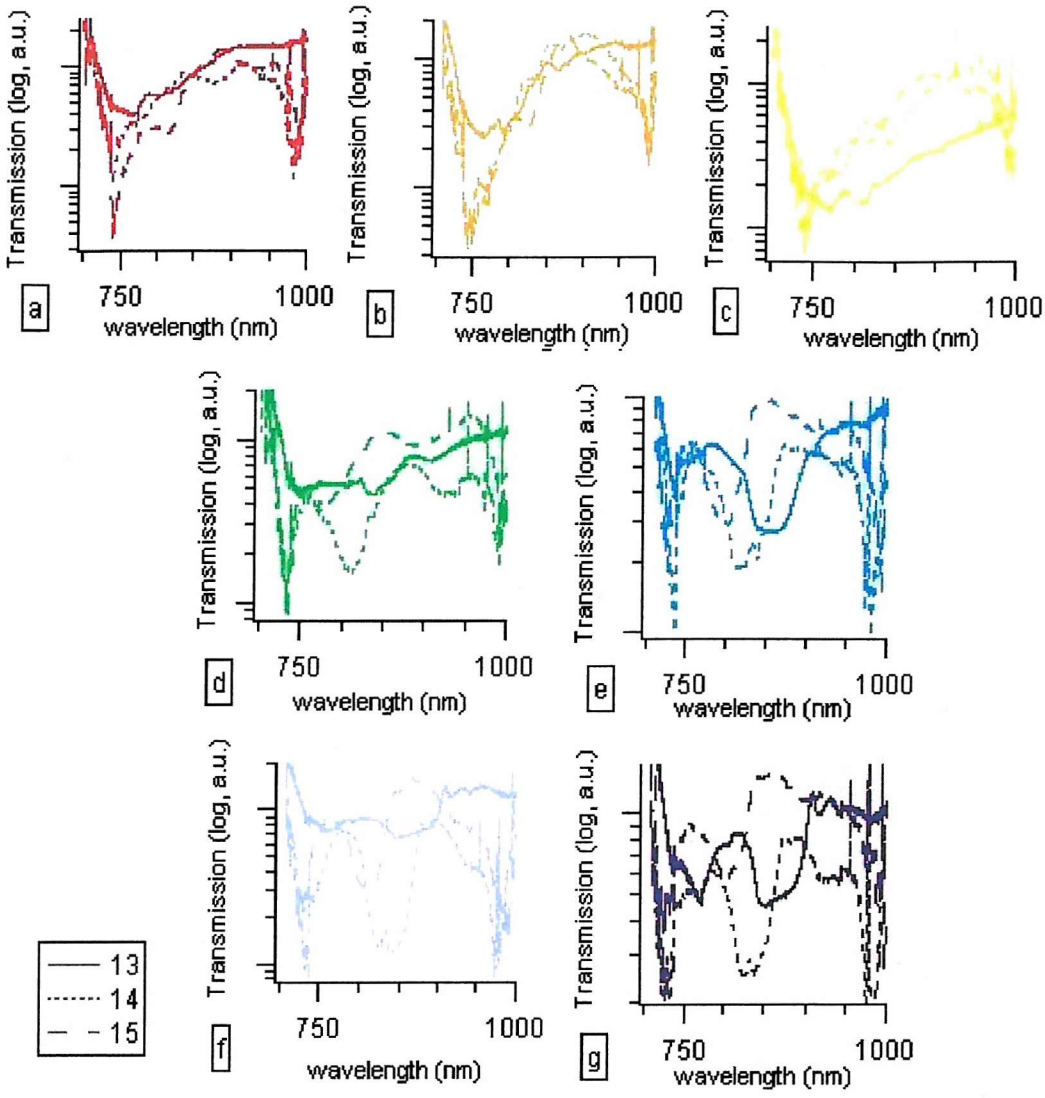

Figure 4.2.10 - TM-polarisation transmission spectra for transmission along 5° increments from the ΓJ direction (a, red) to the ΓX direction (g, violet) for samples r2198#5_13, 14 and 15.

It may be seen from Figures 4.2.9 and 4.2.10 that as the hole diameter for a photonic crystal, and thus the filling fraction, is increased, the resulting photonic bandgap features are shifted towards shorter wavelengths, and therefore towards higher energies.

Samples were also fabricated with 40 and 60 rows, the 40-row samples producing bandgaps at the same wavelengths as the 20-row devices, but with broader features due to increased scattering within the extra rows. This is illustrated by Figures 4.2.11

and 4.2.12 for TE and TM polarisations respectively. As with Figures 4.2.9 and 4.2.10, both samples are represented on the same graph for each of the seven propagation directions ΓJ (a) to ΓX (g). The samples used for these measurements were r2198#5_15 and 41, with 20 and 40 rows, each of the same photonic crystal pattern. As may be seen, many of the bandgap features show up much less clearly for the 40-row samples than for the 20-row samples. This is due to the large transmission loss through the broader photonic crystal. This loss was so great that for the 60-row samples no usable data was obtained.

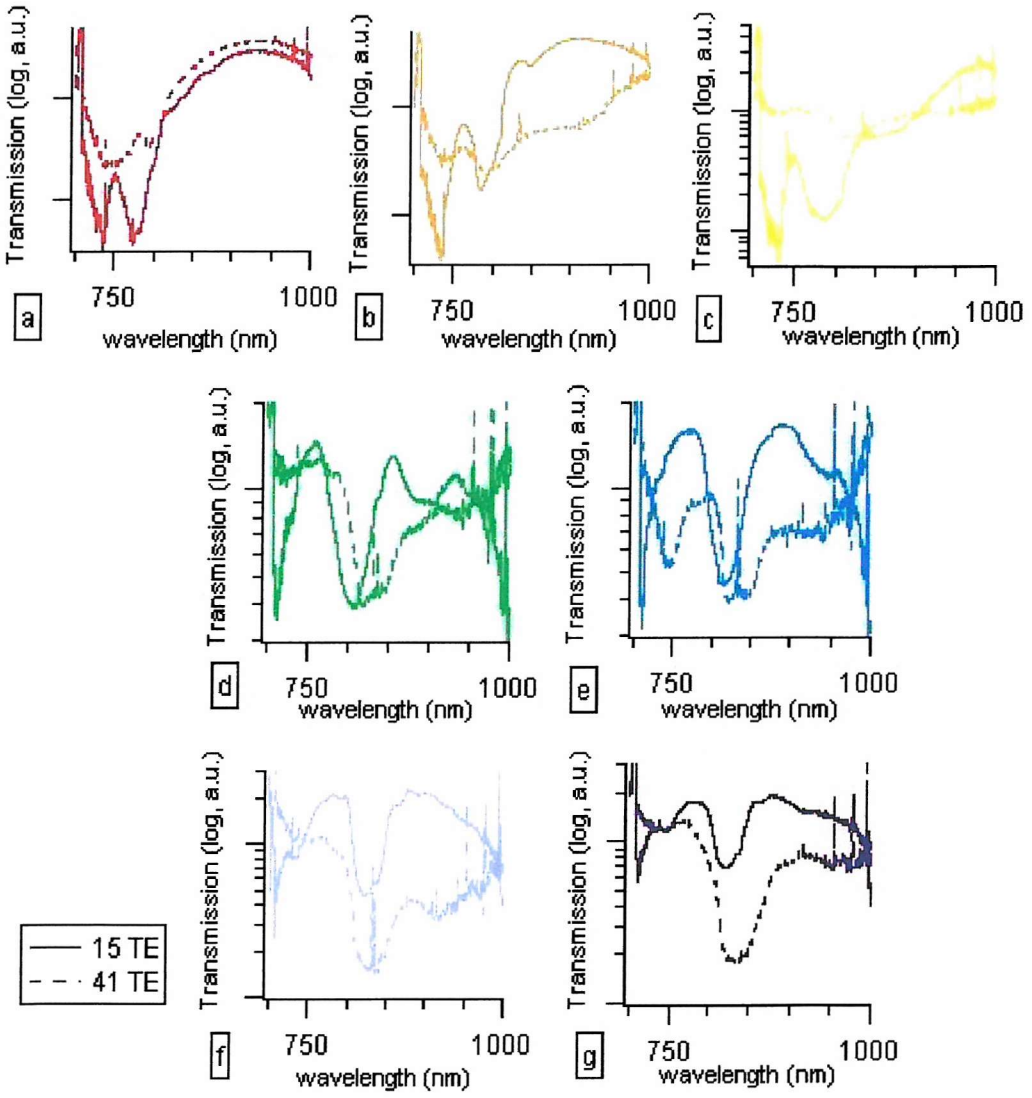

Figure 4.2.11 - TE-polarisation transmission spectra for transmission along 5° increments from the ΓJ direction (a, red) to the ΓX direction (g, violet) for samples r2198#5_15 and 41.

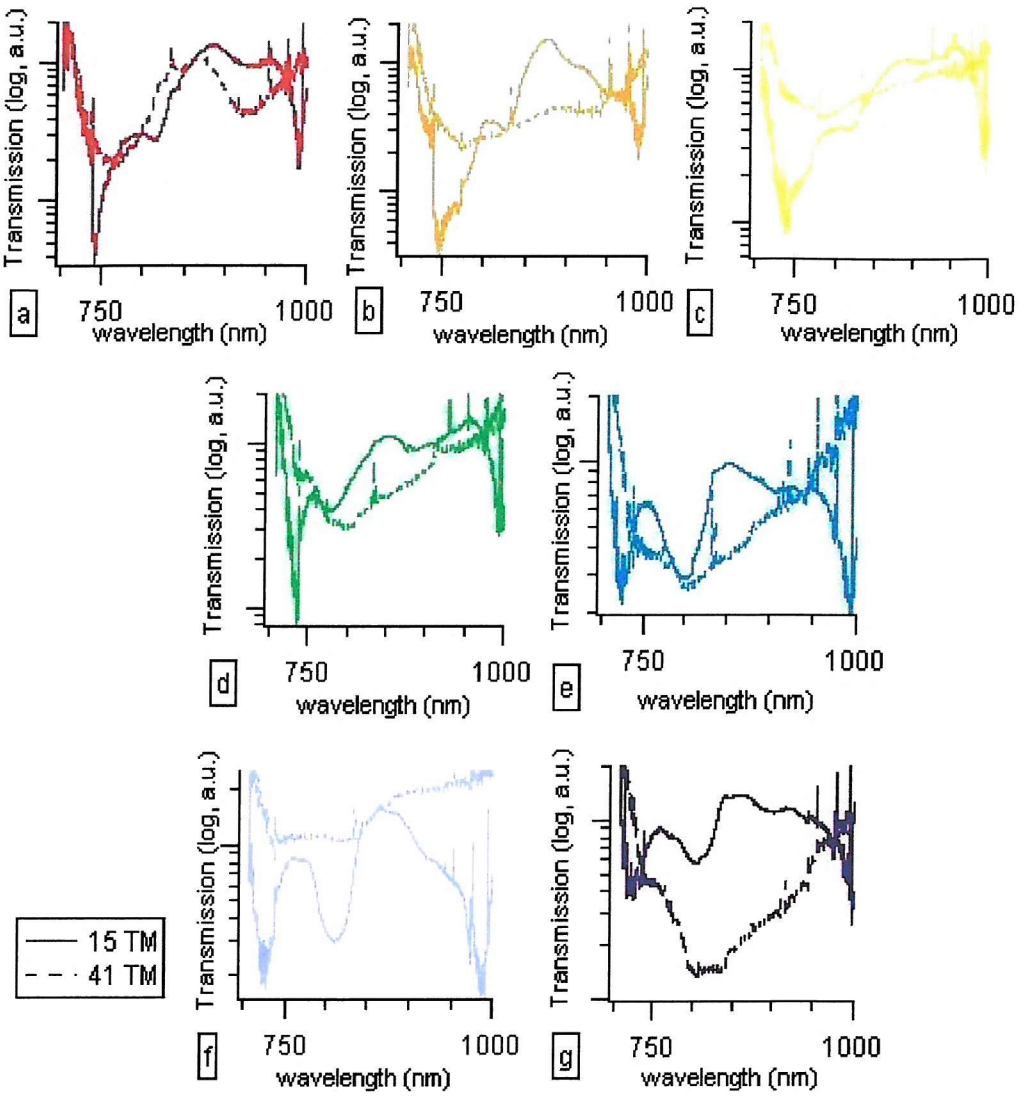

Figure 4.2.12 - TM-polarisation transmission spectra for transmission along 5° increments from the ΓJ direction (a, red) to the ΓX direction (g, violet) for samples r2198#5_15 and 41.

Another comparison may be made of samples with the same hole diameter but with different pitch sizes. The samples used for these measurements were 20-row photonic crystal samples r2198#5_14 and 86, with results for the TE and TM polarisations shown in Figures 4.2.13 and 4.2.14 respectively. Here it may be seen that decreasing the photonic crystal lattice pitch caused the bandgap features to shift towards higher energies

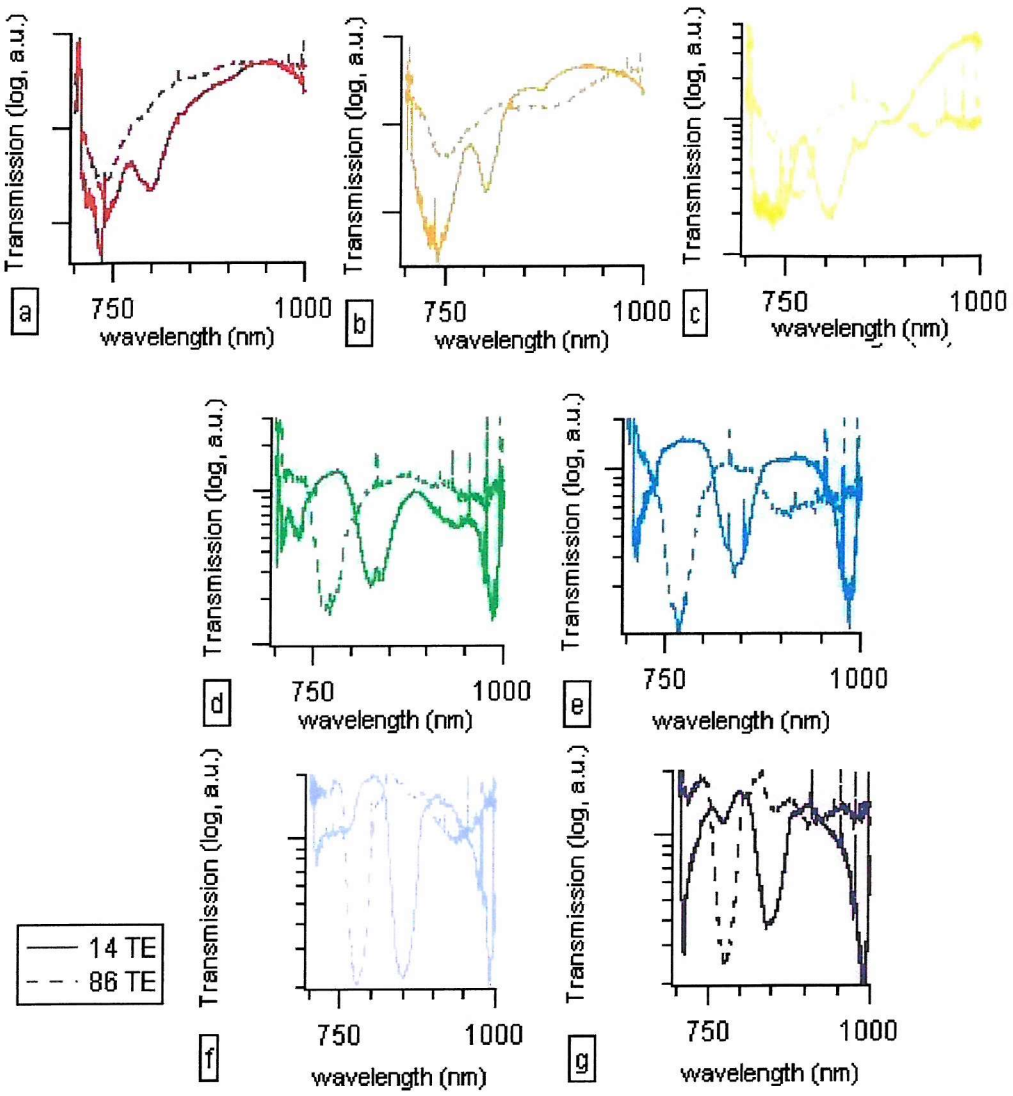

Figure 4.2.13 - TE-polarisation transmission spectra for transmission along 5° increments from the ΓJ direction (a, red) to the ΓX direction (g, violet) for samples r2198#5_14 and 86.

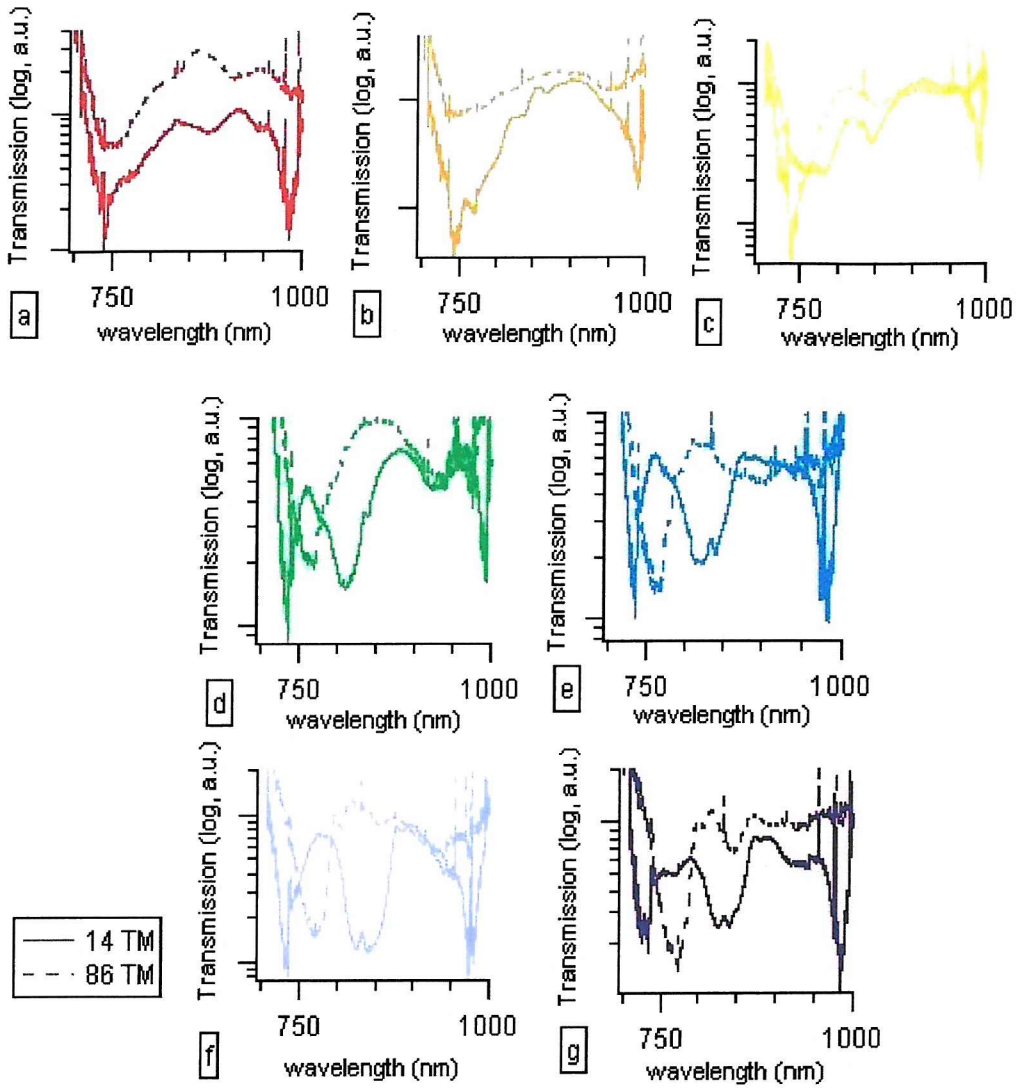

Figure 4.2.14 - TM-polarisation transmission spectra for transmission along 5° increments from the ΓJ direction (a, red) to the ΓX direction (g, violet) for samples r2198#5_14 and 86.

Tthe widths of the bandgaps were extracted, following the rule that the bandgap is determined as the width at the height of the first discernable feature, and the results plotted in Figure 4.2.15.

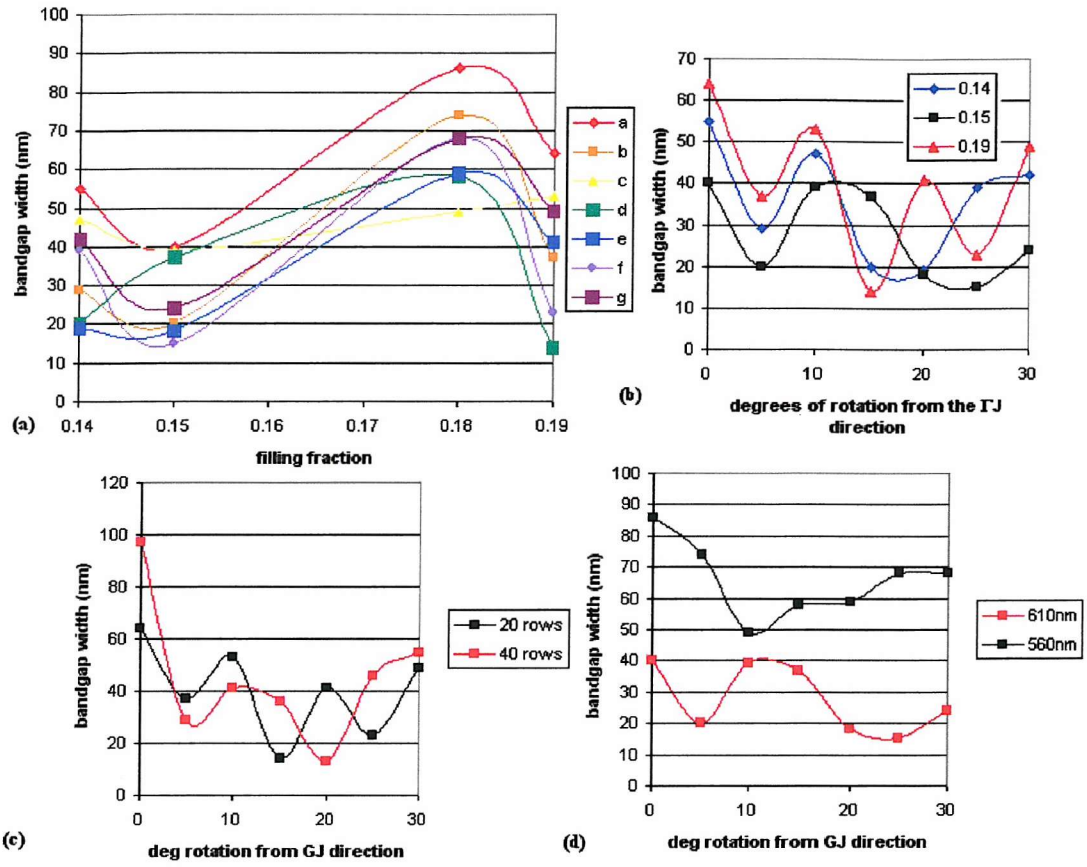

Figure 4.2.15 - extracted TM bandgap widths for (a) propagation directions 0-30° from the ΓJ direction, plotted against the filling fraction, (b) varying filling fractions plotted against the propagation direction, (c) for 20 and 40 row devices, identical pitch and hole diameter, and (d) for varying pitch dimensions, with 250nm hole diameters.

From Figures 4.2.15 (a) and (b) it may be seen that bandgap width varies with both propagation direction as the filling fraction varies. The more important factor for bandgap width appears to be the pitch, rather than the filling fraction as is shown in Figure 4.2.15 (d). The 560nm pitch device was also the one with the filling faction of 0.18 in Figure 4.2.15 (a).

The earlier stated observation that the doubling of the number of rows causes a broadening of bandgap features is not bourne out by the data reported in Figure 4.2.15(c). However this may be explained by the method of width extraction at the height of the first discernable feature in the bandgap. A visual inspection of the data in Figure 4.2.12 shows clearly the broadening in the overall shape of the bandgaps,

but the individual features of the bandgap do remain at essentially the same wavelength.

4.2.3 1st order photonic bandgap measurements

The photonic bandgaps demonstrated in the previous section do not include the primary bandgap, which is situated around 1500nm for photonic crystals of this photonic lattice pitch size. The photonic bandgaps discussed here were higher-order bandgaps. We would anticipate that the higher order bandgaps have narrower features and lower extinction coefficients than the primary bandgap expected from theory [8].

To shift the primary bandgap into the wavelength range of interest for SRSO, photonic crystals were fabricated with smaller lattice pitches, in batch r2351. The design and fabrication of these photonic crystals is discussed in Section 4.1, while the full chip listing for the PRISMS design, with which the wafers were patterned, is in Appendix B.

To measure the photonic bandgaps of the samples, the same setup was used as with the samples from batch r2198, as was shown in Figure 4.2.1. The results obtained are shown in Figure 4.2.16 below, with the upper set of curves showing the untreated data and the lower set showing the derived optical transmission through the photonic crystal. The solid lines are those spectra measured with the excitation spot in position *b* (see Section 4.2.1), and the dashed spectra were measured with the excitation spot in position *c*. The lower set of data is the ratio of the *b* and *c* spectra.

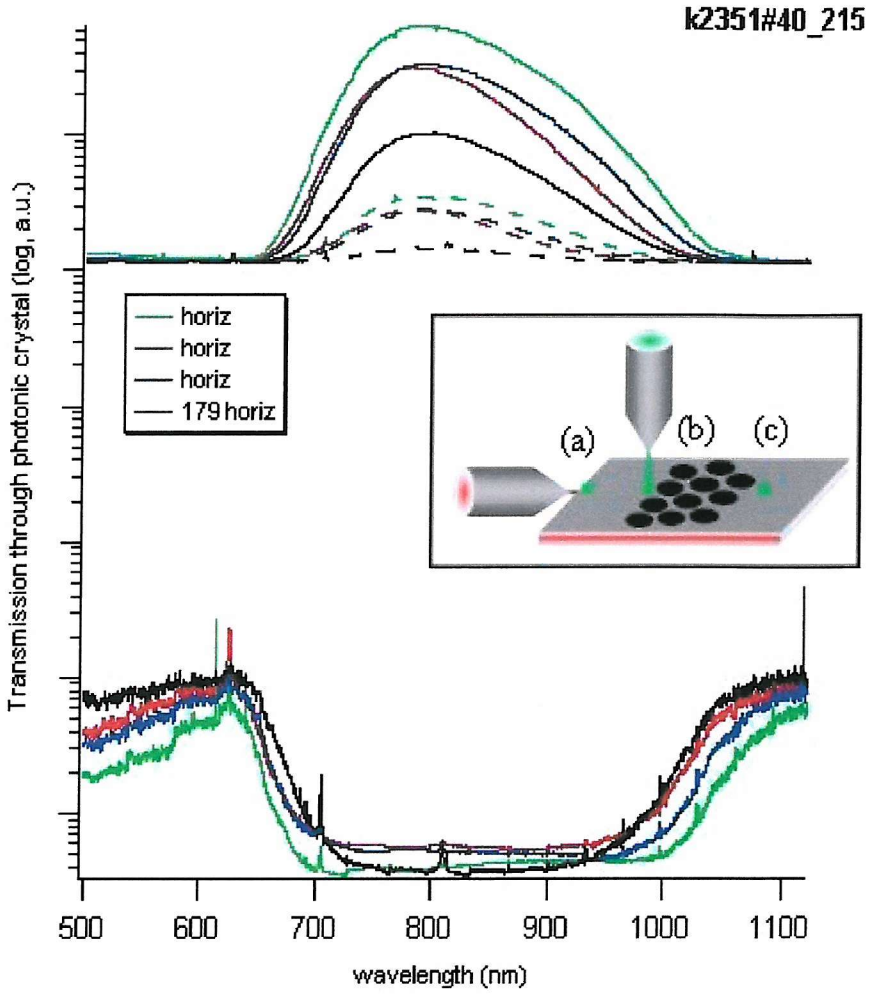

Figure 4.2.16 - TM (horizontal) transmission measurements on samples which should have a first order photonic bandgap in the measured region. Solid curves were measured from position (b) while dashed curves were measured from position (c), from the inset.

The samples measured were samples k2351#40_215 and k2351#40_179. Sample k2351#40_215 was a 150-row device with a lattice pitch of 310nm and a hole diameter of 180nm. Sample k2351#40_179 was a 300-row device with a lattice pitch of 360nm and a hole diameter of 200nm. As is shown in Figure 4.2.16, there was no appreciable difference between the transmission spectra of the two samples.

Using the 2D plane wave simulation technique described in Section 4.3.1 of this thesis, the predicted band diagrams for samples k2351#40_215 and k2351#40_179 were found, as is shown in Figure 4.2.17.

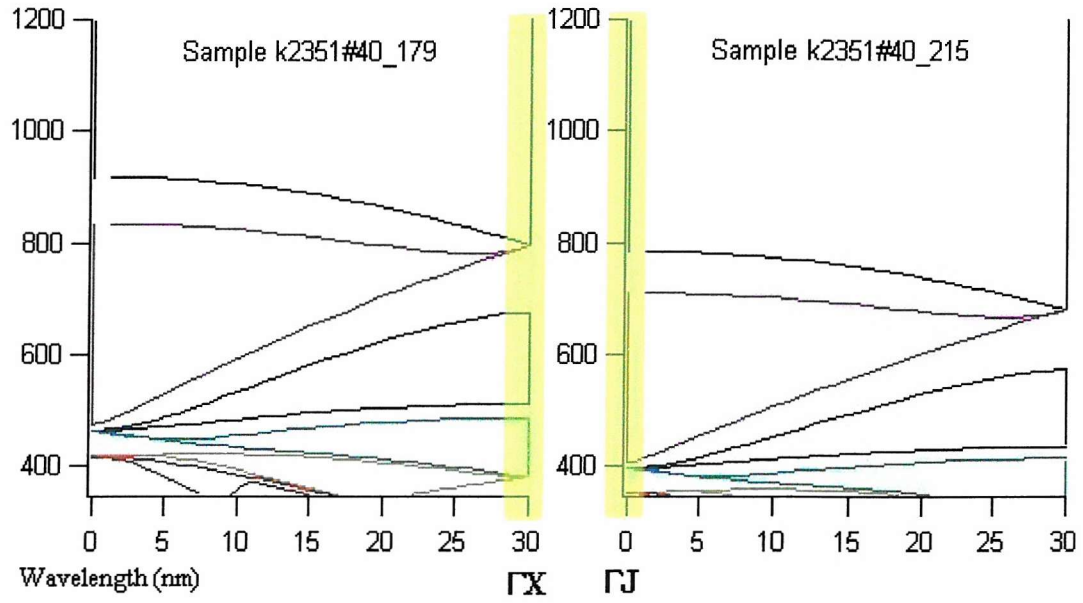

Figure 4.2.17 - the simulated band structure for samples k2351#40_215 and k2351#40_179, TM polarisation. The measured propagation directions for each sample are highlighted in yellow.

The simulation program was designed for photonic crystal samples of the ROTLINES pattern, and so shows the bandgaps for all directions of propagation from ΓJ (0°) to ΓX (30°). Sample k2351#40_179 was patterned such that light traversed the photonic crystal in the ΓX direction, while sample k2351#40_215 was oriented such that light travelled in the ΓJ direction. These propagation directions are highlighted in yellow in Figure 4.2.16. A bandgap perceived in the wavelength region 650-1000nm from sample k2351#40_179 is not the primary bandgap, but instead the secondary, while for k2351#40_215 the perceived bandgap in that wavelength range is the primary bandgap. Other differences between the two samples is the breadth of the bandgaps. The measured bandgap from sample k2351#40_215 should be narrower than the measured bandgap from k2351#40_179.

As is shown in Figure 4.2.16, there is no noticeable difference between the measured "bandgap" from samples k2351#40_215 and k2351#40_179. This "bandgap" also occurs exactly with the range in which photoluminescence may be measured. From these results one must conclude that no bandgap has been measured, and what is shown in Figure 4.2.16 is in fact the optical transmission loss due to the photonic

crystal. This is attributed to the very large number of rows. In the ROTLINES photonic crystal pattern, the greatest number of rows for a measured bandgap was 40. In the PRISMS pattern the thinnest samples had 150 rows.

Measurements were carried out with the photonic crystal holes filled with methanol, a liquid with very low surface tension, to reduce the refractive index contrast between the air holes and the SRSO waveguide into which they had been etched. As discussed in Section 1.3.2, a lower refractive index contrast results in narrower and shallower photonic bandgap features. The scattering loss should also be reduced, allowing some features to be observed. These measurements were unsuccessful, and no primary photonic bandgap features have been observed in SRSO waveguides.

4.3 Simulation overlap

Photonic crystal modelling packages were developed by several members of the Southampton University Silicon-Based Photonics group. The methods developed by several people have been used in this thesis to explain the measured results. In this section each of these methods shall be described briefly, and details of how each method was applied to the particular application of SRSO waveguides shall be discussed.

4.3.1 2-D Plane wave expansion technique

A plane wave solver [9] for photonic bandgaps was developed by Dr Martin Charlton. This program, which operates for both TE and TM polarisations, *solves eigenvectors for specified bands, in order to calculate the Poynting vectors of the field. This gives an indication of the polarisation states of individual modes*. The 2D plane wave solver operates for square, triangular, rectangular, and trapezoidal photonic lattices, although only triangular lattices were used in this thesis. To run the program, the user must enter simulation parameters into a text file, most importantly the values for lattice pitch, hole diameter and the bulk refractive index of the waveguide core material. The simulation parameters text tile is included in Appendix C. With the output type set for MS Excel, a file is generated which contains information about the photonic band structure.

Figure 4.3.1 shows the band structure as calculated by the plane wave expansion program for a photonic crystal with a lattice pitch of 310nm and a hole diameter of 180nm in SRSO of type 'C', such as sample k2351#40_215 in both TE and TM polarisations. These band diagrams are the conventional sort, which may be readily found in any standard text on photonic crystal text book [8].

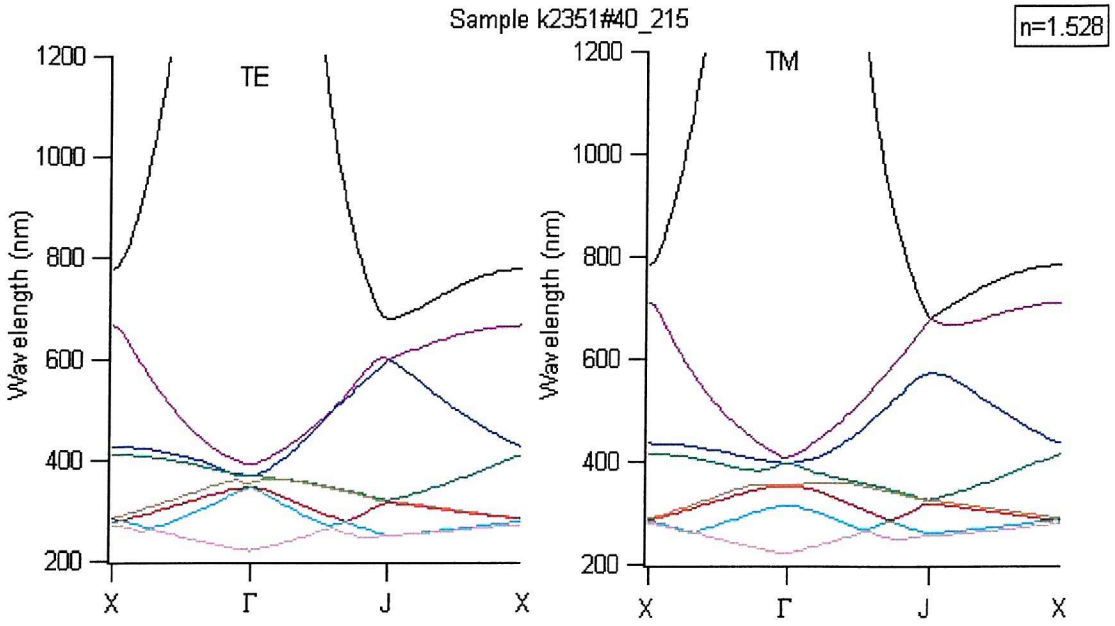

Figure 4.3.1 - Band structure diagrams for photonic crystal sample k2351#40_215, both TE and TM polarisations

Using an IGOR program developed by Prof. Jeremy Baumberg the band diagrams generated by the plane wave expansion method are unfolded to provide a clear picture of how the photonic band gaps appear for propagation in different directions through the photonic crystal. In order to do this the lattice pitch of the simulated photonic crystal, the waveguide core refractive index, and the effective index of the waveguide must be entered into the code for two macros. The waveguide effective refractive index is determined using the methods described in Chapter 2 of this thesis. Using the macro *kset*, the band structures presented in Figure 4.3.1 are unfolded, resulting in a view of how photonic bandgaps will evolve as the direction of propagation is rotated from the ΓJ to the ΓX direction.

Figure 4.3.2 shows the calculated band structure for a photonic crystal with a lattice pitch of 310nm and a hole diameter of 180nm in SRSO of type 'C', such as sample k2351#40_215. Both TE and TM polarisations are included in this diagram.

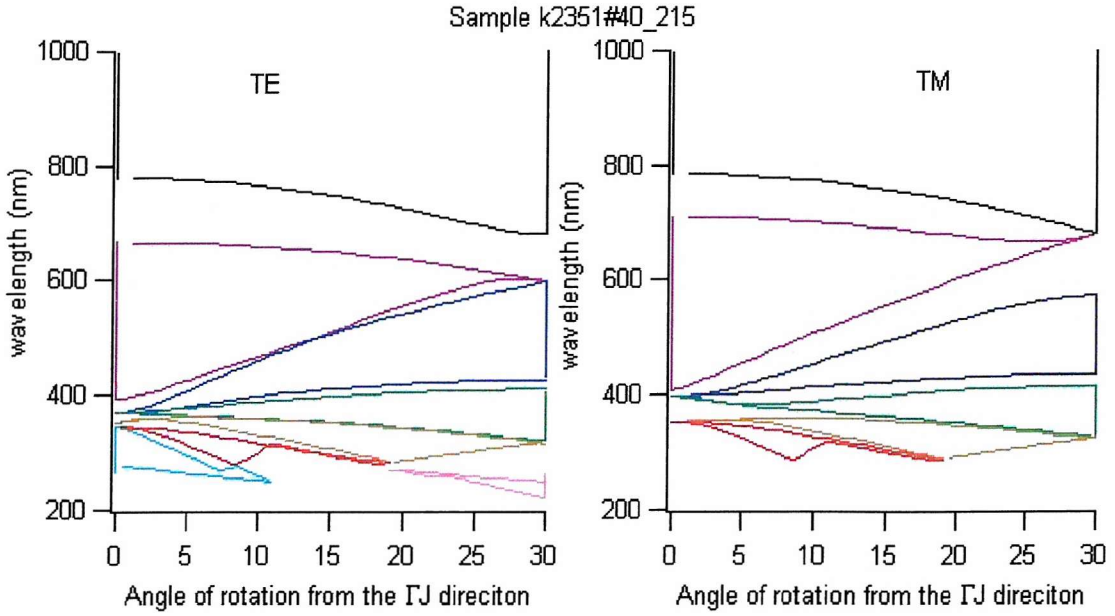

Figure 4.3.2 - TE and TM calculated photonic bandgaps for a photonic crystal such as sample k2351#40_215

Figure 4.3.2 shows the primary and higher-order bandgaps for a photonic crystal with a small lattice pitch. In the TE polarisation the primary photonic bandgap is clearly the broadest. Also, for a small range of wavelengths, the TE primary bandgap is a *complete* photonic bandgap, prohibiting the propagation of light in any direction. This is shown to be not true for the TM polarisation, where the primary bandgap is pinched shut as the direction of propagation through the photonic crystal approaches ΓX. The greatest breadth of the secondary bandgap at direction ΓX is in fact greater than that of the primary bandgap.

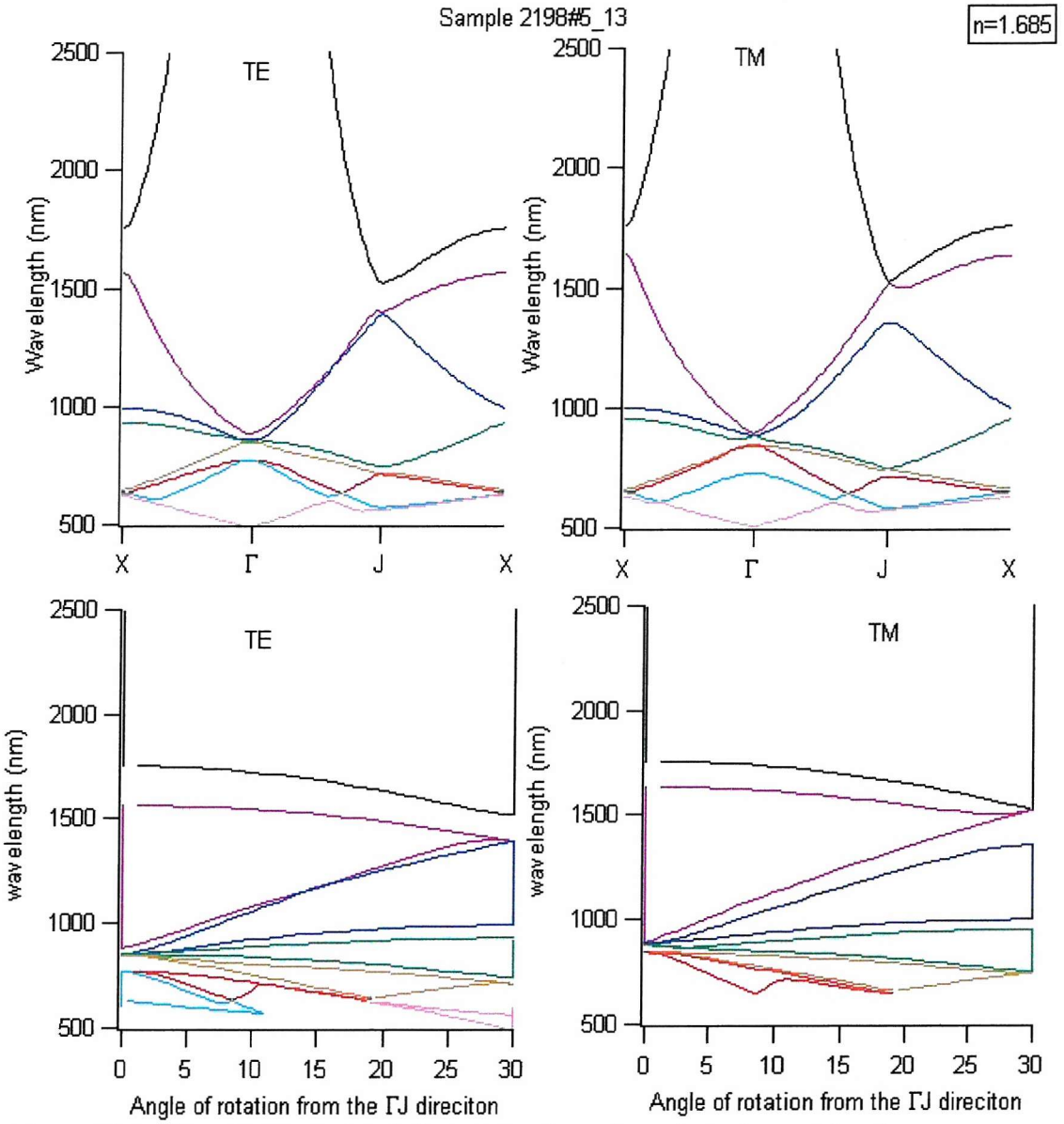

Figure 4.3.3 - TE and TM calculated photonic bandgaps for a photonic crystal such as r2198#5_13, both conventional and unfolded

In Figure 4.3.3 the band structure is shown for a photonic crystal with a large lattice pitch of 610nm and a hole diameter of 240nm, such as r2198#5_13. Both conventional and unfolded lattice bandgap structures are shown. In the case of the larger lattice pitch the primary bandgap (beneath the black curves) are clearly located at much longer wavelengths than the photoluminescence from annealed SRSO (from 600-1000nm).

If the TE band diagram shown in Figure 4.3.3 were rotated such that band structure is plotted against wavelength, the simulated data becomes arranged the same as the experimentally recorded data. Figure 4.3.4 shows calculated TE photonic bandgaps for sample r2198#5_13 for the wavelengths of light for which it was possible to measure the transmission of photonic crystals. For clarity, the wavelengths which permit light to pass are shaded, while the white regions are the band gaps. The inset shows the location of the primary bandgap for this photonic crystal, around 1500nm, and its relative breadth in comparison with the higher-order bandgaps in the shorter wavelength regions which were measured.

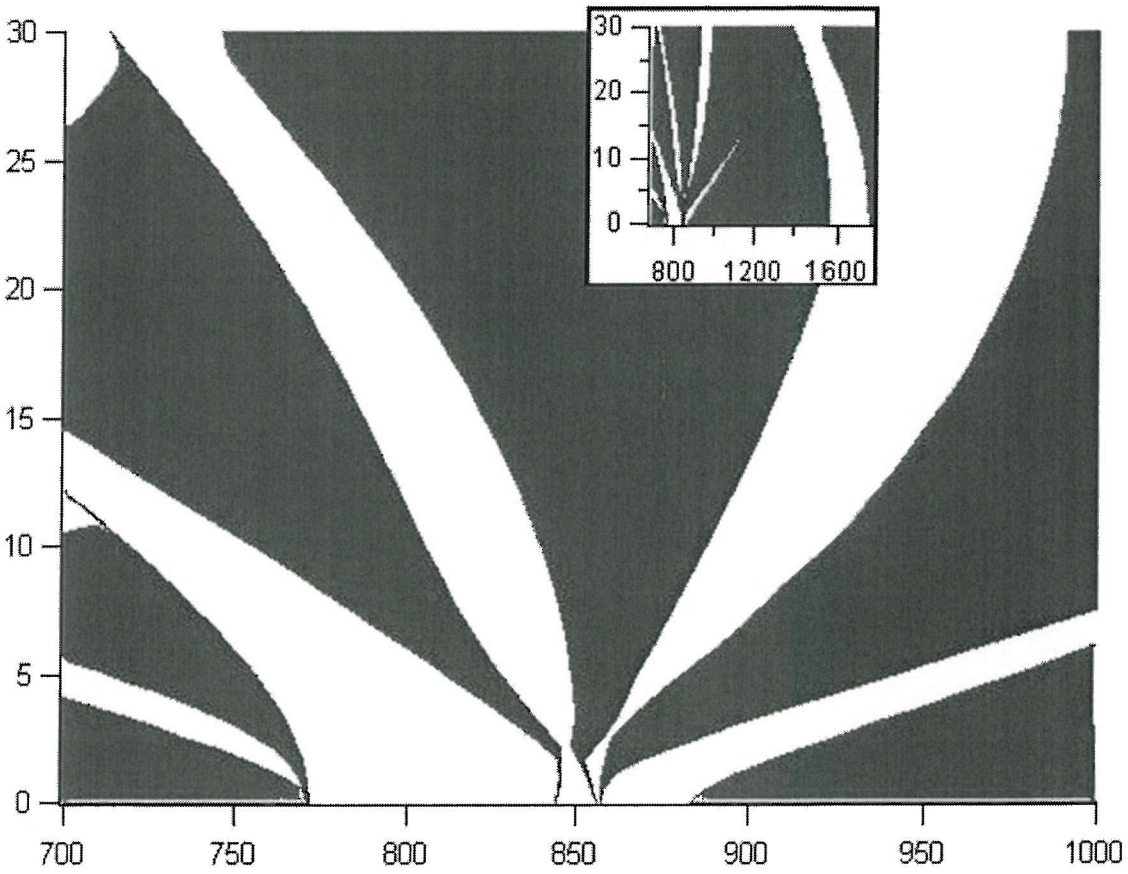

Figure 4.3.4 - Calculated TE bandgaps for photonic crystal sample r2198#5_13 with permitted (shaded) and bandgap (white) regions highlighted. The inset shows the location of the primary bandgap.

If simulated and experimentally measured photonic bandgaps are plotted on the same axis, the result is as shown in Figure 4.3.5. In order to achieve a good overlap

between the experimental and calculated results, it was necessary to shift the calculated results 65nm towards shorter wavelengths. This is as expected from the shortcomings of a 2D model in a 3D waveguide, but in line with previous corroborations between 2D and 3D theories.

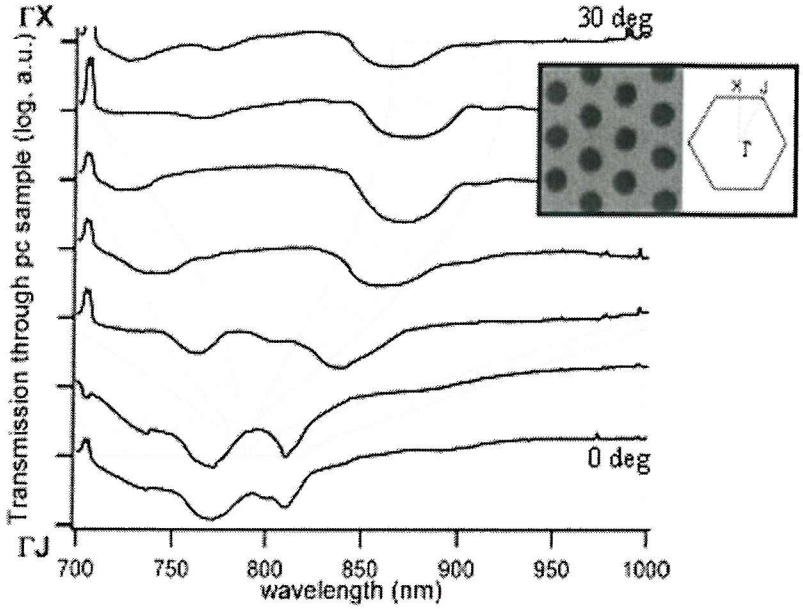

Figure 4.3.5 - Experimental results (black curves) showing photonic bandgaps in waveguides of SRSO. The grey regions behind the curves illustrate the theoretically expected location of bandgaps at the corresponding directions of propagation, found using a 2D plane wave expansion technique. The inset clarifies the meaning of propagation directions ΓX and ΓJ.

4.3.2 3D Finite Difference Time Domain Simulations

Finite Difference Time Domain (FDTD) is a numerical method commonly used for the solution of problems in electro-magnetics, of which the theory of photonic crystals forms a part. First developed in 1966 by Yee [10], the FDTD method uses discretised electric and magnetic fields which are offset from each other in both space and in time. Fields calculated in the past are used to calculate present fields, with the electric and the magnetic fields alternating as time progresses. There is a large amount of literature available on the FDTD method, including a book by A Taflove, an early pioneer in the field. [11-12].

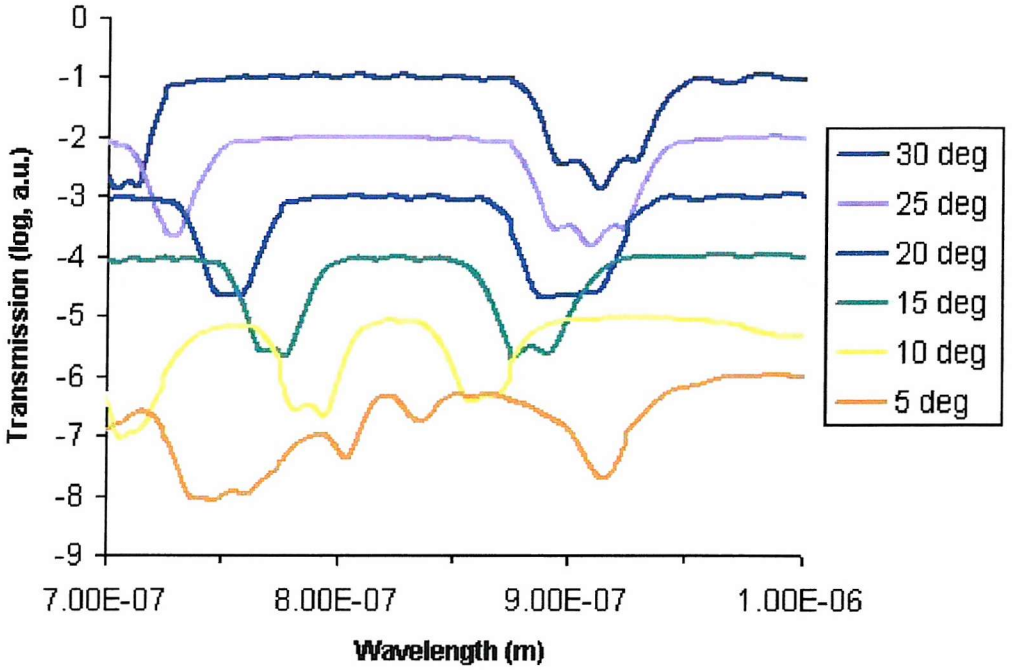

Figure 4.3.6 - Finite Difference Time Domain (FDTD) TE-polarisation simulations for a photonic crystal with a lattice pitch of 610nm and a hole diameter of 250nm.

FDTD simulations were carried out by Dr Majd Zoorob for triangular photonic crystal samples with a refractive index n = 1.7. The simulations were carried out for the same propagation directions as had the experimental measurements. For the purpose of the simulations the samples were assumed to be 500-row photonic crystals rather than the 20 and 40-row samples which had been fabricated and successfully measured. Figure 4.3.6 shows the FDTD simulation results for a photonic crystal with a lattice pitch of 610nm and a hole diameter of 250nm, such as photonic crystal sample r2198#5_14, in the TE polarisation. Similar simulations were carried out for both TE and TM polarisation for a photonic crystal corresponding to samples r2198#5_13 and r2198#5_41. These photonic crystals have the same lattice pitch, 610nm, but have hole diameters of 240nm. The results obtained are shown in Figure 4.3.7.

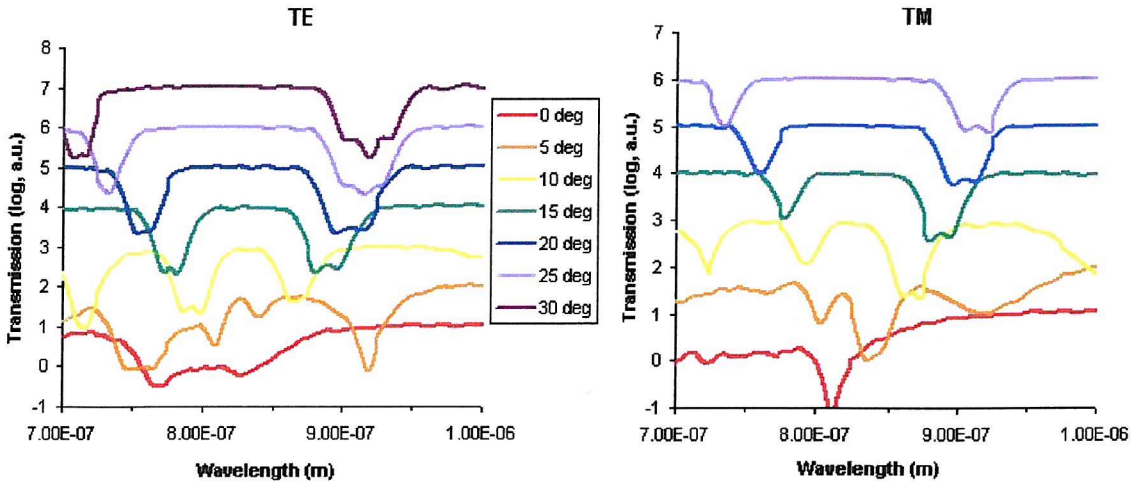

Figure 4.3.7 - TE and TM polarisation FDTD simulations for photonic crystal samples with a lattice pitch of 610nm and a hole diameter of 240nm.

As with the 2D plane-wave expansion simulations, simulation results and experimental data were plotted on the same x-axis. The simulation results for sample r2198#5_13 are shown as dashed lines in Figure 4.3.8, with experimental results presented with solid lines. Each simulated result corresponds with the experimental result placed alongside. It should be noted that the FDTD simulation results were shifted 30nm toward shorter wavelengths to overlap with the experimental results.

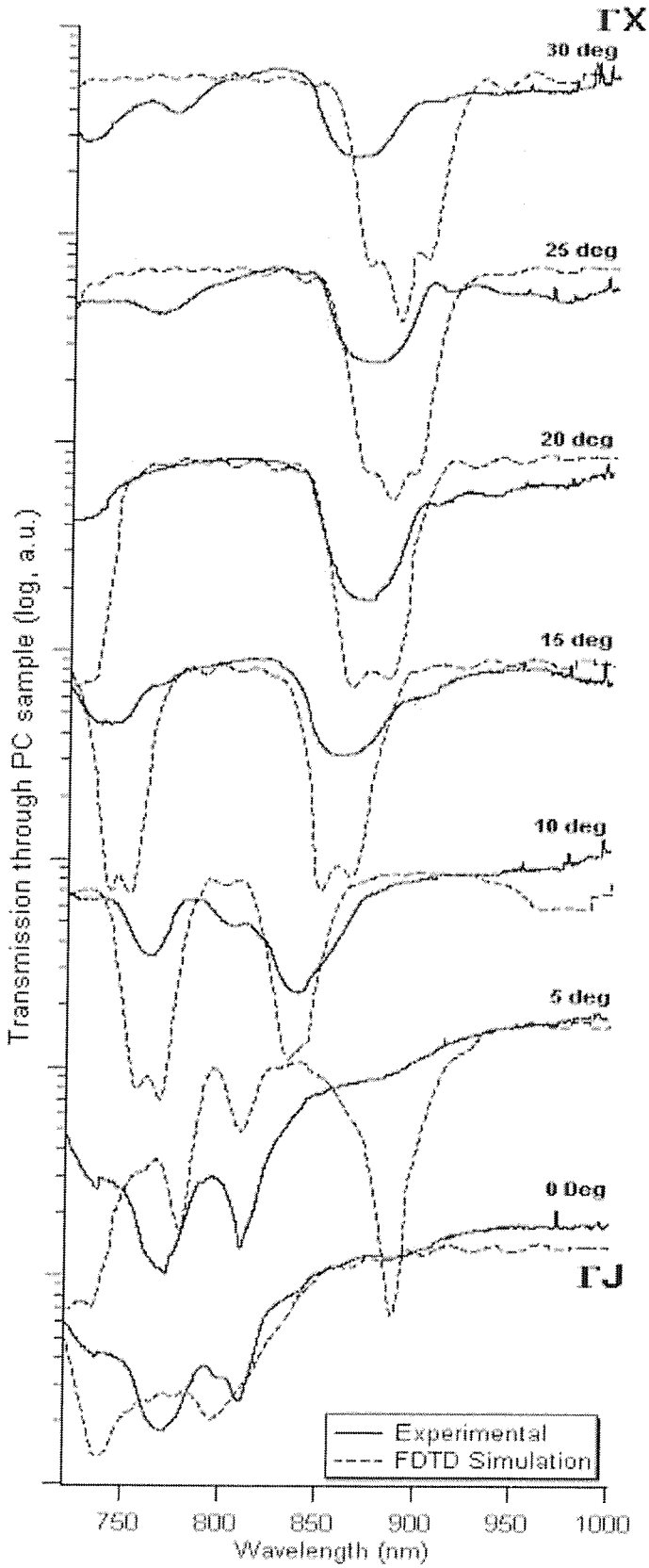

Figure 4.3.8 - Experimental results (solid lines) and FDTD simulation results (dashed lines) showing photonic bandgaps in waveguides of SRSO as the direction of propagation is rotated between the ΓJ and ΓX directions. The curves are on a log scale, and have been offset for clarity

4.3.3 Discussion

The primary results in this section are those presented in Figure 4.3.5 and in Figure 4.3.8. The former illustrates how a 2D plane wave expansion technique is adequate to predict loosely the band structure of a photonic crystal, while the latter illustrates that a fully 3D simulation technique such as Finite Difference Time Domain analysis is a superior method, although it does require significantly more computing power.

Both 2D and 3D techniques required a translation in the wavelength in order to provide a good match with the experimental results. While for the 2D technique this is unavoidable, for the FDTD analysis the discrepancy arose from an error in the simulation parameters. The refractive index assumed for the purpose of simulation was n = 1.7, and not n = 1.85 which was the value later measured for type 'A' SRSO. The refractive index of the core layer is critical to the location of the photonic band features, as is shown in Figure 4.3.9. In this graph, FDTD simulations have been carried out for a photonic crystal with a lattice pitch of 610nm and a hole diameter of 240nm, such as r2198#5_13, with a core refractive index varying from 1.6-1.75. This figure shows that as the core refractive decreases, so does the wavelength at which the same band features occur. An FDTD simulation with n = 1.68 would match the experimental results without the necessary 30 nm redshift.

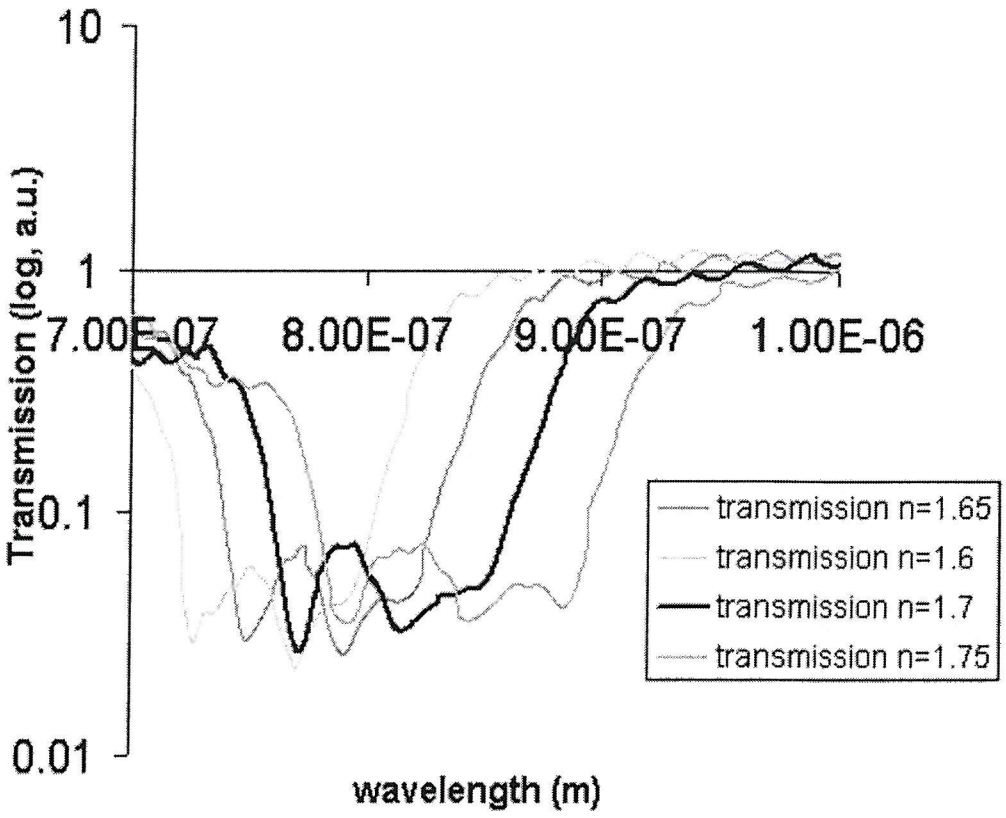

Figure 4.3.9 - Simulated TE-polarisation transmission for a photonic crystal with lattice pitch of 610nm and a hole diameter of 240nm, but with a refractive index ranging from n=1.6-1.75

Both Figures 4.3.5 and 4.3.8 illustrate the good correspondence between experimental results and theory. In both diagrams, a pair of photonic bandgaps (between 3rd and 4th and 4th and 5th bands) may be clearly seen converging as the direction of propagation rotates from ΓX towards ΓJ. The bandgaps centred at 855nm and 750nm at 15° are clearly evident in both theory and experiment. As these bandgaps merge to form a multi-featured gap (along ΓJ), higher and lower-order bandgaps also converge at this degeneracy point. Features apparent for the ΓX propagation direction which are not represented by the FDTD simulation may arise from waveguide transmission features, while the strength and steepness of the models are reduced, probably by angular averaging from scattering of the emission within the PC.

The results presented in this section show a strong correlation between experimental and simulated results gained by very different methods, with the 3D FDTD simulation simulations showing a closer fit to the experimental data than the 2D plane

wave expansion. The only FDTD-simulated feature which does not show up clearly in the experimental results is the 900nm feature at 5°. This is attributed to the low number of rows used in the measured samples relative to the FDTD simulation. These are the first reports we are aware of where both sets of data have been presented and contrasted in this direct manner.

4.4 Conclusions

This chapter was concerned with the fabrication, measurement, and simulation of photonic crystals fabricated in waveguides of Silicon-Rich Silicon Dioxide, the fabrication and the waveguide properties of which, were described in the previous chapter.

The fabrication method developed was a reliable, well-controlled, and repeatable process where electron-beam lithography was used to pattern waveguides which had been coated with first an evaporated layer of chrome, and then with a layer of photoresist. Wet chrome etch was used to transfer the pattern from resist to the chrome layer, which was then itself used as a mask for the dry etch process which followed. The depth of the etch was characterised by repeated optical measurements and, towards the endpoint, by the cleaved separation of portions of the wafer for SEM measurement. To complete the fabrication process, a resist strip and a plasma ash stage was used to remove any residual photoresist or chrome mask. Scanning Electron Microscopy was used intensively throughout the fabrication process to provide visual data on the methods employed.

Alternate processes included the use of an ion beam milling stage in the place of the wet chrome etch. A dry process should result in greater anisotropy in the etched holes, but it was found that the high ion energy resulted in reticulation (unwanted development) of the photoresist layer, and the loss of an entire wafer.

Photonic crystals were fabricated with lattice pitches ranging from 260 - 610nm, with hole diameters ranging from 160 - 460nm. The majority of the fabricated patterns were triangular photonic crystals oriented between the ΓX and ΓJ directions. A few gratings (1D photonic crystals) were also fabricated.

Once the waveguides had been patterned with photonic crystals, they were prepared for optical measurement. Several methods were attempted to improve the efficiency of light coupling into and out of the waveguide core, including sawed edges, polished sawed edges, manual and mechanical cleaving. Of these, it was found that mechanical cleaving provided the best edge, although it was possible to achieve quite satisfactory light coupling into a sawn edge, if it had fortunately remained not badly damaged in the process.

The bandgaps of the fabricated photonic crystals were evaluated by measuring the ratio of transmitted photoluminescence excited at the far side of the photonic crystal, to the transmitted photoluminescence excited at the near side. This method proved successful, and experimental data was gained for higher-order 2D photonic bandgaps fabricated in a luminescent silicon-based material. We believe these are the first reported photonic bandgaps in SRSO.

The experimental results demonstrated how the wavelength at which photonic bandgap features occur is reliant upon the hole diameter (Figures 4.2.9-10), upon the lattice pitch (Figures 4.2.13-14). It was also shown how an increased number of rows resulted in broader but shallower band features (Figures 4.2.11-12), which is attributed to increased scattering off more rows.

As a final set of experimental results, we were unable to demonstrate a primary bandgap in SRSO, despite the successful fabrication of structures with an adequately small lattice pitch, evenly spaced rows, and well-defined holes.

To reinforce the experimental results, simulations were carried out by 2D plane wave expansion techniques, and by 3D Finite Difference Time Domain (FDTD) methods. Both simulation methods provided good overlap with the experimentally obtained results, assisting greatly in the allocation of a measured feature to a calculated band. While it is not expected that the 2D simulation technique will provide a perfect match

for a 3D system, the discrepancy in the 3D FDTD simulation results is ascribed to an error in the refractive index assigned to the core layer for simulation purposes.

In summary, waveguides of photoluminescent SRSO were patterned with 2D triangular photonic crystals, and the photoluminescence of the Si nanocrystals was used to probe the higher-order photonic bandgaps of the structure. Transmission bandgaps were demonstrated experimentally, and FDTD simulation and 2-dimensional plane wave expansion matched closely the data and can thus be used to explain the results satisfactorily. This work opens the way towards integrated photonic-crystal based circuitry within CMOS compatible silicon microelectronics.

4.5 Publications associated with this chapter

R.T. Neal, M.D.C. Charlton, G.J. Parker, C.E. Finlayson, J. J. Baumberg, M.C. Netti, M.E. Zoorob. Photonic Crystal Photoluminescence Modification in Silicon-Rich Silicon Dioxide Waveguides. Oral Presentation, Symposium J, 2003 MRS Spring Meeting, San Francisco, CA

R.T. Neal, C.E. Finlayson, M.E. Zoorob, M.D. Charlton, J.J. Baumberg and G.J. Parker. Photonic Bandgaps in Patterned Waveguides of Silicon-Rich Silicon Dioxide Accepted for publication in Applied Physics Letters, March 29 2004

References

[1] M.E. Zoorob, M.D.B. Charlton, G.J. P arker, J.J. Baumberg, M.C. Netti, Nature, **404** p740-743 (2000)

[2] H. Kosaka, T. Kawashima, A. Tomita, et. al., Journal of Lightwave Technology, **17**(11) p2032-2037 (1999)

[3] P. Ferrand, D. Loi, R. Romestain, Applied Physics Letters, **79**(19) p3017-3019 (2001)

[4] A. Talneau, L. Le Gouezigou , N. Bouadma, M. Kafesaki, C. M. Soukoulis, Applied Physics Letters, **80**(4) p547-549 (2002)

[5] M.C. Netti, M.D.B. Charlton, G.J. Parker, J.J. Baumberg, Applied Physics Letters, **76**(8) p991-993 (2000)

[6] M. Boroditsky, T. F. Krauss, R. Coccioli, R. Vrijen, R. Bhat, Applied Physics Letters, **75**(8) p1036-1038 (1999)

[7] U. Grüning, V. Lehmann, C. M. Engelhardt, Applied Physics Letters, **66**(24) p3254-3256 (1995)

[8] J.D. Joannopoulos, R.D. Meade and J.N. Winn *Photonic Crystals, Molding the Flow of Light.* (Princeton University Press, Princeton, USA, 1995) **ISBN:** 0691037442

[9] K.Sakoda, *Optical Properties of Photonic Crystals.* (Springer, Heidelberg, Germany, 2001)

[10] K.S. Yee, ``Numerical solution of initial boundary value problems involving Maxwell's equations in isotropic media," *IEEE Trans. Antennas Propagat.*, vol. 14, pp. 302-307, Mar. 1966.

[11] A. Taflove, ``Review of the formulation and applications of the finite-difference time-domain method for numerical modeling of electromagnetic wave interactions with arbitrary structures," *Wave Motion*, vol. 10, no. 6, pp. 547-582, 1988.

[12] A. Taflove, *Advances in Computational Electrodynamics, The Finite-Difference Time-Domain Method.* (Artech House, Norwood, USA, 1998) **ISBN:** 0890068348

5 Conclusions

The PhD research which led up to the writing of this thesis was begun in early autumn 2000. At that time there was still great belief in the strength of the telecommunications industry, and the intention of this project was to produce optical devices based upon photonic crystals, operating at 1.55μm, which would have application in the still burgeoning telecommunications market. Within six months what became known as the "technology shares bubble" had collapsed, forcing a change in the ultimate objective of the research.

Rather than focus upon the applications of photonic crystals for the telecommunications industry, already well served by such developments as the Erbium-Doped Fibre Amplifier, it was decided to concentrate the remaining time of the PhD upon potential applications for photoluminescent silicon nanocrystals, formed in silicon-rich silicon dioxide (SRSO).

5.1 Silicon-Based Optical Circuitry, a Review

As was discussed in Chapter 1, photoluminescence from silicon nanocrystals formed in silicon-rich silicon dioxide was first reported in 1993[1]. Work carried out by researchers over the next seven years led to an article published in Nature in November 2000[2], in which not only photoluminescence but also optical gain was reported from silicon nanocrystals. Photonic crystals, incorporated into one and two-dimensional waveguide structures had already been well explored, with the potential applications for photonic crystals for providing essential optical structures such as tight-angle waveguide bends in low refractive-index contrast materials being widely appreciated.

From available literature, it became clear that there was a gap in the current shared understanding. There was no report of the waveguide transmission properties of

photoluminescent SRSO, nor was there any literature demonstrating 2-dimensional photonic crystals formed in waveguides of photoluminescent SRSO.

It was, and still is, believed that there is a need for silicon-based optical circuitry at the boundary between the computer and the massive telecommunications network. More importantly though, there are real potential gains to be had through the use of optical interconnects where circuitry has become too complex, too cluttered, or simply too fast for conventional electrical interconnects to manage.

To explore the potential for optical integrated circuitry, a theoretical investigation of one promising optical component, the Arrayed Waveguide Grating (AWG), was carried out and discussed in Chapter 2. First a modelling program for 2-dimensional planar waveguides was developed, based upon conventional plane-wave techniques derived from basic electromagnetics. This program, the Matlab Modefinder, continued to be used throughout the PhD program as a waveguide modelling tool, and also as a component of a more complex program written to assist with the design of an idealised AWG.

As part of this work, a process was developed for a material which was very suitable for standard integrated optical components and might be formed through deposition by Plasma Enhanced Chemical Vapour Deposition (PECVD). Silicon OxyNitride (SiON) is a material which may be deposited with refractive indices ranging from that of Silicon Dioxide (SiO_2) at n = 1.46 to that of Silicon Nitride (Si_3N_4) at n = 2.02. It was found that waveguides formed SiON which has been adapted from the standard PECVD SiO_2 process formed good optical waveguides for the visible region of the spectrum, while SiON waveguides formed through an adaptation of the PECVD Si_3N_4 process made poor optical waveguides.

The AWG design program developed using the Matlab Modefinder was operated with both SiON and Si_3N_4 waveguide core materials. This program was then used to furnish designs for AWGs consisting of waveguides of different thickness, refractive

index, and for AWGs with varying numbers of waveguide channels or density of multiplexer channel spacings.

No AWG was fabricated to confirm this work. It became clear from our work that while AWGs offered significant theoretical gains over their bulk optical counterparts, they still remained far from optimal for true integrated optical circuitry. The fabrication of an AWG is complex, with strict tolerances on waveguide uniformity on etch anisotropy and selectivity. A potential photonic crystal component showing promise as an even smaller wavelength division multiplexer/demultiplexer was the superprism, introduced in Chapter 1. The potential applications of photonic crystal as compact optical components in silicon-based optical circuits were sufficiently interesting to prompt further study, especially in the emerging field of light emitting nanocrystalline silicon devices.

5.2 Waveguides in Photoluminescent SRSO

Once the process for depositing photoluminescent SRSO layers had been developed, as is described in Chapter 3, planar waveguides were formed with SRSO core layers. As with the SiON waveguides, it was possible to deposit layers with a refractive index range from 1.55-1.71. This range was extended to 1.53-1.92 after the thermal anneal at 1150°C which was necessary to form the photoluminescent silicon nanoparticles, with the SRSO incorporating the largest proportion of silicon having the greatest refractive index change.

Both photoluminescence and waveguide transmission measurements were carried out for waveguides of three fabricated types of SRSO, with several models being proposed to explain the behaviour observed in the different regions of the electromagnetic spectrum. It was found that annealed SRSO emitted a broad band of light from 600-1100nm, while the same material unannealed would emit no light. It was also found that the thermal anneal fabrication stage had a detrimental effect upon the waveguide transmission at wavelengths below 700nm.

Our results showed that the intensity of photoluminescence emission from silicon nanocrystals was dependent upon the duration of the thermal anneal, with the greatest increase in intensity being at the short wavelength end of the nanocrystal emission spectrum. The luminescence spectrum for silicon nanocrystals was shown to be dependent upon the silicon incorporation of the layer, with a higher silicon incorporation leading to a longer wavelength of peak photoluminescence intensity. It is important to note that while silicon incorporation and anneal duration had a strong effect upon the wavelength of peak intensity and upon the luminescence intensity, the wavelength below which there was strong optical absorption remains unchanged.

The optical absorption of the SRSO waveguide layer was attributed to bandgap absorption in delocalised states of the silicon nanocrystals. Photoluminescence is attributed to radiative recombination at interface states between the silicon nanocrystals and the surrounding SiO_2 matrix. While the shift in the wavelength of peak intensity may be considered a result of different cluster size distributions as the silicon incorporation of the SRSO changes, the increase in photoluminescence intensity as a function of anneal time is either due to the continued formation of radiative interface states or to the annealing out of non-radiative recombination pathways associated with defects formed during the amorphous PECVD process.

As an extension of the SRSO waveguide development work, an attempt was made to recreate the alleged gain measured in SRSO waveguides using colinear pump and probe laser beams at varying power densities. Once results had been analysed it was possible to state that the addition of a 514nm pump signal, or increasing the intensity of that pump signal, had no effect upon a white light beam ravelling in the same waveguide. This permits us to state that for this particular SRSO material, there is no optical gain.

It was concluded at the end of Chapter 3 that waveguides of SRSO exhibit favourable optical properties for the portion of the electromagnetic spectrum in which the core

material is photoluminescent. This work prepares the way for integrated devices incorporating luminescent SRSO waveguides as a fundamental component, although not as a laser as was originally hoped.

5.3 Photonic Crystals in SRSO Waveguides

With a process for fabricating waveguides with a core layer of photoluminescent SRSO having been developed, a further process was formed for the etching of 2D photonic crystals through the waveguide. Photonic crystals were fabricated with lattice pitches ranging from 260 - 610nm, and with hole diameters ranging from 160 - 460nm. The majority of fabricated patterns were triangular-lattice photonic crystals oriented between the ΓX and ΓJ directions. A few 1D photonic crystals were also successfully fabricated.

The photonic bandgaps of the fabricated photonic crystals were evaluated by measuring the ratio of transmitted photoluminescence excited at the far side of the photonic crystal, to the transmitted photoluminescence excited at the near side. This method proved successful, and experimental data was gained for higher-order 2D photonic bandgaps fabricated in a luminescent silicon-based material. We believe these are the first reported photonic bandgaps in SRSO.

Experimental results reported in Chapter 4 (Figures 4.2.9-10, 4.2.13-14) demonstrate how the location of photonic bandgap features in all propagation directions in the reduced Brillouin zone is dependent upon the hole diameter and lattice pitch of the photonic crystal. The photonic bandgaps demonstrated in this thesis were all higher order photonic bandgaps. Regrettably, we were unable to demonstrate a primary bandgap in SRSO, despite the successful fabrication of structures with an adequately small lattice pitch, evenly spaced rows, and well-defined holes.

To complement the experimental results, simulations were carried out using 2D plane wave expansion techniques, and 3D Finite Difference Time Domain methods. Both

simulation methods provided good overlap with the experimentally obtained results. Results obtained through simulation were of great utility, especially for the allocation of a measured feature to a particular calculated photonic band. Small adjustments were necessary for the alignment of the simulated to the measured features, of the order of tens of nanometers. While it is not expected that the 2D simulation technique will provide a perfect match for a 3D system, the discrepancy in the 3D Finite Difference Time Domain simulation results is ascribed to an error in the refractive index assigned to the waveguide core layer for simulation purposes.

In summary, waveguides of photoluminescent SRSO were patterned with 2D triangular-lattice photonic crystals, and the photoluminescence of the Si nanocrystals was used to probe the higher-order photonic bandgaps of the structure.

5.4 Final Conclusions and Future Work Pending

Following a study into the state of integrated silicon optical circuitry circa 2001, work was carried out to investigate the applications of photoluminescent silicon nanocrystals in a photonic circuit. Waveguides, as the basic building block of any photonic circuitry, were fabricated by PECVD. These waveguides exhibited low optical loss in the wavelength region in which the SRSO was luminescent, and the optical characteristics over a very large wavelength were reported. SRSO waveguides were found to have good optical transmission below 1300nm, though the activation anneal required to produce photoluminescence in the waveguides was detrimental to the transmission below 700nm. Proposed mechanisms for the material absorption and photoluminescence state that they result from different mechanisms, with the absorption being attributed to the nanocrystals themselves, and with the photoluminescence being due to a radiative decay pathway at the boundary between the silicon and silicon dioxide regions.

Once the waveguides had been well characterised, photonic crystals were incorporated into the luminescent waveguides. 2D triangular lattice patterns were

etched through the waveguide, and provided a means of altering the transmitted photonic crystal spectrum from an excitation spot at one side of the photonic crystal region. This photonic crystal modification of the photoluminescence spectrum allowed identification of angle-tuned photonic bandgaps in close agreement with 2-dimensional plane wave expansion and finite-difference time domain simulations.

The photonic crystals demonstrated in this thesis are higher order bandgaps, which we would anticipate have less broad features and much lower extinction coefficients than for the primary bandgap from theory. The use of 2D photonic crystals and of engineered combinations of 1D and 2D photonic structures, has the potential to allow highly elaborate tailoring of the propagation and group-velocity dispersion of the core photoluminescence through the waveguide structure. We believe this has very exciting implications for the development of integrated photonic-crystal based optical circuits.

Work which may be carried out to progress this work further includes the electrical characterisation of SRSO layers, delayed due to fabrication complications beyond a reasonable timescale to include in this thesis. Layers of chrome, gold, and aluminium were successfully adhered to layers of SRSO, which might be patterned to form a base for lateral electrical characterisation.

It has been proposed that a collaboration between Dr Darren Bagnall and several of his PhD students might see luminescent layers partially masked with a chiral structure which has the reported properties of modifying the polarization of reflected light in a controlled manner [3, 4].

Ultimately, it is hoped that the inclusion of both luminescent SRSO and photonic crystals into silicon-based optoelectronic/optical circuitry will facilitate the melding of the optical and electrical disciplines into a region which may benefit from the strengths of both parent research areas.

Publications resulting from this research

R.T. Neal, M.D.C. Charlton, C.E. Finlayson, M.C. Netti, M.Josey, G.J. Parker. *High Intensity Photoluminescence in Waveguides of Silicon-Rich Silicon dioxide*, Poster Session, Symposium J, 2003 MRS Spring Meeting, San Francisco, CA

R.T. Neal, M.D.C.Charlton, G.J. Parker, C.E. Finlayson, M.C. Netti and J.J. Baumberg. *Ultrabroadband Transmission Measurements on Waveguides of Silicon-Rich Silicon Dioxide*. Applied Physics Letters **83**(22), p4598-4600 (2003)

R.T. Neal, C.E. Finlayson, M.D.C. Charlton, G.J. Parker, J. J. Baumberg, M.C. Netti, M.E. Zoorob, *Ultra-Broadband Spectroscopy of Waveguides of Nanocrystalline Silicon-rich Silica*. Presented in Liverpool to the RSC (2003)

R.T. Neal, M.D.C. Charlton, G.J. Parker, C.E. Finlayson, J. J. Baumberg, M.C. Netti, M.E. Zoorob. *Photonic Crystal Photoluminescence Modification in Silicon-Rich Silicon Dioxide Waveguides*. Oral Presentation, Symposium J, 2003 MRS Spring Meeting, San Francisco, CA

R.T. Neal, C.E. Finlayson, M.E. Zoorob, M.D. Charlton, J.J. Baumberg and G.J. Parker. *Photonic Bandgaps in Patterned Waveguides of Silicon-Rich Silicon Dioxide* Applied Physics Letters **84**(13), p2415-2417 (2004)

References

[1] T. Shimizu-Iwayama, M. Ohshima, T. Niimi, S. Nakao, K. Saitoh, Journal of Physics: Condensed Matter, **5** pL375-L380 (1993)

[2] F. Iacona, G. Franzò, C. Spinella, Journal of Applied Physics, **87**(3) p1295-1303 (2000)

[3]A. S. Schwanecke, A. Krasavin, D. M. Bagnall, A. Potts, A.V. Zayats, and N. I. Zheludev, Physical Review Letters **91**(24) 247404 (2003)

[4]A. Papakostas, A. Potts, D.M. Bagnall, S.L. Prosvirnin, H.J. Coles and N.I. Zheludev, Physical Review Letters **90** (10)107404 (2003)

Appendix A - Matlab Code

A.1 Modefinder for a slab waveguide

```
function solve = solve()
% Plots TE V versus Eeta. Gives TE and TM modes
n1=input('Please enter core index:  ');
n2=input('Please enter cladding index:  ');
d=input('Please enter core depth in microns:  ')*10^-6;
la0=input('Please enter wavelength in microns:  ')*10^-6;
V=2*pi/la0*d*sqrt(n1^2-n2^2);
x=0:0.00001:V/2;

%TE modes
plot(x, rhs(x,V),x,lhs(x),x,lhs2(x))
axis([0 V/2+.2 0 V/2+.2])
xlabel('Eeta')
legend('','Symmetric','Asymmetric')
options=optimset;
Symmetric_Eeta_TE1 =fzero(@Eetafindsym,V/4,options,V);
Symmetric_b_TE1=1-4*Symmetric_Eeta_TE1^2/V^2;
Symmetric_BetaOnK_TE1=sqrt(n2^2+Symmetric_b_TE1*(n1^2-n2^2))
if V/2>pi/2
 Asymmetric_Eeta_TE2 =fzero(@Eetafindasym,V/4,options,V);
 Asymmetric_b_TE2=1-4*Asymmetric_Eeta_TE2^2/V^2;
 Asymmetric_BetaOnK_TE2=sqrt(n2^2+Asymmetric_b_TE2*(n1^2-n2^2))
end

%TM modes
figure
ratio=(n1/n2)^2;
plot(x, rhsTM(x,V, ratio),x,lhs(x),x,lhs2(x))
axis([0 V/2+.2 0 (n1^2/n2^2)*V/2+.2])
xlabel('Eeta')
legend('','Symmetric','Asymmetric')
Symmetric_Eeta_TM1 =fzero(@EetafindsymTM,V/4,options,V, ratio);
Symmetric_b_TM1=1-4*Symmetric_Eeta_TM1^2/V^2;
Symmetric_BetaOnK_TM1=sqrt(n2^2+Symmetric_b_TM1*(n1^2-n2^2))
```

A.2 Modefinder for a rib waveguide

```
function complete = complete()
% finds V from n1, n2, la0, d % H1 line
n1=input('Please enter core index:  ');
n2=input('Please enter cladding index:  ');
d=input('Please enter core depth in microns:  ')*10^-6;
la0=input('Please enter wavelength in microns:  ')*10^-6;
V=2*pi/la0*d*sqrt(n1^2-n2^2);
x=0:0.00001:V/2;
options=optimset;
```

```
Symmetric_Eeta =fzero(@Eetafindsym,V/4,options,V);
Symmetric_b=1-4*Symmetric_Eeta^2/V^2;
Symmetric_BetaOnK=sqrt(n2^2+Symmetric_b*(n1^2-n2^2))

%for two-dimensional refractive index
V=2*pi/la0*d*sqrt(Symmetric_BetaOnK^2-n2^2);
x=0:0.00001:V/2;
Square_Eeta =fzero(@Eetafindsym,V/4,options,V);
Square_b=1-4*Square_Eeta^2/V^2;
Square_BetaOnK=sqrt(n2^2+Square_b*(Symmetric_BetaOnK^2-n2^2))
if V/2>pi/2
 disp('This waveguide is not monomode at the chosen wavelength')
end
```

A.3 AWG design program

```
function complete = complete()
% Completed AWG design program

%Array Waveguide parameters (all dimensions in nm)
wg_width=input('Please enter waveguide width (nm):  ');%500                    in nm
wg_core=wg_width;                % a square waveguide
lambda=1550;                  "% in nm
w=2*pi*lambda;                  %w, in nm
n_core=input('Please enter core index:  ');
n_clad=1.46;  n_surround=1;  n_sub=1.46;  %waveguide parameters
n_mode=modefinder(n_core, n_clad, wg_width*10^-3, lambda*10^-3);  %effective index of
waveguide
n_slab=modefinder_slab(n_core,n_clad,wg_width*10^-3, lambda*10^-3);  %effective index of slab
region
no_phasor_channels=input('Please enter number of phasor channels:  ');
phasor_gap=0;                  %space between exits in the slab
phasor_taper_length=0;            %SN=0
ip_wg_width=wg_width;              %input waveguide is the same as others
ip_wg_gap=phasor_gap;               %same as input
L_slab=.1*10^6;

%first approximations for the awg
lambda_guide=lambda/n_slab;
initial_spot_size=wg_width/2;
op_aperture_length=(wg_width+phasor_gap)*(no_phasor_channels+1);
approx_divergence_angle=atan(lambda_guide/(pi*initial_spot_size));
approx_FSPR_radius=op_aperture_length/(2*approx_divergence_angle);
theta=op_aperture_length/(2*approx_FSPR_radius);
beam_width=approx_FSPR_radius*sin(theta);

%more accurate gaussian solutions
actual_propagation_dist=sqrt(((beam_width/initial_spot_size)^2-
1)*(initial_spot_size^4*pi^2/lambda_guide^2));
actual_wavefront_width=sqrt(1+(lambda_guide^2*actual_propagation_dist^2/(pi^2*initial_spot_size^
4)))*initial_spot_size;
FSPR_radius=approx_FSPR_radius*(1+(initial_spot_size^4*pi^2)/(lambda_guide^2*approx_FSPR_ra
dius^2));  %slab length (radius)
actual_divergence_angle=atan(actual_wavefront_width/actual_propagation_dist);
```

```
radial_phasor_channel_angle=((wg_width+phasor_gap)/(2*pi*FSPR_radius))*360;

n=0:no_phasor_channels-1;          %sets up indexing for waveguide channels: 0 on outside, N on
inside

nc=n_mode;
ns=n_slab;
Nc=nc;
d1=ip_wg_width+ip_wg_gap;          %entry waveguide spacing
D1=wg_width+phasor_gap;            %output waveguide spacing
deltalambda=input('Please enter channel spacing (nm):  ');
deltaL=(ns*d1*D1*lambda)/(Nc*FSPR_radius*deltalambda);
alpha_offset=1;                    %set alpha to smallest possible angle
flag=0;                            %flag is when to break
list=0;                            %initialise list of angles
list2=0;                           %initialise list of radii
list3=0;                           %initialise list of X sizes
list4=0;                           %initialise list of Y sizes
bottom=0;                          %initialise lowest angle
list5=0;                           %initialise list of bend losses
list6=0;                           %initialise list of slab separations
while flag==0
  sums=fiddles(alpha_offset, no_phasor_channels, radial_phasor_channel_angle, lambda,
FSPR_radius, ns, d1, D1, phasor_taper_length, lambda_guide, L_slab, Nc, deltalambda);
  if sums>0.000001                 %if angle is too big
     flag=1;
     if size(list)==1              %ie if the slab separation is too small with this channel spacing
        L_slab=L_slab+.1*10^6;
        alpha_offset=1;            %reset alpha offset to smallest poss angle for new L_slab
        if L_slab>5*10^6
           break
        end
        flag=0;
     elseif BendLossOut>=.5        %ie if loss of smallest bend is too large
        L_slab=L_slab+.1*10^6;
        alpha_offset=1;            %reset alpha offset to smallest poss angle for new L_slab
        if L_slab>5*10^6
           break
        end
        flag=0;
     else
     alpha_offset=list(2);end

  elseif sums<-0.000001            %if angle is too small
     alpha_offset=alpha_offset+1;
     flag=0;
     bottom=1;
  else
     if bottom==1                  %if angle is ok
        list=[list alpha_offset];
        leastR=LeastRadius(alpha_offset, no_phasor_channels, radial_phasor_channel_angle, lambda,
FSPR_radius, ns, d1, D1, phasor_taper_length, lambda_guide, L_slab, Nc, deltalambda);
        SizeX=SizeofX(alpha_offset, no_phasor_channels, radial_phasor_channel_angle, FSPR_radius,
phasor_taper_length, L_slab, deltaL, wg_width);
```

```
        SizeY=SizeofY(alpha_offset, no_phasor_channels, radial_phasor_channel_angle, FSPR_radius,
 phasor_taper_length, L_slab, deltaL, wg_width);
        BendLossOut=BendLoss(wg_width/10^3, leastR/10^3, lambda/10^3, n_clad, n_mode, n_core);
        list2=[list2 leastR];
        list3=[list3 SizeX];
        list4=[list4 SizeY];
        list5=[list5 BendLossOut];
        list6=[list6 L_slab*10^-6];
        alpha_offset=alpha_offset+1;
        flag=0;
      else
        alpha_offset=alpha_offset-1;    %choose largest alpha_offset
      end
    end
  end

 if size(list)==1
   disp('No solution');
 else
 size(list); ans(2); list=list(2:ans);          %remove spurious first argument on all lists
 size(list2); ans(2); list2=list2(2:ans)*10^-3;
 size(list3); ans(2); list3=list3(2:ans);
 size(list4); ans(2); list4=list4(2:ans);
 size(list5); ans(2); list5=list5(2:ans);
 size(list6); ans(2); list6=list6(2:ans);
 size(list); ans(2); howmuch=1:ans;

 %and now start displaying results
 list=[list' list2' list3' list4' list5' list6' howmuch'];
 disp('valid alpha_offsets   bend (um)    X (um)       Y (um)     Bend Loss     Separation (cm)
 Row#');disp(list)
 end
 size(list);
 answer=ans(1);
 flob=input('which row to print? (type "0" to exit)  :  ');
 if flob>0
  picturesub(n_core, wg_width, no_phasor_channels, list(flob), deltalambda, list(flob,6)*10^6)
  printout(list(flob), no_phasor_channels, radial_phasor_channel_angle, lambda, FSPR_radius, ns, d1,
 D1, phasor_taper_length, lambda_guide, list(flob,6)*10^6, Nc, deltalambda);
  disp ('Slab waveguide radius (um)'); disp (FSPR_radius/10^3);
 end
```

A.4 Sub-functions used in modefinders and AWG program

A.4.1 rhs.m

```
function rhs = rhs(x,V)
rhs=sqrt((V/2)^2-x.^2);
```

A.4.2 lhs.m

```
function lhs = lhs(x)
lhs = x.*tan(x);
```

A.4.3 lhs2.m

```
function lhs2= lhs2(x)
lhs2 = -x.*cot(x);
```

A.4.4 Eetafindsym.m

```
function Eetafindsym = Eetafindsym(x,V)
Eetafindsym=x.*tan(x)-sqrt((V/2)^2-x.^2);
```

A.4.5 Eetafindasym.m

```
function Eetafindasym = Eetafindasym(x,V)
Eetafindasym=-x.*cot(x)-sqrt((V/2)^2-x.^2);
```

A.4.6 rhsTM.m

```
function rhsTM = rhsTM(x,V, ratio)
rhsTM=ratio*sqrt((V/2)^2-x.^2);
```

A.4.7 EetafindsymTM.m

```
function EetafindsymTM = EetafindsymTM(x,V, ratio)
EetafindsymTM=x.*tan(x)-ratio*sqrt((V/2)^2-x.^2);
```

A.4.8 Modefinder.m

```
function modefinder = modefinder(core, clad, depth, lambda)
% finds effective refractive index for a square waveguide from n1, n2, la0, d
%doesn't work for n2~d(microns) for some reason
n1=core;
n2=clad;
d=depth*10^-6;
la0=lambda*10^-6;
V=2*pi/la0*d*sqrt(n1^2-n2^2);
x=0:0.00001:V/2;
options=optimset;
Symmetric_Eeta =fzero(@Eetafindsym,V/3,options,V);
Symmetric_b=1-4*Symmetric_Eeta^2/V^2;
Symmetric_BetaOnK=sqrt(n2^2+Symmetric_b*(n1^2-n2^2));

%for two-dimensional refractive index
V=2*pi/la0*d*sqrt(Symmetric_BetaOnK^2-n2^2);
```

```
x=0:0.00001:V/2;
Square_Eeta =fzero(@Eetafindsym,V/3,options,V);
Square_b=1-4*Square_Eeta^2/V^2;
modefinder=sqrt(n2^2+Square_b*(Symmetric_BetaOnK^2-n2^2));
if V/2>pi/2
 disp('This waveguide is not monomode at the chosen wavelength')
end
```

A.4.9 Modefinder_slab.m

```
function modefinder_slab = modefinder_slab(core, clad, depth, lambda)
% finds effective refractive index for a slab waveguide from n1, n2, la0, d
n1=core;
n2=clad;
d=depth*10^-6;
la0=lambda*10^-6;
V=2*pi/la0*d*sqrt(n1^2-n2^2);
x=0:0.00001:V/2;
options=optimset;
Symmetric_Eeta =fzero(@Eetafindsym,V/3,options,V);
Symmetric_b=1-4*Symmetric_Eeta^2/V^2;
modefinder_slab=sqrt(n2^2+Symmetric_b*(n1^2-n2^2));

if V/2>pi/2
 disp('This waveguide is not monomode at the chosen wavelength')
end
```

A.4.10 Fiddles.m

```
function fiddles= fiddles(alpha_offset, no_phasor_channels, radial_phasor_channel_angle, lambda,
        FSPR_radius, ns, d1, D1, phasor_taper_length, lambda_guide, L_slab, Nc, deltalambda)
% Work out if the solution is valid for a certain alpha_offset

alpha=(((no_phasor_channels-1)-(no_phasor_channels-
1)/2)*radial_phasor_channel_angle)+alpha_offset;
n=0:no_phasor_channels-1;
Sn=phasor_taper_length;
deltaL=(ns*d1*D1*lambda)/(Nc*FSPR_radius*deltalambda);
thetasubn=(alpha-(n-(no_phasor_channels-1)/2)*radial_phasor_channel_angle)*pi/180;
thetan=(alpha-((no_phasor_channels-1)-(no_phasor_channels-
1)/2)*radial_phasor_channel_angle)*pi/180;
Rn=(L_slab/2-(FSPR_radius + Sn)*cos(thetan))/sin(thetan);
for i=1:no_phasor_channels
  Rsubn(i)=(L_slab/2-(FSPR_radius+Sn+Rn*thetan+(no_phasor_channels-i)*deltaL/2)...
       *cos(thetasubn(i)))/(sin(thetasubn(i))-thetasubn(i)*cos(thetasubn(i)));
  Ssubn(i)=Sn+(Rn*thetan-Rsubn(i)*thetasubn(i))+(no_phasor_channels-i)*deltaL/2;;
end
fiddles=sum(Rsubn)-sum(abs(Rsubn))-sum(Ssubn)+sum(abs(Ssubn));
```

A.4.11 LeastRadius.m

```
function LeastRadius= LeastRadius(alpha_offset, no_phasor_channels, radial_phasor_channel_angle,
        lambda, FSPR_radius, ns, d1, D1, phasor_taper_length, lambda_guide, L_slab, Nc,
deltalambda)
% Returns the minimum bend radius for each alpha_offset

alpha=(((no_phasor_channels-1)-(no_phasor_channels-
1)/2)*radial_phasor_channel_angle)+alpha_offset;
n=0:no_phasor_channels-1;
Sn=phasor_taper_length;

deltaL=(ns*d1*D1*lambda)/(Nc*FSPR_radius*deltalambda);
FSR=(lambda*FSPR_radius)/(ns*d1);
Nch=(lambda*FSPR_radius)/(ns*d1*D1);
thetasubn=(alpha-(n-(no_phasor_channels-1)/2)*radial_phasor_channel_angle)*pi/180;
thetan=(alpha-((no_phasor_channels-1)-(no_phasor_channels-
1)/2)*radial_phasor_channel_angle)*pi/180;
Rn=(L_slab/2-(FSPR_radius + Sn)*cos(thetan))/sin(thetan);
for i=1:no_phasor_channels
  Rsubn(i)=(L_slab/2-(FSPR_radius+Sn+Rn*thetan+(no_phasor_channels-i)*deltaL/2)...
       *cos(thetasubn(i)))/(sin(thetasubn(i))-thetasubn(i)*cos(thetasubn(i)));
  Ssubn(i)=Sn+(Rn*thetan-Rsubn(i)*thetasubn(i))+(no_phasor_channels-i)*deltaL/2;;
end

LeastRadius=min(Rsubn);
```

A.4.12 SizeofX.m

```
function SizeofX= SizeofX(alpha_offset, no_phasor_channels, radial_phasor_channel_angle,
        FSPR_radius, phasor_taper_length, L_slab, deltaL, wg_width)
% Returns the minimum width for each alpha_offset

alpha=(((no_phasor_channels-1)-(no_phasor_channels-
1)/2)*radial_phasor_channel_angle)+alpha_offset;
Sn=phasor_taper_length;
thetasubn=(alpha-(1-(no_phasor_channels-1)/2)*radial_phasor_channel_angle)*pi/180;
thetan=(alpha-((no_phasor_channels-1)-(no_phasor_channels-
1)/2)*radial_phasor_channel_angle)*pi/180;
Rn=(L_slab/2-(FSPR_radius + Sn)*cos(thetan))/sin(thetan);
  Rsubn=(L_slab/2-(FSPR_radius+Sn+Rn*thetan+(no_phasor_channels-1)*deltaL/2)...
       *cos(thetasubn(1)))/(sin(thetasubn(1))-thetasubn(1)*cos(thetasubn(1)));
  Ssubn=Sn+(Rn*thetan-Rsubn(1)*thetasubn(1))+(no_phasor_channels-1)*deltaL/2;;
  offset=((FSPR_radius+Ssubn)*sin(thetasubn(1))-Rsubn*cos(thetasubn(1)))*10^-3;
rad_inner=(Rsubn-wg_width/2)*10^-3;
rad_outer=(Rsubn+wg_width/2)*10^-3;
theta_circle=-thetasubn(1):2*thetasubn(1)/50:thetasubn(1);
x2=[rad_inner.*sin(theta_circle) rad_outer.*sin(fliplr(theta_circle))];
MinimumX_um=min(x2);
SizeofX=-MinimumX_um*2;
```

A.4.13 SizeofY.m

```
function SizeofY= SizeofY(alpha_offset, no_phasor_channels, radial_phasor_channel_angle,
FSPR_radius, phasor_taper_length, L_slab, deltaL, wg_width)
```

```
% Returns the minimum length for each alpha  offset

alpha=(((no_phasor_channels-1)-(no_phasor_channels-
1)/2)*radial_phasor_channel_angle)+alpha_offset;
Sn=phasor_taper_length;
thetasubn=(alpha-(1-(no_phasor_channels-1)/2)*radial_phasor_channel_angle)*pi/180;
thetan=(alpha-((no_phasor_channels-1)-(no_phasor_channels-
1)/2)*radial_phasor_channel_angle)*pi/180;
Rn=(L_slab/2-(FSPR_radius + Sn)*cos(thetan))/sin(thetan);

 Rsubn=(L_slab/2-(FSPR_radius+Sn+Rn*thetan+(no_phasor_channels-1)*deltaL/2)...
      *cos(thetasubn(1)))/(sin(thetasubn(1))-thetasubn(1)*cos(thetasubn(1)));
 Ssubn=Sn+(Rn*thetan-Rsubn(1)*thetasubn(1))+(no_phasor_channels-1)*deltaL/2;;

 offset=((FSPR_radius+Ssubn)*sin(thetasubn(1))-Rsubn*cos(thetasubn(1)))*10^-3;
rad_inner=(Rsubn-wg_width/2)*10^-3;
rad_outer=(Rsubn+wg_width/2)*10^-3;
theta_circle=-thetasubn(1):2*thetasubn(1)/50:thetasubn(1);
y2=[rad_inner.*cos(theta_circle)+offset rad_outer.*cos(fliplr(theta_circle))+offset];
SizeofY=max(y2);
```

A.4.14 BendLoss.m

```
function BendLoss=BendLoss(wg_width, Rc, lambda, n_clad, n_mode, n_core)
%Bend Loss of waveguide

V=2*pi/lambda*wg_width*sqrt(n_core^2-n_clad^2);    %standard equation from book for V
k0=2*pi/lambda;                                    %again standard equation for k0
Beta=n_mode*k0;
a=wg_width/2;                                      %treat waveguide as cylindrical fiber with radius not depth
U=a*sqrt(k0^2*n_core^2-Beta^2);                    %standard equation from book
W=a*sqrt(Beta^2-k0^2*n_clad^2);                    %standard equation from book
K = besselk(1,W);
BendLoss=4.343*sqrt(pi/(4*a*Rc))*(U/(V*K))^2*(1/W^3/2)*exp(-
        ((2*W^3)/(3*k0^2*a^3*n_core^2))*Rc);
```

A.4.15 Picturesub.m

```
function picturesub= picturesub(n_core, wg_width, no_phasor_channels, alpha_offset, deltalambda,
        L_slab)
% Draw picture of AWG
% Actually solves it again, but all the same thing...

%Array Waveguide parameters (all dimensions in nm)
wg_core=wg_width;                  % a square waveguide
lambda=1550;                       %in nm
n_clad=1.46;  n_surround=1;  n_sub=1.46;          %waveguide parameters (surrounded by SiO2)
n_mode=modefinder(n_core, n_clad, wg_width*10^-3, lambda*10^-3);          %effective n
n_slab=modefinder_slab(n_core,n_clad,wg_width*10^-3, lambda*10^-3);  %effective index of slab
region
min_bend_radius=1850000;
phasor_gap=0;                      %space between exits in the slab
phasor_taper_length=0;             %SN=0
```

```
ip_wg_width=wg_width;          %input waveguide is the same as others
ip_wg_gap=0;                   %all is square.


%first approximations for the awg
lambda_guide=lambda/n_slab;
initial_spot_size=wg_width/2;
op_aperture_length=(wg_width+phasor_gap)*(no_phasor_channels+1);
approx_divergence_angle=atan(lambda_guide/(pi*initial_spot_size));
approx_FSPR_radius=op_aperture_length/(2*approx_divergence_angle);
theta=op_aperture_length/(2*approx_FSPR_radius);
beam_width=approx_FSPR_radius*sin(theta);
propagation_distance=approx_FSPR_radius*cos(theta);
arc_length=2*theta*approx_FSPR_radius;

%more accurate gaussian solutions
actual_propagation_dist=sqrt(((beam_width/initial_spot_size)^2-
        1)*(initial_spot_size^4*pi^2/lambda_guide^2));
actual_wavefront_width=sqrt(1+(lambda_guide^2*actual_propagation_dist^2/(pi^2*initial_spot_size^
4)))*    initial_spot_size;
actual_wavefront_radius=approx_FSPR_radius*(1+(initial_spot_size^4*pi^2)/(lambda_guide^2*appro
x_F      SPR_radius^2));
actual_divergence_angle=atan(actual_wavefront_width/actual_propagation_dist);
actual_arc_length=actual_divergence_angle*actual_wavefront_radius*2;

FSPR_radius=actual_wavefront_radius;
radial_phasor_channel_angle=((wg_width+phasor_gap)/(2*pi*FSPR_radius))*360;

n=0:no_phasor_channels-1;      %sets up indexing for waveguide channels: 0 on outside, N on
inside

nc=n_mode;          %n in waveguides
ns=n_slab;          %n in slab:
Nc=nc;
d1=ip_wg_width+ip_wg_gap;      %entry waveguide spacing
D1=wg_width+phasor_gap;        %output waveguide spacing

alpha=(((no_phasor_channels-1)-(no_phasor_channels-
1)/2)*radial_phasor_channel_angle)+alpha_offset;

Sn=phasor_taper_length;

deltaL=(ns*d1*D1*lambda)/(Nc*FSPR_radius*deltalambda) ;
FSR=(lambda*FSPR_radius)/(ns*d1);
Nch=(lambda*FSPR_radius)/(ns*d1*D1);
thetasubn=(alpha-(n-(no_phasor_channels-1)/2)*radial_phasor_channel_angle)*pi/180;
thetan=(alpha-((no_phasor_channels-1)-(no_phasor_channels-
1)/2)*radial_phasor_channel_angle)*pi/180;
Rn=(L_slab/2-(FSPR_radius + Sn)*cos(thetan))/sin(thetan);
for i=1:no_phasor_channels
  Rsubn(i)=(L_slab/2-(FSPR_radius+Sn+Rn*thetan+(no_phasor_channels-i)*deltaL/2)...
       *cos(thetasubn(i)))/(sin(thetasubn(i))-thetasubn(i)*cos(thetasubn(i)));
  Ssubn(i)=Sn+(Rn*thetan-Rsubn(i)*thetasubn(i))+(no_phasor_channels-i)*deltaL/2;;
end
Arc_Lengthsubn=Rsubn.*thetasubn;
Total_lengthsubn=Arc_Lengthsubn+Ssubn;
```

```
a=2:1:no_phasor_channels-1;
for a=2:1:no_phasor_channels;
  deltaplsuba(a)=Total_lengthsubn(a-1)-Total_lengthsubn(a);
end
%display
figure
hold
for i=1:no_phasor_channels
x1=[-L_slab/2+wg_width/2*cos(pi/2-thetasubn(i)) ...
      -L_slab/2+wg_width/2*cos(pi/2-thetasubn(i))+(FSPR_radius+Ssubn(i))*cos(thetasubn(i))...
       -L_slab/2-wg_width/2*cos(pi/2-thetasubn(i))+(FSPR_radius+Ssubn(i))*cos(thetasubn(i))...
        -L_slab/2-wg_width/2*cos(pi/2-thetasubn(i))]*10^-3;
y1=[-wg_width/2*sin(pi/2-thetasubn(i)) ...
      -wg_width/2*sin(pi/2-thetasubn(i))+(FSPR_radius+Ssubn(i))*sin(thetasubn(i))...
         wg_width/2*sin(pi/2-thetasubn(i))+(FSPR_radius+Ssubn(i))*sin(thetasubn(i))...
          wg_width/2*sin(pi/2-thetasubn(i))]*10^-3;
offset=((FSPR_radius+Ssubn(i))*sin(thetasubn(i))-Rsubn(i)*cos(thetasubn(i)))*10^-3;
rad_inner=(Rsubn(i)-wg_width/2)*10^-3;
rad_outer=(Rsubn(i)+wg_width/2)*10^-3;
theta_circle=-thetasubn(i):2*thetasubn(i)/50:thetasubn(i);
x2=[rad_inner.*sin(theta_circle) rad_outer.*sin(fliplr(theta_circle))];
y2=[rad_inner.*cos(theta_circle)+offset rad_outer.*cos(fliplr(theta_circle))+offset];
x3=[L_slab/2-wg_width/2*cos(pi/2-thetasubn(i)) ...
      L_slab/2-wg_width/2*cos(pi/2-thetasubn(i))-(FSPR_radius+Ssubn(i))*cos(thetasubn(i))...
       L_slab/2+wg_width/2*cos(pi/2-thetasubn(i))-(FSPR_radius+Ssubn(i))*cos(thetasubn(i))...
        L_slab/2+wg_width/2*cos(pi/2-thetasubn(i))]*10^-3;
y3=[-wg_width/2*sin(pi/2-thetasubn(i)) ...
      -wg_width/2*sin(pi/2-thetasubn(i))+(FSPR_radius+Ssubn(i))*sin(thetasubn(i))...
         wg_width/2*sin(pi/2-thetasubn(i))+(FSPR_radius+Ssubn(i))*sin(thetasubn(i))...
          wg_width/2*sin(pi/2-thetasubn(i))]*10^-3;
fill(x1,y1,'r')
fill(x2,y2,'g')
fill(x3, y3, 'r')
end
x4=[-L_slab/2 -L_slab/2+FSPR_radius.*cos(thetasubn) -L_slab/2]*10^-3;
y4=[0 FSPR_radius.*sin(thetasubn) 0]*10^-3;
x5=[L_slab/2 L_slab/2-FSPR_radius.*cos(thetasubn) L_slab/2]*10^-3;
y5=[0 FSPR_radius.*sin(thetasubn) 0]*10^-3;
fill(x4,y4,'b')
fill(x5,y5,'b')
hold
```

A.4.16 Printout

```
function printout= printout(alpha_offset, no_phasor_channels, radial_phasor_channel_angle, lambda,
        FSPR_radius, ns, d1, D1, phasor_taper_length, lambda_guide, L_slab, Nc, deltalambda)
% Print chosen solution

alpha=(((no_phasor_channels-1)-(no_phasor_channels-
1)/2)*radial_phasor_channel_angle)+alpha_offset;
n=0:no_phasor_channels-1;
Sn=phasor_taper_length;
deltaL=(ns*d1*D1*lambda)/(Nc*FSPR_radius*deltalambda);
thetasubn=(alpha-(n-(no_phasor_channels-1)/2)*radial_phasor_channel_angle)*pi/180;
```

```
thetan=(alpha-((no_phasor_channels-1)-(no_phasor_channels-
1)/2)*radial_phasor_channel_angle)*pi/180;
Rn=(L_slab/2-(FSPR_radius + Sn)*cos(thetan))/sin(thetan);
for i=1:no_phasor_channels
  Rsubn(i)=(L_slab/2-(FSPR_radius+Sn+Rn*thetan+(no_phasor_channels-i)*deltaL/2)...
        *cos(thetasubn(i)))/(sin(thetasubn(i))-thetasubn(i)*cos(thetasubn(i)));
  Ssubn(i)=Sn+(Rn*thetan-Rsubn(i)*thetasubn(i))+(no_phasor_channels-i)*deltaL/2;;
end

%and now start displaying results
disp('          n       theta(deg)    Radius (um)   Straight (um)')
solutions=[n'+1 thetasubn'*180/pi Rsubn'*10^-3 Ssubn'*10^-3];
disp('dimensions in microns')
disp(solutions)
```

Appendix B - Chip Layouts

A.1 - Rotated Lines

Row	Column Pitch (nm)	Device ID no	Position (X) Diamteter (nm)	Position (Y) Rows	Pattern Text	Type		
1	11	1	43.25	26	T61D08R2	TRIANGULAR	610	80	20
1	12	2	45.75	26	T61D09R2	TRIANGULAR	610	90	20
1	13	3	48.25	26	T61D10R2	TRIANGULAR	610	100	20
1	14	4	50.75	26	T61D12R2	TRIANGULAR	610	120	20
1	15	5	53.25	26	T61D14R2	TRIANGULAR	610	140	20
1	16	6	55.75	26	T61D16R2	TRIANGULAR	610	160	20
1	17	7	58.25	26	T61D18R2	TRIANGULAR	610	180	20
1 CHIP	18	8	60.75	26	ARTEST16	7.50E-07 MHZ CLOCK ORIGINAL TEST			
1 CHIP	19	9	63.25	26	ARTEST16	2.50E-07 MHZ CLOCK ORIGINAL TEST			
1 CHIP	20	10	65.75	26	ARTEST16	7.50E-07 MHZ CLOCK ORIGINAL TEST			
1	21	11	68.25	26	T61D20R2	TRIANGULAR	610	200	20
1	22	12	70.75	26	T61D21R2	TRIANGULAR	610	210	20
1	23	13	73.25	26	T61D24R2	TRIANGULAR	610	240	20
1	24	14	75.75	26	T61D25R2	TRIANGULAR	610	250	20
1	25	15	78.25	26	T61D28R2	TRIANGULAR	610	280	20
1	26	16	80.75	26	T61D30R2	TRIANGULAR	610	300	20
1	27	17	83.25	26	T61D32R2	TRIANGULAR	610	320	20
18	11	18	43.25	111	T61D35R2	TRIANGULAR	610	350	20
18	12	19	45.75	111	T61D36R2	TRIANGULAR	610	360	20
18	13	20	48.25	111	T61D38R2	TRIANGULAR	610	380	20
18	14	21	50.75	111	T61D39R2	TRIANGULAR	610	390	20
18	15	22	53.25	111	T61D40R2	TRIANGULAR	610	400	20
18	16	23	55.75	111	T61D42R2	TRIANGULAR	610	420	20
18	17	24	58.25	111	T61D44R2	TRIANGULAR	610	440	20
18 CHIP	18	25	60.75	111	ARTEST16	7.50E-07 MHZ CLOCK ORIGINAL TEST			
18 CHIP	19	26	63.25	111	ARTEST16	2.50E-07 MHZ CLOCK ORIGINAL TEST			
18 CHIP	20	27	65.75	111	ARTEST16	7.50E-07 MHZ CLOCK ORIGINAL TEST			

18	21	28	68.25	111	T61D45R2	TRIANGULAR	610	450	20
18	22	29	70.75	111	T61D46R2	TRIANGULAR	610	460	20
18	23	30	73.25	111	T61D08R4	TRIANGULAR	610	80	40
18	24	31	75.75	111	T61D09R4	TRIANGULAR	610	90	40
18	25	32	78.25	111	T61D10R4	TRIANGULAR	610	100	40
18	26	33	80.75	111	T61D12R4	TRIANGULAR	610	120	40
18	27	34	83.25	111	T61D14R4	TRIANGULAR	610	140	40
2	8	35	35.75	31	T61D16R4	TRIANGULAR	610	160	40
2	9	36	38.25	31	T61D18R4	TRIANGULAR	610	180	40
2	10	37	40.75	31	T61D20R4	TRIANGULAR	610	200	40
2	11	38	43.25	31	T61D21R4	TRIANGULAR	610	210	40
2	12	39	45.75	31	T61D24R4	TRIANGULAR	610	240	40
2	13	40	48.25	31	T61D25R4	TRIANGULAR	610	250	40
2	14	41	50.75	31	T61D28R4	TRIANGULAR	610	280	40
2	15	42	53.25	31	T61D30R4	TRIANGULAR	610	300	40
2	16	43	55.75	31	T61D32R4	TRIANGULAR	610	320	40
2	17	44	58.25	31	T61D35R4	TRIANGULAR	610	350	40
2	18	45	60.75	31	T61D36R4	TRIANGULAR	610	360	40
2	19	46	63.25	31	T61D38R4	TRIANGULAR	610	380	40
2	20	47	65.75	31	T61D39R4	TRIANGULAR	610	390	40
2	21	48	68.25	31	T61D40R4	TRIANGULAR	610	400	40
2	22	49	70.75	31	T61D42R4	TRIANGULAR	610	420	40
2	23	50	73.25	31	T61D44R4	TRIANGULAR	610	440	40
2	24	51	75.75	31	T61D45R4	TRIANGULAR	610	450	40
2	25	52	78.25	31	T61D46R4	TRIANGULAR	610	460	40
2	26	53	80.75	31	T61D08R6	TRIANGULAR	610	80	60
2	27	54	83.25	31	T61D09R6	TRIANGULAR	610	90	60
2	28	55	85.75	31	T61D10R6	TRIANGULAR	610	100	60
2	29	56	88.25	31	T61D12R6	TRIANGULAR	610	120	60
2	30	57	90.75	31	T61D14R6	TRIANGULAR	610	140	60
17	8	58	35.75	106	T61D16R6	TRIANGULAR	610	160	60
17	9	59	38.25	106	T61D18R6	TRIANGULAR	610	180	60
17	10	60	40.75	106	T61D20R6	TRIANGULAR	610	200	60
17	11	61	43.25	106	T61D21R6	TRIANGULAR	610	210	60
17	12	62	45.75	106	T61D24R6	TRIANGULAR	610	240	60
17	13	63	48.25	106	T61D25R6	TRIANGULAR	610	250	60
17	14	64	50.75	106	T61D28R6	TRIANGULAR	610	280	60
17	15	65	53.25	106	T61D30R6	TRIANGULAR	610	300	60
17	16	66	55.75	106	T61D32R6	TRIANGULAR	610	320	60
17	17	67	58.25	106	T61D35R6	TRIANGULAR	610	350	60
17	18	68	60.75	106	T61D36R6	TRIANGULAR	610	360	60
17	19	69	63.25	106	T61D38R6	TRIANGULAR	610	380	60
17	20	70	65.75	106	T61D39R6	TRIANGULAR	610	390	60
17	21	71	68.25	106	T61D40R6	TRIANGULAR	610	400	60
17	22	72	70.75	106	T61D42R6	TRIANGULAR	610	420	60
17	23	73	73.25	106	T61D44R6	TRIANGULAR	610	440	60
17	24	74	75.75	106	T61D45R6	TRIANGULAR	610	450	60
17	25	75	78.25	106	T61D46R6	TRIANGULAR	610	460	60
17	26	76	80.75	106	T56D08R2	TRIANGULAR	560	80	20
17	27	77	83.25	106	T56D09R2	TRIANGULAR	560	90	20
17	28	78	85.75	106	T56D10R2	TRIANGULAR	560	100	20
17	29	79	88.25	106	T56D12R2	TRIANGULAR	560	120	20
17	30	80	90.75	106	T56D14R2	TRIANGULAR	560	140	20
3	6	81	30.75	36	T56D16R2	TRIANGULAR	560	160	20
3	7	82	33.25	36	T56D18R2	TRIANGULAR	560	180	20
3	8	83	35.75	36	T56D20R2	TRIANGULAR	560	200	20
3	9	84	38.25	36	T56D21R2	TRIANGULAR	560	210	20
3	10	85	40.75	36	T56D24R2	TRIANGULAR	560	240	20

3	11	86	43.25	36	T56D25R2	TRIANGULAR	560	250	20
3	12	87	45.75	36	T56D28R2	TRIANGULAR	560	280	20
3	13	88	48.25	36	T56D30R2	TRIANGULAR	560	300	20
3	14	89	50.75	36	T56D32R2	TRIANGULAR	560	320	20
3	15	90	53.25	36	T56D35R2	TRIANGULAR	560	350	20
3	16	91	55.75	36	T56D36R2	TRIANGULAR	560	360	20
3	17	92	58.25	36	T56D38R2	TRIANGULAR	560	380	20
3	18	93	60.75	36	T56D39R2	TRIANGULAR	560	390	20
3	19	94	63.25	36	T56D40R2	TRIANGULAR	560	400	20
3	20	95	65.75	36	T56D42R2	TRIANGULAR	560	420	20
3	21	96	68.25	36	T56D08R4	TRIANGULAR	560	80	40
3	22	97	70.75	36	T56D09R4	TRIANGULAR	560	90	40
3	23	98	73.25	36	T56D10R4	TRIANGULAR	560	100	40
3	24	99	75.75	36	T56D12R4	TRIANGULAR	560	120	40
3	25	100	78.25	36	T56D14R4	TRIANGULAR	560	140	40
3	26	101	80.75	36	T56D16R4	TRIANGULAR	560	160	40
3	27	102	83.25	36	T56D18R4	TRIANGULAR	560	180	40
3	28	103	85.75	36	T56D20R4	TRIANGULAR	560	200	40
3	29	104	88.25	36	T56D21R4	TRIANGULAR	560	210	40
3	30	105	90.75	36	T56D24R4	TRIANGULAR	560	240	40
3	31	106	93.25	36	T56D25R4	TRIANGULAR	560	250	40
3	32	107	95.75	36	T56D28R4	TRIANGULAR	560	280	40
16	6	108	30.75	101	T56D30R4	TRIANGULAR	560	300	40
16	7	109	33.25	101	T56D32R4	TRIANGULAR	560	320	40
16	8	110	35.75	101	T56D35R4	TRIANGULAR	560	350	40
16	9	111	38.25	101	T56D36R4	TRIANGULAR	560	360	40
16	10	112	40.75	101	T56D38R4	TRIANGULAR	560	380	40
16	11	113	43.25	101	T56D39R4	TRIANGULAR	560	390	40
16	12	114	45.75	101	T56D40R4	TRIANGULAR	560	400	40
16	13	115	48.25	101	T56D42R4	TRIANGULAR	560	420	40
16	14	116	50.75	101	T56D08R6	TRIANGULAR	560	80	60
16	15	117	53.25	101	T56D09R6	TRIANGULAR	560	90	60
16	16	118	55.75	101	T56D10R6	TRIANGULAR	560	100	60
16	17	119	58.25	101	T56D12R6	TRIANGULAR	560	120	60
16	18	120	60.75	101	T56D14R6	TRIANGULAR	560	140	60
16	19	121	63.25	101	T56D16R6	TRIANGULAR	560	160	60
16	20	122	65.75	101	T56D18R6	TRIANGULAR	560	180	60
16	21	123	68.25	101	T56D20R6	TRIANGULAR	560	200	60
16	22	124	70.75	101	T56D21R6	TRIANGULAR	560	210	60
16	23	125	73.25	101	T56D24R6	TRIANGULAR	560	240	60
16	24	126	75.75	101	T56D25R6	TRIANGULAR	560	250	60
16	25	127	78.25	101	T56D28R6	TRIANGULAR	560	280	60
16	26	128	80.75	101	T56D30R6	TRIANGULAR	560	300	60
16	27	129	83.25	101	T56D32R6	TRIANGULAR	560	320	60
16	28	130	85.75	101	T56D35R6	TRIANGULAR	560	350	60
16	29	131	88.25	101	T56D36R6	TRIANGULAR	560	360	60
16	30	132	90.75	101	T56D38R6	TRIANGULAR	560	380	60
16	31	133	93.25	101	T56D39R6	TRIANGULAR	560	390	60
16	32	134	95.75	101	T56D40R6	TRIANGULAR	560	400	60
4	4	135	25.75	41	T56D42R6	TRIANGULAR	560	420	60
4	5	136	28.25	41	T51D08R2	TRIANGULAR	510	80	20
4	6	137	30.75	41	T51D09R2	TRIANGULAR	510	90	20
4	7	138	33.25	41	T51D10R2	TRIANGULAR	510	100	20
4	8	139	35.75	41	T51D12R2	TRIANGULAR	510	120	20
4	9	140	38.25	41	T51D14R2	TRIANGULAR	510	140	20
4	10	141	40.75	41	T51D16R2	TRIANGULAR	510	160	20
4	11	142	43.25	41	T51D18R2	TRIANGULAR	510	180	20
4	12	143	45.75	41	T51D20R2	TRIANGULAR	510	200	20
4	13	144	48.25	41	T51D21R2	TRIANGULAR	510	210	20
4	14	145	50.75	41	T51D24R2	TRIANGULAR	510	240	20
4	15	146	53.25	41	T51D25R2	TRIANGULAR	510	250	20
4	16	147	55.75	41	T51D28R2	TRIANGULAR	510	280	20

4	17	148	58.25	41	T51D30R2	TRIANGULAR	510	300	20
4	18	149	60.75	41	T51D32R2	TRIANGULAR	510	320	20
4	19	150	63.25	41	T51D35R2	TRIANGULAR	510	350	20
4	20	151	65.75	41	T51D36R2	TRIANGULAR	510	360	20
4	21	152	68.25	41	T51D08R4	TRIANGULAR	510	80	40
4	22	153	70.75	41	T51D09R4	TRIANGULAR	510	90	40
4	23	154	73.25	41	T51D10R4	TRIANGULAR	510	100	40
4	24	155	75.75	41	T51D12R4	TRIANGULAR	510	120	40
4	25	156	78.25	41	T51D14R4	TRIANGULAR	510	140	40
4	26	157	80.75	41	T51D16R4	TRIANGULAR	510	160	40
4	27	158	83.25	41	T51D18R4	TRIANGULAR	510	180	40
4	28	159	85.75	41	T51D20R4	TRIANGULAR	510	200	40
4	29	160	88.25	41	T51D21R4	TRIANGULAR	510	210	40
4	30	161	90.75	41	T51D24R4	TRIANGULAR	510	240	40
4	31	162	93.25	41	T51D25R4	TRIANGULAR	510	250	40
4	32	163	95.75	41	T51D28R4	TRIANGULAR	510	280	40
4	33	164	98.25	41	T51D30R4	TRIANGULAR	510	300	40
4	34	165	100.75	41	T51D32R4	TRIANGULAR	510	320	40
15	4	166	25.75	96	T51D35R4	TRIANGULAR	510	350	40
15	5	167	28.25	96	T51D36R4	TRIANGULAR	510	360	40
15	6	168	30.75	96	T51D08R6	TRIANGULAR	510	80	60
15	7	169	33.25	96	T51D09R6	TRIANGULAR	510	90	60
15	8	170	35.75	96	T51D10R6	TRIANGULAR	510	100	60
15	9	171	38.25	96	T51D12R6	TRIANGULAR	510	120	60
15	10	172	40.75	96	T51D14R6	TRIANGULAR	510	140	60
15	11	173	43.25	96	T51D16R6	TRIANGULAR	510	160	60
15	12	174	45.75	96	T51D18R6	TRIANGULAR	510	180	60
15	13	175	48.25	96	T51D20R6	TRIANGULAR	510	200	60
15	14	176	50.75	96	T51D21R6	TRIANGULAR	510	210	60
15	15	177	53.25	96	T51D24R6	TRIANGULAR	510	240	60
15	16	178	55.75	96	T51D25R6	TRIANGULAR	510	250	60
15	17	179	58.25	96	T51D28R6	TRIANGULAR	510	280	60
15	18	180	60.75	96	T51D30R6	TRIANGULAR	510	300	60
15	19	181	63.25	96	T51D32R6	TRIANGULAR	510	320	60
15	20	182	65.75	96	T51D35R6	TRIANGULAR	510	350	60
15	21	183	68.25	96	T51D36R6	TRIANGULAR	510	360	60
15	22	184	70.75	96	T46D08R2	TRIANGULAR	460	80	20
15	23	185	73.25	96	T46D09R2	TRIANGULAR	460	90	20
15	24	186	75.75	96	T46D10R2	TRIANGULAR	460	100	20
15	25	187	78.25	96	T46D12R2	TRIANGULAR	460	120	20
15	26	188	80.75	96	T46D14R2	TRIANGULAR	460	140	20
15	27	189	83.25	96	T46D16R2	TRIANGULAR	460	160	20
15	28	190	85.75	96	T46D18R2	TRIANGULAR	460	180	20
15	29	191	88.25	96	T46D20R2	TRIANGULAR	460	200	20
15	30	192	90.75	96	T46D21R2	TRIANGULAR	460	210	20
15	31	193	93.25	96	T46D24R2	TRIANGULAR	460	240	20
15	32	194	95.75	96	T46D25R2	TRIANGULAR	460	250	20
15	33	195	98.25	96	T46D28R2	TRIANGULAR	460	280	20
15	34	196	100.75	96	T46D30R2	TRIANGULAR	460	300	20
5	3	197	23.25	46	T46D08R4	TRIANGULAR	460	80	40
5	4	198	25.75	46	T46D09R4	TRIANGULAR	460	90	40
5	5	199	28.25	46	T46D10R4	TRIANGULAR	460	100	40
5	6	200	30.75	46	T46D12R4	TRIANGULAR	460	120	40
5	7	201	33.25	46	T46D14R4	TRIANGULAR	460	140	40
5	8	202	35.75	46	T46D16R4	TRIANGULAR	460	160	40
5	9	203	38.25	46	T46D18R4	TRIANGULAR	460	180	40
5	10	204	40.75	46	T46D20R4	TRIANGULAR	460	200	40
5	11	205	43.25	46	T46D21R4	TRIANGULAR	460	210	40
5	12	206	45.75	46	T46D24R4	TRIANGULAR	460	240	40
5	13	207	48.25	46	T46D25R4	TRIANGULAR	460	250	40
5	14	208	50.75	46	T46D28R4	TRIANGULAR	460	280	40
5	15	209	53.25	46	T46D30R4	TRIANGULAR	460	300	40

5	16	210	55.75	46	T46D08R6	TRIANGULAR	460	80	60
5	17	211	58.25	46	T46D09R6	TRIANGULAR	460	90	60
5	18	212	60.75	46	T46D10R6	TRIANGULAR	460	100	60
5	19	213	63.25	46	T46D12R6	TRIANGULAR	460	120	60
5	20	214	65.75	46	T46D14R6	TRIANGULAR	460	140	60
5	21	215	68.25	46	T46D16R6	TRIANGULAR	460	160	60
5	22	216	70.75	46	T46D18R6	TRIANGULAR	460	180	60
5	23	217	73.25	46	T46D20R6	TRIANGULAR	460	200	60
5	24	218	75.75	46	T46D21R6	TRIANGULAR	460	210	60
5	25	219	78.25	46	T46D24R6	TRIANGULAR	460	240	60
5	26	220	80.75	46	T46D25R6	TRIANGULAR	460	250	60
5	27	221	83.25	46	T46D28R6	TRIANGULAR	460	280	60
5	28	222	85.75	46	T46D30R6	TRIANGULAR	460	300	60
5	29	223	88.25	46	T41D08R2	TRIANGULAR	410	80	20
5	30	224	90.75	46	T41D09R2	TRIANGULAR	410	90	20
5	31	225	93.25	46	T41D10R2	TRIANGULAR	410	100	20
5	32	226	95.75	46	T41D12R2	TRIANGULAR	410	120	20
5	33	227	98.25	46	T41D14R2	TRIANGULAR	410	140	20
5	34	228	100.75	46	T41D16R2	TRIANGULAR	410	160	20
5	35	229	103.25	46	T41D18R2	TRIANGULAR	410	180	20
14	3	230	23.25	91	T41D20R2	TRIANGULAR	410	200	20
14	4	231	25.75	91	T41D21R2	TRIANGULAR	410	210	20
14	5	232	28.25	91	T41D24R2	TRIANGULAR	410	240	20
14	6	233	30.75	91	T41D25R2	TRIANGULAR	410	250	20
14	7	234	33.25	91	T41D08R4	TRIANGULAR	410	80	40
14	8	235	35.75	91	T41D09R4	TRIANGULAR	410	90	40
14	9	236	38.25	91	T41D10R4	TRIANGULAR	410	100	40
14	10	237	40.75	91	T41D12R4	TRIANGULAR	410	120	40
14	11	238	43.25	91	T41D14R4	TRIANGULAR	410	140	40
14	12	239	45.75	91	T41D16R4	TRIANGULAR	410	160	40
14	13	240	48.25	91	T41D18R4	TRIANGULAR	410	180	40
14	14	241	50.75	91	T41D20R4	TRIANGULAR	410	200	40
14	15	242	53.25	91	T41D21R4	TRIANGULAR	410	210	40
14	16	243	55.75	91	T41D24R4	TRIANGULAR	410	240	40
14	17	244	58.25	91	T41D25R4	TRIANGULAR	410	250	40
14	18	245	60.75	91	T41D08R6	TRIANGULAR	410	80	60
14	19	246	63.25	91	T41D09R6	TRIANGULAR	410	90	60
14	20	247	65.75	91	T41D10R6	TRIANGULAR	410	100	60
14	21	248	68.25	91	T41D12R6	TRIANGULAR	410	120	60
14	22	249	70.75	91	T41D14R6	TRIANGULAR	410	140	60
14	23	250	73.25	91	T41D16R6	TRIANGULAR	410	160	60
14	24	251	75.75	91	T41D18R6	TRIANGULAR	410	180	60
14	25	252	78.25	91	T41D20R6	TRIANGULAR	410	200	60
14	26	253	80.75	91	T41D21R6	TRIANGULAR	410	210	60
14	27	254	83.25	91	T41D24R6	TRIANGULAR	410	240	60
14	28	255	85.75	91	T41D25R6	TRIANGULAR	410	250	60
14	29	256	88.25	91	T36D08R2	TRIANGULAR	360	80	20
14	30	257	90.75	91	T36D09R2	TRIANGULAR	360	90	20
14	31	258	93.25	91	T36D10R2	TRIANGULAR	360	100	20
14	32	259	95.75	91	T36D12R2	TRIANGULAR	360	120	20
14	33	260	98.25	91	T36D14R2	TRIANGULAR	360	140	20
14	34	261	100.75	91	T36D16R2	TRIANGULAR	360	160	20
14	35	262	103.25	91	T36D18R2	TRIANGULAR	360	180	20
6	2	263	20.75	51	T36D20R2	TRIANGULAR	360	200	20
6	3	264	23.25	51	T36D21R2	TRIANGULAR	360	210	20
6	4	265	25.75	51	T36D08R4	TRIANGULAR	360	80	40
6	5	266	28.25	51	T36D09R4	TRIANGULAR	360	90	40
6	6	267	30.75	51	T36D10R4	TRIANGULAR	360	100	40
6	7	268	33.25	51	T36D12R4	TRIANGULAR	360	120	40
6	8	269	35.75	51	T36D14R4	TRIANGULAR	360	140	40
6	9	270	38.25	51	T36D16R4	TRIANGULAR	360	160	40
6	10	271	40.75	51	T36D18R4	TRIANGULAR	360	180	40

6	11	272	43.25	51	T36D20R4	TRIANGULAR	360	200	40
6	12	273	45.75	51	T36D21R4	TRIANGULAR	360	210	40
6	13	274	48.25	51	T36D08R6	TRIANGULAR	360	80	60
6	14	275	50.75	51	T36D09R6	TRIANGULAR	360	90	60
6	15	276	53.25	51	T36D10R6	TRIANGULAR	360	100	60
6	16	277	55.75	51	T36D12R6	TRIANGULAR	360	120	60
6	17	278	58.25	51	T36D14R6	TRIANGULAR	360	140	60
6	18	279	60.75	51	T36D16R6	TRIANGULAR	360	160	60
6	19	280	63.25	51	T36D18R6	TRIANGULAR	360	180	60
6	20	281	65.75	51	T36D20R6	TRIANGULAR	360	200	60
6	21	282	68.25	51	T36D21R6	TRIANGULAR	360	210	60
6	22	283	70.75	51	T31D08R2	TRIANGULAR	310	80	20
6	23	284	73.25	51	T31D09R2	TRIANGULAR	310	90	20
6	24	285	75.75	51	T31D10R2	TRIANGULAR	310	100	20
6	25	286	78.25	51	T31D12R2	TRIANGULAR	310	120	20
6	26	287	80.75	51	T31D14R2	TRIANGULAR	310	140	20
6	27	288	83.25	51	T31D16R2	TRIANGULAR	310	160	20
6	28	289	85.75	51	T31D18R2	TRIANGULAR	310	180	20
6	29	290	88.25	51	T31D08R4	TRIANGULAR	310	80	40
6	30	291	90.75	51	T31D09R4	TRIANGULAR	310	90	40
6	31	292	93.25	51	T31D10R4	TRIANGULAR	310	100	40
6	32	293	95.75	51	T31D12R4	TRIANGULAR	310	120	40
6	33	294	98.25	51	T31D14R4	TRIANGULAR	310	140	40
6	34	295	100.75	51	T31D16R4	TRIANGULAR	310	160	40
6	35	296	103.25	51	T31D18R4	TRIANGULAR	310	180	40
6	36	297	105.75	51	T31D08R6	TRIANGULAR	310	80	60
13	2	298	20.75	86	T31D09R6	TRIANGULAR	310	90	60
13	3	299	23.25	86	T31D10R6	TRIANGULAR	310	100	60
13	4	300	25.75	86	T31D12R6	TRIANGULAR	310	120	60
13	5	301	28.25	86	T31D14R6	TRIANGULAR	310	140	60
13	6	302	30.75	86	T31D16R6	TRIANGULAR	310	160	60
13	7	303	33.25	86	T31D18R6	TRIANGULAR	310	180	60
13	8	304	35.75	86	T26D08R2	TRIANGULAR	260	80	20
13	9	305	38.25	86	T26D09R2	TRIANGULAR	260	90	20
13	10	306	40.75	86	T26D10R2	TRIANGULAR	260	100	20
13	11	307	43.25	86	T26D12R2	TRIANGULAR	260	120	20
13	12	308	45.75	86	T26D14R2	TRIANGULAR	260	140	20
13	13	309	48.25	86	T26D08R4	TRIANGULAR	260	80	40
13	14	310	50.75	86	T26D09R4	TRIANGULAR	260	90	40
13	15	311	53.25	86	T26D10R4	TRIANGULAR	260	100	40
13	16	312	55.75	86	T26D12R4	TRIANGULAR	260	120	40
13	17	313	58.25	86	T26D14R4	TRIANGULAR	260	140	40
13	18	314	60.75	86	T26D08R6	TRIANGULAR	260	80	60
13	19	315	63.25	86	T26D09R6	TRIANGULAR	260	90	60
13	20	316	65.75	86	T26D10R6	TRIANGULAR	260	100	60
13	21	317	68.25	86	T26D12R6	TRIANGULAR	260	120	60
13	22	318	70.75	86	T26D14R6	TRIANGULAR	260	140	60
13	23	319	73.25	86	T21D08R2	TRIANGULAR	210	80	20
13	24	320	75.75	86	T21D09R2	TRIANGULAR	210	90	20
13	25	321	78.25	86	T21D10R2	TRIANGULAR	210	100	20
13	26	322	80.75	86	T21D08R4	TRIANGULAR	210	80	40
13	27	323	83.25	86	T21D09R4	TRIANGULAR	210	90	40
13	28	324	85.75	86	T21D10R4	TRIANGULAR	210	100	40
13	29	325	88.25	86	T21D08R6	TRIANGULAR	210	80	60
13	30	326	90.75	86	T21D09R6	TRIANGULAR	210	90	60
13	31	327	93.25	86	T21D10R6	TRIANGULAR	210	100	60
13	32	328	95.75	86	G26D06R2	GRATING	260	60	20
13	33	329	98.25	86	G26D06R4	GRATING	260	60	40
13	34	330	100.75	86	G26D08R2	GRATING	260	80	20
13	35	331	103.25	86	G26D08R4	GRATING	260	80	40
13	36	332	105.75	86	G26D10R2	GRATING	260	100	20
7	1	333	18.25	56	G31D06R2	GRATING	310	60	20

7	2	334	20.75	56	G31D06R4	GRATING	310	60	40
7	3	335	23.25	56	G31D06R6	GRATING	310	60	60
7	4	336	25.75	56	G31D08R2	GRATING	310	80	20
7	5	337	28.25	56	G31D08R4	GRATING	310	80	40
7	6	338	30.75	56	G31D08R6	GRATING	310	80	60
7	7	339	33.25	56	G31D10R2	GRATING	310	100	20
7	8	340	35.75	56	G31D10R4	GRATING	310	100	40
7	9	341	38.25	56	TRTEST16	2.50E-07 MHZ CLOCK ORIGINAL TEST CHIP			
7	10	342	40.75	56	G31D12R2	GRATING	310	120	20
7	11	343	43.25	56	G31D12R4	GRATING	310	120	40
7	12	344	45.75	56	G31D12R6	GRATING	310	120	60
7	13	345	48.25	56	G36D06R2	GRATING	360	60	20
7	14	346	50.75	56	G36D06R4	GRATING	360	60	40
7	15	347	53.25	56	G36D06R6	GRATING	360	60	60
7	16	348	55.75	56	TRTEST16	7.50E-07 MHZ CLOCK ORIGINAL TEST CHIP			
7	17	349	58.25	56	G36D08R4	GRATING	360	80	40
7	18	350	60.75	56	G36D08R6	GRATING	360	80	60
7	19	351	63.25	56	G36D10R2	GRATING	360	100	20
7	20	352	65.75	56	G36D10R4	GRATING	360	100	40
7	21	353	68.25	56	G36D10R6	GRATING	360	100	60
7	22	354	70.75	56	G36D12R2	GRATING	360	120	20
7	23	355	73.25	56	G36D12R4	GRATING	360	120	40
7	24	356	75.75	56	ARTEST16	7.50E-07 MHZ CLOCK ORIGINAL TEST CHIP			
7	25	357	78.25	56	G36D14R2	GRATING	360	140	20
7	26	358	80.75	56	G36D14R4	GRATING	360	140	40
7	27	359	83.25	56	G36D14R6	GRATING	360	140	60
7	28	360	85.75	56	G36D16R2	GRATING	360	160	20
7	29	361	88.25	56	G36D16R4	GRATING	360	160	40
7	30	362	90.75	56	G36D16R6	GRATING	360	160	60
7	31	363	93.25	56	G41D06R2	GRATING	410	60	20
7	32	364	95.75	56	G41D06R4	GRATING	410	60	40
7	33	365	98.25	56	G41D06R6	GRATING	410	60	60

7	34	366	100.75	56	G41D08R2	GRATING	410	80	20
7	35	367	103.25	56	G41D08R4	GRATING	410	80	40
7	36	368	105.75	56	TRTEST16	7.50E-07 MHZ CLOCK ORIGINAL TEST CHIP			
7	37	369	108.25	56	GRTEST16	2.50E-07 MHZ CLOCK ORIGINAL TEST CHIP			
12	1	370	18.25	81	TRTEST16	2.50E-07 MHZ CLOCK ORIGINAL TEST CHIP			
12	2	371	20.75	81	G41D10R6	GRATING	410	100	60
12	3	372	23.25	81	G41D12R2	GRATING	410	120	20
12	4	373	25.75	81	G41D12R4	GRATING	410	120	40
12	5	374	28.25	81	G41D12R6	GRATING	410	120	60
12	6	375	30.75	81	G41D14R2	GRATING	410	140	20
12	7	376	33.25	81	G41D14R4	GRATING	410	140	40
12	8	377	35.75	81	G41D14R6	GRATING	410	140	60
12	9	378	38.25	81	G41D16R2	GRATING	410	160	20
12	10	379	40.75	81	G41D16R4	GRATING	410	160	40
12	11	380	43.25	81	G41D16R6	GRATING	410	160	60
12	12	381	45.75	81	G41D18R2	GRATING	410	180	20
12	13	382	48.25	81	G41D18R4	GRATING	410	180	40
12	14	383	50.75	81	G41D18R6	GRATING	410	180	60
12	15	384	53.25	81	G41D20R2	GRATING	410	200	20
12	16	385	55.75	81	G41D20R4	GRATING	410	200	40
12	17	386	58.25	81	G41D20R6	GRATING	410	200	60
12	18	387	60.75	81	G46D06R2	GRATING	460	60	20
12	19	388	63.25	81	G46D06R4	GRATING	460	60	40
12	20	389	65.75	81	G46D06R6	GRATING	460	60	60
12	21	390	68.25	81	G46D08R2	GRATING	460	80	20
12	22	391	70.75	81	G46D08R4	GRATING	460	80	40
12	23	392	73.25	81	G46D08R6	GRATING	460	80	60
12	24	393	75.75	81	G46D10R2	GRATING	460	100	20
12	25	394	78.25	81	G46D10R4	GRATING	460	100	40
12	26	395	80.75	81	G46D10R6	GRATING	460	100	60
12	27	396	83.25	81	G46D12R2	GRATING	460	120	20
12	28	397	85.75	81	G46D12R4	GRATING	460	120	40
12	29	398	88.25	81	G46D12R6	GRATING	460	120	60
12	30	399	90.75	81	G46D14R2	GRATING	460	140	20
12	31	400	93.25	81	G46D14R4	GRATING	460	140	40
12	32	401	95.75	81	G46D14R6	GRATING	460	140	60
12	33	402	98.25	81	G46D16R2	GRATING	460	160	20
12	34	403	100.75	81	G46D16R4	GRATING	460	160	40
12	35	404	103.25	81	G46D16R6	GRATING	460	160	60
12	36	405	105.75	81	G46D18R2	GRATING	460	180	20
12	37	406	108.25	81	G46D18R4	GRATING	460	180	40
8	1	407	18.25	61	G46D18R6	GRATING	460	180	60
8	2	408	20.75	61	G46D20R2	GRATING	460	200	20
8	3	409	23.25	61	G46D20R4	GRATING	460	200	40
8	4	410	25.75	61	G46D20R6	GRATING	460	200	60
8	5	411	28.25	61	G46D22R2	GRATING	460	220	20

8	6	412	30.75	61	G46D22R4	GRATING	460	220	40
8	7	413	33.25	61	G46D22R6	GRATING	460	220	60
8	8	414	35.75	61	G46D24R2	GRATING	460	240	20
8	9	415	38.25	61	G46D24R4	GRATING	460	240	40
8	10	416	40.75	61	G46D24R6	GRATING	460	240	60
8	11	417	43.25	61	G46D26R2	GRATING	460	260	20
8	12	418	45.75	61	G46D26R4	GRATING	460	260	40
8	13	419	48.25	61	G46D26R6	GRATING	460	260	60
8	14	420	50.75	61	G51D06R2	GRATING	510	60	20
8	15	421	53.25	61	G51D06R4	GRATING	510	60	40
8	16	422	55.75	61	G51D06R6	GRATING	510	60	60
8	17	423	58.25	61	G51D08R2	GRATING	510	80	20
8	18	424	60.75	61	G51D08R4	GRATING	510	80	40
8	19	425	63.25	61	G51D08R6	GRATING	510	80	60
8	20	426	65.75	61	G51D10R2	GRATING	510	100	20
8	21	427	68.25	61	G51D10R4	GRATING	510	100	40
8	22	428	70.75	61	G51D10R6	GRATING	510	100	60
8	23	429	73.25	61	G51D12R2	GRATING	510	120	20
8	24	430	75.75	61	G51D12R4	GRATING	510	120	40
8	25	431	78.25	61	G51D12R6	GRATING	510	120	60
8	26	432	80.75	61	G51D14R2	GRATING	510	140	20
8	27	433	83.25	61	G51D14R4	GRATING	510	140	40
8	28	434	85.75	61	G51D14R6	GRATING	510	140	60
8	29	435	88.25	61	G51D16R2	GRATING	510	160	20
8	30	436	90.75	61	G51D16R4	GRATING	510	160	40
8	31	437	93.25	61	G51D16R6	GRATING	510	160	60
8	32	438	95.75	61	G51D18R2	GRATING	510	180	20
8	33	439	98.25	61	G51D18R4	GRATING	510	180	40
8	34	440	100.75	61	G51D18R6	GRATING	510	180	60
8	35	441	103.25	61	G51D20R2	GRATING	510	200	20
8	36	442	105.75	61	G51D20R4	GRATING	510	200	40
8	37	443	108.25	61	G51D20R6	GRATING	510	200	60
11	1	444	18.25	76	G51D22R2	GRATING	510	220	20
11	2	445	20.75	76	G51D22R4	GRATING	510	220	40
11	3	446	23.25	76	G51D22R6	GRATING	510	220	60
11	4	447	25.75	76	G51D24R2	GRATING	510	240	20
11	5	448	28.25	76	G51D24R4	GRATING	510	240	40
11	6	449	30.75	76	G51D24R6	GRATING	510	240	60
11	7	450	33.25	76	G51D26R2	GRATING	510	260	20
11	8	451	35.75	76	G51D26R4	GRATING	510	260	40
11	9	452	38.25	76	G51D26R6	GRATING	510	260	60
11	10	453	40.75	76	G51D28R2	GRATING	510	280	20
11	11	454	43.25	76	G51D28R4	GRATING	510	280	40
11	12	455	45.75	76	G51D28R6	GRATING	510	280	60
11	13	456	48.25	76	G51D30R2	GRATING	510	300	20
11	14	457	50.75	76	G51D30R4	GRATING	510	300	40
11	15	458	53.25	76	G51D30R6	GRATING	510	300	60
11	16	459	55.75	76	G56D06R2	GRATING	560	60	20
11	17	460	58.25	76	G56D06R4	GRATING	560	60	40
11	18	461	60.75	76	G56D06R6	GRATING	560	60	60
11	19	462	63.25	76	G56D08R2	GRATING	560	80	20
11	20	463	65.75	76	G56D08R4	GRATING	560	80	40
11	21	464	68.25	76	G56D08R6	GRATING	560	80	60
11	22	465	70.75	76	G56D10R2	GRATING	560	100	20
11	23	466	73.25	76	TRTEST16	2.50E-07 MHZ CLOCK ORIGINAL TEST CHIP			
11	24	467	75.75	76	G56D10R6	GRATING	560	100	60
11	25	468	78.25	76	G56D12R2	GRATING	560	120	20

11	26	469	80.75	76	G56D12R4	GRATING	560	120	40
11	27	470	83.25	76	G56D12R6	GRATING	560	120	60
11	28	471	85.75	76	G56D14R2	GRATING	560	140	20
11	29	472	88.25	76	G56D14R4	GRATING	560	140	40
11	30	473	90.75	76	G56D14R6	GRATING	560	140	60
11	31	474	93.25	76	TRTEST16	2.50E-07 MHZ CLOCK ORIGINAL TEST CHIP			
11	32	475	95.75	76	TRTEST16	7.50E-07 MHZ CLOCK ORIGINAL TEST CHIP			
11	33	476	98.25	76	TRTEST16	2.50E-07 MHZ CLOCK ORIGINAL TEST CHIP			
11	34	477	100.75	76	TRTEST16	7.50E-07 MHZ CLOCK ORIGINAL TEST CHIP			
11	35	478	103.25	76	TRTEST16	2.50E-07 MHZ CLOCK ORIGINAL TEST CHIP			
11	36	479	105.75	76	TRTEST16	7.50E-07 MHZ CLOCK ORIGINAL TEST CHIP			
11	37	480	108.25	76	ARTEST16	2.50E-07 MHZ CLOCK ORIGINAL TEST CHIP			
9	1	481	18.25	66	ARTEST16	2.50E-07 MHZ CLOCK ORIGINAL TEST CHIP			
9	2	482	20.75	66	ARTEST16	7.50E-07 MHZ CLOCK ORIGINAL TEST CHIP			
9	3	483	23.25	66	GRTEST16	2.50E-07 MHZ CLOCK ORIGINAL TEST CHIP			
9	4	484	25.75	66	GRTEST16	7.50E-07 MHZ CLOCK ORIGINAL TEST CHIP			
9	5	485	28.25	66	GRTEST16	2.50E-07 MHZ CLOCK ORIGINAL TEST CHIP			
9	6	486	30.75	66	GRTEST16	7.50E-07 MHZ CLOCK ORIGINAL TEST CHIP			
9	7	487	33.25	66	GRTEST16	2.50E-07 MHZ CLOCK ORIGINAL TEST CHIP			
9	8	488	35.75	66	T26D14R2	TRIANGULAR	260	140	20
9	9	489	38.25	66	T26D08R4	TRIANGULAR	260	80	40
9	10	490	40.75	66	T26D09R4	TRIANGULAR	260	90	40
9	11	491	43.25	66	T26D10R4	TRIANGULAR	260	100	40
9	12	492	45.75	66	T26D12R4	TRIANGULAR	260	120	40
9	13	493	48.25	66	T26D14R4	TRIANGULAR	260	140	40
9	14	494	50.75	66	T26D08R6	TRIANGULAR	260	80	60
9	15	495	53.25	66	T26D09R6	TRIANGULAR	260	90	60
9	16	496	55.75	66	T26D10R6	TRIANGULAR	260	100	60
9	17	497	58.25	66	T26D12R6	TRIANGULAR	260	120	60
9	18	498	60.75	66	GRTEST16	7.50E-07 MHZ CLOCK ORIGINAL TEST CHIP			
9	19	499	63.25	66	ARTEST16	2.50E-07 MHZ CLOCK ORIGINAL TEST CHIP			
9	20	500	65.75	66	ARTEST16	7.50E-07 MHZ CLOCK ORIGINAL TEST CHIP			
9	21	501	68.25	66	T26D14R6	TRIANGULAR	260	140	60
9	22	502	70.75	66	T31D14R4	TRIANGULAR	310	140	40

9	23	503	73.25	66	T31D16R4	TRIANGULAR	310	160	40
9	24	504	75.75	66	T31D18R4	TRIANGULAR	310	180	40
9	25	505	78.25	66	T31D08R6	TRIANGULAR	310	80	60
9	26	506	80.75	66	T31D09R6	TRIANGULAR	310	90	60
9	27	507	83.25	66	T31D10R6	TRIANGULAR	310	100	60
9	28	508	85.75	66	T31D12R6	TRIANGULAR	310	120	60
9	29	509	88.25	66	T31D14R6	TRIANGULAR	310	140	60
9	30	510	90.75	66	T31D16R6	TRIANGULAR	310	160	60
9	31	511	93.25	66	T31D18R6	TRIANGULAR	310	180	60
9	32	512	95.75	66	T26D08R2	TRIANGULAR	260	80	20
9	33	513	98.25	66	T26D09R2	TRIANGULAR	260	90	20
9	34	514	100.75	66	T26D10R2	TRIANGULAR	260	100	20
9	35	515	103.25	66	T26D12R2	TRIANGULAR	260	120	20
9	36	516	105.75	66	ARTEST16	7.50E-07 MHZ CLOCK ORIGINAL TEST			
CHIP									
9	37	517	108.25	66	ARTEST16	2.50E-07 MHZ CLOCK ORIGINAL TEST			
CHIP									
10	1	518	18.25	71	ARTEST16	2.50E-07 MHZ CLOCK ORIGINAL TEST			
CHIP									
10	2	519	20.75	71	T36D10R2	TRIANGULAR	360	100	20
10	3	520	23.25	71	T36D12R2	TRIANGULAR	360	120	20
10	4	521	25.75	71	T36D14R2	TRIANGULAR	360	140	20
10	5	522	28.25	71	T36D16R2	TRIANGULAR	360	160	20
10	6	523	30.75	71	T36D18R2	TRIANGULAR	360	180	20
10	7	524	33.25	71	T36D20R2	TRIANGULAR	360	200	20
10	8	525	35.75	71	T36D21R2	TRIANGULAR	360	210	20
10	9	526	38.25	71	T36D08R4	TRIANGULAR	360	80	40
10	10	527	40.75	71	T36D09R4	TRIANGULAR	360	90	40
10	11	528	43.25	71	T36D10R4	TRIANGULAR	360	100	40
10	12	529	45.75	71	T36D12R4	TRIANGULAR	360	120	40
10	13	530	48.25	71	T36D14R4	TRIANGULAR	360	140	40
10	14	531	50.75	71	T36D16R4	TRIANGULAR	360	160	40
10	15	532	53.25	71	T36D18R4	TRIANGULAR	360	180	40
10	16	533	55.75	71	T36D20R4	TRIANGULAR	360	200	40
10	17	534	58.25	71	T36D21R4	TRIANGULAR	360	210	40
10	18	535	60.75	71	T36D08R6	TRIANGULAR	360	80	60
10	19	536	63.25	71	T36D09R6	TRIANGULAR	360	90	60
10	20	537	65.75	71	T36D10R6	TRIANGULAR	360	100	60
10	21	538	68.25	71	T36D12R6	TRIANGULAR	360	120	60
10	22	539	70.75	71	T36D14R6	TRIANGULAR	360	140	60

10	23	540	73.25	71	T36D16R6	TRIANGULAR	360	160	60
10	24	541	75.75	71	T36D18R6	TRIANGULAR	360	180	60
10	25	542	78.25	71	T36D20R6	TRIANGULAR	360	200	60
10	26	543	80.75	71	T36D21R6	TRIANGULAR	360	210	60
10	27	544	83.25	71	T31D08R2	TRIANGULAR	310	80	20
10	28	545	85.75	71	T31D09R2	TRIANGULAR	310	90	20
10	29	546	88.25	71	T31D10R2	TRIANGULAR	310	100	20
10	30	547	90.75	71	T31D12R2	TRIANGULAR	310	120	20
10	31	548	93.25	71	T31D14R2	TRIANGULAR	310	140	20
10	32	549	95.75	71	T31D16R2	TRIANGULAR	310	160	20
10	33	550	98.25	71	T31D18R2	TRIANGULAR	310	180	20
10	34	551	100.75	71	T31D08R4	TRIANGULAR	310	80	40
10	35	552	103.25	71	T31D09R4	TRIANGULAR	310	90	40
10	36	553	105.75	71	T31D10R4	TRIANGULAR	310	100	40
10	37	554	108.25	71	T31D12R4	TRIANGULAR	310	120	40

A.2 - Prisms

ID No	Column Position (Y)	Row	Name	GJ	Pitch (nm)	Diameter (nm)		Rows	Position (X)
1	6	1	BLANK				44.5	26	
2	7	1	BLANK				49.5	26	
3	8	1	BLANK				54.5	26	
4	9	1	PR5TEST1					59.5	26
	9	MHZ	CLOCK TRIANGULAR		SQUARE		RECT	RATIO	01:01.5
5	10	1	PR5TEST1					64.5	26
	8	MHZ	CLOCK TRIANGULAR		SQUARE		RECT	RATIO	01:01.5
6	11	1	BLANK				69.5	26	
7	12	1	BLANK				74.5	26	
8	13	1	BLANK				79.5	26	
9	6	18	BLANK				44.5	111	
10	7	18	BLANK				49.5	111	
11	8	18	BLANK				54.5	111	
12	9	18	PR4TEST1					59.5	111
	7	MHZ	CLOCK PRISM	TEST	CHIP				
13	10	18	PR4TEST1					64.5	111
	8	MHZ	CLOCK PRISM	TEST	CHIP				
14	11	18	BLANK				69.5	111	
15	12	18	BLANK				74.5	111	
16	13	18	BLANK				79.5	111	
17	4	2	ETCHTEST					34.5	31
	8	MHZ	CLOCK RIE	ETCH	TEST	CHIP			
18	5	2	ETCHTEST					39.5	31
	8	MHZ	CLOCK RIE	ETCH	TEST	CHIP			
19	6	2	ETCHTEST					44.5	31
	8	MHZ	CLOCK RIE	ETCH	TEST	CHIP			
20	7	2	ETCHTEST					49.5	31
	8	MHZ	CLOCK RIE	ETCH	TEST	CHIP			
21	8	2	ETCHTEST					54.5	31
	8	MHZ	CLOCK RIE	ETCH	TEST	CHIP			
22	9	2	ETCHTEST					59.5	31
	8	MHZ	CLOCK RIE	ETCH	TEST	CHIP			
23	10	2	TA26D18R1	0	260	180	150	64.5	31
24	11	2	TB26D18R1	1	260	180	150	69.5	31
25	12	2	TA26D18R3	0	260	180	300	74.5	31
26	13	2	TB26D18R3	1	260	180	300	79.5	31
27	14	2	TA26D18R6	0	260	180	600	84.5	31
28	15	2	BLANK				89.5	31	
29	4	17	TB26D18R6	1	260	180	600	34.5	106
30	5	17	TA26D16R1	0	260	160	150	39.5	106

31	6	17	TB26D16R1	1	260	160	150	44.5	106
32	7	17	TA26D16R3	0	260	160	300	49.5	106
33	8	17	TB26D16R3	1	260	160	300	54.5	106
34	9	17	TA26D16R6	0	260	160	600	59.5	106
35	10	17	TB26D16R6	1	260	160	600	64.5	106
36	11	17	TA31D18R1	0	310	180	150	69.5	106
37	12	17	TB31D18R1	1	310	180	150	74.5	106
38	13	17	TA31D18R3	0	310	180	300	79.5	106
39	14	17	TB31D18R3	1	310	180	300	84.5	106
40	15	17	TA31D18R6	0	310	180	600	89.5	106
41	3	3	TB31D18R6	1	310	180	600	29.5	36
42	4	3	TA31D16R1	0	310	160	150	34.5	36
43	5	3	TB31D16R1	1	310	160	150	39.5	36
44	6	3	TA31D16R3	0	310	160	300	44.5	36
45	7	3	TB31D16R3	1	310	160	300	49.5	36
46	8	3	TA31D16R6	0	310	160	600	54.5	36
47	9	3	TB31D16R6	1	310	160	600	59.5	36
48	10	3	TA36D21R1	0	360	210	150	64.5	36
49	11	3	TB36D21R1	1	360	210	150	69.5	36
50	12	3	TA36D21R3	0	360	210	300	74.5	36
51	13	3	TB36D21R3	1	360	210	300	79.5	36
52	14	3	TA36D21R6	0	360	210	600	84.5	36
53	15	3	TB36D21R6	1	360	210	600	89.5	36
54	16	3	TA36D20R1	0	360	200	150	94.5	36
55	3	16	TB36D20R1	1	360	200	150	29.5	101
56	4	16	TA36D20R3	0	360	200	300	34.5	101
57	5	16	TB36D20R3	1	360	200	300	39.5	101
58	6	16	TA36D20R6	0	360	200	600	44.5	101
59	7	16	TB36D20R6	1	360	200	600	49.5	101
60	8	16	TA41D21R1	0	410	210	150	54.5	101
61	9	16	TB41D21R1	1	410	210	150	59.5	101
62	10	16	TA41D21R3	0	410	210	300	64.5	101
63	11	16	TB41D21R3	1	410	210	300	69.5	101
64	12	16	TA41D21R6	0	410	210	600	74.5	101
65	13	16	TB41D21R6	1	410	210	600	79.5	101
66	14	16	TA41D24R1	0	410	240	150	84.5	101
67	15	16	TB41D24R1	1	410	240	150	89.5	101
68	16	16	TA41D24R3	0	410	240	300	94.5	101
69	2	4	TB41D24R3	1	410	240	300	24.5	41
70	3	4	TA41D24R6	0	410	240	600	29.5	41
71	4	4	TB41D24R6	1	410	240	600	34.5	41
72	5	4	TA41D25R1	0	410	250	150	39.5	41
73	6	4	TB41D25R1	1	410	250	150	44.5	41
74	7	4	TA41D25R3	0	410	250	300	49.5	41
75	8	4	TB41D25R3	1	410	250	300	54.5	41
76	9	4	TA41D25R6	0	410	250	600	59.5	41
77	10	4	TB41D25R6	1	410	250	600	64.5	41
78	11	4	TA26D18R1	0	260	180	150	69.5	41
79	12	4	TB26D18R1	1	260	180	150	74.5	41
80	13	4	TA26D18R3	0	260	180	300	79.5	41
81	14	4	TB26D18R3	1	260	180	300	84.5	41
82	15	4	TA26D18R6	0	260	180	600	89.5	41
83	16	4	TB26D18R6	1	260	180	600	94.5	41
84	17	4	TA26D16R1	0	260	160	150	99.5	41
85	2	15	ETCHTEST					24.5	96
	8	MHZ	CLOCK RIE	ETCH	TEST	CHIP			
86	3	15	ETCHTEST					29.5	96
	8	MHZ	CLOCK RIE	ETCH	TEST	CHIP			
87	4	15	ETCHTEST					34.5	96
	8	MHZ	CLOCK RIE	ETCH	TEST	CHIP			
88	5	15	ETCHTEST					39.5	96
	8	MHZ	CLOCK RIE	ETCH	TEST	CHIP			

89	6	15	ETCHTEST					44.5	96
	8	MHZ	CLOCK RIE	ETCH	TEST	CHIP			
90	7	15	ETCHTEST					49.5	96
	8	MHZ	CLOCK RIE	ETCH	TEST	CHIP			
91	8	15	ETCHTEST					54.5	96
	8	MHZ	CLOCK RIE	ETCH	TEST	CHIP			
92	9	15	ETCHTEST					59.5	96
	8	MHZ	CLOCK RIE	ETCH	TEST	CHIP			
93	10	15	TB26D16R1	1	260	160	150	64.5	96
94	11	15	TA26D16R3	0	260	160	300	69.5	96
95	12	15	TB26D16R3	1	260	160	300	74.5	96
96	13	15	TA26D16R6	0	260	160	600	79.5	96
97	14	15	TB26D16R6	1	260	160	600	84.5	96
98	15	15	TA31D18R1	0	310	180	150	89.5	96
99	16	15	TB31D18R1	1	310	180	150	94.5	96
100	17	15	BLANK				99.5	96	
101	2	5	TA31D18R3	0	310	180	300	24.5	46
102	3	5	TB31D18R3	1	310	180	300	29.5	46
103	4	5	TA31D18R6	0	310	180	600	34.5	46
104	5	5	TB31D18R6	1	310	180	600	39.5	46
105	6	5	TA31D16R1	0	310	160	150	44.5	46
106	7	5	TB31D16R1	1	310	160	150	49.5	46
107	8	5	TA31D16R3	0	310	160	300	54.5	46
108	9	5	TB31D16R3	1	310	160	300	59.5	46
109	10	5	TA31D16R6	0	310	160	600	64.5	46
110	11	5	TB31D16R6	1	310	160	600	69.5	46
111	12	5	TA36D21R1	0	360	210	150	74.5	46
112	13	5	TB36D21R1	1	360	210	150	79.5	46
113	14	5	TA36D21R3	0	360	210	300	84.5	46
114	15	5	TB36D21R3	1	360	210	300	89.5	46
115	16	5	TA36D21R6	0	360	210	600	94.5	46
116	17	5	TB36D21R6	1	360	210	600	99.5	46
117	2	14	TA36D20R1	0	360	200	150	24.5	91
118	3	14	TB36D20R1	1	360	200	150	29.5	91
119	4	14	TA36D20R3	0	360	200	300	34.5	91
120	5	14	TB36D20R3	1	360	200	300	39.5	91
121	6	14	TA36D20R6	0	360	200	600	44.5	91
122	7	14	TB36D20R6	1	360	200	600	49.5	91
123	8	14	TA41D21R1	0	410	210	150	54.5	91
124	9	14	TB41D21R1	1	410	210	150	59.5	91
125	10	14	TA41D21R3	0	410	210	300	64.5	91
126	11	14	TB41D21R3	1	410	210	300	69.5	91
127	12	14	TA41D21R6	0	410	210	600	74.5	91
128	13	14	TB41D21R6	1	410	210	600	79.5	91
129	14	14	TA41D24R1	0	410	240	150	84.5	91
130	15	14	TB41D24R1	1	410	240	150	89.5	91
131	16	14	TA41D24R3	0	410	240	300	94.5	91
132	17	14	TB41D24R3	1	410	240	300	99.5	91
133	1	6	BLANK				19.5	51	
134	2	6	TA41D24R6	0	410	240	600	24.5	51
135	3	6	TB41D24R6	1	410	240	600	29.5	51
136	4	6	TA41D25R1	0	410	250	150	34.5	51
137	5	6	TB41D25R1	1	410	250	150	39.5	51
138	6	6	TA41D25R3	0	410	250	300	44.5	51
139	7	6	TB41D25R3	1	410	250	300	49.5	51
140	8	6	TA41D25R6	0	410	250	600	54.5	51
141	9	6	TB41D25R6	1	410	250	600	59.5	51
142	10	6	TA26D18R1	0	260	180	150	64.5	51
143	11	6	TB26D18R1	1	260	180	150	69.5	51
144	12	6	TA26D18R3	0	260	180	300	74.5	51
145	13	6	TB26D18R3	1	260	180	300	79.5	51
146	14	6	TA26D18R6	0	260	180	600	84.5	51

147	15	6	TB26D18R6	1	260	180	600	89.5	51
148	16	6	TA26D16R1	0	260	160	150	94.5	51
149	17	6	TB26D16R1	1	260	160	150	99.5	51
150	18	6	BLANK				104.5	51	
151	1	13	PR5TEST1					19.5	86
	7	MHZ	CLOCK TRIANGULAR		SQUARE		RECT	RATIO	01:01.5
152	2	13	TA26D16R3	0	260	160	300	24.5	86
153	3	13	TB26D16R3	1	260	160	300	29.5	86
154	4	13	TA26D16R6	0	260	160	600	34.5	86
155	5	13	TB26D16R6	1	260	160	600	39.5	86
156	6	13	TA31D18R1	0	310	180	150	44.5	86
157	7	13	TB31D18R1	1	310	180	150	49.5	86
158	8	13	TA31D18R3	0	310	180	300	54.5	86
159	9	13	TB31D18R3	1	310	180	300	59.5	86
160	10	13	TA31D18R6	0	310	180	600	64.5	86
161	11	13	TB31D18R6	1	310	180	600	69.5	86
162	12	13	TA31D16R1	0	310	160	150	74.5	86
163	13	13	TB31D16R1	1	310	160	150	79.5	86
164	14	13	TA31D16R3	0	310	160	300	84.5	86
165	15	13	TB31D16R3	1	310	160	300	89.5	86
166	16	13	TA31D16R6	0	310	160	600	94.5	86
167	17	13	TB31D16R6	1	310	160	600	99.5	86
168	18	13	PR5TEST1					104.5	86
	7	MHZ	CLOCK TRIANGULAR		SQUARE		RECT	RATIO	01:01.5
169	1	7	PR5TEST1					19.5	56
	7	MHZ	CLOCK TRIANGULAR		SQUARE		RECT	RATIO	01:01.5
170	2	7	TA36D21R1	0	360	210	150	24.5	56
171	3	7	TB36D21R1	1	360	210	150	29.5	56
172	4	7	TA36D21R3	0	360	210	300	34.5	56
173	5	7	TB36D21R3	1	360	210	300	39.5	56
174	6	7	TA36D21R6	0	360	210	600	44.5	56
175	7	7	TB36D21R6	1	360	210	600	49.5	56
176	8	7	TA36D20R1	0	360	200	150	54.5	56
177	9	7	TB36D20R1	1	360	200	150	59.5	56
178	10	7	TA36D20R3	0	360	200	300	64.5	56
179	11	7	TB36D20R3	1	360	200	300	69.5	56
180	12	7	TA36D20R6	0	360	200	600	74.5	56
181	13	7	TB36D20R6	1	360	200	600	79.5	56
182	14	7	TA41D21R1	0	410	210	150	84.5	56
183	15	7	TB41D21R1	1	410	210	150	89.5	56
184	16	7	TA41D21R3	0	410	210	300	94.5	56
185	17	7	TB41D21R3	1	410	210	300	99.5	56
186	18	7	PR5TEST1					104.5	56
	7	MHZ	CLOCK TRIANGULAR		SQUARE		RECT	RATIO	01:01.5
187	1	12	BLANK				19.5	81	
188	2	12	TA41D21R6	0	410	210	600	24.5	81
189	3	12	TB41D21R6	1	410	210	600	29.5	81
190	4	12	TA41D24R1	0	410	240	150	34.5	81
191	5	12	TB41D24R1	1	410	240	150	39.5	81
192	6	12	TA41D24R3	0	410	240	300	44.5	81
193	7	12	TB41D24R3	1	410	240	300	49.5	81
194	8	12	TA41D24R6	0	410	240	600	54.5	81
195	9	12	TB41D24R6	1	410	240	600	59.5	81
196	10	12	TA41D25R1	0	410	250	150	64.5	81
197	11	12	TB41D25R1	1	410	250	150	69.5	81
198	12	12	TA41D25R3	0	410	250	300	74.5	81
199	13	12	TB41D25R3	1	410	250	300	79.5	81
200	14	12	TA41D25R6	0	410	250	600	84.5	81
201	15	12	TB41D25R6	1	410	250	600	89.5	81
202	16	12	TA26D18R1	0	260	180	150	94.5	81
203	17	12	TB26D18R1	1	260	180	150	99.5	81

204	18	12	BLANK				104.5	81	
205	1	8	TA26D18R3	0	260	180	300	19.5	61
206	2	8	TB26D18R3	1	260	180	300	24.5	61
207	3	8	TA26D18R6	0	260	180	600	29.5	61
208	4	8	TB26D18R6	1	260	180	600	34.5	61
209	5	8	TA26D16R1	0	260	160	150	39.5	61
210	6	8	TB26D16R1	1	260	160	150	44.5	61
211	7	8	TA26D16R3	0	260	160	300	49.5	61
212	8	8	TB26D16R3	1	260	160	300	54.5	61
213	9	8	TA26D16R6	0	260	160	600	59.5	61
214	10	8	TB26D16R6	1	260	160	600	64.5	61
215	11	8	TA31D18R1	0	310	180	150	69.5	61
216	12	8	TB31D18R1	1	310	180	150	74.5	61
217	13	8	TA31D18R3	0	310	180	300	79.5	61
218	14	8	TB31D18R3	1	310	180	300	84.5	61
219	15	8	TA31D18R6	0	310	180	600	89.5	61
220	16	8	TB31D18R6	1	310	180	600	94.5	61
221	17	8	TA31D16R1	0	310	160	150	99.5	61
222	18	8	TB31D16R1	1	310	160	150	104.5	61
223	1	11	TA31D16R3	0	310	160	300	19.5	76
224	2	11	TB31D16R3	1	310	160	300	24.5	76
225	3	11	TA31D16R6	0	310	160	600	29.5	76
226	4	11	TB31D16R6	1	310	160	600	34.5	76
227	5	11	TA36D21R1	0	360	210	150	39.5	76
228	6	11	TB36D21R1	1	360	210	150	44.5	76
229	7	11	TA36D21R3	0	360	210	300	49.5	76
230	8	11	TB36D21R3	1	360	210	300	54.5	76
231	9	11	TA36D21R6	0	360	210	600	59.5	76
232	10	11	TB36D21R6	1	360	210	600	64.5	76
233	11	11	TA36D20R1	0	360	200	150	69.5	76
234	12	11	TB36D20R1	1	360	200	150	74.5	76
235	13	11	TA36D20R3	0	360	200	300	79.5	76
236	14	11	TB36D20R3	1	360	200	300	84.5	76
237	15	11	TA36D20R6	0	360	200	600	89.5	76
238	16	11	TB36D20R6	1	360	200	600	94.5	76
239	17	11	TA41D21R1	0	410	210	150	99.5	76
240	18	11	TB41D21R1	1	410	210	150	104.5	76
241	1	9	TA41D21R3	0	410	210	300	19.5	66
242	2	9	TB41D21R3	1	410	210	300	24.5	66
243	3	9	TA41D21R6	0	410	210	600	29.5	66
244	4	9	TB41D21R6	1	410	210	600	34.5	66
245	5	9	TA41D24R1	0	410	240	150	39.5	66
246	6	9	TB41D24R1	1	410	240	150	44.5	66
247	7	9	TA41D24R3	0	410	240	300	49.5	66
248	8	9	TB41D24R3	1	410	240	300	54.5	66
249	9	9	BLANK				59.5	66	
250	10	9	PR5TEST1					64.5	66
	7	MHZ	CLOCK	TRIANGULAR		SQUARE	RECT	RATIO	01:01.5
251	11	9	TA41D24R6	0	410	240	600	69.5	66
252	12	9	TB41D24R6	1	410	240	600	74.5	66
253	13	9	TA41D25R1	0	410	250	150	79.5	66
254	14	9	TB41D25R1	1	410	250	150	84.5	66
255	15	9	TA41D25R3	0	410	250	300	89.5	66
256	16	9	TB41D25R3	1	410	250	300	94.5	66
257	17	9	TA41D25R6	0	410	250	600	99.5	66
258	18	9	TB41D25R6	1	410	250	600	104.5	66
259	1	10	TA26D18R1	0	260	180	150	19.5	71
260	2	10	TB26D18R1	1	260	180	150	24.5	71
261	3	10	TA26D18R3	0	260	180	300	29.5	71
262	4	10	TB26D18R3	1	260	180	300	34.5	71
263	5	10	TA26D18R6	0	260	180	600	39.5	71
264	6	10	TB26D18R6	1	260	180	600	44.5	71

265	7	10	TA26D16R1	0	260	160	150	49.5	71
266	8	10	TB26D16R1	1	260	160	150	54.5	71
267	9	10	PR5TEST1					59.5	71
	8	MHZ	CLOCK TRIANGULAR		SQUARE		RECT	RATIO	01:01.5
268	10	10	BLANK				64.5	71	
269	11	10	TA26D16R3	0	260	160	300	69.5	71
270	12	10	TB26D16R3	1	260	160	300	74.5	71
271	13	10	TA26D16R6	0	260	160	600	79.5	71
272	14	10	TB26D16R6	1	260	160	600	84.5	71
273	15	10	TA31D18R1	0	310	180	150	89.5	71
274	16	10	TB31D18R1	1	310	180	150	94.5	71
275	17	10	TA31D18R3	0	310	180	300	99.5	71
276	18	10	TB31D18R3	1	310	180	300	104.5	71

Appendix C - 2D Planewave Solver

C.1 Simulation_Parameters.txt

```
RELEASE NOTES for version 3:
**************************

GENERAL DESCRIPTION:
*********************
3D plane wave solver
TE and TM modes become mixed up.
SOlves eigenvectors for specified bands, in order to calculate poynting vector of field. THis gives
indication of polarization states of individual modes.

SUMMARY OF FUNCTIONALITY:
*************************
Band diagrams:
        Generalized (Trapezoidal) lattice
                Correct irreducible Brilloin zone circuit for generalized (trapezoidal) lattice

Field reconstruction plots
Density of States
Dispersion surface contour plots:
        works for exel or mathematica file output.
        works properly for trapezoidal lattice.

*********************************************************************************
*********
Options setting variables
*********************************************************************************
*********
Lattice types:
s for square,
t for triangular
r for rectangular (orthogonal axes definable aspect ratio.)
e for trapezoidal lattice (This is a cmpletely general lattice where vectors are specified by angle and
aspect ratio)
*********************************************************************************
*********

// Run time debugging Options (data to be displayed on screen)
kxy                                                     = 1
                // test k-vector sample number for debugging purpose
debug                                                   = n
show TEeigenvalue solutions                             = y
show TM         eigenvalue solutions                    = y
show TE effective phase index                           = n
show TM effective phase index                           = n
save solutions repeatedly                               = n
                        // currently doesnt work if set to 'y'
show density of states solutions                        = n
```

```
display smaple k vectors                                                    = y
        y or n
display sample k vector gradients                                           = n

//      Program options
construct a band diagram or dispersion surface plot                         = y
construct a field plot for selected band and k-vector sample                = n
reconstruct     the dielectric function (fo double check all is OK)         = n
                y or n
lattice shape                                                               = t
output_scaling                                                              = w
                w for wavelength ,f for normalised frequency
file_type                                                                   = e
                data file type m for Mathematica, e for excel n for none

*********************************************************************************
*********
Photonic crystal parameters
*********************************************************************************
*********
diagram types:
0 for standard band diagram specified by angles
1 for selected directions only from Gamma point
2 for selected directions all B.Z. sections.
3 for dispersion surface contour plots
4 for density of states plot
*********************************************************************************
*********

lattice pitch (nm)                                                          = 310.0
epsb (Bulk)                                                                 = 2.334784
epsa (Holes / rods)                                                         = 1
number of plane waves                                                       = 9
hole diameter (nm)                                                          = 180.0
number of bands  to be saved                                                = 20
aspect ratio (x : y) (vector length reduction factors)                      = 1             1

                // applicable to lattice types d and e.
vector angle (deg)                                                          = 90
                // applicable to lattice type e only.
diagram type                                                                = 0

*********************************************************************************
*********
k-vector circuit parameters for BAND DIAGRAMS

*********************************************************************************
*********
sample angles in degrees from A-vector.
note zero corresponds to Gamma-X direction in reciprocal space
*********************************************************************************
*********

number of kvector samples                                                   = 30
                        // number of k-vector samples / B.Z. section.
```

```
number of sample angles                                                    = 10
                    // applicble to diagram types 1 and 2 only
actual sample angles                                                       = 0          5
        10      15      20      25      30      35      40      45
                // applicble to diagram types 1 and 2 only

**********************************************************************************
*********
k-vector parameters for DISPERSION SURFACE CONTOUR PLOTS
**********************************************************************************
*********

// parameters for dispersion surface contour plots
k-vector sampling grid resolution (x,y) (samples per unit cell)            = 10
dispersion surface contour plot area (no. unit_cells)                      = 3

**********************************************************************************
*********
k-vector parameters for DENSITY OF STATES integration
**********************************************************************************
*********

k-vector sampling grid resolution (x,y)                                    = 10
                // also for dispersion surface contour plots
integration resolution      range                                          = 10
                // for DOS only
lowest_wavelength                                                          = 200
                // for DOS only
highest_wavelength                                                         = 2000
                // for DOS only
minimum sampling segment angle  (deg)                                      = 0
                // for DOS only
maximum sampling segment angle  (deg)                                      = 30
                // for DOS only

**********************************************************************************
*********
parameters for field reconstruction plots//
**********************************************************************************
*********

propagation angle (deg)                                                    = 5
k-vector magnitude (scaled w.r.t. BZ perimeter boundary)                   = 1.0
sample dispersion band                                                     = 1
field plot area (no. unit cells)                                           = 4

**********************************************************************************
*********
Fourier transform function plot parameters   (for debugging purpose)

**********************************************************************************
*********

fourier transform function plot area                                       = 20
```

```
*****************************************************************************
*********
dielectric function plot paramators

*****************************************************************************
*********

dielectric function plot area (unit cells)                    = 3

*****************************************************************************
*********
output file paths and names          (spaces in text strings are not allowed at present)


*****************************************************************************
*********

output file path                                              =
C:\Plane_wave_data
fourier coefficeint matrix file                               =
matrix_test_file1.dat
fourier transform plot file                                   = ftr_file.dat
dielectric function plot file                                 = dielectric.dat
band structure results file                                   = trapezium.dat
TE field reconstruction file                                  = TE_field.dat
TM field reconstruction file                                  = TM_field.dat

*****************************************************************************
*********
```

Appendix D - Batch Listings and Wafer Numbers

This is not a complete batch listing of all processing work carried out in the PhD. Rather it is intended as a guide to assist in the reading of the thesis. The omitted batches contained repetitive and unoriginal work required for the other batches, such as the thermal oxidation of silicon wafers to be used in later batches.

K2047dt - Si_3N_4-based waveguides

- All Wafers	2.1μm thermal SiO_2
- #1-10	125nm LPCVD Si_3N_4
- #11-20	231nm LPCVD Si_3N_4
- #1-9,11-19	200nm PECVD SiO_2

K2048dt - PECVD Si_3N_4

- All Wafers	2.1μm thermal SiO_2
- #1-2	1685Å PECVD Si_3N_4
- #1-2	116Å PECVD Si_3N_4 to bring up to 1801Å
- #1	2087Å PECVD SiO_2
- #3-4	2422Å PECVD Si_3N_4
- #3	2087Å PECVD SiO_2
- #5	6563Å PECVD Si_3N_4
- #6	3402Å PECVD Si_3N_4
- #6	1689Å PECVD Si_3N_4 to bring up to 5091Å

K2049dt - IR Waveguides (thick Si_3N_4 waveguides)

- All Wafers	2.1μm thermal SiO_2
- #1-3	5071Å PECVD Si_3N_4
- #4,5,9	4955Å PECVD Si_3N_4
- #10-12	4880Å PECVD Si_3N_4
- #13-15	4753Å PECVD Si_3N_4
- #1-3	1962Å PECVD SiO_2 cladding
- #4,5,9	1962Å PECVD SiO_2 cladding
- #10-12	1962Å PECVD SiO_2 cladding
- #12	Taken over to Chilworth for transmission measurements
- #15	Chopped up for PL measurements
- #1-5,9	chrome evaporated 25nm
- #5	photolithography, but not etched
- #1,2,9	phtoolithography and etched
- #2,3,13,14	in for 50nm chrome evaporation

R2058r- PECVD OxyNitride Development

Layers of SiON on Si Check Wafers

- #1 777/140 sccm SiH_4/N_2O, 50sccm NH_3 500mT, 10W, 20min
- #2 777/200 sccm SiH_4/N_2O, 50sccm NH_3 500mT, 10W, 20min
- #3 350/375 sccm SiH_4/N_2O, 20sccm NH_3 1000mT, 20W, 10min
- #4 400/300 sccm SiH_4/N_2O, 20sccm NH_3 1000mT, 20W, 10min
- #5-6 525/250 sccm SiH_4/N_2O, 20sccm NH_3 1000mT, 20W, 5min
- #7-8 615/215 sccmSiH_4/N_2O, 20sccm NH_3 1000mT, 20W, 5min
- #9-10 777/75 sccm SiH_4/N_2O, 50sccm NH_3 500mT, 10W, 20min
- #11-12 777/91 sccm SiH_4/N_2O, 50sccm NH_3 500mT, 10W, 20min
- #13-14 780/82 sccm SiH_4/N_2O, 50sccm NH_3 500mT, 10W, 20min
- #15-16 780/86 sccm SiH_4/N_2O, 50sccm NH_3 500mT, 10W, 20min
- #17-18 780/101 sccm SiH_4/N_2O, 50sccm NH_3 500mT, 10W, 20min
- #19 777/78 sccm SiH_4/N_2O, 50sccm NH_3 500mT, 10W, 20min

Waveguides of SiON

- #20-21 2.1μm thermal SiO_2
- #20 350/375 sccm SiH_4/N_2O, 20sccm NH_3 1000mT, 20W, 190s
- #21 777/100 sccm SiH_4/N_2O, 50sccm NH_3 500mT, 10W, 16min

R2062r - PECVD Si-nc (finished)

Layers of SRSO on Si Check Wafers

- #1,2 500/120 sccm SiH_4/N_2O, 500mT, 20W, 15min
- #3 448/202 sccm SiH_4/N_2O, 500mT, 20W, 15min
- #4 406/244 sccm SiH_4/N_2O, 500mT, 20W, 15min
- #5 371/279 sccm SiH_4/N_2O, 500mT, 20W, 15min
- #2 chrome evaporated 50nm

R2140r - More nanocrystals

Layers of Si:Si_3N_4 on Si Check Wafers

- #1 700Å PECVD Si_3N_4
- #2 800Å PECVD 778sccm SiH_4, 25sccm NH_3
- #3 1000Å PECVD 778sccm SiH_4, 10sccm NH_3

Anneal time experiment on SRSO epi-layers

- #12 2.1μm thermal SiO_2
- #6-10, 12 PECVD SRSO deposition (448/202 sccm SiH_4/N_2O, 15 min)
- #6, #12 Anneal at 1150°C for 1 hr
- #7 Anneal at 1150°C for 30 min
- #8 Anneal at 1150°C for 3 hr
- #9 Anneal at 1200°C for 1 hr
- #12 Chrome evaporation 50nm

R2198r - Photonic Crystals formed in Waveguides of SRSO - ROTLINES pattern

- All wafers 2.1μm thermal SiO_2

Waveguides of PECVD Si_3N_4

- #9 2000Å PECVD Si_3N_4
- #10 4000Å PECVD Si_3N_4
- #9,10 Cleaved in 2 and half annealed 1hr 1150deg

Waveguides in SRSO

- #1-3 3000Å Si-rich SiO_2 (at 1000mT)
- #5-8 4000Å Si-rich SiO_2 (at 1000mT)
- #1-6, 8 Annealed 1hr 1150deg (n.b. #4 annealed thermal oxide)
- #1-3,5-7,9,10 2000Å SiO2
- #7 Removed for optical measurements in ORC

Fabrication of photonic crystals

- #1-3,6,5 Chrome evaporation 50nm
- #1 Ebeam done, chrome etch done, plasma etch done. Good. Sawn
- #2, Ebeam , Ion Beam Milling done (useless)
- #3 Ebeam , Ion Beam Milling, and etching done (useless)
- #5 Ebeam done, wet chrome, plasma etch done. Looks good. Sawn
- #6 Prisms2 - Sawn and sent to chilworth

R2256 - More Photonic Crystals in SRSO Waveguides - SQLINES patterns

These samples deposited at lower pressure so poor optical waveguides

- All wafers 2.1μm thermal SiO_2
- #1-12 4000Å Si-rich SiO_2 (at 500mT)
- #1-12 Annealed 1 hr 1150°C
- #1-12 2000Å SiO_2
- #1-12 Evaporate 120nm chrome
- #1-12 Hardbake and resist spin
- #12 ebeam done, chrome wet etch 1'45+10+15+10s
- #12 20s more development, 2 mins wet chrome (metals room).
- #12 30ish mins plasma etch+20+7mins - ruined
- #1 Roasted over in the ORC IBM - ruined
- #2 Finished and removed for measurement
- #3 Finished (SQLines1) - Finished and removed for measurement
- #4 Finished (SQLines2) - Mapped

k2351 - SRSO checks and waveguides for PL and transmission measurements

- #1-28 blank checks, #29-40 2.1um oxidised wafers

Anneal time investigation

- #1-7 Deposit 3400Å si-rich n=1.71 (at 1000mT)
- #8-14 Deposit 4060Å su-rich n=1.62 (at 1000mT)
- #15-21 Deposit 4400Å si-rich n=1.57 (at 1000mT)
- #22-28 Deposit 4400Å si-rich n=1.55 (at 1000mT)
- #2,9,16,22 Anneal .5h at 1150°C
- #3,10,17,23 Anneal 2hr at 1150°C
- #5,12,19,25 Anneal 3hr + 1hr at 1150°C
- #6,13,20,26 Anneal 6hr at 1150°C
- #7,14,21,28 Anneal 10hr at 1150°C

Deposition pressure investigation

- #29 Deposit 500mT 450/203 SiH_4/N_2O
- #30 Deposit 1000mT 450/201 SiH_4/N_2O
- #29,30 Deposit 200nm SiO_2

Waveguide transmission investigation

Waveguide Thickness

- #31 5min 451/202 SiH_4/N_2O 1000mT "A"
- #32 10min 451/202 SiH_4/N_2O 1000mT
- #31,32 200nm SiO_2

Transmission for different Si concentrations

- #31,32 Anneal 1hr 1150deg
- #33 6 mins 502/150 SiH_4/N_2O 1000mT
- #34 6 mins 408/244 SiH_4/N_2O 1000mT "B"
- #35 6 mins 373/280 SiH_4/N_2O 1000mT "C"
- #33-35 200nm SiO_2

Transmission for different anneal times

- #36 448/202 6 min wg == 'A'
- #37 406/244 6 min wg == 'B'
- #38 371/279 6 min wg == 'C'
- #36-8 Anneal cleaved quarters for .5hr, 1hr, 3hr, 6hr
- #2,3,5-7,9,10,12-14,16,17,29-21,22,23,25,26,28 Removed for PL measurements
- #36,37,38 Waveguide transmission and gain measurements (Chilworth)

Photonic crystal fabrication PRISMS pattern

- #39 6 mins 450/203 SiH_4/N_2O 1002mT
- #39 200nm SiO_2

- #40 6 mins 371/279 SiH_4/N_2O 1003mT
- #40 200nm SiO_2
- #39,40 6 hr anneal at 1150°C
- #39,40 Sent away to QUDOS for ebeam
- #40 5 min descum in gold asher
- #40 100s + 15s wet Cr etch
- #40 30 min dry etch in orange box
- #40 90 min gold ash, 5 min wet Cr etch
- #39 100s wet Cr etch
- #39 30 min dry etch in orange box

k2455 - SRSO waveguides for stock

- #1-5 2100nm SiO_2
- #6-8 2130nm SiO_2
- #9-12 2080nm SiO_2
- #1-3 6 mins SRSO 502/151 SiH_4/N_2O
- #4-6 6 mins SRSO 450/200 SiH_4/N_2O
- #7-9 6 mins SRSO 409/244 SiH_4/N_2O
- #10-12 6 mins SRSO 373/279 SiH_4/N_2O
- #1-12 Anneal 6 hr at 1150°C, 6 hr 750°C

k2482 - Metal evaporation onto SRSO for electrical measurements (incomplete)

- #1-3 30s 503/150 SiH_4/N_2O
- #4-6 30s 449/202 SiH_4/N_2O
- #7-9 25s 407/242 SiH_4/N_2O
- #10-12 25s 373/278 SiH_4/N_2O
- All wafers Cleaved into quarters (a,b,c,d)
- b quarters 1hr anneal
- c quarters 3hr anneal
- d quarters 6 hr anneal
- All wafers Spun resist onto fronts
- All wafers Stuck onto dummy wafers with resist and hardbaked
- All wafers Evaporate 100nm Aluminium onto back
- All wafers Remove quarters from dummies by heating and FN clean